Laser Ablation and Surface Structuring of Selected Solid Targets

A thesis submitted for the degree of

Doctor of Philosophy

to the

Jawaharlal Nehru University

by

Nancy Verma

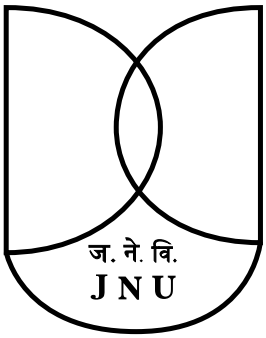

Light and Matter Physics Group
Raman Research Institute,
Bengaluru, INDIA.

February, 2022

Dedicated to

My teachers, my family and my friends

Declaration

I, **Nancy Verma**, hereby declare that the work presented in this thesis titled **'Laser Ablation and Surface Structuring of Selected Solid Targets'** is completely original. This research work is carried out under the supervision of **Prof. Reji Philip** at the **Raman Research Institute, Bengaluru, India**. This dissertation is the result of my own work unless otherwise stated. No part of this thesis has been submitted elsewhere for the award of any degree, diploma, membership, fellowship or any other similar title of any university or institution. I also declare that this thesis has been passed through the **Turnitin** software to check for plagiarism.

Prof. Reji Philip
Thesis Supervisor
Raman Research Institute,
Bengaluru - 560080,
INDIA.

Nancy Verma
Student

Date:

Place:

Certificate

This is to certify that the work contained in the thesis titled **'Laser Ablation and Surface Structuring of Selected Solid Targets'**, submitted by **Nancy Verma** (Enrollment No. - RRI/2015/010) to **Jawaharlal Nehru University** for the award of the degree of **Doctor of Philosophy** in Physical Sciences, is the bonafide record of original research work carried out by the candidate from August 2015 - February 2022, under my guidance and supervision at the **Raman Research Institute**, Bengaluru, India. The results embodied in the thesis have not been submitted to any other University or Institute for the award of any degree or diploma.

Prof. Tarun Souradeep Ghosh
Director
Raman Research Institute,
Bengaluru - 560080,
INDIA.

Prof.Reji Philip
Thesis Supervisor

Acknowledgements

My Ph.D. tenure has been a period of immense learning and growth on both scientific and personal levels. My journey to achieving this significant milestone would not have been possible without the constant support and guidance from the people around me.

First and foremost, I would like to express my heartfelt gratitude to my guide, Prof. Reji Philip, for his immense support and skillful guidance. He has always encouraged me to explore new ideas and nurtured me throughout these years. I have always admired his patience and calm nature during all situations. The faith and confidence he showed in me have uplifted me during the stressful time and kept me ongoing. I thank him for providing me with the opportunity of joining his group and working under his supervision.

A special thanks to my thesis advisory members, Prof. Andal Narayanan and Prof. Sadiq Rangwala, for their constructive and timely feedback. I am thankful for all the insightful discussions which kept me on track. I am also thankful to the former director of the institute, Prof. Ravi Subrahmanyan, and the present director, Prof. Tarun Souradeep Ghosh, for their help and support.

I would also like to thank my collaborators, Prof. S. S. Harilal and Prof. Balaram Sahoo, for their fruitful discussions and critical suggestions. I express my special appreciation and thanks to Dr. Anoop K. K. for introducing me to the

exciting field of laser structuring and mentoring me throughout my Ph.D. tenure. I appreciated the time spent discussing various research ideas and our joined publications. I sincerely thank Dr. Jinto Thomas, Dr. Jijil J.J. Nivas, Dr. Smijesh N., Dr. Kavya H. Rao, and Dr. Rajeev Kumar for helping and teaching me various experimental techniques.

I am incredibly grateful to Mr. K. M. Yatheendran for all the help in characterizing my samples and technical support. He has always been very patient and kind to me. I also thank Mrs. Meena and Mr. Mugundhan for their technical support in my experiments.

Soon after joining the Ultrafast and Nonlinear Optics (UNO) Group, I interacted with UNO lab members, who welcomed me and helped me when I started working in the lab. I express my gratitiude to all my senior labmates, Dr. Anoop K. K., Mr. Shafi Ollakkan, Dr. Pranitha Sankar, Mr. Ajay Kumar, and Mr. Gaurav Tiwari. I thank all the former members of our lab Priya Dominic, Agnes George, Anjali V Murali, Aji Alexander, Nithin Joy, Kiran Michael, Arjun K. K., and Ashly Jose, for helping me and creating a cheerful environment in the lab. A special thanks to Priya and Arjun for assisting me in the experiments. I also want to thank my present labmates, Beryl C., Amogh M.S., Sebin Xavier, and Cyril, for their help and support. I thank all the students and faculty members of the LAMP group for sharing optical components and instruments.

I express my heartfelt gratitude to the RRI administration for facilitating the scientific environment. I sincerely thank the former and present administrative officers C. S. R. Murthy and Naresh V. S. for support in various matters. I express my gratitude to Marisa, Radha, Vidya, Subbu, Sachin, Harini, Mamta, Shailaja, and Prema for helping me with all the official work.

I am very thankful to Savitha for her affection and support. She has always been caring and kind to me throughout my Ph.D. tenure. I appreciate and thank Shiva and Manju for all their help and support.

I sincerely thank the library staff, especially Meera, M. Manjunath, Manjunath K., Nagaraj, and Vani, for providing a pleasant environment and helping me throughout my tenure.

I gratefully acknowledge the civil and electrical department staff, G. B. Suresh, Sasidharan, Sridhar (late), Muneeswaran, Chetan, and others, who came to our rescue many times. I sincerely thank all the RRI staff, including the computer department, accounts section, purchase section, EEG department, canteen, medical staff, security, and transport, for their help and support.

I sincerely appreciate and thank Ibrahim Ji, Anand Ji, Hari, and all the staff of RRI workshop. They provided solutions to all our practical and experimental design-related issues by accurately bringing them into reality.

I feel blessed to have so many fabulous friends at RRI. I thank all my batchmates, specially Adwaith, Arsalan, Akash, Irla, Nishant, Sanhita, Maheswar, Saichand, Silpa and Bhagya. A special thanks to Sanhita and Adwaith for hearing my nonsense and talking sense to me. I had some great seniors who welcomed me with open hearts; making me feel at home. I express my heartfelt gratitude to Nazma, Meera, Shreeja, Varun, Gayathri, Deepak, Sushil, Rahul, Reena, Raj, Nomaan, Adwaith, Anand, Palak, Chandeshwar, Saurabh, Sukhveer, Vishnu, Arsalan, Nishant, Sebanti, Gunjan, Manami, Akhil, Vaibhav and all others. Words fall short to express the happiness I felt with them. Sunday cooking with them followed by long walks and random funny talks are the events I will always cherish. I thank Umaji, Sharadaji, Padmaji, Mangla

Ji, and Rathnammaji for providing us with homely food. A special thanks to all my juniors.

I also thank my friends Gaurav, Manish, Keshav, Akash, Vikas, Priyank, Dhanshree for all the scientific discussions and support. I thank Devanshi Bhardwaj for all her help and support. Thanks for being such a fantastic companion and friend.

I am indebted to all my B.Sc. and M.Sc. teachers, especially Prof. Hari Prakash (late) and Prof. Ranjana Prakash (late), for their encouragement and support. I owe a big thanks to my M.Sc. thesis supervisor Prof. Vivek Kumar Tiwari, for supporting me and providing a motivating environment.

My wholehearted thanks and gratitude to my family, especially my mother (Anju Verma), my father (Ashutosh Verma), and my brother (Ashish Verma), for their unconditional support and motivation throughout my Ph.D. tenure. Thank you for being a constant source of inspiration and having an uncompromised faith in me, and I hope that I have made you proud. Last but certainly not the least, Anant, for being so caring and supportive. It means the world to me to have you by my side, no matter what. Thanks for always being there for me.
Thanks to all of you for being a part of my life and making me what I am today.

Nancy Verma

Synopsis

Studies in light-matter interaction have grown exponentially since the invention of the first pulsed laser by T. H. Maiman in 1960. While developments like mode-locking (ML) have enabled the generation of light pulses with temporal widths shorter than a few tens of picoseconds (ps), innovations like chirped pulse amplification (CPA) have resulted in the production of fs laser pulses with peak powers ranging from terawatts (TW) to multi-petawatts (PW). These advances in laser technology have opened up various new domains of ultrafast laser-matter interaction. For example, ultrafast lasers facilitate precision laser processing with tremendous practical applications in diverse fields. Furthermore, the unprecedented intensities provided by ultrafast laser pulses are sufficient for the production of dense plasmas, enabling high-order harmonic generation (HHG) for the realization of extreme ultraviolet (EUV) light sources.

When a laser pulse is incident on a target, surface ablation and material removal occur in the irradiated region if the pulse energy exceeds the binding energy (ablation threshold) of the material. In particular, soft laser ablation can create surface features of various shapes and sizes depending on laser parameters such as laser fluence, wavelength, pulse width, spatial and temporal profiles of the beam, irradiation geometry, and processing environment (liquid or background gas). In general, these surface features are categorized as coherent structures and non-coherent structures. Coherent structures (mostly ripples) originate from the oscillating radiation field which is generated by the interference between the incident laser light and the surface scattered wave, result-

ing in an inhomogeneous energy distribution on the surface. In some cases, it is governed by the propagating excited surface plasmon polaritons (SPP). The spatial periodicity of coherent structures will be proportional to the laser wavelength. The ripples are oriented perpendicular to the incident polarization direction (electric vector) of the incident light. These ripples, called laser-induced periodic surface structures (LIPSS), were first observed on various semiconductor surfaces by Birnbaum in 1965. The spatial period and orientation of non-coherent structures are not associated with the wavelength and polarization of the laser beam, and their appearance is subject to the ambient pressure and laser intensity. Compared to ps and ns laser pulses, fs-laser processing has two significant benefits:

- rapid non-thermal energy deposition results in minimal heat-affected zone (HAZ), significantly reducing surface debris and recast layers to the surrounding area, and
- the ablation threshold is reduced for the same laser wavelength and irradiation geometry,

allowing the fabrication of sub-wavelength nano-structures when irradiated close to the ablation threshold. At higher fluences, the electric field strength overcomes the coulombic field resulting in the ejection of electrons from atoms and molecules by multi-photon excitation. Under such high irradiance, matter transforms into a collection of ionized species called plasma. Together, fs and ns laser ablation enable us to understand laser-matter interaction at both low and high fluence and intensity regimes.

This thesis reports investigations of intense laser-matter interaction in selected target materials (semiconductor, dielectric, and metal) employing fs and ns laser pulses. We have used a regeneratively amplified Ti:Sapphire laser system which produces pulses of 100 fs duration with 10 mJ energy in the near-infrared wavelength regime (800 nm). Various morphological changes of the

irradiated materials, and the optical and electrical properties of the plasma emanating from the irradiated targets, are explored. The organization of the thesis is as follows:

Chapter 1 gives a brief introduction to intense laser-matter interaction (laser ablation of solid targets in particular), underlying mechanisms of material ablation, and surface functionalization employing fs and ns laser pulses. A detailed discussion on laser-induced surface structuring and their applications is provided.

Chapter 2 describes the experimental techniques employed in this work. It provides a detailed description of the characterization techniques, fs and ns laser sources, spectrometers, and vacuum systems used in the work.

Chapter 3 presents studies of the relative enhancement of optical and ion emissions from a laser-induced periodic surface structured silicon sample, used as a target for laser-produced plasma generation. The structures are fabricated using 800 nm, 100 fs pulses obtained from a regeneratively amplified Ti:sapphire laser system. The LIPSS patterns strongly depend on the laser pulse energy, state of polarization, irradiation dose on the target, and the background gas pressure. The role of laser wavelength is studied by using the second harmonic output of the laser (400 nm) also for fabrication. Large area (5×4 mm^2) surface structuring has been carried out at atmospheric pressure after optimizing the laser parameters at 800 nm wavelength. The patterned silicon surface shows a substantial reduction in the reflection of incident light over a wide range of wavelengths compared to plain silicon.

Moreover, when used for laser-induced breakdown spectroscopy experiments, enhanced optical emission and ion current have been observed from the patterned surface. This enhancement indicates increased coupling of laser energy to the surface in the case of patterned silicon (shown in Figure 1). While spectral lines emitted by doubly ionized silicon have been observed from the patterned surface, the plain surface gives lines from singly ionized silicon only.

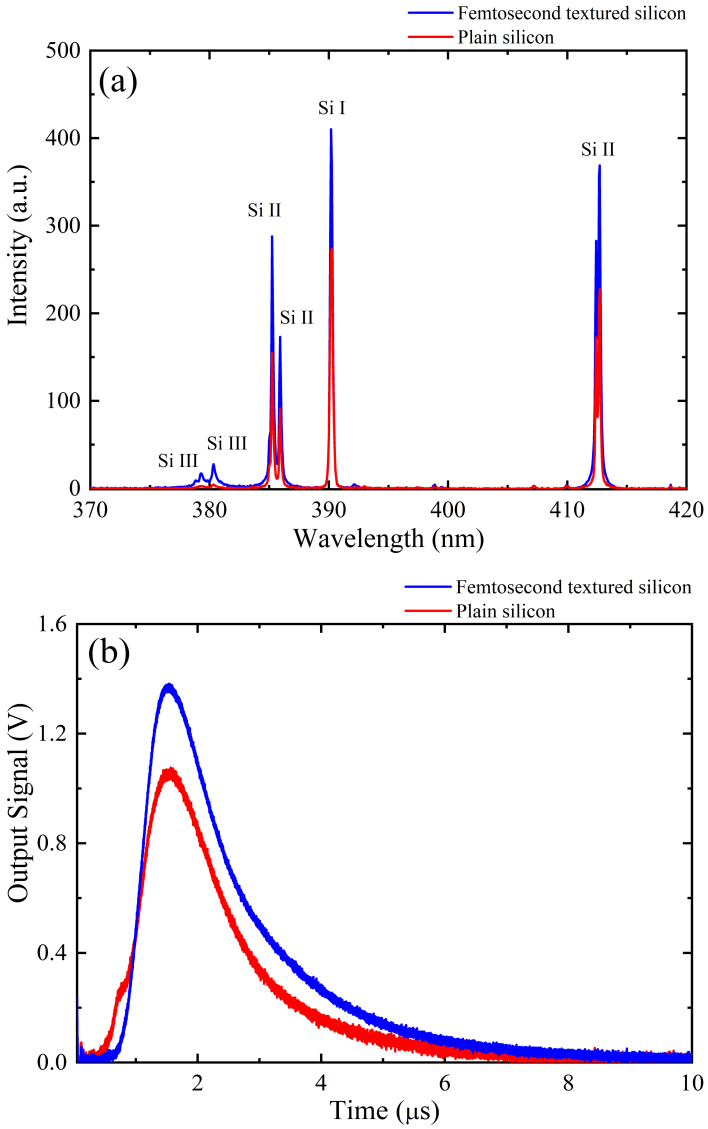

Figure 1: Relative intensity enhancement seen in the (a) laser-induced breakdown spectroscopy (LIBS) data, and (b) ion current signals, from plasma generated on the structured silicon surface. Blue color represents signals from structured silicon, while red color represents signals from the unprocessed silicon target.

A discernible enhancement has been measured in both optical ($50\% - 90\%$) and electrical (34%) signals measured from the plasma generated on the patterned surface.

Chapter 4 describes laser-induced surface structuring of selected dielectric materials (fused silica and quartz) by means of fs laser ablation to explore the effect of crystallinity on LIPSS. fs-LIPSS of two different types referred to as

Low spatial frequency LIPSS (LSFL) and High spatial frequency LIPSS (HSFL), with distinct spatial periodicity and orientation, have been inscribed. Single and multi-pulse ablation thresholds and efficacy factors are calculated. With the optimization of laser parameters, large area surface (6×6 mm^2) texturing is achieved by the raster scanning method to explore modifications in the optical and wetting properties. Contact angle (CA) measurements show the formation of superhydrophilic textured surfaces, which have potential applications in anti-fouling, anti-reflective surfaces, and biosensors.

Chapter 5 reports the fabrication and characterization of large area micro-/nano-textured silicon surfaces using Nd:YAG laser pulses of nanoseconds duration (7 ns). An area of $6\times$ 6 mm^2 has been textured by the parallel line scanning method to create hierarchical structures, consisting of microscale channels and self-organized surface nano-capillaries decorated with randomly distributed silicon nanoparticles.

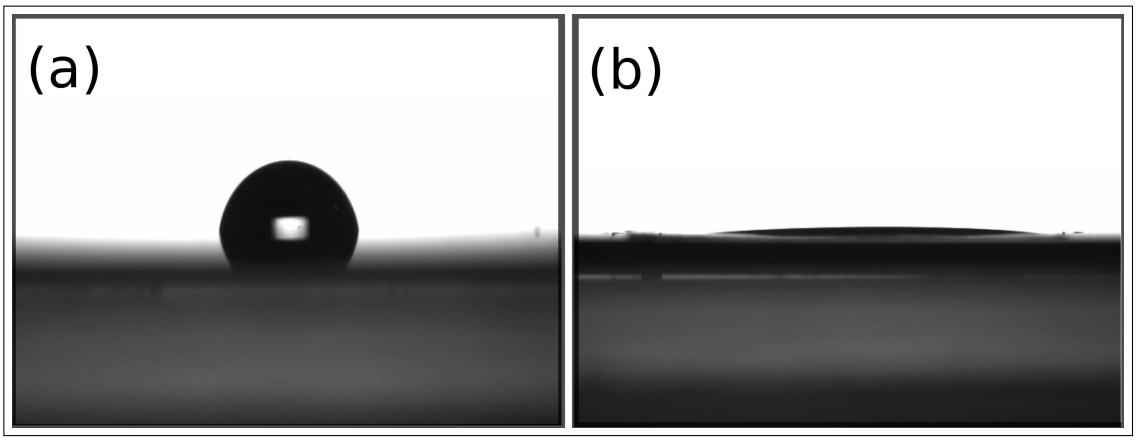

Figure 2: Photographs of distilled water (1µL) droplets on silicon surfaces: (a) untreated silicon with CA = 80.9° $\pm$ 0.6°, and (b) textured silicon processed at the fluence F_p = 0.94 J/cm^2 with CA = 5.4°$\pm$ 0.6°.

The combination of micro-channels and nano-capillaries results in a superhydrophilic silicon surface (shown in Figure 2), with the contact angle reduced substantially from about 80° to nearly 5°. In contrast to most of the reports given in the literature, the superhydrophilicity of the surface remains stable without

a shift to hydrophobicity, even after exposure to the atmosphere for about three months. Thus, long-lasting and durable superhydrophilic silicon has been obtained by using maskless, compact, and cost-effective nanosecond laser writing without the need to employ any chemical post-processing. Potential applications of these surfaces include heat exchangers, biosensors, cell adhesives, and self-cleaning solar cells.

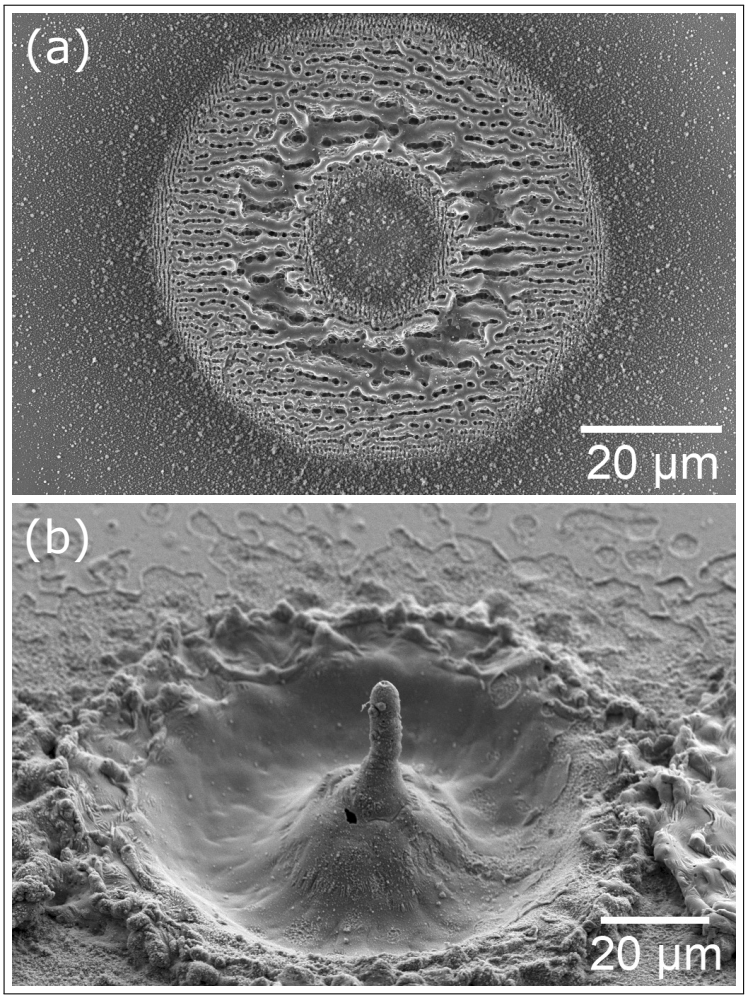

Figure 3: SEM images of the textures developed by a vortex beam in (a) loose focusing, and (b) tight focusing conditions, producing various hierarchical structures and microneedles, respectively.

Chapter 6 illustrates the generation and characterization of optical vortex (OV) beams by using spiral phase plates of topological charge ($\ell = 4$). Surface structuring is carried out with fs OV beam with orbital angular momen-

tum (OAM) and different states of polarization (SoP) in the transverse plane, enabling the generation of complex surfaces. Figure 3 shows SEM images of the textures developed by the structured beam in loose (Figure 3(a)) and tight (Figure 3(b)) focusing conditions. These structured beams demonstrate the fabrication of micro-needles on crystalline silicon(100), which has several practical applications.

Chapter 7 summarizes the important observations and conclusions drawn from the experiments reported in this thesis. Possible directions for future work are outlined.

Prof. Reji Philip
Thesis Supervisor
Raman Research Institute,
Bengaluru - 560080,
INDIA.

Nancy Verma
Student

List of Publications

A. Journal Publications:

Publications included in the thesis

1. Fabrication of durable superhydrophilic silicon surfaces using nanosecond laser pulses
   Nancy Verma, K. K. Anoop, Priya Dominic, and Reji Philip, *Journal of Applied Physics*, **128**, no. 13, 135304, 2020.

2. Enhancement of optical emission and ion currents in a laser produced silicon plasma by femtosecond laser-induced periodic surface structuring
   Anoop, K. K., **Nancy Verma**, Nithin Joy, Sivanandan S. Harilal, and Reji Philip, *Physics of Plasmas*, **25**, no. 6, 063304, 2018.

3. Femtosecond and nanosecond laser-assisted processing of crystalline silicon: Morphology and optical properties
   Nancy Verma, Anoop, K. K., Nithin Joy, and Reji Philip *(To be communicated)*

4. Femtosecond laser induced surface texturing of fused silica and quartz
   Nancy Verma, and Reji Philip, *(To be communicated)*

5. Formation of silicon microneedles by irradiation using femtosecond optical vortex pulses
   Nancy Verma, and Reji Philip, *(To be communicated)*

Publications not included in the thesis

1. Modulating non-linear optical absorption through controlled graphitization of carbon nanostructures containing Fe3C-graphite core-shell

nanoparticles
Kumar, Rajeev, Ajay Kumar, **Nancy Verma**, A. V. Anupama, Reji Philip, and Balaram Sahoo. *Carbon*, **153**, 545-556, 2019.

2. Ni nanoparticles coated with nitrogen-doped carbon for optical limiting applications
Kumar, Rajeev, Ajay Kumar, **Nancy Verma**, Vijay Khopkar, Reji Philip, and Balaram Sahoo, *ACS Applied Nano Materials*, **3**, 8618-8631, 2020.

3. FeCoCr alloy-nanoparticle embedded bamboo-type carbon nanotubes for non-linear optical limiting application
Kumar, Rajeev, Ajay Kumar, **Nancy Verma**, Reji Philip, and Balaram Sahoo, *Journal of Alloys and Compounds*, **849**, 156665, 2020.

4. Effect of the band gap and the defect states present within band gap on the non-linear optical absorption behaviour of yttrium aluminium iron garnets
Kumar, Ajay, Rajeev Kumar, **Nancy Verma**, A. V. Anupama, Harish K. Choudhary, Reji Philip, and Balaram Sahoo, *Optical Materials*, **108**,110163, 2020.

5. Mechanistic insights into the optical limiting performance of carbonaceous nanomaterials embedded with core–shell type graphite encapsulated Co nanoparticles
Kumar, Rajeev, Ajay Kumar, **Nancy Verma**, Reji Philip, and Balaram Sahoo, *Physical Chemistry Chemical Physics*, **22**, no. 46, 27224-27240, 2020.

B. Conference Publications:

1. Ultrashort laser-induced periodic surface structures on crystalline silicon
Anoop, K. K., **Nancy Verma**, Joy Nithin, and Philip Reji, *In AIP Conference Proceedings*, vol. 2244, no. 1, p. 070019. AIP Publishing LLC, 2020.

Contents

List of Figures

List of Tables

List of Abbreviations

2D-FFT	Two-Dimensional Fast Fourier Transform
AFG	Arbitrary Function Generator
AFM	Atomic Force Microscope
AOM	Acousto-Optic Modulator
ATI	Above Threshold Ionization
BBO	Beta Barium Borate
C.A.	Contact Angle
CPA	Chirped Pulse Amplification
DPO	Digital Phosphor Oscilloscope
EDS	Energy Dispersive X-ray Spectroscopy
FC	Faraday Cup
fs	femtoseconds
GVD	Group Velocity Dispersion
HAZ	Heat Affected Zone
HSFL	High Spatial Frequency LIPSS
IB	Inverse Bremsstrahlung
IR	Infrared

LIBS	Laser-Induced Breakdown Spectroscopy
LIDT	Laser-Induced Damage Threshold
LIPSS	Laser Induced Periodic Surface Structure
LPP	Laser-Produced Plasma
LSFL	Low Spatial Frequency LIPSS
ML	Mode-Locking
MPI	Multi-Photon Ionization
N.A.	Numerical Aperture
NBOHCs	Non-Bridging Oxygen Hole Centers
Nd:YAG	Neodymium doped Yttrium Aluminium Garnet
NPs	Nanoparticles
ns	nanoseconds
OAM	Orbital Angular Momentum
ODCs	Oxygen-Deficient Centers
OTBI/OBI	Over the Barrier Ionization
OTOF	Optical Time of Flight
OV-LIFT	Optical Vortex Laser-Induced Forward Mass Transfer
OV	Optical Vortex
PC	Pockels Cell
PL	Photoluminescence
PMT	Photomultiplier Tube
PORs	Peroxy Radicals
ps	picoseconds
RR	Radiation Remnants

SAM	Spin Angular Momentum
SDG	Synchronization and Delay Generator
SEM	Scanning Electron Microscope
SERS	Surfac-Enhanced Raman Spectroscopy
SEW	Surface Electromagnetic Waves
SFA	Strong-Field Approximation
SHG	Second Harmonic Generation
SLM	Spatial Light Modulator
SoP	State of Polarization
SP-plate	Spiral Phase Plate
SPM	Self-Phase Modulation
SPP	Surface Plasmon Polariton
STOC	Spin-to-Orbital Conversion
SWG	Subwavelength Grating
TAM	Total Angular Momentum
TI	Tunnel Ionization
TMP	Turbomolecular Pump
TPA	Two-Photon Absorption
TTM	Two-Temperature Model
XPS	X-Ray Photoelectron Spectroscopy

Chapter 1

Introduction

This chapter describes the fundamentals of intense light-matter interaction and the underlying mechanisms of laser ablation. The two-temperature model, illustrating the dynamics of laser energy transfer and subsequent lattice heating, is explained. Generation of laser-induced periodic surface structures, and their characteristics, are discussed. Applications of laser-induced surface structures are outlined.

1.1 Overview of light-matter interaction

The invention of the laser in 1960 by T. H. Maiman [1] was a path-breaking discovery which initiated novel experimental investigations of light-matter interactions. Lasers are excellent light sources characterized by their monochromaticity, spatial and temporal coherence, and high average and peak intensities. Since the 1970s, stable and powerful short pulses produced by solid-state Nd:YAG lasers are being widely used in light-matter interaction studies. The development of the mode-locking (ML) technique [2, 3], followed by the introduction of chirped pulse amplification (CPA) [4], lead to the generation of light pulses with temporal widths as short as a few tens of picoseconds (ps) to a few femtoseconds (fs). These advances in laser technology have resulted in the design of state-of-the-art laser systems which can deliver pulses of a few

fs duration with peak powers ranging from terawatts (TW) to multi-petawatts (PW), enabling a host of new investigations including the exploration of ultra-fast dynamics in atoms and molecules. The versatility of these intense lasers, especially the tunability of pulse-width and wavelength, has lead to remarkable progress in laser-assisted material processing, with great impact on real world applications.

1.1.1 Optical field absorption and ionization mechanism

Nonlinear processes induced by the laser irradiation of solids are mostly governed by laser parameters such as the pulse duration (τ_p), wavelength (λ_L), and especially the intensity (I_p) or fluence (F_p). Apart from the laser parameters, the optical, thermal and mechanical properties of the target also affect light-matter interaction. The nonlinear processes which are relevant at different intensity regimes are shown in Figure 1.1. At moderate/low intensities ($< 10^{12}$ W/cm^2), variation of the polarization (P) of a medium with the applied electric field (E) can be written as a Taylor series expansion (in scalar form) as:

$$P = \epsilon_0[\chi^{(1)}E + \chi^{(2)}E^2 + \chi^{(3)}E^3 + ...] \tag{1.1}$$

where $\epsilon_0 = 8.85 \times 10^{-12}$ A-s/V-m is the electric permittivity of free space, $\chi^{(1)}$ is the linear susceptibility, and $\chi^{(2)}$ and $\chi^{(3)}$ are the second and third order nonlinear susceptibilities[1] respectively. The first term in equation 1.1 represents the linear regime of optics, and the higher order terms describe the nonlinear optical regime. The E-field of the laser pulse, being significantly weaker than the static Coulomb field of the atoms, perturbs the quantum states of the atoms under non-resonant excitation conditions. Under such conditions, nonlinear interactions are well defined by the perturbative approach, and these processes are categorized under perturbative nonlinear optics. Second-order nonlinearity

[1] $\chi^{(n)}$ has unit (m/V)$^{n-1}$

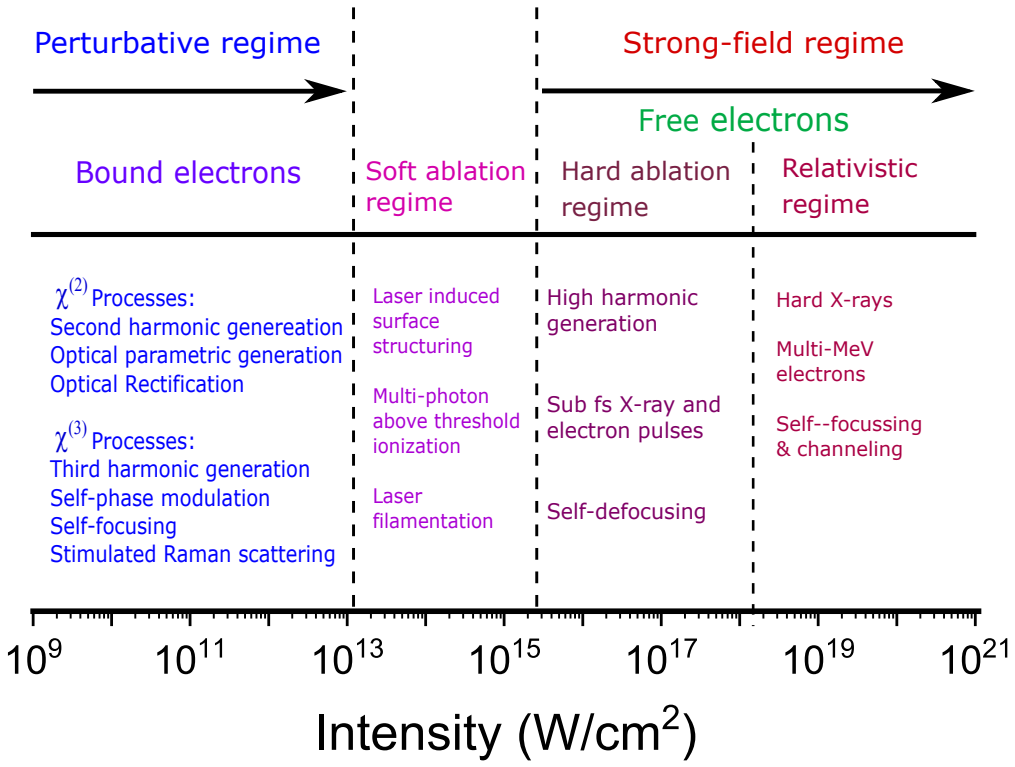

Figure 1.1: Nonlinear optical phenomena relevant for different irradiation intensity regimes. The figure is adapted from ref [5].

which arises due to the effect of $\chi^{(2)}$ in the media gives rise to nonlinear phenomena such as second harmonic generation (SHG), sum-frequency generation (SFG), difference frequency generation (DFG), and parametric conversion [6, 7]. $\chi^{(2)}$ processes can occur only in noncentrosymmetric crystals, i.e., crystals that do not exhibit inversion symmetry. On the other hand, third-order nonlinear processes (described by the $\chi^{(3)}$ susceptibility) can occur in both centrosymmetric and non-centrosymmetric media. Examples of $\chi^{(3)}$ processes are Third Harmonic Generation (THG), optical Kerr effect, stimulated Raman scattering (SRS), and stimulated Brillouin scattering (SBS) [6, 7].

When the irradiation intensity is greater than 10^{13} W/cm^2, different types of extreme nonlinear optical interactions become significant (Figure 1.2). These interactions can be described by the strong-field approximation (SFA) theory proposed by Keldysh in 1964 [8]. In the strong field regime, the E-field of the

laser is either comparable or greater than the static Coulomb field of the atom ($\approx 10^9$ V/cm), so that the atomic potential gets modified/suppressed. In such conditions the outer-shell electrons cannot remain in the bound state, and ionization occurs. These released electrons get caught by the E-field potential of the laser and start oscillating under the influence of the ponderomotive force. Depending upon the irradiation intensity, ionization can occur due to processes such as multi-photon ionization (MPI)[2], tunnel ionization (TI) and over the barrier ionization (OTBI or OBI). According to the Keldysh theory, the two limiting cases of strong-field regime, i.e., MPI and TI, can be described based on the value of an adiabatic parameter referred to as Keldysh parameter (γ) [8], given by:

$$\gamma = \frac{\omega_0}{\omega_t} = \sqrt{\frac{I_p}{2U_p}} \tag{1.2}$$

where ω_0 is the frequency of the laser, I_p is the ionization potential of the atom, and U_p is the ponderomotive energy[3] of the free electrons [9]. ω_t can be described as the tunneling frequency, which is defined as:

$$\omega_t = \frac{eE_0}{\sqrt{2mI_p}} \tag{1.3}$$

where e, m are the electric charge and the rest mass of the electron respectively, and E_0 is the time-dependent amplitude of the E-field of the laser. From equations 1.2 and 1.3 it is evident that γ is inversely proportional to the applied electric field. In the case of semiconductors and dielectrics, the single photon energy $E = \hbar\omega$ (1.55 eV for λ = 800 nm) is too small compared to the typical band gap of the material, and ionization cannot occur by the normal photon excitation process. However, ionization can occur through the MPI process, in which the simultaneous absorption of multiple photons from the laser field will

[2]MPI is also referred to as above threshold ionizaton (ATI).

[3]The cycle-averaged quiver energy of a free electron associated with its oscillatory motion under the influence of an E-field is called ponderomotive energy $U_p = \frac{e^2(E_0)^2}{4mw_0{}^2}$.

meet the energy requirement for ionization [10]. The MPI regime is categorized by $\gamma \gg 1$, occurring in the intensity range 10^{13}-10^{14} W/cm^2, and the kinetic energy of the freed electron is given by [11]

$$E_k = (n+m)\hbar\omega - I_p \tag{1.4}$$

where n is the minimum number of photons required for ionization ($n\hbar\omega = I_p$), and m is the number of excess photons absorbed by the inverse bremsstrahlung (IB) process which contributes to the kinetic energy of the electron.

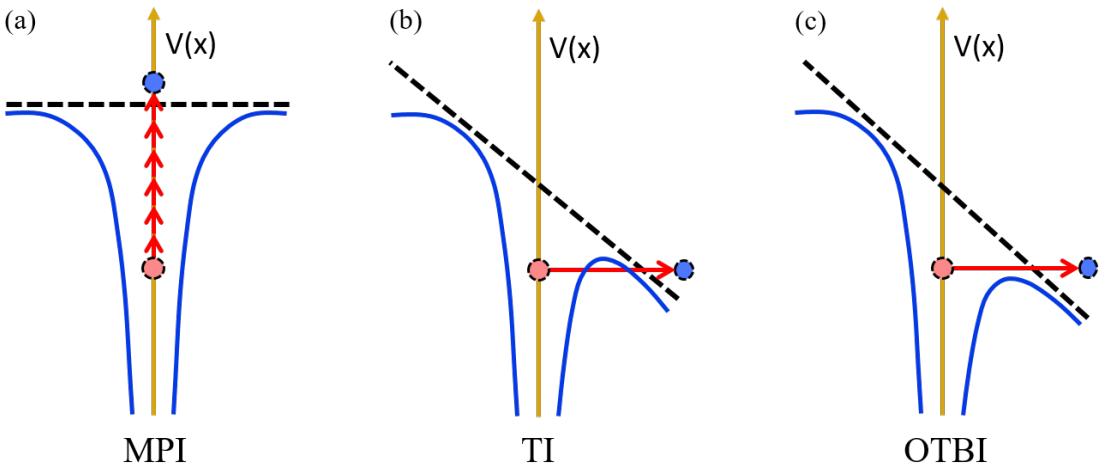

Figure 1.2: Schematic representation of (a) multi-photon ionization (MPI), (b) tunnel ionization (TI), and (c) over the barrier ionization (OTBI).

At higher intensities ($> 10^{14}$ W/cm^2), the E-field of the laser becomes so strong that it starts modifying/suppressing the Coulomb potential. In this case ionization can occur through two pathways: TI and OTBI [12], both of which are associated with $\gamma \ll 1$. Tunneling ionization occurs when the intense laser field suppresses the Coulomb barrier of the atom to that extent where the electron can successfully tunnel through the distorted potential barrier [8, 10, 12]. At extreme intensities ($> 10^{15}$), the Coulomb barrier can be completely suppressed under the influence of the laser field such that it falls below the bound electron's energy, and the electron can escape easily leading to OTBI.

Irrespective of the ionization mechanism, these free electrons accelerate ponderomotively, gain kinetic energy within the E-field of the laser, and subsequently collide with bound electrons. If the energy transfer is sufficient during the collision, more bound electrons will be released. This process is referred to as impact ionization, which grows exponentially to produce more free electrons via multiple iterations resulting in a process called avalanche ionization. Matter in the focal volume of the laser gets significantly ionized with the free electron density reaching the critical value of 10^{22} cm^{-3} to 10^{23} cm^{-3}, leading to a collection of electrons and ions exhibiting quasi-neutrality and collective behaviour, which is known as plasma. This localized plasma responds to the E-field of the laser and has a very high electrical conductivity. Coulomb repulsion between similar charges causes a rapid expansion of the plasma in the form of a plume, which is referred to as Coulomb explosion. Intense laser-matter interaction often leads to a combination of permanent material damage, modified material properties, and even the removal of material from the target surface, known as laser ablation [13].

1.2 Fundamentals of laser ablation

The fact that focused laser pulses can be used as effective tools for material removal was realized soon after the invention of the first laser. Energetic laser pulses, when focused on a solid material, bring macroscopic amounts of matter to extreme conditions by creating a heat affected zone (HAZ), which results in transient or permanent modifications of the surface. This phenomenon of material removal upon irradiation with pulses of energy exceeding the binding energy of matter is called laser ablation [13]. The first pioneering work of laser ablation was reported in 1962 by Franken Brech and Lee Cross [14], in which they collected and spectrally dispersed the light emitted from an iron plasma generated by focusing a 5 J ruby laser pulse onto a razor blade. This experiment

gave birth to the now well established technique called laser-induced breakdown spectroscopy (LIBS) for quantitative and qualitative elemental analysis.

1.2.1 Interplay of different processes and their timescales

Ultrafast laser-matter interaction and the subsequent removal of material involves a complex interplay between non-thermal and thermal processes (Figure 1.3). When a fs pulse irradiates a solid target, ionization of the target takes place through the processes discussed in the previous section. After ionization, the freed electrons further absorb laser radiation through inverse Bremsstrahlung and resonance absorption phenomena, independent of the initial state or type (such as metal, semiconductor or dielectrics) of the target material [15–17]. The non-thermal (fast) and thermal (slow) processes are discussed in the following sections.

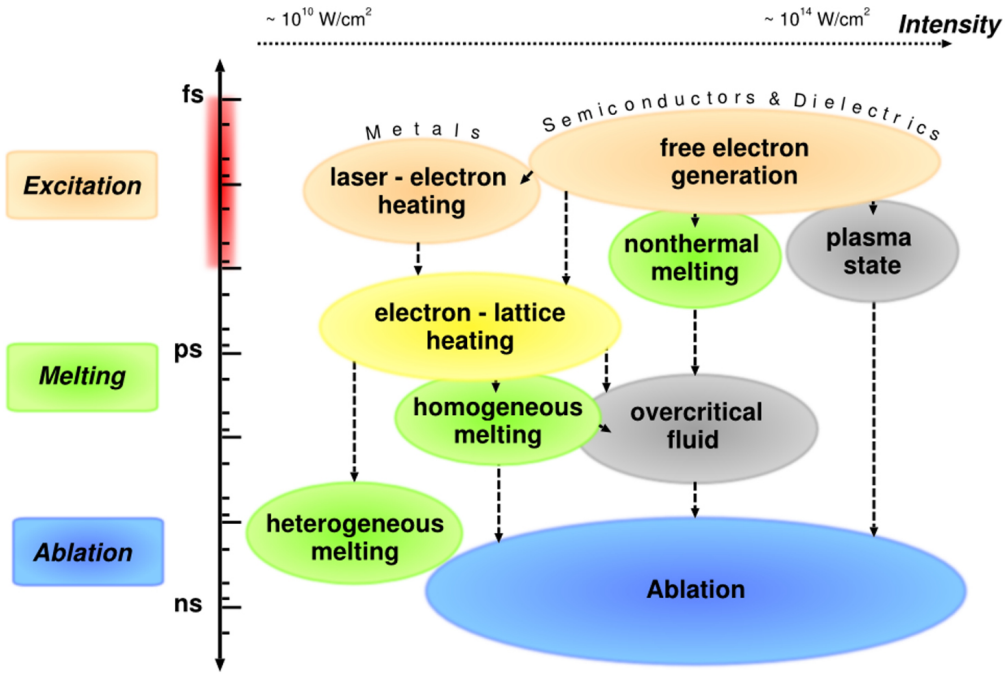

Figure 1.3: Typical timescales and intensity ranges of the phenomena and processes associated with the irradiation of a solid with an ultrashort (fs duration) laser pulse. The timescale of melting may vary for different processes, and lies roughly in the ps regime. Material removal (ablation) lasts up to the ns regime. This figure is adapted from ref [18].

1.2.1.1 Non-thermal processes

One of the important non-thermal processes responsible for particle ejection from the surface within few hundreds of fs is Coulomb explosion. In this case, ionization by the aforementioned processes generates free electrons by stripping the outer shell electrons from the atom. These electrons, when ejected rapidly from the target's surface, create a charge cloud of the positively charged atoms that are left behind. When this charge density becomes sufficiently strong, the ions in this ensemble will explode non-thermally due to mutual repulsion, giving rise to energetic ions having velocities higher than those achieved by ions in thermal emission. This phenomenon is called Coulomb explosion [19], and it is mostly observed in dielectric [19–21] and semiconductor materials [22–24] compared to metals [25, 26], since metals posses excess free electrons which balance the repulsive force in the positive ion charge cloud. The velocities of the ejected charged particles from the target's surface are determined by the repulsive Coulomb forces, whereas neutral species achieve their velocities on collision with fast electrons and ions. Another non-thermal process which causes melting within a few hundreds of femtoseconds in semiconductors is ultrafast melting [27]. This process is associated with the excitation of charge carriers into the conduction band, giving rise to antibonding states due to the conversion of interatomic forces. After rapid excitation by fs irradiation the lattice order of semiconductors such as silicon and germanium disappears within few hundreds of femtoseconds [28].

1.2.1.2 Thermal processes

When the transfer of the deposited laser energy from the target to the lattice is mediated through electron-phonon interactions, followed by lattice heating, melting and evaporation of the material, the process is known as thermal ablation. In comparison to electronic ejection (non-thermal process), thermal processes take place at a much slower time scale. The thermal process occurs

through different ejection mechanisms such as vaporization, boiling and phase explosion/explosive boiling, depending on the pulse width of the laser and the temperature attained by the ablated volume. Thermal processes dominate when the pulse width of the laser is longer than the electron-lattice relaxation time. For ns and longer pulses the material has enough time to change into a molten state, and material ejection takes place by boiling and evaporation from a liquid phase [29, 30]. On the other hand, the dynamics of ultrafast pulse absorption and ablation is completely different since it is driven by direct solid-plasma transition [30, 31]. The absorption of ultrashort radiation by free electrons does not overlap with the thermal dissipation process of energy transfer to the lattice system which happens on the picosecond time-scale. Therefore, the difference between the temperatures of the electron subsystem and the lattice results in a non-equilibrium condition. The distinct dynamics of these two subsystems is described by the two-temperature model (TTM) [32, 33], which is discussed in the following section.

1.2.2 The two-temperature model

The two-temperature model (TTM) is a semi-classical temperature diffusion model which was proposed by Anisimov et al. [32] to illustrate the dynamics of femtosecond laser energy transfer and subsequent heating in metals. When a fs laser pulse falls on a metallic surface, the pulse energy is absorbed by outer-shell electrons through the inverse Bremsstrahlung mechanism. Due to the extremely short electron-electron interaction time, the excited electrons thermalize almost instantaneously. However, this thermalization is not simultaneously followed by the lattice (here the atomic/ionic skeleton of bulk matter is referred to as lattice for both crystalline and amorphous materials) which remains cold (room temperature T≈300 K) compared to the hot electrons. This difference between the temperatures of the electron and lattice subsystems results in a non-equilibrium condition. However, the system will be driven into thermal

equilibrium through electron-phonon thermalization and electron diffusion out of the ablated region. Thus, the energy transport mechanism in femtosecond laser-matter interaction occurs in two steps: (i) Absorption of laser radiation by free electrons and the re-establishment of Fermi distribution after the electron relaxation time (happening over a few fs), (ii) energy dissipation to the lattice subsystem through electron-phonon collision mechanism which happens over the timescale of tens of ps (known as thermalization time). The temporal evolution of the electron and lattice subsystems can be described by the coupled nonlinear equations

$$C_e \frac{\partial T_e}{\partial t} = \frac{\partial}{\partial z}\left(\chi_e \frac{\partial T_e}{\partial z}\right) - G(T_e - T_l) + Q \tag{1.5}$$

$$C_l \frac{\partial T_l}{\partial t} = \frac{\partial}{\partial z}\left(\chi_l \frac{\partial T_l}{\partial z}\right) - G(T_e - T_l) \tag{1.6}$$

where T_e and T_l are the temperatures of the electrons and the lattice respectively, z is the coordinate directed from the target surface to the bulk, and C_e, χ_e and C_l, χ_l are the specific heat capacities[4] and the coefficient of thermal conductivity of the electrons and the lattice subsystem, respectively. G is the electron-lattice coupling constant[5]. Q is the laser energy absorbed by the electrons which can be written as,

$$Q = I(t) A \alpha \exp\{-\alpha z\} \tag{1.7}$$

where α is the material absorption coefficient, I(t) is the laser intensity, and A is the absorptivity[6] of the material.

The three different time scales, namely, electron relaxation time ($\tau_e = C_e/G$), lattice heating time ($\tau_l = C_l/G$), and laser pulse duration (τ_p), play vital roles in the early stage evolution of ultrafast laser-matter interaction. The electrons

[4]Unit of the specific heat capacity is J.cm^{-3}.K^{-1}

[5]The electron-lattice coupling constant can be defined as $G = \frac{C_e}{\tau}$ where τ is the characteristic exchange time of the electron subsystem.

[6]The absorptivity (A) of the material is related to the reflectivity R through $A = (1 - R)$.

obtain a high transient temperature compared to the lattice due to their lesser heat capacity. It takes relatively larger time for energy to be transferred from the excited electrons to the phonons, since the phonon mass is much greater than the electron mass. Therefore, at this stage, the thermal conductivity of the lattice can be neglected. Another determining parameter in laser-matter interaction is the pulse width of the laser. The interaction can be divided into three different temporal regimes, namely, femtosecond, picosecond and nanosecond pulse laser ablation.

In the case of femtosecond laser ablation, the laser pulse width is much shorter compared to the characteristic electron relaxation time ($\tau_p \ll \tau_e$), which varies from 1 ps (for metals) to tens of ps (semiconductors and dielectrics) [30]. The specific heat capacity and thermal conductivity of the electron can be written as $C_e = C_e{}' T_e$ and $\chi_e = \chi_0(T_l)\frac{T_e}{T_l}$ respectively, where $\chi_0(T_l)$ is the typical thermal conductivity of metals at equilibrium. Due to this short timescale, the electron-phonon coupling term and the electron thermal conductivity term can be neglected, so that the coupled nonlinear equation 1.5 reduces to

$$C_e' \frac{\partial {T_e}^2}{\partial t} = 2 I_a \alpha \exp\{-\alpha z\} \tag{1.8}$$

Here $I(t) = I_0$ is supposed to be constant, and $I_a = I_0 A$. Solving the above equation gives

$$T_e(t) = \left\{ T_0^2 + \frac{2 I_a \alpha}{C_e'} t \exp\{-\alpha z\} \right\}^{\frac{1}{2}} \tag{1.9}$$

where $T_0 = T_e(0)$ is the initial temperature. By the end of the laser pulse the electron temperature achieved will be T_e

$$T_e(\tau_p) \simeq \left\{ \frac{2 F \alpha}{C_e'} \right\}^{\frac{1}{2}} \exp\left\{ \frac{-z}{\delta} \right\} \tag{1.10}$$

$$T_l \simeq \frac{F_a \alpha}{C_l} \exp\{-\alpha z\} \tag{1.11}$$

It is assumed that $T_e(\tau_p) \gg T_0$, and that the absorption of laser fluence ($F = I_a\tau_p$) takes place only up to a skin depth $\delta = \frac{2}{\alpha}$. As the laser pulses are very short, fs- ablation results in the rapid and direct creation of plasma from the target. The lattice gets heated up relatively slower (in picosecond timescales) along with a rapid expansion of the plasma, and the lattice temperature can be given by equation 1.11. During the timescales of these processes thermal conduction into the lattice is not significant. This results in an appreciable reduction of the HAZ surrounding the ablated region, leading to smaller feature sizes upon ablation. The negligible thermal damage and the consistency of ablation for different materials proves that fs laser pulses are ubiquitous tools for precise laser structuring, which has many novel applications.

In the case of picosecond laser interaction with matter, the characteristic timescales are in the order: $\tau_e \ll \tau_p \ll \tau_l$, such that the characteristic electron energy relaxation time is much smaller than the pulse duration of the laser. Here T_e can be considered to be quasi-stationary. Since the timescale of lattice heating is still greater than the pulse duration, the contribution of T_e can be neglected giving

$$T_l \simeq T_e\left(1 - \exp\left(\frac{-t}{\tau_l}\right)\right) \simeq \left(\frac{t}{\tau_l}\right)T_e \tag{1.12}$$

Here it is evident that the lattice temperature is much lower than the electron temperature in the picosecond time regime. As we know, electron energy relaxation happens due to energy exchange with the lattice. Hence, electron temperature and lattice temperature at the end of the laser pulse are given by,

$$T_e \simeq \frac{I_a\alpha}{G}\exp\{-\alpha z\} \tag{1.13}$$

$$T_l \simeq \frac{F\alpha}{C_l}\exp\{-\alpha z\} \tag{1.14}$$

As seen from the above equation, lattice temperature at the end of the laser pulse is determined by the electron cooling time. Picosecond laser ablation in-

volves electron plasma formation along with the presence of liquid phase in the ablated region, which reduces precision in laser machining.
Finally, in the case of nanosecond laser pulses, the timescales are related as $\tau_e \ll \tau_l \ll \tau_p$, such that the pulse will be present even after the thermalization of the electron-lattice subsystem. Thus, electrons and lattice achieve thermal equilibrium, i.e. $T_e = T_l = T$. The coupled nonlinear equations reduce to

$$C_l \frac{\partial T}{\partial t} = \frac{\partial}{\partial z}\left(\chi_e \frac{\partial T}{\partial z}\right) + Q \tag{1.15}$$

In this regime, the energy deposited on the target over nanosecond time scales is spent for heating up the target surface to the melting point, and then to the vaporization temperature. Each metal has a threshold energy for evaporation (energy required to exceed the specific heat of evaporation Ω) given by [34],

$$F > F_{th} \simeq \rho \Omega D^{1/2} \times \tau_p^{1/2} \tag{1.16}$$

where D is the heat diffusion coefficient and ρ is the density. It is clear that the threshold fluence for evaporation with nanosecond laser pulses increases by a factor $\tau_p^{\frac{1}{2}}$. In this regime, ablation is more complicated since the time available for a thermal wave to propagate into the target is large, creating a large area of the melted material surface which is not ideal for laser processing.

1.3 Laser-assisted surface structuring

The phenomenon of laser ablation in the soft ablation regime causes material removal from the surface, subsequently generating a comparatively rough surface. The roughness of the ablated surface originates from secondary micro-scale and/or nano-scale features which form in and around the irradiated area due to a variety of mechanisms (such as post-ablation melting and re-solidification or splashing of a liquid surface due to the recoil pressure)

depending on the rate of ablation. In principle, these surface features exhibit a clear correlation with different irradiation parameters along with intrinsic physical properties of the target. These generated surface features are usually defined as laser induced surface structures (Figure 1.4).

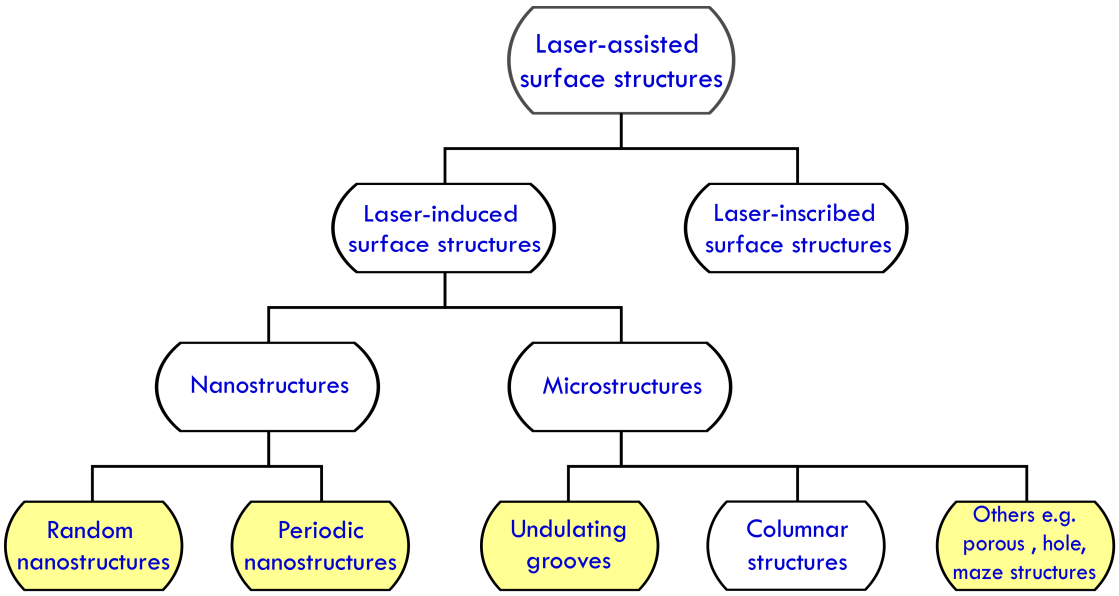

Figure 1.4: Classification of laser-assisted surface structures. Structures relevant for the work reported in this thesis are marked in yellow.

In general, these surface features can be categorized into (i) coherent and (ii) non-coherent structures. Laser-induced surface structures strongly depend upon laser radiation parameters such as wavelength, polarization, incident pulse energy, angle of incidence etc [35]. It is worth mentioning that the generated surface structures tend to follow a specific pattern/periodicity when irradiated with a laser fluence equivalent to the ablation threshold of the target material. These quasi-periodic features, often called ripples, are generally referred to as "Laser induced periodic surface structures (LIPSSs)" [36]. The formation of LIPSS is one of the most actively investigated surface phenomena from the time of their first observation in 1965 by Birnbaum et.al [37]. The spatial periodicity (Λ) of these ripples is found to be close to the laser wavelength (λ), and their preferential orientation is found to be normal to

the incident polarization direction (electric-field vector). On the other hand, the spatial period and orientation of non-coherent structures are not directly associated with the wavelength and polarization of the laser beam, and their appearance is subject to the ambient pressure and laser intensity. They appear at higher intensities than coherent structures, and exhibit a wave-like topography with a spatial period which is much larger than the incident laser wavelength. Depending on the materials and specific irradiation conditions, the generation of these structures facilitate surface functionalization through different features size, ranging in size from a few tens of nm to several microns. Surface structuring has many applications in the fields of opto-electronics, plasmonics, micro/nano-fluidics, biomedicine, chemical sensing and mechanical engineering [35, 38–41]. Commercial ultrafast (fs-ps pulse width) lasers being easily available, precision laser processing stands out as a novel and versatile technology which has attracted substantial research interest because of its many advantages, which include

- Ability to process almost all types of materials, including metals, semiconductors, dielectrics, and polymers;

- Feasibility of processing non-planar surfaces, using CW as well as pulsed lasers having pulse durations down to a few-fs;

- Capability to produce micro/nanostructures with surface areas in a large range, and;

- Single-step, maskless processing at a high speed under normal ambient conditions, without needing a clean room environment.

1.3.1 Mechanisms of LIPSS formation and LIPSS characteristics

The generation and evolution of LIPSS shows similar characteristics in all materials, but in general two distinct variety of LIPSS are observed according to their spatial periods (Λ), which are commonly classified as (i) low spatial frequency LIPSS (LSFL) and (ii) high spatial frequency LIPSS (HSFL). For normal incident radiation LSFL usually exhibits a spatial period which is approximately equal to or a little smaller than the irradiation wavelength ($\lambda/2 \leq \lambda_{LSFL} \leq \lambda$), while HSFL (also referred to as deep-subwavelength structure) has periods smaller than half of the irradiation wavelength ($\lambda_{HSFL} \leq \lambda/2$). Both types of LIPSS (LSFL and HSFL) can be further divided into two subcategories (see Figure 1.5). In the case of highly absorbing materials e.g. semiconductors and metals, LSFL is found to be oriented perpendicular to the polarization of the irradiating beam. This type of LIPSS (called LSFL-I) exhibits spatial periods close to the laser wavelength. The spatial period Λ_{LSFL} of the LSFL generated on metals through laser irradiation with a linearly polarized beam placed in a dielectric medium is given by

$$\Lambda_{LSFL} = \frac{\lambda}{[Re(\eta) \pm \sin\theta]}, \qquad where\ \ \eta = \left(\frac{\epsilon_d \epsilon_{metal}}{\epsilon_d + \epsilon_{metal}}\right)^{\frac{1}{2}} \tag{1.17}$$

here λ is the incident laser light wavelength, θ is the angle of the incident light, η is the effective refractive index of the dielectric-metal interface for surface plasmons, ϵ_d is the dielectric constant of the ambient dielectric medium, ϵ_{metal} is the dielectric constant of the metal, and Re[η] is the real part of η. However, in the case of wide band gap materials (i.e. dielectric materials) where ablation occurs through MPI mechanism, another type of LSFL is observed. These LSFL-II structures are usually oriented parallel to the polarization of the irradiating beam and exhibit spatial periods close to $\lambda_{LSFL} = \lambda/\eta$, where $\eta = \epsilon^{1/2}$

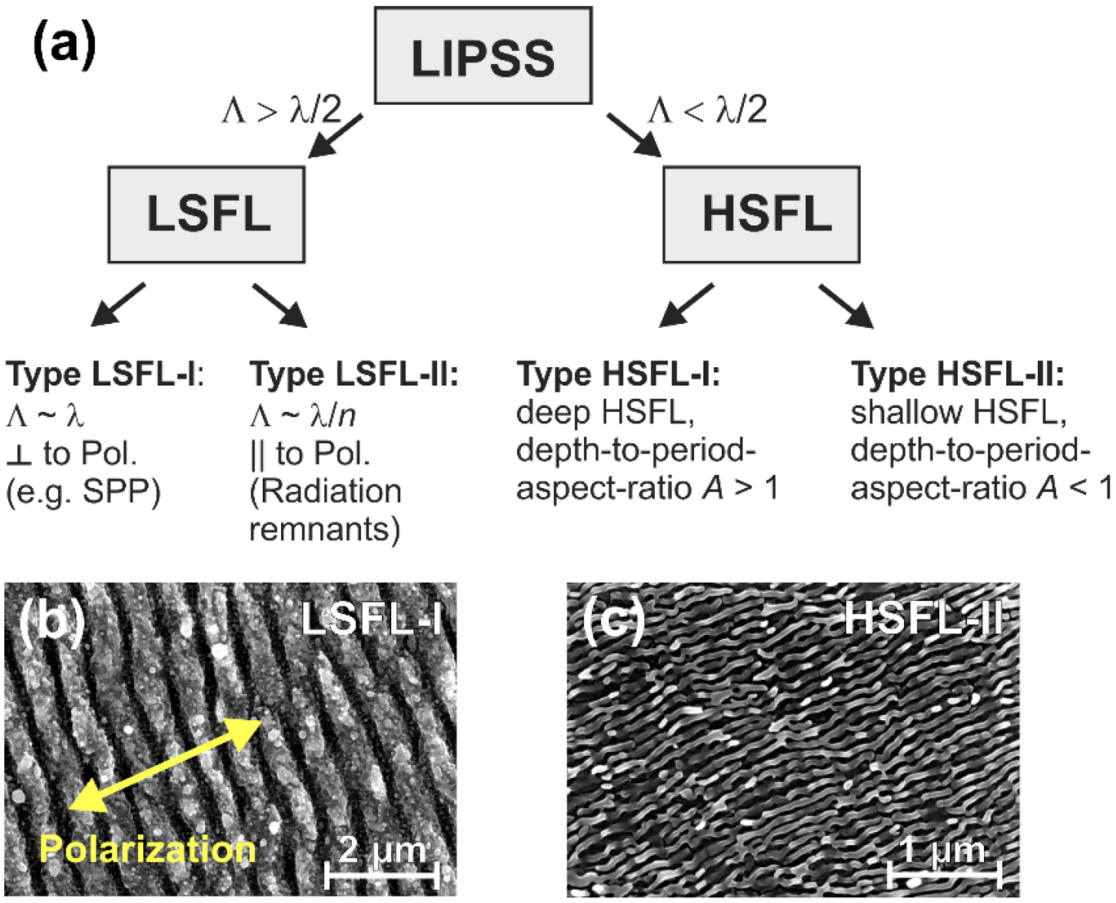

Figure 1.5: (a) Categorization of LIPSS into different types of LSFL and HSFL. (b,c) SEM micrographs of Ti-6Al-4V surfaces after irradiation with multiple fs-laser pulses in air, showing LSFL-I (near wavelength-sized ripples), and HSFL-II (sub-wavelength) (pulse duration = 30 fs, center wavelength λ = 790 nm, pulse repetition frequency 1 kHz), respectively. The yellow arrow in (b) marks the direction of laser beam polarization. These figures are adapted from [42, 43].

is the refractive index of the dielectric material. These structures are associated with Radiation Remnants (RR)[7], predicted by Sipe et al. for transparent materials [44]. In contrast, high spatial frequency LIPSS (HSFL) exhibiting periods less than $\lambda/2$ manifest in two different forms: (i) HSFL-I consisting of very narrow (few tens of nm) and deep surface ripples (hundreds of nm), i.e., having

[7]The RR are a specific non-propagating electromagnetic mode close to the rough surface which enables energy extraction and transfer from the incident radiation to the material at the associated spatial frequencies.

depth-to-period aspect ratio $A > 1$, and (ii) HSFL-II which exhibit very shallow (few tens of nm) surface gratings having depth-to-period aspect ratio $A < 1$. HSFL-I are prominently observed in dielectrics and semiconductors exhibiting periods of $\lambda_{HSFL} \simeq \lambda/(2\eta)$ whereas HSFL-II are mostly seen on metals. However, these two HSFL types are not distinguished in recent scientific literature, and the origin of HSFLs are not yet completely understood. HSFLs are preferentially observed upon irradiation with pulse widths ranging from sub-ps to few fs, when the beam fluence is slightly less than the ablation threshold.

Currently, the most widely accepted theory of LIPSS formation is based on the interference of incident laser radiation with surface electromagnetic waves (SEW) generated at the rough surface of the target, which includes the surface plasmon polaritons (SPPs) [44, 45]. In simple terms, the interference leads to a spatially modulated intensity distribution at the surface. This spatially modulated energy is transferred to the electronic system via optical absorption. Through electron-phonon coupling, the energy is then transferred to the lattice within picosecond timescales. This may lead to spatially modulated melting or even ablation. As a result of material removal and melting (thermocapillary effects, etc.), LIPSS appears as a permanent surface relief.

The idea that LIPSS formation is based on the interference between incident laser beam and surface electromagnetic waves (SEW) was initially presented by Emmony et al. in 1973 [46]. Later, the research groups of John E. Sipe and Henry M. van Driel [36, 44] investigated LIPSS formation theoretically and experimentally via electromagnetic theory, and coined the term LIPSS in scientific literature. They introduced the efficacy factor, a scalar-valued function, which is proportional to the inhomogeneous energy deposition into the ablated material. In 2009, Sipe's thoery was combined with a Drude model for considering the optical response of quasi-free conduction band electrons of materials excited by laser irradiation, and this combined theory signified the importance of transient changes of the dielectric permittivity in semiconductors at the early stage

of LIPSS formation [47]. In 2012 Skolski et al. developed an alternative numerical method by employing finite-difference time domain (FDTD) calculations to solve Maxwells equations at a statistically rough surface [48].

In addition to the interference theory, other mechanisms have also been proposed to explain LIPSS formation. For instance, self-organization, second harmonic generation, excitation of SPPs, Coulomb explosion etc, have been suggested for the origin of HSFLs. Reif et al. has proposed a mechanism for HSFL via self-organization of the irradiated material, associated with a surface instability caused by diffusion of atoms and surface erosion effects [49, 50]. For LSFL formation, capillary waves excitation at the molten surface layer and subsequent freezing upon resolidification [51], hydrodynamic melt flows, or convection [52] have been proposed. It is worth noting that in most cases LIPSS are observed after multi-pulse irradiation, which enhances the characteristics and appearance of the structures [51]. In general, a positive feedback mechanism is essential, because during repetitive pulse irradiation, the feedback mechanism selects specific spatial periods of the surface roughness distribution for optimal radiation absorption.

Furthermore, important developments have recently been made regarding theoretical modeling, specifically in electromagnetic FDTD [48], [31,32] and hydrodynamic [52], and molecular dynamics(MD) simulations [53], which incorporate post-irradiation matter reorganization mechanisms. As of today, both theoretical approaches, namely (i) electromagnetic and (ii) material reorganization, are merging into a joint view where the irradiation conditions describe which aspect (materials specific electromagnetic or reorganization) can dominate. A detailed review is provided in [54].

1.3.2 Applications of laser-induced surface structuring

Micro-/nano-structuring of materials using ultrashort and short laser pulses in a single-step process enables various surface functionalizations for numer-

ous technical applications. The practical advantage of laser-induced surface structuring lies in the tunability, cost efficiency and robustness. It is possible to control the geometry of the structures by precisely controlling laser parameters such as angle of incidence, polarization, number of pulses/irradiation dose, and incident energy. The processing environment (ambient pressure) also has a significant role. Various applications of LIPSS have been reviewed in detail [55]. A schematic of the applications of laser-induced surface structuring and surface functionalization is shown in Figure 1.6. The most prominent application of

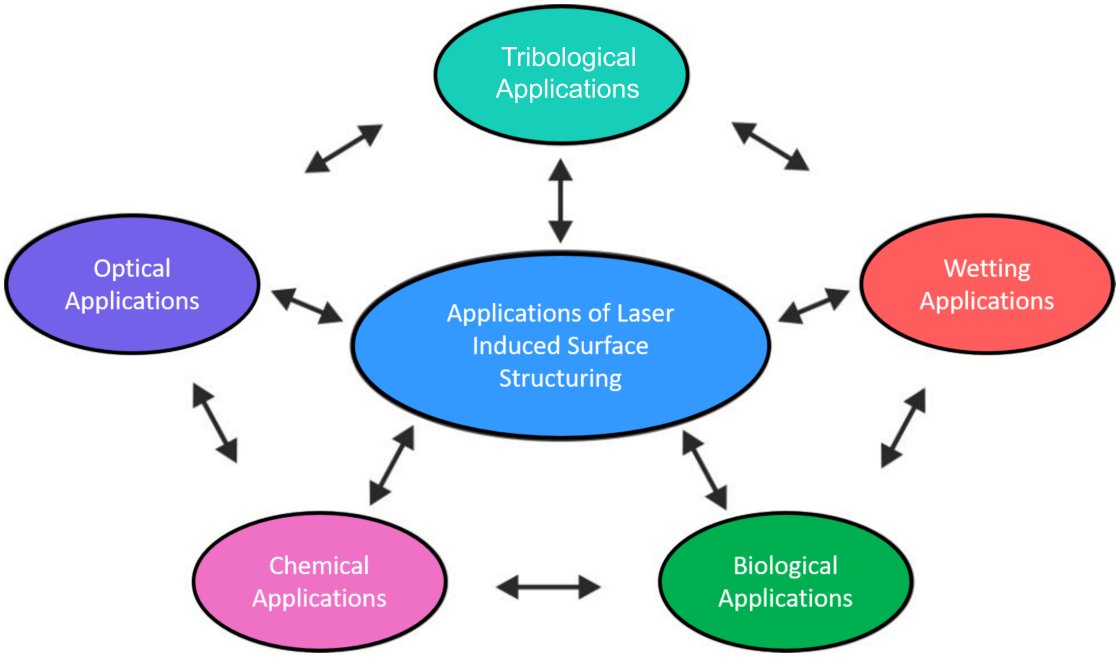

Figure 1.6: Overview of various applications of laser-induced surface structuring. Arrows indicate relations between specific applications/functionalities (adapted from [55]).

LIPSS is related to the fact that their spatial periodicity is of the order of the wavelength of the excitation laser. Therefore, they exhibit features similar to diffraction gratings which render "structural color" for all variety of material. With variations in size, orientation of ripples and possible angles of incidence and observation, many shades of color are attainable over the visible range of the spectrum. Therefore, laser induced surface structuring can be used for the coloration of surfaces without using additional chemicals or coatings. This ef-

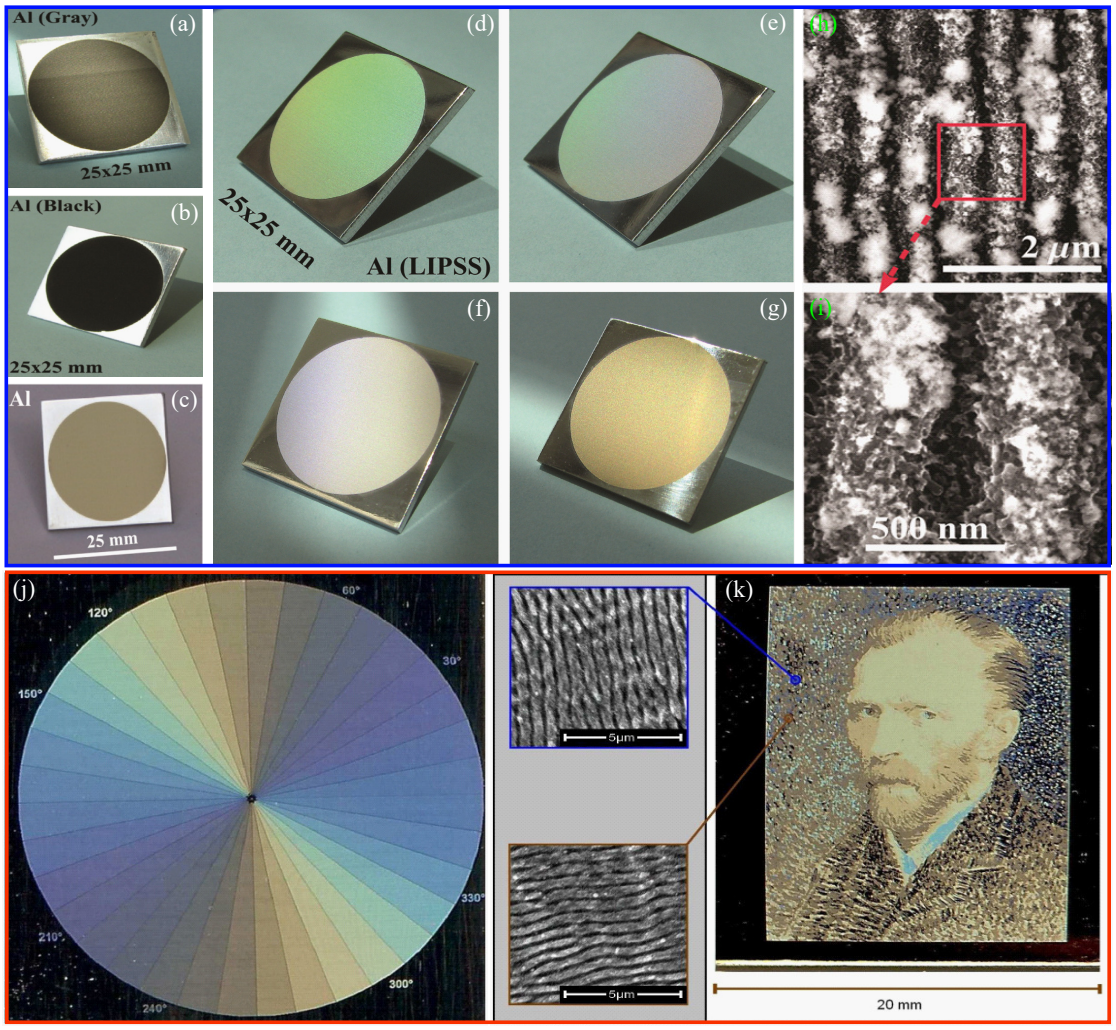

Figure 1.7: Colored aluminum produced by femtosecond laser pulses. Photographs (a-c) show gray, black and golden aluminum respectively processed at 0.16 J/cm^2, revealing viewing angle independent surface coloration. (d)–(g) are photographs of the same Al sample processed at a lower fluence (0.05 J/cm^2), exhibiting different colors upon changing the viewing angle, and the corresponding SEM micrographs (h,i) show the surface structure with a zoomed view of the marked region (adapted from [56]). (j) shows a multi-colored stainless steel (316L) disc with 36 sections, each having a different ripple orientation (from 0° to 360°). (k) is an example of color picture fabrication on stainless steel (316L), obtained by generating controlled nanostructures by femtosecond laser processing (adapted from [57]).

fect was first explored for fs-laser-generated LIPSS on metals (aluminum, platinum, gold etc.) by Vorobyev and Guo [35, 56] (shown in Figure 1.7(a-i)). This technique was also used to fabricate black silicon by generating micro-grooves, which was a breakthrough step considering the increased absorption (90%) ob-

tained by processing the silicon surface [58]. Modifications in the optical properties of silicon provide the possibility to extend the spectral range of Si-based opto-electronic devices into the infrared region, with applications including infrared light detection and photovoltaics [59]. In 2010, Dusser et al. systematically investigated the influence of crucial laser parameters such as irradiation energy, beam polarization, focusing etc, and demonstrated chemical-free processing for creating the portrait of Vincent Van Gogh on a polished stainless steel surface (shown in Figure 1.7(j,k)) by realizing large area color marking [57]. The controlled coloration of surfaces by laser micro-/nano-structuring leads to a multitude of applications including laser marking, decoration, optical data storage, encryption, and anti-counterfeiting. Furthermore, the complexity of replicating the intrinsic irregularity of LIPSS makes them attractive as safety tags.

Similar to the optical properties, the wetting properties also get modified by laser structuring. The wettability of a surface depends on the surface chemistry and surface morphology of the sample. The height of the hierarchical micro-scale conical features and the number of nanoscale secondary protrusions decorating the LIPSS and spikes increase with laser fluence, resulting in a significant increase of the overall roughness. In the last decade, laser-assisted micro-/nano-structuring has been established as a powerful technique to tailor wetting properties that can be potentially exploited for numerous applications. More importantly, these wetting properties can be customized with a large degree of control by altering the surface morphology through a proper choice of the processing parameters. Modification of the wetting response of Si from hydrophilic to superhydrophobic with contact angle $153^\circ \pm 1^\circ$ has been achieved through laser micromachining in SF_6 background followed by silanization [60]. The feasibility of tailoring the wettability of materials including metals [61], polymers and semiconductors [62] within a wide range, from superhydrophilicity to superhydrophobicity, has raised an increasing interest for applications

including self-cleaning surfaces (known as Lotus-effect), biomimetic surfaces, microfluidics for directional liquid transport, and waterproof coatings for automotive and aerospace vehicles, and textiles [35, 61, 63].

Other applications of Laser-induced surface structures include growth and colonization of cells and fabrication of antibacterial surfaces. Rebollar et al. [64] have studied the growth of different cell cultures on polystyrene (PS) films patterned by ns-laser processed LIPSS with different spatial periods. They reported that the adhesion and proliferation of the cells is enhanced for the LIPSS-covered polymer. Furthermore, it was observed that the cells align along the orientation of LIPSS. However, the alignment depends on the type of the cell when the spatial period of the structures exceeds a value of 200 nm. This idea of manipulating cell-growth on a LIPSS-covered surface can be extended to bacterial films, which pose high risks in multiple medical and industrial settings. These biofilms are a collection of microbes that get attached to the surface. Cunha et al. [65] have demonstrated reduced adhesion of Staphylococcus aureus bacterial biofilm on titanium-alloy surfaces patterned by fs-LIPSS (LSFL), compared to polished surfaces which are untreated. The fs laser processing technique proved to be efficient for controlling bacterial colonization. In fact both the situations, where bacterial adhesion is either favored or repulsed, were realized experimentally. Epperlein et al. [66] investigated biofilm formation of S. aureus and Escherichia coli (E. coli) bacteria on corrosion-resistant fs-laser-processed LSFL-covered steel surfaces. These results prove that LIPSS morphologies are excellent choices for efficient production of anti-adhesion, antibacterial surfaces.

Tribological performance improvement of surfaces has been observed due to the generation of LIPSS on inorganic materials under both lubricated and non-lubricated conditions (for details refer to [67]). Reduction of friction and wear was observed for patterned metals under various tribological test conditions [40, 55, 67], which emphasizes the immense potential of LIPSS in tribological applications.

1.4 Objectives of the thesis

Laser ablation and surface structuring of solid targets is an ongoing area of research which grew exponentially in the last two decades becasue of its diverse applications. Controlled ablation processes with ns and fs lasers present the opportunity to generate hierarchical micro-/nano-scale patterns, along with quasi-periodic surface structures exhibiting periodicities close to or less than the irradiation wavelength. The excellent control achievable in structuring has established fs and ns lasers as versatile and ubiquitous tools for surface texturing with high precision. Since the surface properties of solid targets (optical, wetting, mechanical, etc.) are governed by their morphology, laser-induced surface structuring is an ideal tool for surface modification. This thesis aims to understand the physics involved in the laser ablation of solid targets in the context of laser-induced surface structuring applications. In particular, we experimentally investigate the generation of LIPSS on silicon and fused silica for different irradiation parameters. Modifications in the irradiated targets' optical, chemical, and wetting properties are systematically explored. In addition to the conventional Gaussian beam, we employ an optical vortex (OV) beam to fabricate an array of silicon micro-needles for surface-enhanced Raman spectroscopy (SERS) applications. To summarize, the objectives of this thesis are the following:

- Perform experiments to investigate the role of different irradiation parameters (such as wavelength, pulse duration, polarization of the incident beam) on LIPSS formation on silicon,

- Perform laser-induced breakdown spectroscopy (LIBS) experiments on patterned surfaces to explore the effect of LIPSS on optical and ion emissions from the plasma,

- Explore the effect of crystallanity in the LIPSS in dielectric materials (fused silica and quartz),

- Carry out experiments to modify the surface wetting property of silicon by irradiation with nanosecond pulses, and study the long-term stability of surface wetting characteristics,

- Generate OV beams by using a spiral phase plate of topological charge $\ell = 4$, and use them to create laser-induced surface features for SERS applications.

1.5 Organization of the thesis

The thesis is organized into seven chapters as follows:

Chapter 1 gives an introduction to laser ablation and surface structuring. It provides a brief description of the underlying mechanisms involved in fs and ns laser-induced surface structuring. Major applications of laser-structured surfaces are discussed.

Chapter 2 describes the experimental techniques employed in this work. It provides a detailed description of the femtosecond and nanosecond laser sources, characterization tools, spectrometers, and vacuum systems used for the investigations.

Chapter 3 presents studies of enhanced optical and ion emissions from the laser-produced plasma generated on a structured silicon surface. The roles of laser wavelength, pulse duration and background pressure on LIPSS are also investigated.

Chapter 4 describes fs-laser-induced surface structuring of the dielectric materials fused silica and quartz. The effect of crystallinity on LIPSS is studied. Contact angle (C.A.) measurements reveal the formation of superhydrophilic fused silica surfaces which have potential applications in anti-fouling, anti-reflective surfaces, and biosensors.

Chapter 5 reports the fabrication and characterization of large area micro-/nano-textured silicon surfaces using nanoseconds (7 ns) laser pulses. An area

of $6\times$ 6 mm^2 has been textured by the parallel line scanning method resulting in a superhydrophilic silicon surface, with the contact angle reduced substantially from 80° to 5°. Potential applications of these surfaces include heat-exchangers, biosensors, cell adhesives, and self-cleaning solar cells.

Chapter 6 illustrates the generation and characterization of optical vortex (OV) beams by using a spiral phase plate of topological charge ($\ell = 4$). Surface structuring is carried out employing the fs OV beam, enabling the generation of complex surfaces. Micro-needles have been fabricated on crystalline silicon(100), which have several practical applications.

Chapter 7 gives a summary of the work done. A brief overview of future directions also is given.

Bibliography

[1] Theodore H Maiman et al. Stimulated optical radiation in ruby. *Nature*, 187(1476-4687):493–494, 1960.

[2] Willis E Lamb Jr. Theory of an optical maser. *Physical Review*, 134(6A):A1429, 1964.

[3] LE Hargrove, Richard L Fork, and MA Pollack. Locking of he–ne laser modes induced by synchronous intracavity modulation. *Applied Physics Letters*, 5(1):4–5, 1964.

[4] Donna Strickland and Gerard Mourou. Compression of amplified chirped optical pulses. *Optics communications*, 55(6):447–449, 1985.

[5] Thomas Brabec and Ferenc Krausz. Intense few-cycle laser fields: Frontiers of nonlinear optics. *Reviews of Modern Physics*, 72(2):545, 2000.

[6] Robert W Boyd. The nonlinear optical susceptibility. *Nonlinear optics*, 3:1–67, 2008.

[7] Richard L Sutherland. *Handbook of nonlinear optics*. CRC press, 2003.

[8] LV Keldysh et al. Ionization in the field of a strong electromagnetic wave. *Sov. Phys. JETP*, 20(5):1307–1314, 1965.

[9] SV Popruzhenko. Keldysh theory of strong field ionization: history, applications, difficulties and perspectives. *Journal of Physics B: Atomic, Molecular and Optical Physics*, 47(20):204001, 2014.

[10] Vladimir S Popov. Tunnel and multiphoton ionization of atoms and ions in a strong laser field (keldysh theory). *Physics-Uspekhi*, 47(9):855, 2004.

[11] Y Gontier, M Poirier, and M Trahin. Multiphoton absorptions above the ionisation threshold. *Journal of Physics B: Atomic and Molecular Physics*, 13(7):1381, 1980.

[12] D Descamps, J Norin, C Lyngå, S Buil, A L'Huillier, C-G Wahlström, SL Sorensen, O Björneholm, M Gisselbrecht, M Meyer, et al. Applications of high-order harmonic generation. In *AIP Conference Proceedings*, volume 525, pages 337–348. American Institute of Physics, 2000.

[13] Laser Ablation. Desorption, edited by jc miller and rf haglund. *Experimental Methods in the Physical Sciences*, 30, 1998.

[14] FJAS Brech. Optical microemission stimulated by a ruby laser. *Appl. Spectrosc.*, 16(2):59, 1962.

[15] Patrick Mora. Theoretical model of absorption of laser light by a plasma. *The Physics of Fluids*, 25(6):1051–1056, 1982.

[16] M Mahdavi and SF Ghazizadeh. Linear absorption mechanisms in laser plasma interactions. *Journal of Applied Sciences*, 12(1):12–21, 2012.

[17] Yun-Qian Cui, Wei-Min Wang, Zheng-Ming Sheng, Yu-Tong Li, and Jie Zhang. Laser absorption and hot electron temperature scalings in laser–plasma interactions. *Plasma Physics and Controlled Fusion*, 55(8):085008, 2013.

[18] B Rethfeld, K Sokolowski-Tinten, D Von Der Linde, and SI Anisimov. Timescales in the response of materials to femtosecond laser excitation. *Applied Physics A*, 79(4):767–769, 2004.

[19] R Stoian, D Ashkenasi, A Rosenfeld, and EEB Campbell. Coulomb explosion in ultrashort pulsed laser ablation of al 2 o 3. *Physical review B*, 62(19):13167, 2000.

[20] Min Huang, Fuli Zhao, Ya Cheng, Ningsheg Xu, and Zhizhan Xu. Mechanisms of ultrafast laser-induced deep-subwavelength gratings on graphite and diamond. *Physical Review B*, 79(12):125436, 2009.

[21] Jürgen Reif, Florenta Costache, S Eckert, and Matthias Henyk. Mechanisms of ultra-short laser pulse ablation from ionic crystals. *Applied Physics A*, 79(4):1229–1231, 2004.

[22] Hatem Dachraoui, Wolfgang Husinsky, and Gerhard Betz. Ultra-short laser ablation of metals and semiconductors: evidence of ultra-fast coulomb explosion. *Applied Physics A*, 83(2):333–336, 2006.

[23] W. G. Roeterdink, L. B. F. Juurlink, O. P. H. Vaughan, J. Dura Diez, M. Bonn, and A. W. Kleyn. Coulomb explosion in femtosecond laser ablation of si(111). *Applied Physics Letters*, 82(23):4190–4192, 2003.

[24] Hatem Dachraoui and Wolfgang Husinsky. Thresholds of plasma formation in silicon identified by optimizing the ablation laser pulse form. *Physical review letters*, 97(10):107601, 2006.

[25] Hatem Dachraoui and Wolfgang Husinsky. Fast electronic and thermal processes in femtosecond laser ablation of au. *Applied physics letters*, 89(10):104102, 2006.

[26] AA Rukhadze, KZ Rukhadze, and VP Tarakanov. Simulation of coulomb explosion of metals. *Technical Physics*, 53(2):264–267, 2008.

[27] Nadezhda M Bulgakova, Igor M Burakov, Yuri P Meshcheryakov, Razvan Stoian, Arkadi Rosenfeld, and Ingolf V Hertel. Theoretical models and

qualitative interpretations of fs laser material processing. *Journal of Laser Micro/Nanoengineering*, 2(1):76–86, 2007.

[28] Klaus Sokolowski-Tinten, Christian Blome, Clemens Dietrich, Alexander Tarasevitch, M Horn Von Hoegen, Dietrich von der Linde, Andrea Cavalleri, J Squier, and Martin Kammler. Femtosecond x-ray measurement of ultrafast melting and large acoustic transients. *Physical Review Letters*, 87(22):225701, 2001.

[29] BC Stuart, MD Feit, AM Rubenchik, BW Shore, and MD Perry. Laser-induced damage in dielectrics with nanosecond to subpicosecond pulses. *Physical review letters*, 74(12):2248, 1995.

[30] Boris N Chichkov, C Momma, Stefan Nolte, F Von Alvensleben, and A Tünnermann. Femtosecond, picosecond and nanosecond laser ablation of solids. *Applied physics A*, 63(2):109–115, 1996.

[31] A Zoubir, L Shah, K Richardson, and M Richardson. Practical uses of femtosecond laser micro-materials processing. *Applied Physics A*, 77(2):311–315, 2003.

[32] SI Anisimov, BL Kapeliovich, TL Perelman, et al. Electron emission from metal surfaces exposed to ultrashort laser pulses. *Zh. Eksp. Teor. Fiz*, 66(2):375–377, 1974.

[33] Lan Jiang and Hai-Lung Tsai. Improved two-temperature model and its application in ultrashort laser heating of metal films. 2005.

[34] Carsten Momma, Boris N Chichkov, Stefan Nolte, Ferdinand von Alvensleben, Andreas Tünnermann, Herbert Welling, and Bernd Wellegehausen. Short-pulse laser ablation of solid targets. *Optics communications*, 129(1-2):134–142, 1996.

[35] Anatoliy Y Vorobyev and Chunlei Guo. Direct femtosecond laser surface nano/microstructuring and its applications. *Laser & Photonics Reviews*, 7(3):385–407, 2013.

[36] HM Van Driel, JE Sipe, and Jeff F Young. Laser-induced periodic surface structure on solids: a universal phenomenon. *Physical Review Letters*, 49(26):1955, 1982.

[37] Milton Birnbaum. Semiconductor surface damage produced by ruby lasers. *Journal of Applied Physics*, 36(11):3688–3689, 1965.

[38] Camilo Florian, Sabrina V Kirner, Jörg Krüger, and Jörn Bonse. Surface functionalization by laser-induced periodic surface structures. *Journal of Laser Applications*, 32(2):022063, 2020.

[39] Stephan Gräf. Formation of laser-induced periodic surface structures on different materials: fundamentals, properties and applications. *Advanced Optical Technologies*, 9(1-2):11–39, 2020.

[40] Jörn Bonse, Sabrina V. Kirner, and Jörg Krüger. *Laser-Induced Periodic Surface Structures (LIPSS)*, pages 1–59. Springer International Publishing, Cham, 2020.

[41] E Stratakis, Jörn Bonse, J Heitz, Jan Siegel, GD Tsibidis, E Skoulas, A Papadopoulos, A Mimidis, A-C Joel, P Comanns, et al. Laser engineering of biomimetic surfaces. *Materials Science and Engineering: R: Reports*, 141:100562, 2020.

[42] Jörn Bonse, Sandra Höhm, Sabrina V Kirner, Arkadi Rosenfeld, and Jörg Krüger. Laser-induced periodic surface structures—a scientific evergreen. *IEEE Journal of selected topics in quantum electronics*, 23(3), 2016.

[43] Sabrina V Kirner, Thomas Wirth, Heinz Sturm, Jörg Krüger, and Jörn Bonse. Nanometer-resolved chemical analyses of femtosecond laser-

induced periodic surface structures on titanium. *Journal of Applied Physics*, 122(10):104901, 2017.

[44] JE Sipe, Jeff F Young, JS Preston, and HM Van Driel. Laser-induced periodic surface structure. i. theory. *Physical Review B*, 27(2):1141, 1983.

[45] Sergei Aleksandrovich Akhmanov, Vladimir I Emel'yanov, Nikolai I Koroteev, and Vladimir Nikolaevich Seminogov. Interaction of powerful laser radiation with the surfaces of semiconductors and metals: nonlinear optical effects and nonlinear optical diagnostics. *Soviet Physics Uspekhi*, 28(12):1084, 1985.

[46] DC Emmony, RP Howson, and LJ Willis. Laser mirror damage in germanium at 10.6 μm. *Applied Physics Letters*, 23(11):598–600, 1973.

[47] Jörn Bonse, Arkadi Rosenfeld, and Jörg Krüger. On the role of surface plasmon polaritons in the formation of laser-induced periodic surface structures upon irradiation of silicon by femtosecond-laser pulses. *Journal of Applied Physics*, 106(10):104910, 2009.

[48] JZP Skolski, GRBE Römer, J Vincenc Obona, V Ocelik, J Th M De Hosson, et al. Laser-induced periodic surface structures: Fingerprints of light localization. *Physical review B*, 85(7):075320, 2012.

[49] Jürgen Reif, Florenta Costache, Matthias Henyk, and Stanislav V Pandelov. Ripples revisited: non-classical morphology at the bottom of femtosecond laser ablation craters in transparent dielectrics. *Applied Surface Science*, 197:891–895, 2002.

[50] Juergen Reif, Olga Varlamova, Sebastian Uhlig, Sergej Varlamov, and Michael Bestehorn. On the physics of self-organized nanostructure formation upon femtosecond laser ablation. *Applied Physics A*, 117(1):179–184, 2014.

[51] Jeff F Young, JE Sipe, and HM Van Driel. Laser-induced periodic surface structure. iii. fluence regimes, the role of feedback, and details of the induced topography in germanium. *Physical Review B*, 30(4):2001, 1984.

[52] George D Tsibidis, Costas Fotakis, and Emmanuel Stratakis. From ripples to spikes: A hydrodynamical mechanism to interpret femtosecond laser-induced self-assembled structures. *Physical Review B*, 92(4):041405, 2015.

[53] DS Ivanov, VP Lipp, A Blumenstein, F Kleinwort, VP Veiko, E Yakovlev, Vladimir Roddatis, ME Garcia, B Rethfeld, J Ihlemann, et al. Experimental and theoretical investigation of periodic nanostructuring of au with ultrashort uv laser pulses near the damage threshold. *Physical Review Applied*, 4(6):064006, 2015.

[54] Jörn Bonse and Stephan Gräf. Maxwell meets marangoni—a review of theories on laser-induced periodic surface structures. *Laser & Photonics Reviews*, 14(10):2000215, 2020.

[55] Jörn Bonse, Sabrina V Kirner, Sandra Höhm, Nadja Epperlein, Dirk Spaltmann, Arkadi Rosenfeld, and Jörg Krüger. Applications of laser-induced periodic surface structures (lipss). In *Laser-based Micro-and Nanoprocessing XI*, volume 10092, page 100920N. International Society for Optics and Photonics, 2017.

[56] A Y Vorobyev and Chunlei Guo. Colorizing metals with femtosecond laser pulses. *Applied Physics Letters*, 92(4):041914, 2008.

[57] Benjamin Dusser, Z Sagan, Hervé Soder, Nicolas Faure, Jean-Philippe Colombier, Michel Jourlin, and Eric Audouard. Controlled nanostructrures formation by ultra fast laser pulses for color marking. *Optics express*, 18(3):2913–2924, 2010.

[58] C Wu, CH Crouch, L Zhao, JE Carey, R Younkin, JA Levinson, E Mazur, RM Farrell, P Gothoskar, and A Karger. Near-unity below-band-gap ab-

sorption by microstructured silicon. *Applied Physics Letters*, 78(13):1850–1852, 2001.

[59] James E Carey, Catherine H Crouch, Mengyan Shen, and Eric Mazur. Visible and near-infrared responsivity of femtosecond-laser microstructured silicon photodiodes. *Optics letters*, 30(14):1773–1775, 2005.

[60] Vassilia Zorba, Emmanuel Stratakis, Marios Barberoglou, Emmanuel Spanakis, Panagiotis Tzanetakis, Spiros H Anastasiadis, and Costas Fotakis. Biomimetic artificial surfaces quantitatively reproduce the water repellency of a lotus leaf. *Advanced materials*, 20(21):4049–4054, 2008.

[61] Anne-Marie Kietzig, Savvas G Hatzikiriakos, and Peter Englezos. Patterned superhydrophobic metallic surfaces. *Langmuir*, 25(8):4821–4827, 2009.

[62] Emmanuel Stratakis, Anca Mateescu, Marios Barberoglou, Maria Vamvakaki, Costas Fotakis, and Spiros H Anastasiadis. From superhydrophobicity and water repellency to superhydrophilicity: smart polymer-functionalized surfaces. *Chemical Communications*, 46(23):4136–4138, 2010.

[63] Ralf Blossey. Self-cleaning surfaces—virtual realities. *Nature materials*, 2(5):301–306, 2003.

[64] Esther Rebollar, Irene Frischauf, Michael Olbrich, Thomas Peterbauer, Steffen Hering, Johannes Preiner, Peter Hinterdorfer, Christoph Romanin, and Johannes Heitz. Proliferation of aligned mammalian cells on laser-nanostructured polystyrene. *Biomaterials*, 29(12):1796–1806, 2008.

[65] Alexandre Cunha, Anne-Marie Elie, Laurent Plawinski, Ana Paula Serro, Ana Maria Botelho do Rego, Amélia Almeida, Maria C Urdaci, Marie-Christine Durrieu, and Rui Vilar. Femtosecond laser surface texturing of titanium as a method to reduce the adhesion of staphylococcus aureus and biofilm formation. *Applied Surface Science*, 360:485–493, 2016.

[66] Nadja Epperlein, Friederike Menzel, Karin Schwibbert, Robert Koter, Jörn Bonse, Janin Sameith, Jörg Krüger, and Jörg Toepel. Influence of femtosecond laser produced nanostructures on biofilm growth on steel. *Applied Surface Science*, 418:420–424, 2017.

[67] Jörn Bonse, Sabrina V Kirner, Michael Griepentrog, Dirk Spaltmann, and Jörg Krüger. Femtosecond laser texturing of surfaces for tribological applications. *Materials*, 11(5):801, 2018.

Chapter 2

Experimental methods and techniques

This chapter describes the experimental methods used for femtosecond and nanosecond laser ablation and surface structuring of selected solid targets. Laser sources producing short and ultrashort laser pulses of 7 nanoseconds (ns) and 100 femtoseconds (fs) duration, respectively, have been employed to fabricate laser-induced surface structures and to generate dense laser-produced plasmas. The chapter also includes a brief description of the optical setup and instrumentation used for generating optical vortex (OV) beams for surface modification.

2.1 Introduction

Powerful lasers are versatile tools that have received substantial research interest in the past decade due to various applications in the fields of micro- and nano-fabrication, and laser ablation. Monochromaticity and wavelength tunability of the state-of-the-art lasers enhance the processing efficiency for all kinds of materials (metals, semiconductors, glasses, and polymers) even with non-planar surfaces. Another advantage of direct laser processing is the generation of various types of hierarchical surface structures of nano-/micro-scale.

Unlike other conventional techniques such as lithography and chemical vapor deposition (CVD), laser-induced surface structuring is a single-step process that does not require cleanroom facility [1, 2]. Furthermore, ultrashort pulses of fs duration enable high precision for the produced geometry because of the minimal heat-affected zone (HAZ). This thesis addresses fs and ns laser-induced surface structuring by employing conventional laser beams with a Gaussian intensity profile, and also an unconventional Optical Vortex (OV) beam having a dough-nut shaped intensity profile. OV beams can possess orbital angular momentum (OAM) in addition to different states of polarization (e.g., azimuthal, radial, spiral, etc.), and they can be generated by using a unique optic known as spiral phase plate (SP-plate).

The experimental tools used in this thesis consist of three types, namely (i) laser systems, (ii) vacuum systems, and (iii) detection systems. The details of laser systems are discussed in the next section, followed by vacuum systems and detection systems. The major part of the experiments have been carried out at atmospheric pressure, but some experiments have been performed under high vacuum (10^{-5} Torr) as well. These experiments illustrate the important features and applications of surface structuring [3].

2.2 Laser systems

Lasers producing sufficiently high optical intensity are essential for soft ablation (surface structuring) and hard ablation (laser-produced plasmas). One of the major advantages of using lasers for material processing is that precise control of energy deposition on the designated area becomes possible. The work reported in the present thesis is carried out by using femtosecond and nanosecond laser systems. The femtosecond laser system consists of two major components:

- Femtosecond laser Oscillator (`Tsunami, Spectra Physics`) pumped

by a CW Nd:YVO_4 laser (`Millennia Pro-S, Spectra Physics`)

- Femtosecond regenerative amplifier (`TSA-10, Positive Light`) employing Chirped pulse amplification (CPA), pumped by a Q-switched Nd:YAG laser (`Quanta Ray, Spectra Physics`)

These laser systems are discussed below.

2.2.1 Femtosecond oscillator system

The femtosecond oscillator (`Tsunami, Spectra Physics`) is a solid-state laser consisting of a titanium-doped sapphire (Ti:Sapphire) crystal as the lasing medium (Figure 2.1). Ti:Sapphire crystals are made by introducing Ti_2O_3 into the melt of Al_2O_3, and titanium ions (Ti^{3+}) are responsible for laser action. Absorption transitions cover a broad range of wavelengths extending from 400 nm to 600 nm, and fluorescence transitions occur from the excited state's lower vibrational levels to the ground state's upper vibrational levels. Due to the overlap of the long-wavelength side of the absorption band with the short-wavelength side of the fluorescence band, lasing is possible only for wavelengths longer than 670 nm. The Ti:Sapphire crystal facilitates tunability over a broad range in the near-infrared region (700 - 1000 nm). Tunability depends on the pump power, mirror losses, and tuning element losses.

The pulse width of the oscillator is affected by the cavity parameters and the optical components. It consists of a ten mirror folded cavity. An acousto-optic modulator (AOM) ensures the generation of pulses at a repetition rate of 82 MHz by regenerative mode-locking. The AOM employs an active feedback mechanism, where the RF signal which drives the AOM is derived directly from the cavity. The regenerative mode-locking configuration eliminates the major drawback of the active mode-locking technique by automatically adjusting the drive signal to the modulator according to the cavity length. Multiple optical components in the laser cavity, in addition to the self-phase

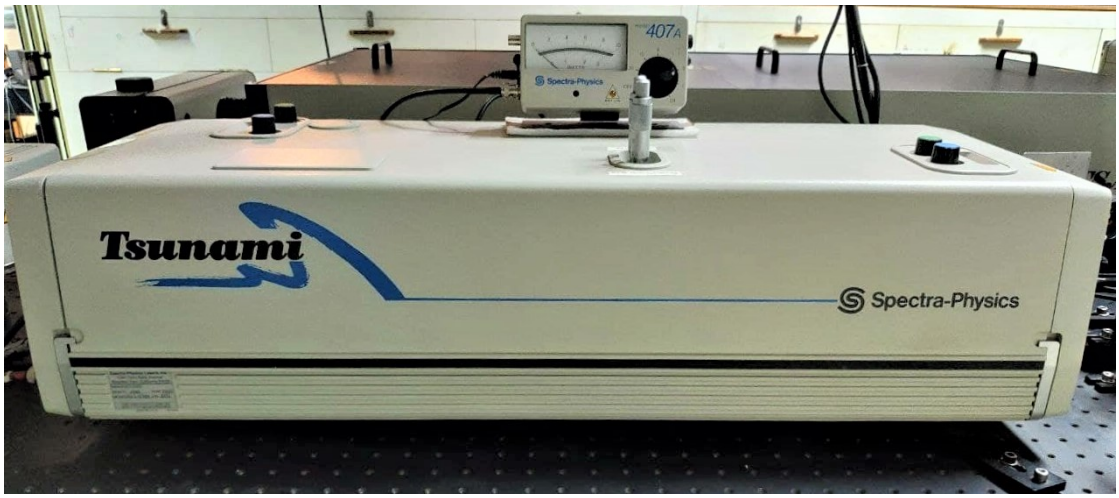

Figure 2.1: Photograph of the femtosecond laser oscillator.

modulation (SPM) occuring in the Ti:Sapphire crystal, introduce positive group velocity dispersion (GVD). To compensate for the positive GVD, two pairs of prisms are introduced in the cavity to create an equivalent negative GVD. The output wavelength is tuned using a variable slit located in the path of the dispersed beam.

The Ti:Sapphire crystal, which has a length of 1 cm, is pumped by a contin-

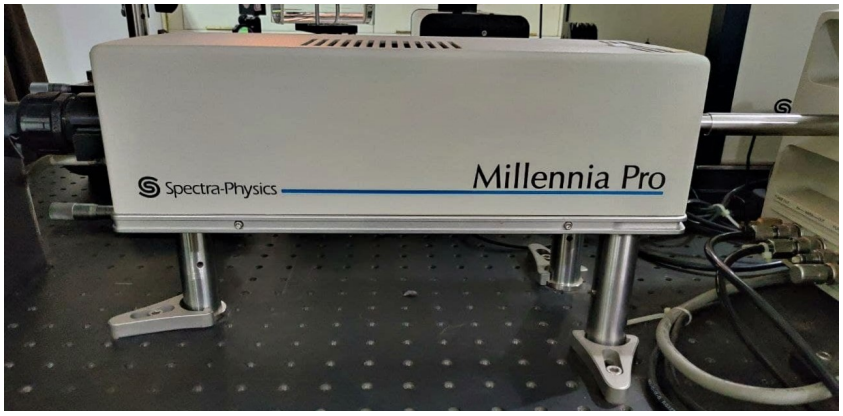

Figure 2.2: Photograph of the Nd:YVO_4 pump laser for the femtosecond oscillator.

uous wave (CW) Nd:Vanadate (Nd:YVO_4) diode-pumped laser (`Millennia Pro-S, Spectra-Physics`) shown in Figure 2.2. A CW diode laser (809 nm, 40 W) pumps the Nd:YVO_4 crystal via an optical fiber module. A compact chiller regulates the Nd:YVO_4 crystal temperature in the laser head via water

re-circulation. The fundamental emission (1064 nm) from the Nd:YVO_4 crystal is converted into the second harmonic (532 nm) using a Lithium Triborate (LBO) crystal. The maximum output power of the Millennia Pro S laser is 5.2 W. The beam has a diameter of 2.3 mm with the TEM_{00} (Gaussian) spatial intensity distribution. The femtosecond oscillator produces pulses of duration < 80 fs at a repetition rate of 82 MHz. The output wavelength is tunable from 720 nm to 850 nm for our system, and a maximum average power output of 550 mW is obtained at the peak of the tuning curve (790 nm).

2.2.2 Femtosecond regenerative amplifier

Most ablation applications of ultrashort pulses require energies in the range of millijoules (mJ), which is not available from conventional Ti:Sapphire oscillators (which produce much lower energies, typically ≈ 10 nJ). Direct amplification of ultrashort pulses from the nJ to the mJ level is not possible because the high peak intensities involved will surpass the damage thresholds of the laser media and optical components used in optical amplifiers. The research work of D. Strickland and G. Mourou (1985) [4] led to the adoption of the CPA (chirped pulse amplification) technique into the optical region, making the amplification of ultrashort pulses feasible without component damage.

CPA works in three stages; (i) pulse stretching, (ii) pulse amplification, and (iii) pulse compression. Figure 2.3 shows the schematic diagram of the CPA technique. Femtosecond laser pulses of nJ energy from the oscillator are first stretched in time to hundreds of ps width by employing two gratings. These stretched pulses are then amplified in a Ti:Sapphire crystal to several tens of millijoules energy in the regenerative cavity. Finally, a grating pair compresses the pulses back to the original pulse width. Energy for amplification is obtained from another laser that pumps the amplifier crystal.

Our regenerative amplifier (`TSA-10`) houses a Ti:Sapphire crystal which is pumped by a frequency-doubled Nd:YAG laser having maximum pulse energy

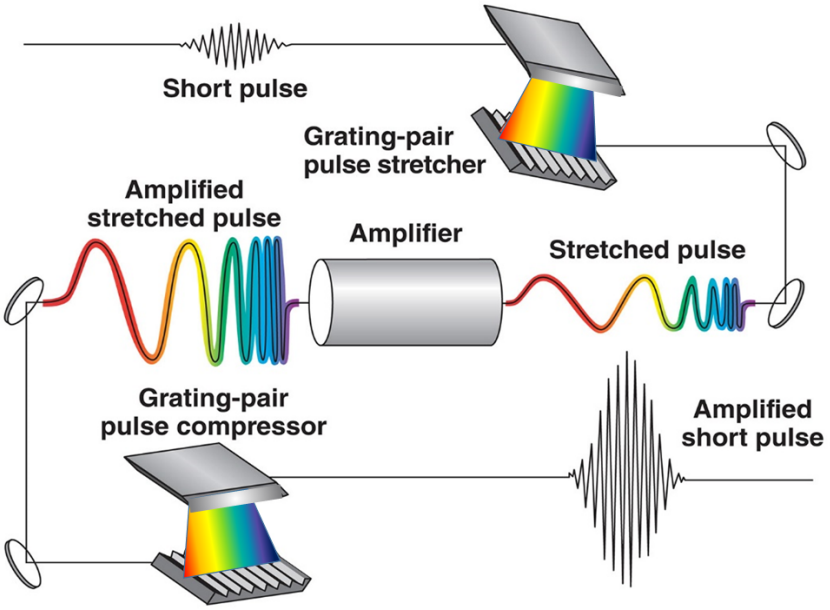

Figure 2.3: Schematic representation of the CPA technique (figure is adapted from [5]).

of 280 mJ, operating at 10 Hz repetition rate. The femtosecond pulse train from the ultrafast oscillator (at 82 MHz), routed by a mirror into the TSA-10, is initially sent to the pulse stretcher. The stretcher introduces a positive chirp such that different frequency components travel at different speeds, elongating the pulse to about 300 ps width. Afterwards, a quarter-waveplate ($\lambda/4$) and Pockels cell (PC1) in the regenerative cavity act together to trap a single pulse from the 82 MHz pulse train. The regenerative cavity consists of a Ti:Sapphire crystal as the amplifying medium, which gets optically pumped by the Nd:YAG laser. The trapped pulses oscillate in the regenerative cavity and gain energy in each trip as they pass through the crystal. After several round trips (typically 20), when the pulses gain sufficient energy, the tallest pulse is reflected out of the cavity with the help of an electro-optic switch (cavity-dumping). The fast electro-optic switch consists of a Pockels cell (PC2) and a polarizer, which can pick a single pulse from the amplified pulses. By this method, an input pulse of a few nJ energy gets amplified to around 3 mJ energy.

For further amplification, the cavity-dumped pulse is then directed to a

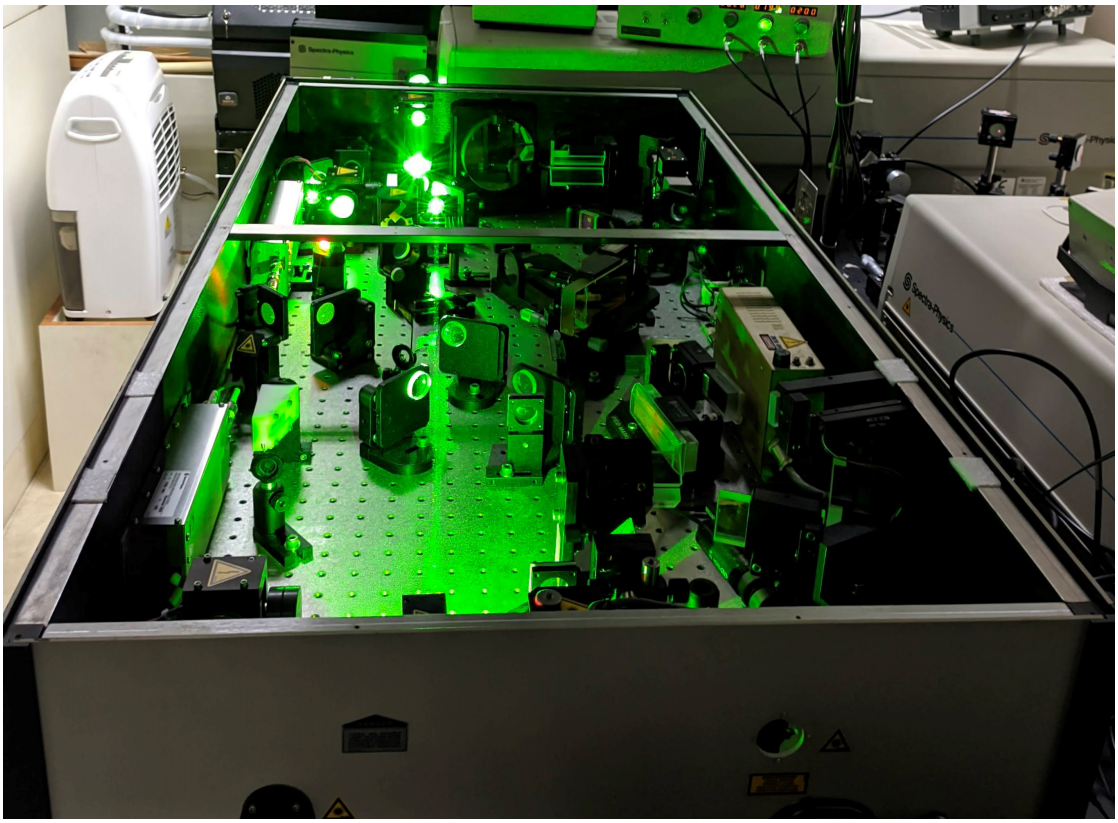

Figure 2.4: Femtosecond chirped-pulse regenerative amplifier system used for the experiments.

double-pass linear amplifier (a Ti:Sapphire crystal), which has a gain of about 4. The amplified output from the double-pass amplifier is then compressed back to the original pulse width (100 fs) by introducing a negative chirp by using a pulse compressor (grating). Thus, the TSA-10 can generate 100 fs pulses of more than 10 mJ energy at a repetition rate of 10 Hz, which have been used in the present experimental work (shown in Figure 2.4). The timings associated with the switching of the Pockels cells is very critical for the CPA system. The input Pockels cell must be switched at the same time, when only a single pulse from the 82 MHz train enters the resonator cavity. This is done by switching the Pockels Cell in synchronization with the RF signal generated by the AOM of the femtosecond oscillator, with the help of a Synchronization and Delay Generator (SDG) unit.

2.2.3 Nanosecond laser system

The Chirped pulse amplification (CPA) based regenerative amplifier unit (`TSA-10`) requires optical pumping, which is provided by a Q-switched neodymium-doped yttrium aluminum garnet (Nd:YAG) laser (`Quanta Ray, Spectra Physics`). Nd:YAG is a popular four-level solid-state laser emitting at 1064 nm, with triply ionized neodymium as the active medium. In our laser, the Nd:YAG crystal is pumped by two flash lamps whose output matches the principal absorption bands of the crystal in the red and near-infrared regions. The fundamental emission is frequency-doubled to 532 nm in a potassium di-deuterium phosphate (KDP) crystal, producing 7 ns, 275 mJ pulses at a repetition rate of 10 Hz. These high-energy pulses are generated by means of Q-switching, which is a method for achieving energetic short (but not ultrashort) light pulses by modulating the intracavity losses, and thus the Q factor of the laser cavity. The Q-switching assembly consists of a polarizer, a Pockels cell (voltage-controlled waveplate), and a quarter-waveplate ($\lambda/4$). By fast-switching the high voltage applied to the Pockels cell, the stored energy in the cavity is allowed to exit from the resonator in a short duration, generating a ns pulse output.

2.3 Vacuum systems

Laser ablation of target is directly influenced by the surrounding gas and its pressure because of the several complex dynamical process involved in laser-matter interaction. Hence, the ambient gas (e.g. nitrogen) and pressure (which could be down to vacuum in some cases) are crucial in these experiments. The basic components required to control ambient conditions in laser ablation experiments are the following: (i) vacuum chamber, (ii) dry pump and turbo-molecular pump, and (iii) target motion controller. We have performed experiments in background pressures ranging from 760 Torr (atmospheric pressure)

to 10^{-5} Torr.

2.3.1 Vacuum chamber

The vacuum chamber used in this work is cylindrical in shape and horizontally placed (length = 75 cm, diameter = 25 cm). It is connected to a bigger cylindrical chamber of approximately 300 litres volume, which is vertically placed (1 m diameter, 40 cm height). The irradiation targets are placed in the smaller chamber, which has five viewports and one connecting port to the bigger chamber. A high-vacuum compatible target holding translation stage and an electrical feedthrough are connected to the 100 CF port located at the top of the small chamber (Figure 2.5).

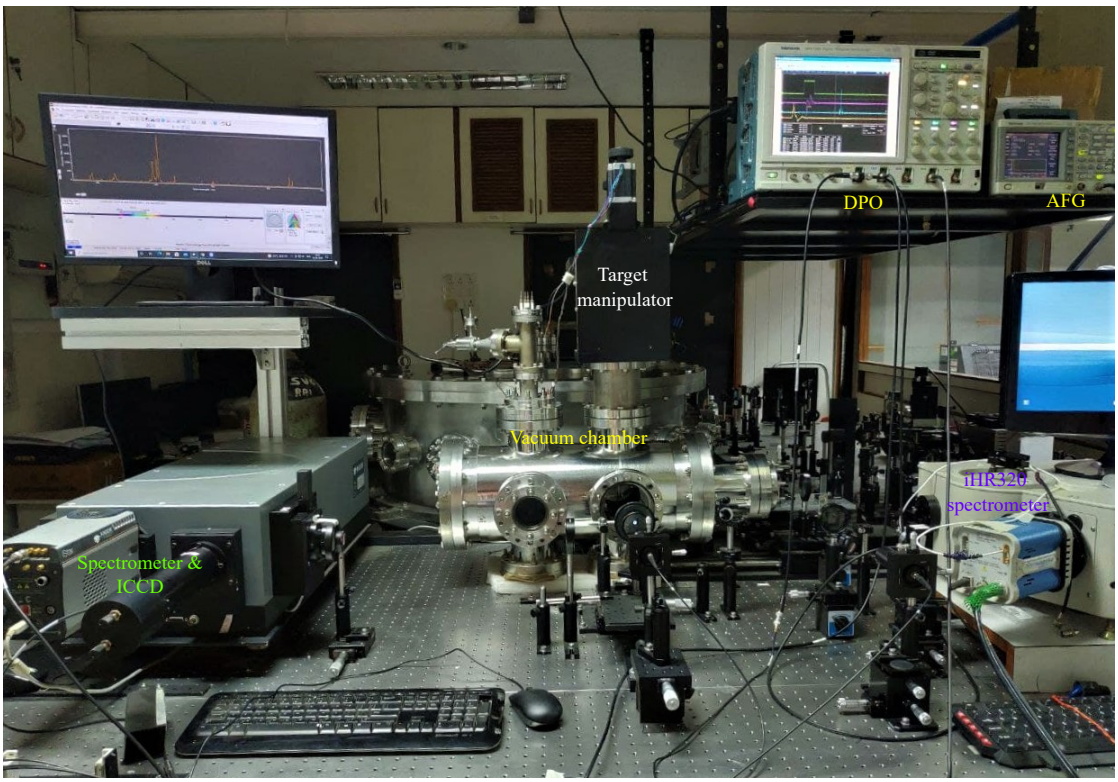

Figure 2.5: Vacuum chamber and target manipulator used for the experiments. The bigger chamber can be seen in the background. Spectrometers also can be seen.

2.3.2 Vacuum pumps

The ambient pressures required for our experiments are in the range of 760 Torr to 10^{-5} Torr. To create high-vacuum a powerful pumping system is required, which typically consists of a roughing pump to reach the background pressure of 10^{-2} Torr, which is followed by a high vacuum pump, e.g., rotary vane pump or turbomolecular pump (TMP). While a rotary vane pump causes oil contamination, oil-free vacuum is obtained by employing a turbomolecular pump. We use a turbomolecular pump (`Model TPU 2101 PC, Pfeiffer, 2000 rev/s`) which is backed by a dry pump (`Model Unidry DBP 050-4, Pfeiffer, 180 rpm`) to obtain clean vacuum.

The Turbomolecular pump consists of pairs of very fast spinning rotating rotor blades and stationary stator blades. The working of the TMPs is based on the transfer of kinetic energy to the gas molecules by hitting them with the fast rotors, and then pushing them out of the system. TMP needs a background pressure of about 5×10^{-2} Torr to start its operation, for which we use the dry pump as a primary pump to evacuate the chamber down to 5×10^{-2} Torr. The rough vacuum (ranging from 760 Torr to 10^{-3} Torr) is measured with a Pirani gauge, while the higher vacuum is measured using a cold cathode gauge (measuring range of 7.5×10^{-3} Torr to 1.5×10^{-9} Torr). The cold cathode gauge (Penning gauge) is an ionization gauge that generates a discharge between two metal electrodes upon the application of a high DC voltage to ionize the gas present in the chamber. Thus, the discharge current is proportional to the pressure of the chamber. In our experiments, the TMP, in conjunction with the dry pump, lowers the chamber pressure down to 5×10^{-6} Torr in about 25 minutes. When the ambient gas is nitrogen, the pressure inside the vacuum chamber is controlled through a needle valve and a regulator.

During laser ablation experiments, the target needs to be moved after every shot(or after a few laser shots) to ablate the fresh sample surface. To facilitate target movement we have used a stepper-motor controlled XY translation stage,

which is attached to the chamber via Wilson seal to the vacuum compatible target holder fixed inside. This setup provides movements in both horizontal and vertical directions (50 mm in both directions) with an accuracy of 12.5 µm. Precise automated motion in the X and Y directions is achieved by a custom-made electronic circuit, which is controlled by a LabVIEW program. Control signals from the PC are given via the LPT port (parallel port) to the target manipulator. Details of this circuit are provided elsewhere [6].

2.4 Detection systems

Detection systems are an integral part of the experiments presented in this thesis, which include fast photodiodes, energy/power meters, beam profiler, intensity autocorrelator, CCD cameras, spectrometers, and digital phosphor oscilloscope. A fast mechanical shutter synchronized with the 'Advance Q-switch' trigger signal from the Nd:YAG laser, along with a 25 MHz arbitrary function generator (AFG 3022B, Tektronix), is used to control the number of laser pulses falling on the target. A Si-PIN fast photodiode (ET-2030, Electro-Optic Technology Inc., USA) having a rise time of $\approx$ 300 ps is used to trigger the spectrometer and ICCD camera. The spectral bandwidths of the femtosecond oscillator and amplifier are measured using a portable spectrometer (Flame, Ocean Optics) for calculating the time-bandwidth product. The spatial profile of the beam and the focal spot size are measured with the help of a 12-bit CCD beam profiler (BC106N-VIS, Thorlabs Inc., USA). Laser pulse energy and average power are measured by employing (i) pyroelectric energy meter (RjP-735, Laser Probe Inc.), (ii) pyroelectric power meter and energy meter (Laserstar, Ophir), and (iii) Analog power meter with thermopile sensor (407 A, Spectra Physics). Details of the other detectors used in our measurements are given below.

2.4.1 Spectrometer

To record the spectra of optical emissions emanating from laser-produced plasma of solid targets, we have used a Czerny-Turner spectrometer (`iHR320`, `Horiba Jobin Yvon`). It has a spectral resolution of about 0.06 nm at the CCD detector. A compact CCD camera from Horiba Jobin Yvon (`Synapse`) and a photomultiplier tube (PMT) from Hamamatsu (`R943-02`, rise time ≈3 ns) are attached to the spectrometer (Figure 2.6).

Figure 2.6: Photograph of the iHR320 spectrometer equipped with CCD and PMT detectors.

The iHR320 is a fully automated triple grating spectrometer with a focal length of 320 mm (f/4.1 aperture). The on-axis grating turret drive can accommodate three gratings with three different resolutions, which can be individually selected via an Origin program written in the `Visual BASIC` platform. The CCD can collect emission spectra within the spectral range of 150 nm to 1500 nm, while the PMT can record optical time of flight (OTOF) data of the plasma components. We performed laser-induced breakdown spectroscopy (LIBS) of nano-structured silicon using iHR320, and the results are discussed in detail in chapter 3.

2.4.2 Charge detector: Faraday Cup

The Faraday cup is an electrically biased metal cup that can be used to collect charged particles from a plasma plume. The collected ions or electrons will form a current which is measured. We used a Faraday cup from `Kimball Physics Inc., Model FC-71A`, which consists of a hollow copper cylinder with a mesh in front of it (Figure 2.7). The charge collection area is 5 mm^2,

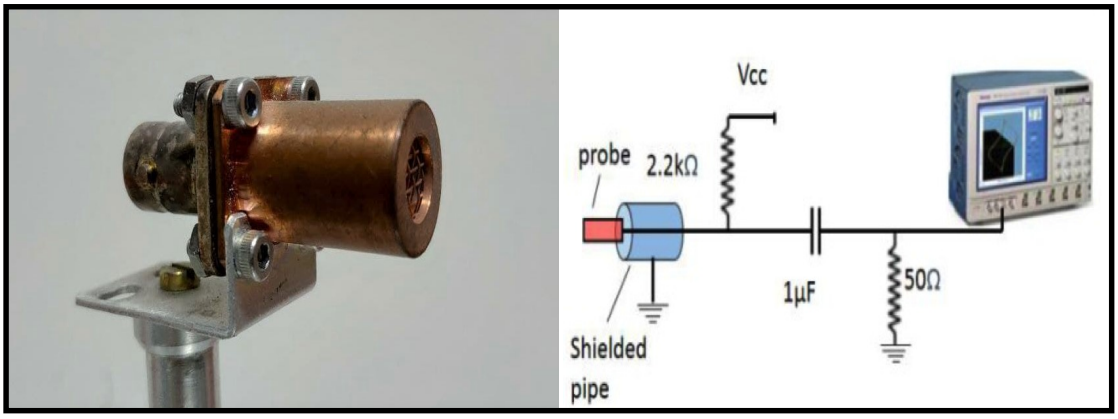

Figure 2.7: Photograph of the Faraday cup (left panel) and the electrical diagram of the ion probe circuit (right panel).

and an outer grounded cylinder provides shielding. An electrical connection is made via the base of the Faraday cup, terminating in a BNC connector. The signal passes through the vacuum feedthrough, to a digital phosphor oscilloscope. The Faraday cup should be voltage biased to reduce the scattering of electrons or ions collected in the cup, and also to reduce the collection of secondary electrons. Typically, -30 V can be applied for positive ions, while for electrons and negative ions it is +30 V. Biasing is done by placing DC voltage source between the vacuum feedthrough and the oscilloscope.

2.4.3 Digital phosphor oscilloscope

We used a fast digital phosphor oscilloscope (`DPO7354, Tektronix`) with four input channels for displaying and measuring the optical time of flight

(OTOF) signals taken with the Faraday cup. The scope has an analog bandwidth of 3.5 GHz. The real-time sampling rate is 40 GS/s while operating with a single channel, which reduces to 10 GS/s when all four channels are active simultaneously. Since the rise time of this DPO (110 picoseconds) is an order of magnitude smaller than that of the PMT (2 ns), it can measure the OTOF signals accurately. The instrument works on Windows XP platform and facilitates the storage of both ASCII data and screen capture for further analysis.

2.5 Laser ablation using structured light

According to classical electrodynamics and quantum mechanics, light possesses not only energy, but also momentum. This momentum, which is responsible for radiation pressure, can be either linear or angular in nature. Experiments explaining radiation pressure have revealed that light transfers its momentum to matter by generating a mechanical pressure during scattering and absorbing events [7]. Nowadays, the linear momentum of light is being routinely employed for trapping and cooling atoms and molecules. According to Poynting's theory, circularly polarized light carries an intrinsic spin angular momentum (SAM). A single-photon carries SAM = $\pm\hbar$ (depending only on the beam's polarization and not on its phase) along with the linear momentum $p = \hbar k$ (where $k = 2\pi/\lambda$) [8, 9].

In 1992, Allen et al. of Leiden University predicted that light with an azimuthal phase dependence of $\exp\{i\ell\phi\}$ (here angle ϕ is the azimuthal coordinate in the beam's cross-section) possesses an angular momentum, which is independent of the state of polarization. This angular momentum is referred to as orbital angular momentum (OAM) and can have a value of $\mathcal{L} = \ell\hbar$ per photon where ℓ corresponds to the number of twists in the helical wavefront in one wavelength of propagation. ℓ can take any integer value, positive or negative, indicating the handedness of the helical wavefront with respect to the

beam direction [7, 10] (Figure 2.8). However, unlike SAM, OAM is independent of the polarization state of the beam, but it depends on the spatial distribution of the field. Thus, SAM and OAM represent two discrete forms of degrees of freedom of light beams. The sum of SAM and OAM gives the total angular momentum of any light field. The beam possessing SAM can be generated simply by using a quarter-wave plate ($\lambda/4$), which converts linear polarization to circular polarization. However, in order to generate a beam carrying OAM we need the help of some optical devices, which enable spin-to-orbital conversion (STOC) of the angular momentum of light [11]. The fundamental concept behind this is the manipulation of the beam's polarization in order to introduce a space-variant Pancharatnam-Berry phase[1] [12]. The beams generated using STOC devices have an unconventional beam profile, and they are referred to as structured beams. Structured beams (possessing a screw dislocation or phase singularity) carry OAM, and an Optical Vortex (OV) beam is an example of a structured beam.

The work presented in this thesis includes direct fs and ns laser ablation of suitable targets for generating surface structures, by employing Gaussian as well as OV beams. OV beams have a spiral phase wavefront around the optical axis, and this causes a singularity point where the phase is undefined. These beams can have various states of polarization such as azimuthal, radial, spiral, etc, depending upon the input beam polarization. In our case, we have used a special diffractive optical element called Spiral Phase Plate (SPP) to generate the OV beam, which will be described in the next section.

2.5.1 Spiral phase plate

The OV beams can be obtained by imposing a spiral phase distribution onto the input beam. Various methods such as astigmatic lens converter, computer gen-

[1]These phase devices are also referred to as Pancharatnam-Berry optical elements (PBOE).

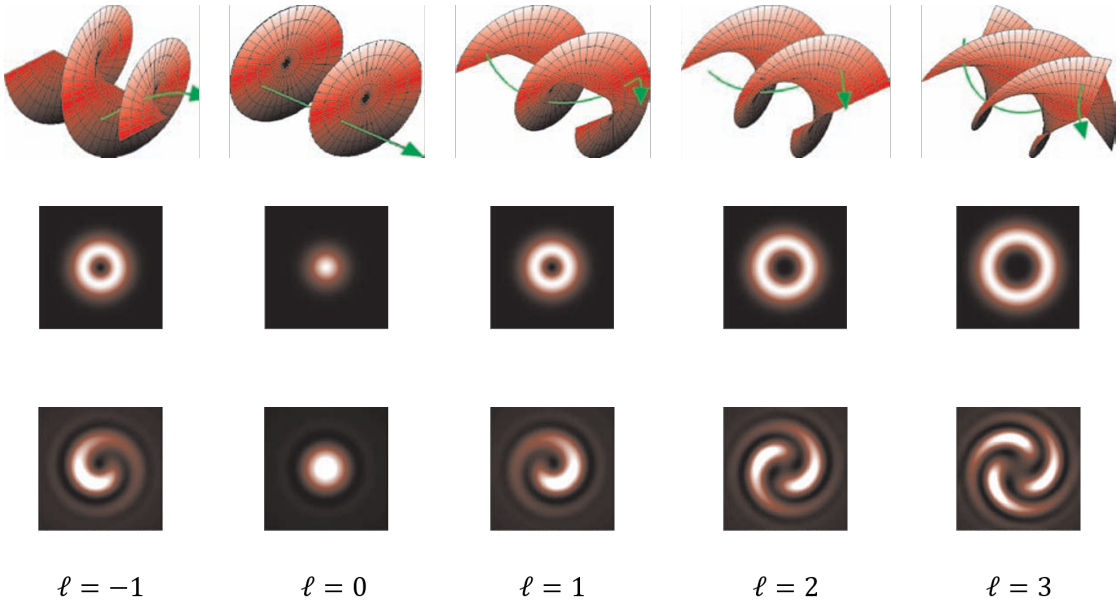

Figure 2.8: Schematic representation of OV beams carrying different ℓ values: pictures of the instantaneous phase (top panel), annular intensity profiles (center panel), and interference pattern of an OV beam with a plane wave, exhibiting a spiral intensity pattern (bottom panel). Green arrows show the Poynting vector following a spiral trajectory around the axis (top panel). The number of spiral arms (bottom panel) equals the number of intertwined helical phase fronts of the helical beam. This figure is adapted from [9].

erated fork hologram [13], spatial light modulator (SLM) [14], Q-plates [15, 16] and spiral phase plate [17] can be used to generate OV beams carrying OAM. A spiral phase plate (SP-plate) is a light-transmitting plane-parallel plate, one side of which is a staircase kind of relief. The thickness of the SP-plate increases in order to introduce a phase retardation which is proportional to the azimuthal angle around a point in the middle of the plate. When an input beam is passed through an SP-plate it acquires a helical wavefront, because the variable phase retardation is proportional to the azimuthal angle around the propagation axis. In our experiment we have used a SP-plate (`Holo/Or Ltd, VL-218-1-Y-A`) of topological charge $\ell = 4$, which provides an azimuthal phase of $2\ell\pi$. The schematic representation of OV beam generation using the SP-plate is shown in Figure 2.9. The spatial intensity profile of the OV beam as a function of the radius r along the diameter of the beam generated by using the SP-plate of topo-

logical charge $\ell = 4$ is displayed in Figure 2.10.

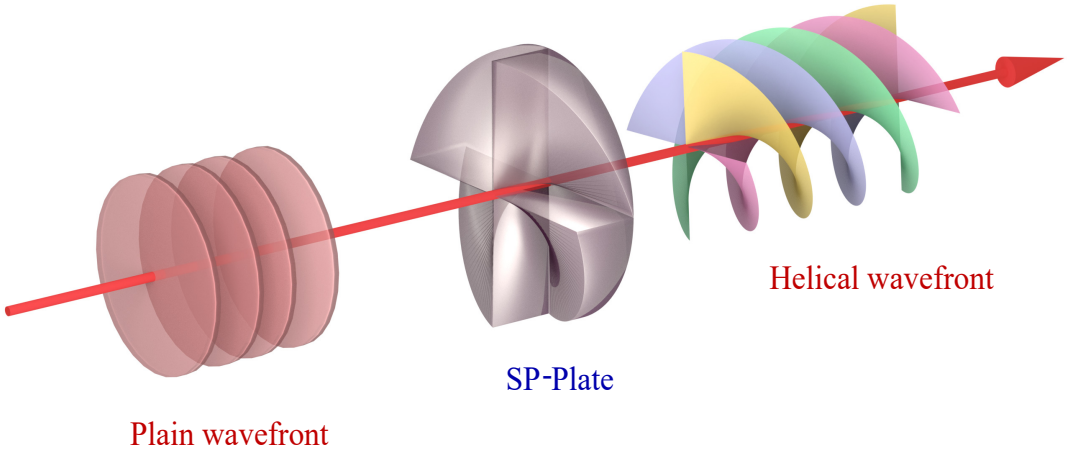

Figure 2.9: Schematic representation of OV beam generation using the SP-plate of topological charge $\ell = 4$.

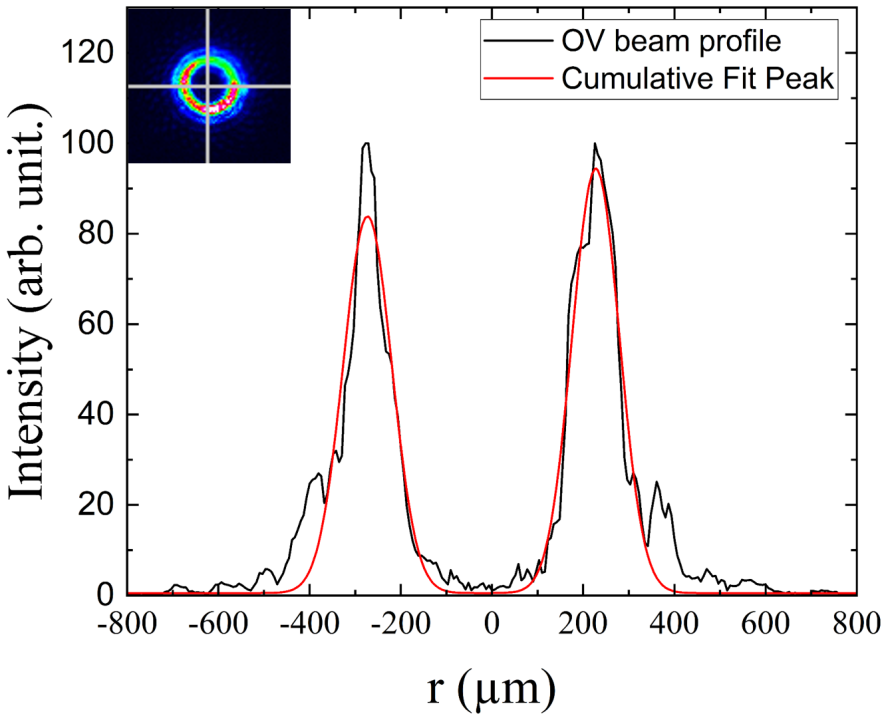

Figure 2.10: Spatial intensity profile (horizontal cross-section) of the OV beam generated by using the SP-plate of topological charge $\ell = 4$. r is the radial distance along the diameter od the beam. The inset image shows the OV beam profile, captured using the Thorlabs beam profiler.

2.6 Surface characterization techniques

In order to investigate and characterize the structures generated on targets by laser irradiation, we have employed various instruments such as scanning electron microscope (SEM), atomic force microscope (AFM),UV-Vis spectrometer, Raman spectrometer, energy dispersive X-ray (EDX) spectrometer, X-Ray photoelectron Spectrometer (XPS), and contact angle meter. The details of these systems are provided in the following sections.

2.6.1 Scanning electron microscopy (SEM)

Generally, the characterization of any surface is carried out with the help of SEM. We obtained and analyzed details of laser-induced surface features and modified surface morphologies by using a Field Emission Scanning Electron Microscope (`FESEM, Carl Zeiss ULTRA Plus`). In the SEM, a focused beam of energetic electrons (3 to 20 keV) is used to generate secondary electrons (SE) and back-scattered electrons (BSE) from the surface of a sample. Signals derived from electron-sample interactions are collected using two detectors: (i) In-Lens (IL) detector, and (ii) secondary electron `Everhart Thornley (ET-SE)` detector. These signals provide important information about the samples, such as external morphology (texture) and chemical composition. Crystalline structure and orientation also can be obtained. With the help of the IL detector we have achieved micrographs with good contrast and high lateral resolution. On the other hand, better topographic information (in the case of silicon micro-needles) is obtained using the conventional secondary electron detector. SEM micrographs provide crucial information about the laser modified surface, such as spatial periodicity of ripples and grooves, ablation area (for threshold calculation), size of the nanoparticles deposited back on the surface during ablation, etc. A thin layer of platinum is sputtered onto laser-irradiated fused silica and quartz samples using (`Quorum Q150 R`) to

prevent charging while imaging.

2.6.2 Energy dispersive X-ray (EDX) spectroscopy

When highly energetic electrons (15 keV to 20 keV) interact with a material, X-rays are generated along with BSE. This leads to the generation of characteristic X-rays, revealing the elements present in the sample. An energy-dispersive Si(Li) crystal-based detector is used to separate characteristic X-rays of different elements into an energy spectrum. This spectrum is then used to analyze the composition of the samples. Our FESEM system is equipped with Energy dispersive X-ray (EDX) spectrometer (`X-Max, Oxford Instruments`) for carrying out fast detection of the elemental composition of materials. The efficiency of the detector will be limited if two elements have characteristic spectra which lie too close, within the resolution of the detector. Hence, elements with lower atomic numbers cannot be characterized efficiently using X-ray emission.

2.6.3 X-Ray photoelectron spectroscopy (XPS)

We have used a surface-sensitive technique, XPS [18], for quantitative measurement of different elements and their chemical or oxidation states. An X-ray beam (Al K_α or Mg K_α) falls on the material's surface, which gives rise to photoelectrons. The kinetic energy (K.E.) of these electrons can be calculated from the equation:

$$K.E. = h\nu - B.E. - \phi \tag{2.1}$$

where $h\nu$ is the energy of the incident photon, B.E. is the binding energy of the ejected photoelectron, and ϕ is the work function which depends on the sample. B.E. of these photoelectrons is directly associated with the chemical state of the atom from which they are ejected. Thus, B.E. is indicative of the chemical and electronic state of the sample. We have measured XPS spectra of laser-irradiated Si samples by using an `ESCALAB MKIV` spectrometer which employs

Al K_α (1486.6 eV) radiation and automatic charge neutralization. Survey spectra showing all the elements present in the sample and high-resolution spectra of selected binding energy regions, have also been collected for detailed analysis of the chemical state of different elements. We have used the C1s spectrum of adventitious carbon (with B.E. = 284.8 eV) as a reference. The analysis of the measured spectra is done using Fityk software after Shirley type background correction.

2.6.4 Atomic force microscopy (AFM)

In addition to the SEM, we have also used an AFM (`Pico Scan 3000, Molecular Imaging`) to characterize the three-dimensional topography of laser irradiated surfaces at high resolution (order of few nm). The working of this microscope is based on the interactions between a sharp, probing tip and the surface. AFM images are obtained by the lateral movement of the probing tip, which raster scans the surface of the sample. The deflections of the tip cantilever are digitized as a function of its lateral position by using a piezoelectric diode. Due to its high lateral and vertical resolution, the AFM is appropriate for characterizing very shallow surface features, allowing the measurement of small crater depths and volumes. In addition, AFM measurement can be directly performed in air rather than in vacuum, and it does not require the sample surface to be conductive (like in the case of SEM). However, AFM has a few disadvantages, including low dynamic range (typically less than 2 µm), and limited scanning area (typically up to 75 x 75 μm^2). Moreover, if there is considerable topology variation on the surface the tip would not be able to measure, and the image will be distorted due to noise.

2.6.5 Raman spectroscopy

Raman spectroscopy is based on the inelastic scattering of photons by molecules. Inelastic scattering of monochromatic radiation by molecules results

in scattered radiation which consists of high and low-frequency components. The scattered radiation gives information about the vibrational energy states of the molecule, becoming the fingerprint of the specific molecule. We used structured Si surfaces as substrates for surface-enhanced Raman spectroscopy (SERS) measurements. A confocal Raman spectrometer (`Model-T64000, Horiba Jobin Yvon`) having 514, 632, and 785 nm excitation wavelengths at 2.0 mW power, was used in the back-scattering geometry to collect Raman spectra from the laser irradiated targets, using the dye Rhodamine 6G (R6G) as analyte. Each spectrum has been measured at two different accumulations to avoid noise in the spectra. Gratings with 1800 l/mm and 2400 l/mm rulings have been used for the measurements, with accumulation times of 20 s and 30 s.. Before collecting each Raman spectrum, the spectrometer is calibrated using the Si non-dispersive peak which is situated at a Stokes shift of 520.7 cm^{-1}.

2.6.6 UV-Vis spectroscopy

The reflectance and transmittance spectra of the laser structured surfaces have been recorded by using a `Jasco V-570` UV-Vis-NIR spectrophotometer. Diffused and specular reflectance have been measured with the help of an integrated sphere (INS-470), equipped with the same instrument. Deuterium and tungsten halogen lamps are used as light sources, allowing detection in the wavelength range 220 to 2000 nm.

2.6.7 Contact angle measurements

The wettability is an important surface property, which describes the ability of a liquid to either spread or adhere on a solid surface. It is determined by the equilibrium between the intermolecular interactions of the adhesive (liquid to surface) and cohesive (liquid to liquid) type [19–21]. The degree of wetting of any solid surface by a liquid is determined by contact angle (CA) measurements. The CA is determined at the triple point where the solid, liquid and vapour in-

terfaces intersect each other (Figure 2.11 a). Considering water as the liquid, the

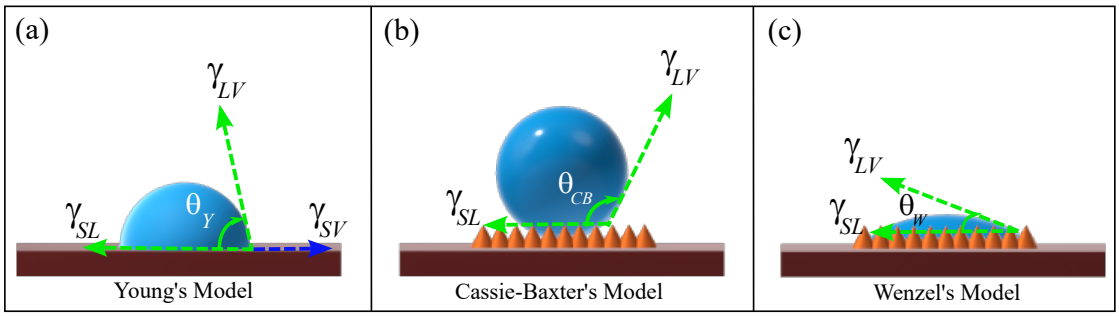

Figure 2.11: Representation of the various models describing the wettability of a solid surface.

wetting state of solid surfaces can be classified as hydrophobic with contact angles higher than 90°, and hydrophilic with contact angles lower than 90°. Apart from these states, two extreme wetting states are also found in nature, known as superhyrophobic (CA $>$ 150°), such as self-cleaning lotus (Nelumbo nucifera) leaves, and superhydrophilic (CA $<$ 10°), such as water harvesting wings of the Namib desert beetle. According to Young's model [22], at the contact angle (θ_Y) the liquid drop is in thermodynamic equilibrium under the action of three interfacial tensions: solid-vapour (γ_{SV}), solid-liquid (γ_{SL}), and liquid-vapour (γ_{LV}), described by the Young's equation,

$$\gamma_{LV}\cos(\theta_Y) = \gamma_{SV} - \gamma_{SL} \tag{2.2}$$

However the Young's equation is valid only for smooth solid surfaces, which is not the case in general. Typically, any solid surface will have some finite roughness, and for such surfaces the Young's model fails to predict the CA accurately. To improve the accuracy in CA measurement, Cassie–Baxter [23] and Wenzel et al. [24] proposed theoretical models which describe the effects of macroscopic surface roughness on the wettability of solid surfaces. For highly hydrophobic surfaces the Cassie-Baxter model (Figure 2.11 b) is usually considered because the multiscale surface morphology provides tiny air pockets, which enhance the hydrophobicity of the surface. On the other hand, hydrophilicity (homoge-

neous wetting) is best explained by the Wenzel model (Figure 2.11 c). According to Wenzel's theory, wetting of surfaces that have a CA less than 90° can be improved by increasing the surface roughness. The relation between surface roughness and contact angle is given by,

$$cos\theta_W = rcos\theta_f \tag{2.3}$$

where θ_W and θ_f are the apparent (macroscopic) and Young (intrinsic) contact angles measured on rough and flat surfaces of the same material, respectively, and r is the roughness factor (correction factor) defined as the ratio between the actual and projected surface areas of the sample. Another key parameter which affects the wettability of any solid surface is the chemical composition which determines the surface free energy. High surface energy leads to hydrophilicity and low surface energy leads to hydrophobicity.

We have used an optical contact angle goniometer (`DM 501, Kyowa`) to measure the CA of the surfaces. Static contact angle measurements have been performed to understand the effect of fs-laser irradiation on the wetting properties of structured silicon surfaces by using the sessile drop method [25]. In CA measurements, a droplet of distilled water of volume 1 µL is gently positioned on the surface using a micro-syringe, and images are captured to measure the angle formed at the solid-liquid interface. Further details are discussed in chapter 5.

2.7 Laser texturing set up at a glance

The schematic of the experimental setup used for laser-induced surface structuring is shown in Figure 2.12. Laser ablation and structuring have been performed utilizing both fs and ns laser pulses. An electro-mechanical mechanical shutter synchronized with the Q-switch signal of the Nd:YAG laser is used for controlling the number of pulses falling on the target. Motorized X and Y trans-

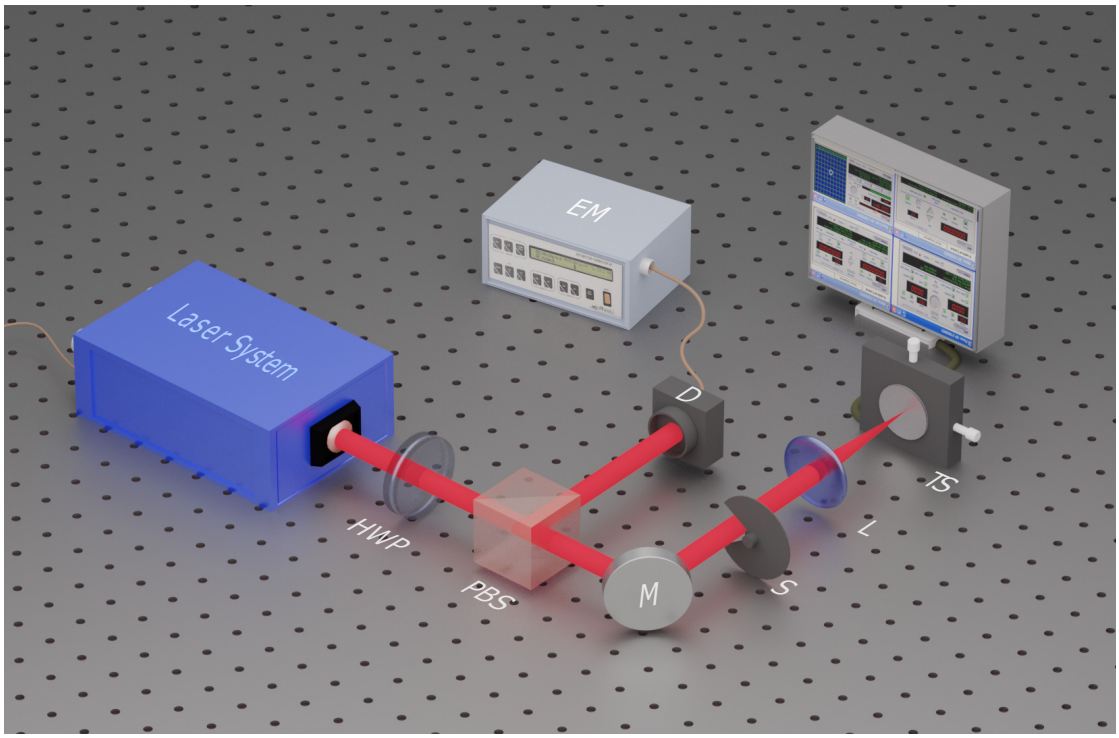

Figure 2.12: Schematic of the experimental set up used for laser-induced surface structuring. HWP - half-wave plate, PBS - polarizing beam splitter, M - mirror, S - electromechanical shutter, L - focusing lens, TS - motorized XY translational stage, D - pyroelectric detector, and EM - energy meter. The sample is mounted on the XY translation stage.

lation stages operated with the help of a LabVIEW program are used to translate the target are required.

2.8 Summary

The instruments and techniques employed for the measurements reported in this thesis are described in this chapter. A general layout of the experimental setup is provided. Changes to this experimental layout, if any, are discussed in detail in the experimental sections of the related chapters.

Bibliography

[1] Anatoliy Y Vorobyev and Chunlei Guo. Direct femtosecond laser surface nano/microstructuring and its applications. *Laser & Photonics Reviews*, 7(3):385–407, 2013.

[2] Carsten Momma, Stefan Nolte, B N Chichkov, F v Alvensleben, and A Tünnermann. Precise laser ablation with ultrashort pulses. *Applied surface science*, 109:15–19, 1997.

[3] KK Anoop, Nancy Verma, Nithin Joy, Sivanandan S Harilal, and Reji Philip. Enhancement of optical emission and ion currents in a laser produced silicon plasma by femtosecond laser-induced periodic surface structuring. *Physics of Plasmas*, 25(6):063304, 2018.

[4] Donna Strickland and Gerard Mourou. Compression of amplified chirped optical pulses. *Optics communications*, 55(6):447–449, 1985.

[5] Rkei. Chirped-pulse amplification. https://www.lle.rochester.edu/index.php/1985/03/01/chirped-pulse-amplification/, Mar 2021. [Online; accessed 10-January-2022].

[6] Suchand Sandeep. *Investigations of nonlinear optical effects and ultrafast laser Induced plasma in nanostructured media*. PhD thesis, Raman Research Institute.

[7] Les Allen, Marco W Beijersbergen, RJC Spreeuw, and JP Woerdman. Orbital angular momentum of light and the transformation of laguerre-gaussian laser modes. *Physical review A*, 45(11):8185, 1992.

[8] Lorenzo Marrucci, Carlo Manzo, and Domenico Paparo. Optical spin-to-orbital angular momentum conversion in inhomogeneous anisotropic media. *Physical review letters*, 96(16):163905, 2006.

[9] Miles Padgett, Johannes Courtial, and Les Allen. Light's orbital angular momentum. *Physics today*, 57(5):35–40, 2004.

[10] L Allen, MJ Padgett, and M Babiker. Iv the orbital angular momentum of light. *Progress in optics*, 39:291–372, 1999.

[11] Lorenzo Marrucci, Ebrahim Karimi, Sergei Slussarenko, Bruno Piccirillo, Enrico Santamato, Eleonora Nagali, and Fabio Sciarrino. Spin-to-orbital conversion of the angular momentum of light and its classical and quantum applications. *Journal of Optics*, 13(6):064001, 2011.

[12] Lorenzo Marrucci, C Manzo, and D Paparo. Pancharatnam-berry phase optical elements for wave front shaping in the visible domain: switchable helical mode generation. *Applied Physics Letters*, 88(22):221102, 2006.

[13] V Yu Bazhenov, MS Soskin, and MV Vasnetsov. Screw dislocations in light wavefronts. *Journal of Modern Optics*, 39(5):985–990, 1992.

[14] Andrew Forbes, Angela Dudley, and Melanie McLaren. Creation and detection of optical modes with spatial light modulators. *Advances in Optics and Photonics*, 8(2):200–227, 2016.

[15] Filippo Cardano, Ebrahim Karimi, Sergei Slussarenko, Lorenzo Marrucci, Corrado de Lisio, and Enrico Santamato. Polarization pattern of vector vortex beams generated by q-plates with different topological charges. *Applied optics*, 51(10):C1–C6, 2012.

[16] Lorenzo Marrucci. The q-plate and its future. *Journal of Nanophotonics*, 7(1):078598, 2013.

[17] Keiichi Sueda, G Miyaji, Noriaki Miyanaga, and M Nakatsuka. Laguerre-gaussian beam generated with a multilevel spiral phase plate for high intensity laser pulses. *Optics express*, 12(15):3548–3553, 2004.

[18] CJ Powell and Mo P Seah. Precision, accuracy, and uncertainty in quantitative surface analyses by auger-electron spectroscopy and x-ray photoelectron spectroscopy. *Journal of Vacuum Science & Technology A: Vacuum, Surfaces, and Films*, 8(2):735–763, 1990.

[19] Donggyu Kim, Nicola M Pugno, and Seunghwa Ryu. Wetting theory for small droplets on textured solid surfaces. *Scientific reports*, 6(1):1–8, 2016.

[20] Doris M Spori, Tanja Drobek, Stefan Zürcher, Mirjam Ochsner, Christoph Sprecher, Andreas Mühlebach, and Nicholas D Spencer. Beyond the lotus effect: roughness influences on wetting over a wide surface-energy range. *Langmuir*, 24(10):5411–5417, 2008.

[21] Toshihiro Tanaka, Joonho Lee, and Piotr R. Scheller. Chapter 1.5 - interfacial free energy and wettability. In Seshadri Seetharaman, editor, *Treatise on Process Metallurgy*, pages 61–77. Elsevier, Boston, 2014.

[22] T. Young. Iii. an essay on the cohesion of fluids. *Philosophical Transactions of the Royal Society of London*, pages 65 – 87.

[23] B D Cassie, A. B. D. Cassie, and S. Baxter. Of porous surfaces,. *Transactions of the Faraday Society*, 40(5):546–551, 1944.

[24] Robert N. Wenzel. Resistance of solid surfaces to wetting by water. *Industrial and Engineering Chemistry*, 28(8):988–994, 1936.

[25] Nancy Verma, KK Anoop, Priya Dominic, and Reji Philip. Fabrication of durable superhydrophilic silicon surfaces using nanosecond laser pulses. *Journal of Applied Physics*, 128(13):135304, 2020.

Chapter 3

Femtosecond laser texturing of silicon

This chapter discusses the generation of various surface structures on crystalline silicon (100) by irradiation using 100 femtosecond laser pulses having a Gaussian spatial profile. The influence of irradiation parameters such as pulse energy, number of pulses and laser wavelength on the surface morphology is illustrated. The role of background pressure on the appearance of quasi-periodic structures is studied. Experimental conditions are optimized for fabricating large area nanostructured surfaces, and the effect of surface structuring on the optical and morphological properties is investigated. Characterization of a fs laser-induced plasma generated on the nanostructured surface reveals enhanced optical emission and increased ion currents.

3.1 Introduction

Direct laser surface structuring of solid targets and the subsequent modification of their optical, mechanical, chemical, biological, and other properties has been an intensive research topic over the past three decades [1–6]. Even though laser-induced surface structuring was first reported by Birnbaum in 1965, most of the theoretical and experimental investigations happened only by the begin-

ning of the 1980s [1–3, 7–9]. Various types of laser-induced surface structures including periodic patterns can be fabricated in the micro- and nano-scale by gentle laser ablation. Among all, laser-induced periodic surface structuring is a widely accepted method because of the flexibility it offers in the fabrication process. The precision offered by fs laser ablation is preferred in most of the LIPSS fabrications in recent years owing to its advantages (less heat affected zone, no laser-plasma interaction) over conventional nanosecond laser processing [5, 6]. Femtosecond laser-induced periodic surface structures (fs-LIPSS) has been studied in a variety of solids (for example metals, semiconductors, dielectric, and polymers) by using irradiation energies close to their ablation thresholds. LIPSS formation depends not only on the irradiation conditions, but also on the material properties and ambient condition. The typical LIPSS patterns, often termed "ripples," are oriented according to the laser polarization, with the spatial periodicity scaling with the laser wavelength. In addition, other quasi-periodic structures called "grooves" have also been observed, which show a preferential alignment parallel to the laser polarization, orthogonal to the ripples [4–6].

The underlying physical mechanisms of LIPSS formation are still a topic of debate; however, two different theories have been proposed, namely, the (i) "static" (interference) model, and the (ii) "dynamic" (self-organization) model [8, 10–12]. Upon laser irradiation, collective longitudinal oscillations of electrons called surface plasmon polaritons (SPPs) can be excited which propagate along the conductor-dielectric interface. According to the static model, the interference of the incident laser beam with the excited SPPs results in a spatially modulated energy distribution on the surface which results in grating-like structures [8, 10]. On the other hand, according to the dynamic model, laser irradiation induces a high degree of instability at the target surface, and the resulting perturbed surface then relaxes through self-organization [11, 12]. The spatial period and orientation of LIPSSs strongly

depend on the laser irradiation conditions, i.e., pulse energy (E), number of pulses (N), and state of polarization (SoP). The detailed categorization of LIPSSs has been given in section 1.3. In most metals and semiconductors, LSFL orientation is perpendicular to the laser polarization while HSFL orientation and the grooves are found to be parallel to the laser polarization. Contrary cases of ripple orientation have also been reported in some materials due to the material properties [4–6].

Silicon is one of the most extensively used materials in the field of photovoltaic cells, infrared (IR) detectors and opto-electronic devices. The main aspect of most of these applications is light collection and its conversion afterwards, but collection efficiency of silicon usually suffers because of high reflection loss at the air-silicon interface due to the abrupt change of refractive index. Previous studies have shown that one dimensional (1-D) surface gratings can significantly modify the optical properties of semiconductors and efficiently suppress reflection [13–15]. These 1-D gratings are usually fabricated on silicon using optical or electron beam lithography techniques. Vorobyev et al. [16] reported that fs-LIPSS suppresses both the total hemispherical as well as specular polarized reflectance of silicon surface significantly over the entire studied wavelength range (250-2500 nm). They have reported that ultrashort laser processed LIPSSs exhibits clear polarization dependence in the visible range for both total and specular reflectance. Therefore, fs-LIPSS essentially gives a polarization-sensitive antireflection surface in the visible spectral range. Recently Sarbada et al. reported the low reflective properties of picosecond laser-induced periodic surface structures (ps-LIPSS) created on polycrystalline silicon. They have achieved almost 36% decrease in the average reflectance of a Si wafer textured with LIPSS in the wavelength range of 400-860 nm [17]. LIPSSs have presented a successful path towards structural coloration, superhydrophobic/superhydrophilic surfaces, efficient substrates for SERS (surface enhanced Raman spectroscopy), etc [5, 6]. These applications are of great im-

portance in the fields of materials science, medicine and industry, making LIPSS an ubiquitous and powerful tool among the different types of surface structuring techniques.

This chapter presents experimental findings on surface structures generated by irradiation with fs-laser pulses on crystalline silicon (100) targets. The characteristics of the ripples, grooves and their dependency on laser parameters (wavelength and polarization state) and irradiation conditions (pulse energy and number of pulses) are discussed. We also address the influence of background on the morphology of the structured surface. After optimizing the irradiation conditions we fabricate a large area (5×4 mm^2) consisting of nanostructures, to investigate the influence of surface texturing on the optical properties of fs laser structured silicon. In addition, we investigate optical and ion emissions emanating from a laser-produced plasma generated from a laser-structured Si sample target. From laser-induced breakdown spectroscopy (LIBS) and ion emission measurements we observe an enhancement in both optical and ion emissions. The optical emission spectrum is measured using a high-resolution spectrometer, and ion dynamics is recorded using a negatively biased Faraday cup (FC). The dependence of optical emission and ion dynamics on ambient pressure also is investigated. Even though enhancements in X-ray and field emission from various nanostructured targets have been reported previously in literature, the nature of optical emission and ion generation from fs-LIPSS targets, irradiated by intense laser pulses, is seldom investigated [18–21]. Enhancements observed in both LIBS and FC signals imply that a large amount of energy is absorbed when laser pulses interact with nanostructured surfaces. Furthermore, Periodic surface structuring and subsequent reduction in reflectivity resulting in enhanced absorption open up several possibilities in photovoltaics, IR detectors, and other surface science applications.

3.2 Experimental details

The schematic of the experimental setup is given in Figure 2.8. LIPSS are fabricated on crystalline silicon (100) using ultrashort pulses generated from a Ti:sapphire laser system (TSA, Positive Light), delivering 10 mJ, 100 fs pulses at 800 nm with a repetition rate of 10 Hz. Since laser pulse energy (E), polarization (P), number of pulses (N), nature of the target, and ambient conditions are very crucial parameters in femtosecond laser surface structuring, precise control of each of these parameters is necessary for each stage of fabrication [5, 6]. We use a half-wave plate in combination with a polarizing cubic beam-splitter in the optical path to regulate the energy of the laser pulse and to select the required polarization state. A fast electro-mechanical shutter, synchronized with the 'Q-switch Out' of the Nd:YAG laser system, is used for controlling the number of laser pulses falling on the target.

To understand the influence of the laser wavelength on the ablation threshold and formation of LIPSS, we use the second harmonic wavelength (400 nm) obtained by introducing a barium borate (BBO) crystal in the beam path. The remnant of the fundamental wavelength is filtered out using a suitable band pass filter. The laser beam is focused on the silicon target at normal incidence using a plano-convex lens of focal length $f_L = 40$ cm. The Si wafer is mounted on a high precision linear translation stage (Newport M-ILS50PP) so that it can be moved after each ablation event. The effect of ambient conditions on LIPSS fabrication is studied by keeping the target in a high vacuum chamber, where the background pressure can be varied in a wide range (5×10^{-5} Torr to 760 Torr) using a dry pump and turbo molecular pump (Pfeiffer). The topography of the processed silicon surfaces is analyzed using a high-resolution field emission scanning electron microscope (FESEM ULTRA Plus, Carl Zeiss).

In order to study the optical properties of fs-LIPSS surfaces, we fabricated a large area (5×4 mm^2) nanostructured surface using 100 fs, 800 nm pulses under

atmospheric conditions (as opposed to lithographic setups which require high vacuum escalating the cost). Since the laser runs at 10 Hz, a very slow translation stage velocity (0.01 mm/s along the x-axis) and optimized laser conditions (E and N) are used for line by line scanning. Properly overlapped scanning (along the y-axis) results in uniform surface structuring over a large area. The reflectance of the structured samples is measured in the UV/VIS/NIR range by using an integrating sphere coupled to a spectrophotometer (JASCO V-570). A CCD coupled high-resolution (0.06 nm) spectrometer iHR320 (HORIBA Jobin Yvon) is employed to record LIBS emission spectra, and a negatively biased Faraday cup (Kimbal Physics) is used for measuring ion emission from the laser-produced plasma [22, 23]. LIBS and Faraday cup measurements are carried out in high vacuum conditions with an input laser intensity I = 1.1 $\times$ 10^{14} W/cm^2. To differentiate the behaviour of laser-induced surface structures from unprocessed silicon, we have recorded LIBS emission spectra and ion currents from both processed (Si-LIPSS) and unprocessed silicon targets.

3.3 Laser-induced periodic surface structuring of silicon

When a material is irradiated by using multiple fs laser pulses with the pulse energy kept close to the ablation threshold, various self assembled structures appear on the surface, whose morphology varies from subwavelength ripples to microgrooves and quasi-periodic microspikes [24]. The formation of these surface features is strongly governed by the irradiation conditions (energy of the incident pulse and number of the pulses falling on the surface). Therefore, with the fine tuning of irradiation conditions and laser parameters, particular surface features can be optimized. In order to understand the formation of various types of LIPSS a systematic study is performed to find the laser-induced damage threshold, which will be discussed in the next section.

3.3.1 Laser-induced ablation threshold calculation

Femtosecond laser-matter interaction at fluences close to the damage threshold leads to gentle ablation and subsequent micro-/nano-structure formation. The determination of single pulse ($F_{\text{th}}(1)$) or multipulse ($F_{\text{th}}(N)$) damage threshold plays a crucial role in LIPSS fabrication. We estimate laser-induced damage thresholds for the silicon target for both 800 nm and 400 nm irradiation, by plotting the area of the laser ablated spot as a function of the incident pulse energy [25]. For a beam with Gaussian intensity profile, the damaged area is related to the incident pulse energy through the relation

$$\sigma = \frac{\sigma_0}{2} \ln\left(\frac{E}{E_{\text{th}}}\right) \tag{3.1}$$

where σ_0 is the area of the Gaussian beam at the $1/e^2$ point on the energy distribution, E is the laser pulse energy, and E_{th} is the threshold energy required to ablate the target. Figure 3.1 represents the variation in the damaged area as a function of the logarithm of the pulse energy, ln(E), for silicon target ablation with pulses of wavelength 800 nm and 400 nm, respectively. The slopes and y-intercepts of these graphs are used for determining the beam spot size on the silicon target, and the threshold energy and threshold fluence for target damage. The obtained values of peak threshold fluence ($F_{\text{th}}(1)$), when ablating with 800 and 400 nm pulses, are 0.32 ± 0.01 J/cm^2 and 0.09 ± 0.01 J/cm^2, respectively. It is also noted that the threshold is slightly lower for silicon in atmospheric conditions compared to high vacuum. This observed difference in threshold fluence (in the presence of air) is due to air breakdown which occurs near the target surface in the early stages of fs laser ablation, and subsequent cascade ionization, in the target material. The formation of filaments in the presence of ambient gas may also influence the breakdown in threshold values [26]. The estimated values of multi-pulse (N = 100) and single pulse (N = 1) laser ablation thresholds of the silicon target in atmospheric and vacuum conditions for 800 nm and 400 nm

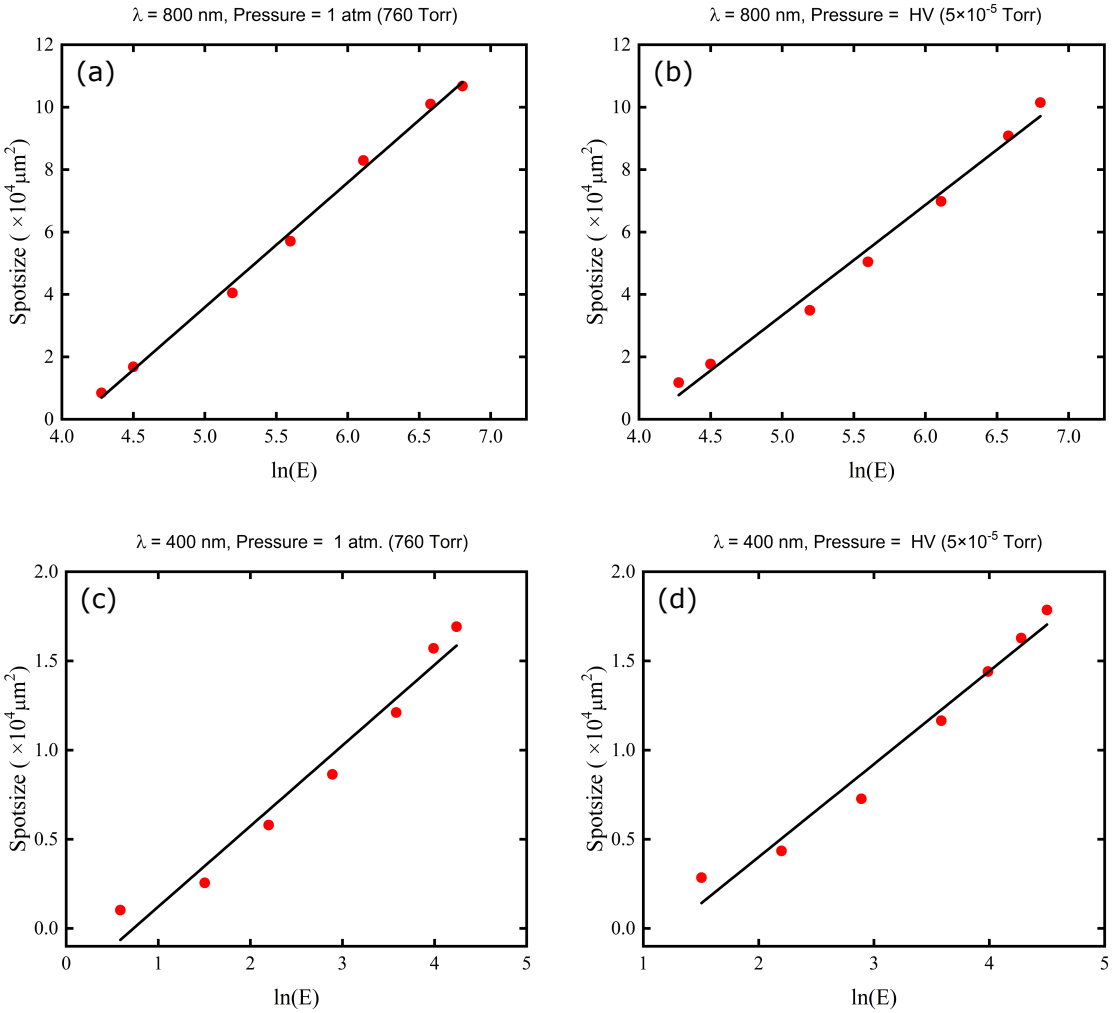

Figure 3.1: Increase in the ablated area of the silicon target as a function of the logarithm of the pulse energy, ln(E). (a) and (b) are for atmospheric and high vacuum conditions, respectively, for 800 nm pulses. (c) and (d) present the same data for 400 nm pulses. N = 100 in all cases.

pulses are shown in Table 3.1. It is clear that the ablation threshold fluence for silicon is lower for shorter wavelength pulses (higher photon energy), and the obtained fluence values are consistent with previous reports [27–29]. The single pulse damage threshold can be obtained by considering the incubation factor of silicon target at 100 fs [28, 29]. All the Si-LIPSS fabrications carried out in this report are performed at fluences close to the ablation threshold values. At higher fluences [$> 2 \times F_{\text{th}}(1)$], the ablated area gets covered with micro-structures or craters, depending on the nature of the material. The lower threshold fluence at

Ablation condition	Peak threshold fluence $F_{th}(N)$ (J/cm^2)	Peak threshold fluence $F_{th}(1)$ (J/cm^2)
$\lambda = 800$ nm, atmosphere	0.15	0.32 $\pm$0.01
$\lambda = 800$ nm, high vacuum	0.16	0.34 $\pm$ 0.02
$\lambda = 400$ nm, atmosphere	0.04	0.09 $\pm$ 0.01
$\lambda = 400$ nm, high vacuum	0.06	0.14 $\pm$ 0.01

Table 3.1: Femtosecond laser-induced ablation threshold of silicon target under atmospheric and high vacuum conditions, for 800 nm and 400 nm pulses, with N = 100.

shorter wavelength can be explained by considering the optical properties of silicon as a function of wavelength [30–32]. The reflectivity (R) of polished silicon is 49% at 400 nm and 33% at 800 nm, while the linear absorption coefficient (α) is two orders of magnitude higher at 400 nm (9.3$\times$10^4 cm^{-1}) compared to that at 800 nm (8.5 $\times$ 10^2 cm^{-1}) [33]. Since the intensity corresponding to threshold fluence is of the order 10^{13} W/cm^2, two-photon absorption (TPA) also plays a significant role in light absorption. The reported value of TPA absorption coefficient (β) at 800 nm is 1.8 cm/GW, while the same at 400 nm is 5 - 10 cm/GW, as obtained from Ref. [34] by extrapolating the scaling rule reported in Ref. [35]. Therefore, by considering the reflectivity, and the linear and nonlinear absorption coefficients of silicon, it can be concluded that the absorption and coupling of light onto the target is more efficient at 400 nm compared to 800 nm, resulting in a lower ablation threshold fluence for shorter wavelengths.

3.3.2 Formation of Si-LIPSS under different ambient pressures

While most of the structures shown in this chapter are fabricated using 800 nm fs-pulses, some are fabricated using 400 nm fs-pulses, in order to explore the role of wavelength (photon energy) in LIPSS fabrication. The standard normal incidence geometry is used for target irradiation. Since LIPSS formation is very

sensitive to the number of overlaid laser pulses irradiating the target (N) and the pulse energy (E), we have carried out the fabrication process as a function of N and E. A clear, periodic structure is obtained on silicon when E and N are ≈ 80 μJ and 100 μJ, respectively (shown in Figure 3.2), and these optimized conditions are used for pressure dependent studies and large area surface structuring. Figure 3.2 shows SEM micrographs of fs-LIPSS fabricated on crystalline silicon under different background pressures (5×10^{-5} Torr, 5×10^{-3} Torr, 10^{-1} Torr, 10 Torr, and 760 Torr respectively) using 800 nm fs pulses. The single pulse peak fluence on the target is found to be $0.42\pm.02$ J/cm^2. The right column of Figure 3.2 shows the zoomed view of the corresponding micrograph in the left column.

The prominent influence of the ambient pressure on the structures is evident in the SEM micrographs. The preferential orientation of periodic surface structures developed on silicon is perpendicular to the incident laser polarization, with the spatial period either close to or slightly lower than the laser wavelength. This type of periodic surface structure is typically known as low spatial frequency LIPSS (LSFL), and its generation mechanism is explained by the interference of the incident laser pulse with the excited surface plasmon polaritons [8, 10, 36]. A slight increase in LIPSS period has been observed when the pressure reduces from atmosphere to 10 Torr, and the period stays almost steady thereafter with further decrease in pressure. The spatial period (d) of LIPSS is around 610-640 nm at atmospheric conditions, which increases to 620-720 nm when the pressure reduces to high vacuum. The spatial period of LIPSS (d) is related to the laser wavelength, the angle of incidence, and material parameters through the following relation:

$$d = \frac{\lambda_{laser}}{Re(\eta) \pm \sin\theta} \tag{3.2}$$

where λ_{laser} is the incident laser light wavelength, θ is the angle of incidence, and η is the effective refractive index of the dielectric-metal interface for surface

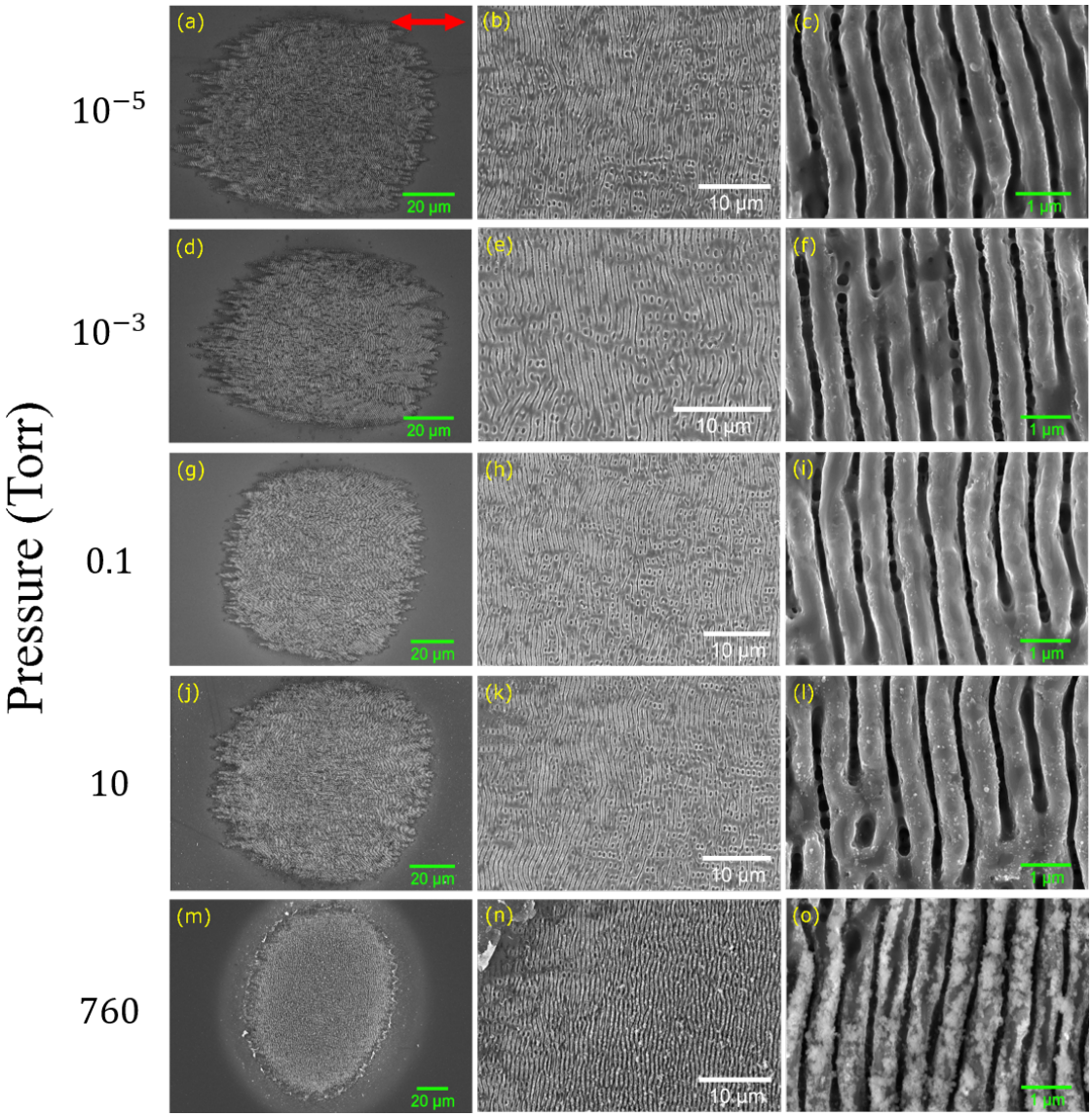

Figure 3.2: SEM micrographs of femtosecond laser induced periodic surface structures fabricated on silicon at different ambient pressures. Each structure is produced by delivering 100 pulses, each with 80 µJ energy, at 800 nm. The middle and right panel show different magnified views of the center portions of the corresponding ablation spots given in the left panel. The arrow (red color) in the top left micrograph indicates the laser polarization direction.

plasmons. The measured values of d are consistent with the static (interference) model of LIPSS formation [2, 10, 36]. Femtosecond laser ablation of solid targets is a direct route for synthesizing tiny nanoparticles (NPs) in the size range 10-20 nm [37]. Under atmospheric conditions, a large number of ejected NPs settle

back on the structured surface. NPs count goes down when we reduce the ambient pressure to 10 Torr, and thereafter, minimal or almost nil amount of NPs is observed at lower pressures (from 0.1 Torr to 5×10^{-5} Torr).

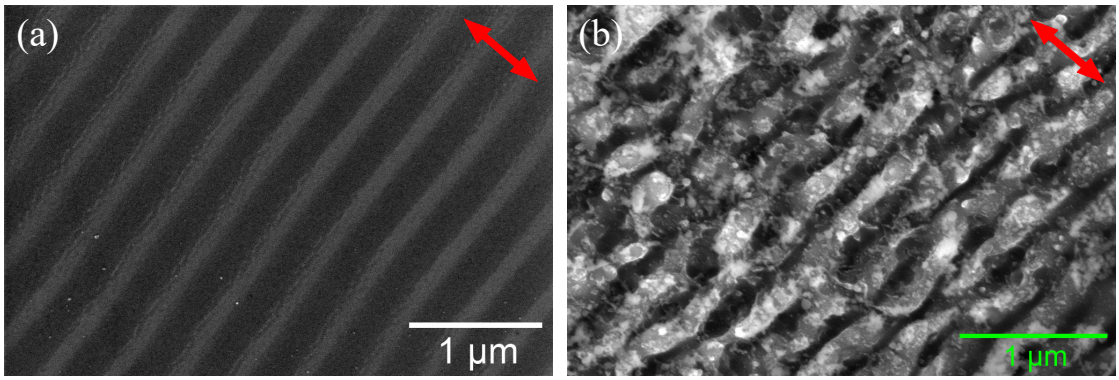

Figure 3.3: SEM micrographs of Si-LIPSS fabricated under (a) high vacuum and (b) atmospheric pressure. Ultrashort pulses at 400 nm with pulse energy E = 4 μJ and pulse number N = 100 have been used for surface structuring. Red arrows represent the laser polarization direction.

At atmospheric pressure the ambient gas pushes the NPs back to the target surface, which results in cluster formation in and around the ablated spot. At lower pressures the ejected NPs move freely in the forward direction resulting in very clean periodic surface structures on the silicon substrate. These observations suggest that fabrication in vacuum gives clean LIPSS whereas fabrication at atmospheric pressure gives nanoparticle/cluster sputtered LIPSS. We have also investigated the role of laser wavelength on LIPSS fabrication using ultrashort 400 nm pulses in both atmospheric and vacuum conditions. To realize the role of polarization in LIPSS fabrication, the polarization of the incident laser beam is changed using a half-wave plate in the optical path. The fundamental beam (λ = 800 nm) is removed using a short band pass filter kept after the second harmonic crystal in the experiment.

Figure 3.3 shows SEM micrographs of Si-LIPSS fabricated using pulse energy E = 4μJ and N = 100 (equivalent single pulse fluence is F = 0.18 $\pm$ 0.01 J/cm^2), in high vacuum and atmospheric pressure, respectively. Since the photon energy is twice as high compared to structuring using 800 nm, a slight in-

crease in fluence above the threshold results in a crater. The induced ripples are again oriented perpendicular to the laser polarization, which confirms the role of local electric field oscillation and validity of the static (interference) model of LIPSS formation [8, 10]. The measured values of d are 340 $\pm$ 20 nm and 380 $\pm$ 12 nm, in atmospheric and high vacuum conditions, respectively. Comparing Figures 3.2 and 3.3, one can easily see that the ambient pressure and SoP of laser have decisive roles in LIPSS fabrication. The processed surfaces exhibit enhanced surface areas compared to unprocessed silicon. Since the generated ripples are of the order of the irradiating wavelength, significant enhancement in surface area can be achieved by using fs pulses with shorter wavelengths.

As the laser fluence and/or the number of pulses increases, another type of quasi-periodic surface structure emerges on the silicon surface with the preferential orientation parallel to the laser polarization, covering the underlying ripples. These types of structures with spatial period (d) greater than the wavelength are known as supra-wavelength LIPSS or grooves. The mechanism behind the formation of these supra-wavelength LIPSS and the influence of various experimental parameters (e.g., laser wavelength, pulse repletion rate, ambient pressure, etc.) along with their morphological features is yet not explored in detail. For example, in the case of semiconductors, contrary to the ripples period, grooves period increases with increase in the number of laser pulses [24]. Shutong He et al. proposed that grooves form above the ripples as a result of the progressive aggregation of nanoparticles(generated during fs-LIPSS formation) followed by clusters of nanoparticles fusing together, and further modulation of the deposited energy occurring at high excitation levels [24, 38]. Their experimental findings showed that the width of the deep wrinkles separating the ripples gradually increases as a function of fluence or number of pulses, resulting in a progressive reduction of the thickness of the underlying LSFLs. Another prominent model developed by Tsibidis et al. provides insights into grooves formation by complementing TTM and electromagnetic process with

hydrodynamics [24, 39]. On the contrary, the Finite Difference Time Domain (FDTD) method based model suggests that the origin of grooves is related to the progressive evolution of the topography of a rough surface driven by feedback effects associated with multi-pulse irradiation [40–43].

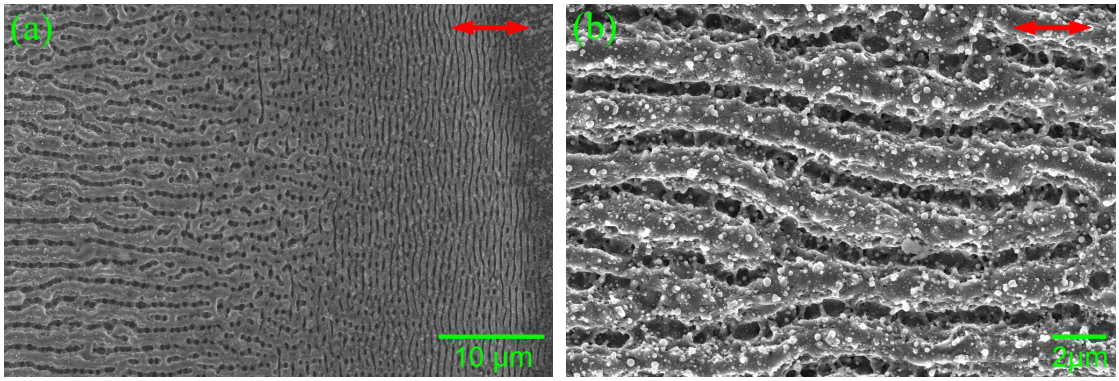

Figure 3.4: SEM micrographs of processed silicon, fabricated using ultrashort pulses (800 nm pulses, N = 100). (a) E = 100 µJ, (b) Magnified view of grooves fabricated using E = 200 µJ. The center region of ablation has quasi-periodic grooves and the outer region is filled with ripples. Red arrow represents the laser polarization direction.

Figures 3.4(a) and (b) show SEM micrographs illustrating the morphological changes of surface structures of such type of structures fabricated using 100 laser pulses at 800 nm using pulse energies of 100 µJ and 200 µJ, respectively. This SEM micrograph clearly shows the role of energy deposition in different types of structure formation. The region where more energy is deposited (centre part of the Gaussian beam) is full of quasi-periodic grooves with orientation parallel to the laser polarization, while the outer region is filled with ripples with orientation perpendicular to the beam polarization. The measured value of groove periodicity (d) is in the range 1.4 µm - 1.8 µm. Further increase in energy destroys the grooves and forms irregular micro-structures, finally resulting in a deep crater. Similar behaviour was observed with 5 µJ pulses at 400 nm as well (micrographs not shown). The groove formation mechanism is directly related to the amount of energy deposited on the target, which is in turn related to the optical penetration depth. The effective optical penetration depth is related to the reflectance, linear and nonlinear absorption coefficients, through the

relation

$$l = \left[\alpha + \frac{(1-R)\beta F}{\tau}\right]^{-1} \tag{3.3}$$

where F is the applied fluence and τ is the laser pulse duration (100 fs). Since the values of α and β are high at lower wavelengths, pulses at 400 nm deposit their energy on a much smaller volume compared to 800 nm pulses. Because of this, a slight increase in fluence (at 400 nm) above the threshold transforms the structures from periodic ripples to quasi-periodic grooves, soon resulting in a crater. The energy deposition mechanism onto the silicon target at different wavelengths confirms that effective groove generation is possible with small pulse energy (5 µJ) at shorter wavelengths, and ripple fabrication is possible with high energy (60 µJ) at longer wavelengths. Since our interest of investigation is the fabrication of nanoscale ripples and subsequent enhancement in light coupling onto the target material, most of our investigations are performed with 800 nm pulses with energies just above the ablation threshold value, i.e., in the range $E = 60 - 80$ µJ.

3.4 Large area Si-LIPSS fabrication and tailoring of the optical properties

We use ultrashort pulses at atmospheric pressure for LIPSS fabrication because performing experiments under vacuum conditions is time-consuming and not cost-economical. Optimized conditions for Si-LIPSS are obtained for 800 nm ultrashort pulses with E = 80 µJ and N = 100, and these are then used for large area surface structuring by line-by-line scanning. The optimized scan speed is fixed at 0.01 mm/s for raster scanning and a time of 500 seconds is needed to scan a single line. Proper overlap is ensured between the lines (by considering $1/e^2$ of the width of the scanned line) during scanning. Figure 3.5 depicts SEM micrographs and the magnified views of the processed silicon target, showing

periodic surface structures fabricated in large scale by employing controlled laser ablation.

Nanoparticles and nanoclusters get deposited back on the processed target (shown in Figure 3.5(c,d)) because of the background pressure. Sarbada et al., and Zhu et al. have earlier reported LIPSS fabrication with ultrashort pulses under ambient conditions, and they have confirmed that the presence of periodic and random structures on the processed surface can reduce the reflectivity to a great extent [17, 44]. We have carried out preliminary reflection measurements with processed and unprocessed silicon targets, and a substantial reduction in the reflectance is observed with processed silicon (shown in Figure 3.5(e)). We measure the diffused reflection from Si-LIPSS with the help of an integrating sphere. The significant reduction seen in reflectivity is because of the enhanced surface area achieved via the fs-LIPSS process, resulting in multiple reflections on the processed silicon surface. Multiple reflections also lead to an enhanced absorption of light, with more input light coupling onto the silicon target.

From Figure 3.5(e), it is clear that we have obtained a considerable reduction in the average reflectance in the near IR (75%), visible (75% - 81%), and UV (76% - 81%) regions with direct laser surface structuring. Moreover, absorbance in the UV-VIS-NIR region has enhanced largely after fs-LIPSS fabrication because the disordered amorphous silicon does not exhibit a definite bandgap [44]. Photon energies used in our experiments are either 1.55 eV (at 800 nm) or 3.09 eV (at 400 nm). Since the optical bandgap is 1.1 eV ($\Lambda = 1.1\mu$m), silicon is essentially transparent for the wavelength range 1.1 µm - 10 µm and opaque for $\lambda < 1.1\mu$m. It has also been shown that optical properties of silicon can be tailored through surface structuring and doping [13, 45, 46].

In the past, Vorobyev and Guo have produced surface gratings superimposed with randomly distributed sub-wavelength nanostructures, which suppressed the reflection of both s- and p-polarized light over a wide range of angles [16]. We can understand the reduction in reflectance by categorizing

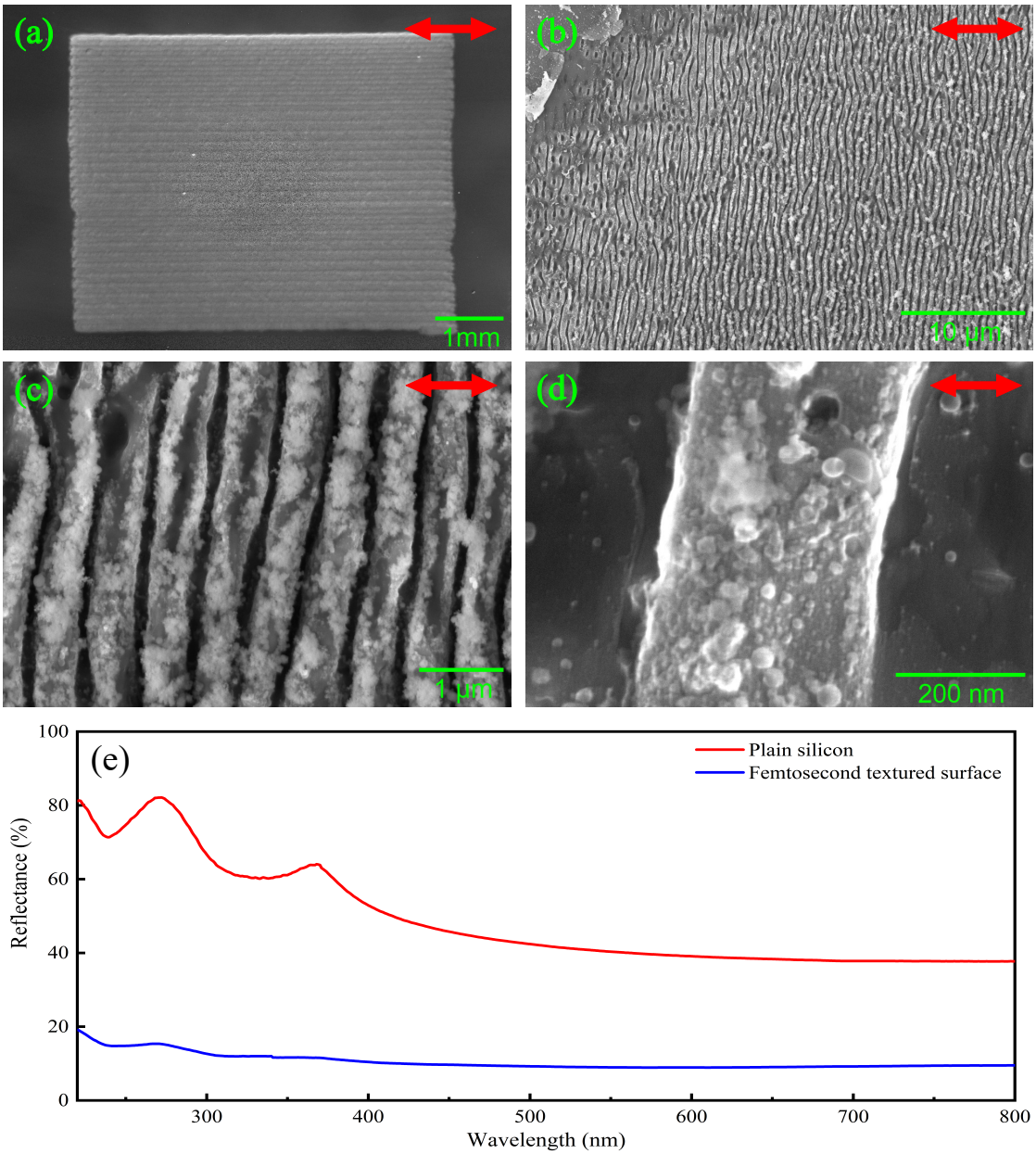

Figure 3.5: SEM micrographs of large area Si-LIPSS fabricated using 800 nm ultrashort pulses in atmospheric conditions. (b), (c), and (d) show zoomed views of (a). Note the different magnifications on each SEM micrograph. (e) shows reflectance spectra measured for plain silicon and fs-LIPSS textured silicon. Red arrows represent the laser polarization direction.

light reflection into the following three cases: $d < \lambda$, $d > \lambda$, and $d \simeq \lambda$. It is known that subwavelength gratings (SWGs), i.e., $d < \lambda$, exhibit antireflection behaviour [15, 47], which can be described by an effective medium the-

ory [14, 48]. In this theory, SWG is modelled as a homogeneous layer with a thickness equal to the grating groove depth and an effective refractive index characterized by a filling factor of the grating. For $d > \lambda$, also known as the geometrical optics region, reflection of light can be reduced by light trapping in the grating grooves as in cavities [49]. Finally, for $d \simeq \lambda$, which is also known as the strong diffraction region, surface gratings on undoped silicon exhibit antireflection behaviour [50]. Since the measured d of periodic structures in our experimental conditions is either higher (grooves) or lower (ripples) than the incident laser wavelength, the structured surface suppresses the reflectivity to a great extent.

3.4.1 Laser-induced breakdown spectroscopy (LIBS) measurements

To further investigate the enhancement in the efficiency of light getting coupled to the nanostructured target, we performed laser-induced plasma experiments using structured as well as plain samples. The experimental setup is similar to Ref [23], but a different laser system and spectrometer (discussed in chapter 2), are used for the investigation. For generating the plasma we use the same Ti:sapphire laser that is used for nanostructuring, but at a higher intensity of $I = 1.1 \times 10^{14}$ W/cm^2. The target to be irradiated is kept under high vacuum (10^{-5} Torr) in the vacuum chamber. A high-temperature laser plasma is produced on the sample surface, and the emission spectra of the plasma are recorded using a CCD-coupled spectrometer. LIBS (sometimes also called laser-induced plasma spectroscopy (LIPS) or laser spark spectroscopy (LSS)) is a powerful elemental analysis technique which gives information about the various atomic and ionic constituents of the plasma. During the past 30 years the LIBS technique has made substantial advances, which has led to its establishment as an efficient qualitative and quantitative analysis technique. The main goal of the LIBS technique is to create an optically thin plasma (which is in ther-

modynamic equilibrium), whose elemental composition is the same as that of the sample. Upon fulfillment of these conditions, the measured spectral line intensities and spectral line widths of various species (ions and neutrals) are used to estimate the corresponding plasma temperatures, and also the associated electron densities. From these informations, the relative abundance of the elements contained in the plasma can be estimated. Similarly, free charges in the plasma result in an ion current, which is measured using a negatively biased Faraday cup.

Figure 3.6(a) shows the time integrated emission spectra (for 100 ms) obtained using Si-LIPSS (blue colour) and Si plain wafer (Red colour) targets. Excited atoms (Si I) and singly ionized silicon (Si II) contribute mostly to the LIBS emission spectra [51]: we observe intense emission lines at 385.60 nm (Si II), 386.26 nm (Si II), 390.55 nm (Si I), 412.80 nm (Si II), and 413.08 nm (Si II) in the measured range of 370 - 420 nm. For the Si-LIPSS target, the intensities of emission lines from Si I and Si II are found to increase by about 50% - 90%, compared to that from the plain Si wafer. This increase in emission intensity is because of the enhanced light coupling, which occurs due to the periodic surface structures present on the target surface. Moreover, two additional lines at 380.65 nm (Si III) and 379.61 nm (Si III), emitted by doubly ionized Si, are visible from the Si-LIPSS target. This clearly indicates an increase in the plasma temperature, arising from the improved energy coupling to the nanostructured target. Since emission intensity is a crucial factor in remote LIBS analysis, the fabrication of periodic surface structures on the target material (just before doing LIBS) should thus enhance the plasma emission intensity by a considerable level.

Figure 3.6(b) shows time of flight (TOF) signals of ions measured from plasma generated on processed and unprocessed silicon surfaces using a Faraday Cup (FC). The FC is kept at an angle of 20° with respect to the plume axis, and at a distance of 4 cm from the target surface. A negative bias voltage

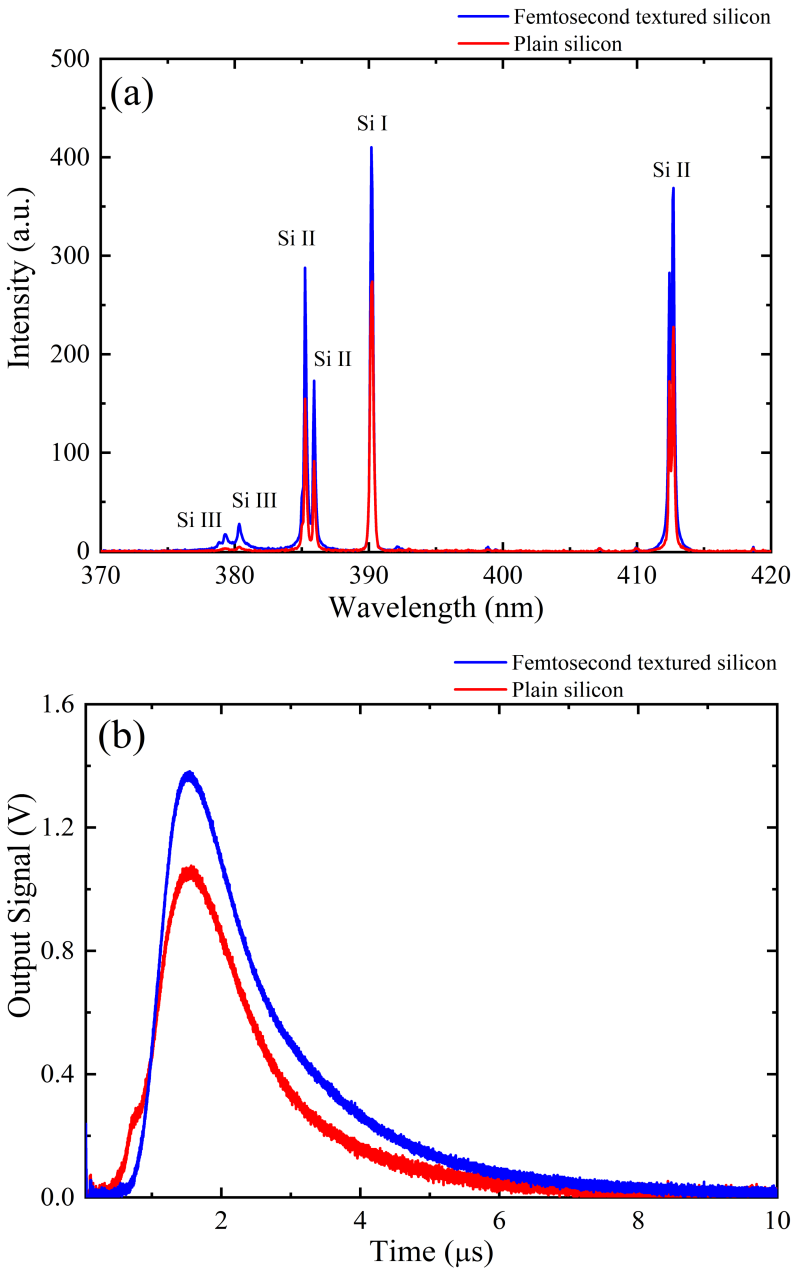

Figure 3.6: Relative intensity enhancement seen in (a) LIBS spectra, and (b) ion current signals, for a laser-produced plasma generated on fs-LIPSS structured silicon surface.

on the FC allows the collection of positive ions in the laser produced silicon plasma. When the biasing voltage is sufficiently high to prevent the electrons with highest thermal energies in the plasma from reaching the FC, the collected charge become saturated at a V_{cc} of approximately 15 V. The FC is biased at a constant working voltage within the saturation region, i.e., at V_{cc}=20 V, during

measurement. The FC current signal provides an ion time-of-flight (TOF) signal that is proportional to both ion density, n_i, and ion flow velocity, u_i, through the relationship: $I(t) = eAn_i(t)u_i(t)$, where e is the electron charge, A is the FC collecting area, and t is the TOF measured relative to the arrival of the laser pulse [23, 52, 53]. The output from fast photodiode placed near the window of the vacuum chamber gives the signal for triggering the oscilloscope. This trigger point defines 'zero time' for the TOF measurements. The ion TOF profiles are integrated to investigate the ion yield (ions/cm^2). While we obtained an ion yield of 5.24 $\times$ 10^{12}/cm^2 with a plain Si surface, for the structured Si surface it was 7.0 $\times$ 10^{12}/cm^2, showing an enhancement of about 34%. A particular feature which is seen in the case of fs-LPP is the observation of a faster kinetic energy peak in the ion temporal profiles, which has been reported by several groups. Researchers have suggested various phenomena which could give rise to the faster ionic peak, e.g., low-Z contamination of the target surface or singly charged peak of the target material [53, 54]. Later, B. Verhoff et al., have attributed this peak to space-charge effects [55]. According to them, at higher laser intensities, the electrons gain energy in excess of the Fermi energy and escape from the target. The escaped electrons lead to the rapid ion acceleration by the electrostatic field of charge separation. Therefore, we believe that the space charge effect can accelerate ions to higher energies in a plasma prior to the lower energy ions seen in the second peak, which is similar to the hydrodynamic component observed in ns LPP. However, this peak is not visible when structured Si substrate is used as the target in fs-laser ablation. The possible reason behind the disappearance of the peak could be the suppression/distortion of the electrostatic field due to structure induced laser trapping/coupling. This causes a delay to the faster ion peak, which essentially merges with the slow ionic peak.

The ion peak velocity given by $V_p = L/t_p$ (where t_p is the time at which the TOF signal shows a maximum, for a given distance L from the target surface)

remained the same for both surfaces at approximately 3×10^6 cm/s, for a distance (L) of 4 cm. The enhancement seen in both LIBS and FC signals from the Si-LIPSS surface indicates that periodic surface structuring is a powerful technique for increasing the optical coupling between the source and the target. Processed surfaces with reflectivity less than 10% in the UV-VIS-IR range have numerous possibilities in photovoltaics, IR detection, and other optoelectronics applications. The high yield of energetic ions obtained from the Si-LIPSS surface also opens up novel possibilities in high energy density physics (HEDP) applications.

3.5 Summary

This chapter discusses various aspects of ultrashort laser-induced periodic surface structuring of crystalline silicon, and provides in-depth information about the generation of various quasi-periodic structures and the mechanisms involved in their formation. We investigate the role of laser parameters (laser pulse energy (E), wavelength (λ) and polarization), and irradiation parameters (number of pulses (N), ambient pressure) on the fabrication of fs-LIPSS patterns. In particular, we investigate the influence of different ambient pressures ranging from 10^{-5} Torr to 760 Torr on ripples formation. Our experimental findings indicate that at higher pressure the re-deposition of nanoparticles of ablated material onto the target occurs, which significantly influences the generation and morphology of the surface structures. By optimizing the irradiation conditions (E = 80 µJ and N = 100 at 800 nm, and E = 4 µJ and N = 100 at 400 nm, respectively) large area LIPSS surfaces have been fabricated. The spatial period of the induced structures is found to be slightly lower than that of the laser wavelength in both cases, verifying the validity of the static (interference) model of LIPSS formation. A substantial reduction in optical reflectivity is observed from the structured surface because of multiple

reflections from the nanostructures. Laser-induced breakdown spectroscopy (LIBS) measurements exhibit a discernible enhancement in the optical emission intensity of the plasma by 50% - 90%, while FC measurements show an enhancement in ion current by about 34%. These results clearly reveal that laser coupling is enhanced when nanostructured silicon is used as target. Another interesting indication of enhanced light coupling is the unique appearance of spectral lines associated with doubly ionized Si species from the Si-LIPSS target. These experiments establish laser-induced periodic surface structuring as a versatile tool for making low reflectivity (high absorptivity) surfaces, which have numerous applications in photonics, materials science, high energy density physics, and bio-physics.

Bibliography

[1] HM Van Driel, JE Sipe, and Jeff F Young. Laser-induced periodic surface structure on solids: a universal phenomenon. *Physical Review Letters*, 49(26):1955, 1982.

[2] Jeff F Young, JS Preston, HM Van Driel, and JE Sipe. Laser-induced periodic surface structure. ii. experiments on ge, si, al, and brass. *Physical Review B*, 27(2):1155, 1983.

[3] Jeff F Young, JE Sipe, and HM Van Driel. Laser-induced periodic surface structure. iii. fluence regimes, the role of feedback, and details of the induced topography in germanium. *Physical Review B*, 30(4):2001, 1984.

[4] Jörn Bonse, Jörg Krüger, S Höhm, and A Rosenfeld. Femtosecond laser-induced periodic surface structures. *Journal of Laser Applications*, 24(4):042006, 2012.

[5] Anatoliy Y Vorobyev and Chunlei Guo. Direct femtosecond laser surface nano/microstructuring and its applications. *Laser & Photonics Reviews*, 7(3):385–407, 2013.

[6] Jörn Bonse, Sandra Höhm, Sabrina V Kirner, Arkadi Rosenfeld, and Jörg Krüger. Laser-induced periodic surface structures—a scientific evergreen. *IEEE Journal of selected topics in quantum electronics*, 23(3), 2016.

[7] Zhou Guosheng, PM Fauchet, and AE Siegman. Growth of spontaneous periodic surface structures on solids during laser illumination. *Physical Review B*, 26(10):5366, 1982.

[8] JE Sipe, Jeff F Young, JS Preston, and HM Van Driel. Laser-induced periodic surface structure. i. theory. *Physical Review B*, 27(2):1141, 1983.

[9] F Keilmann and YH Bai. Periodic surface structures frozen into co 2 laser-melted quartz. *Applied Physics A*, 29(1):9–18, 1982.

[10] Jörn Bonse, Arkadi Rosenfeld, and Jörg Krüger. On the role of surface plasmon polaritons in the formation of laser-induced periodic surface structures upon irradiation of silicon by femtosecond-laser pulses. *Journal of Applied Physics*, 106(10):104910, 2009.

[11] Juergen Reif, Olga Varlamova, and Florenta Costache. Femtosecond laser induced nanostructure formation: self-organization control parameters. *Applied Physics A*, 92(4):1019–1024, 2008.

[12] Sebastian Uhlig. *Self-organized surface structures with ultrafast white-light: First investigation of LIPSS with supercontinuum*. Springer, 2015.

[13] Peter J Hesketh, Jay N Zemel, and Benjamin Gebhart. Polarized spectral emittance from periodic micromachined surfaces. i. doped silicon: the normal direction. *Physical Review B*, 37(18):10795, 1988.

[14] Mark Auslender, David Levy, and Shlomo Hava. One-dimensional antireflection gratings in (100) silicon: a numerical study. *Applied optics*, 37(2):369–373, 1998.

[15] RE Smith, ME Warren, JR Wendt, and GA Vawter. Polarization-sensitive subwavelength antireflection surfaces on a semiconductor for 975 nm. *Optics letters*, 21(15):1201–1203, 1996.

[16] AY Vorobyev and Chunlei Guo. Antireflection effect of femtosecond laser-induced periodic surface structures on silicon. *Optics Express*, 19(105):A1031–A1036, 2011.

[17] Shashank Sarbada, Zhifeng Huang, Yung C Shin, and Xiulin Ruan. Low-reflectance laser-induced surface nanostructures created with a picosecond laser. *Applied Physics A*, 122(4):453, 2016.

[18] PP Rajeev, P Taneja, P Ayyub, Arvinder Singh Sandhu, and G Ravindra Kumar. Metal nanoplasmas as bright sources of hard x-ray pulses. *Physical review letters*, 90(11):115002, 2003.

[19] Mahreen Akram, Shazia Bashir, Sohail Abdul Jalil, Muhammad Shahid Rafique, Asma Hayat, and Khaliq Mahmood. Laser induced surface structuring of cu for enhancement of field emission properties. *Materials Research Express*, 5(2):025029, 2018.

[20] M Krishnamurthy, Sudipta Mondal, Amit D Lad, Kartik Bane, Saima Ahmed, V Narayanan, R Rajeev, Gourab Chatterjee, Prashant Kumar Singh, G Ravindra Kumar, et al. Enhanced x-ray emission from bacteria. In *International Conference on Fibre Optics and Photonics*, pages T3C–1. Optical Society of America, 2012.

[21] A Lübcke, M Schnürer, L Ehrentraut, R Wehner, R Grunwald, E McGlynn, D Byrne, and S Lowry. Encycl, interfacial chem. *Surf. Sci. Electrochem*, 420, 2018.

[22] N Smijesh and Reji Philip. Emission dynamics of an expanding ultrafast-laser produced zn plasma under different ambient pressures. *Journal of Applied Physics*, 114(9):093301, 2013.

[23] KK Anoop, MP Polek, R Bruzzese, S Amoruso, and Sivanandan S Harilal. Multidiagnostic analysis of ion dynamics in ultrafast laser ablation of

metals over a large fluence range. *Journal of Applied Physics*, 117(8):083108, 2015.

[24] George D Tsibidis, Costas Fotakis, and Emmanuel Stratakis. From ripples to spikes: A hydrodynamical mechanism to interpret femtosecond laser-induced self-assembled structures. *Physical Review B*, 92(4):041405, 2015.

[25] JM Liu. Simple technique for measurements of pulsed gaussian-beam spot sizes. *Optics letters*, 7(5):196–198, 1982.

[26] Sivanandan S Harilal, J Yeak, and Mark C Phillips. Plasma temperature clamping in filamentation laser induced breakdown spectroscopy. *Optics Express*, 23(21):27113–27122, 2015.

[27] Jörn Bonse, Steffen Baudach, Jörg Krüger, Wolfgang Kautek, and Matthias Lenzner. Femtosecond laser ablation of silicon–modification thresholds and morphology. *Applied Physics A*, 74(1):19–25, 2002.

[28] Chandra SR Nathala, Ali Ajami, Wolfgang Husinsky, Bilal Farooq, Sergey I Kudryashov, Albena Daskalova, Irina Bliznakova, and Andreas Assion. Ultrashort laser pulse ablation of copper, silicon and gelatin: effect of the pulse duration on the ablation thresholds and the incubation coefficients. *Applied Physics A*, 122(2):107, 2016.

[29] Jostein Thorstensen and Sean Erik Foss. Temperature dependent ablation threshold in silicon using ultrashort laser pulses. *Journal of Applied Physics*, 112(10):103514, 2012.

[30] David R Lide et al. Crc handbook of chemistry and physics, internet version 2005, 2005.

[31] Martin A Green. Self-consistent optical parameters of intrinsic silicon at 300 k including temperature coefficients. *Solar Energy Materials and Solar Cells*, 92(11):1305–1310, 2008.

[32] Alan D Bristow, Nir Rotenberg, and Henry M Van Driel. Two-photon absorption and kerr coefficients of silicon for 850–2200 nm. *Applied Physics Letters*, 90(19):191104, 2007.

[33] David E Aspnes and AA Studna. Dielectric functions and optical parameters of si, ge, gap, gaas, gasb, inp, inas, and insb from 1.5 to 6.0 ev. *Physical review B*, 27(2):985, 1983.

[34] DH Reitze, TR Zhang, Wm M Wood, and Michael C Downer. Two-photon spectroscopy of silicon using femtosecond pulses at above-gap frequencies. *JOSA B*, 7(1):84–89, 1990.

[35] BS Wherrett. Scaling rules for multiphoton interband absorption in semiconductors. *JOSA B*, 1(1):67–72, 1984.

[36] Alexey M Bonch-Bruevich, Mikhail N Libenson, Vladimir S Makin, and Vladimir V Trubaev. Surface electromagnetic waves in optics. *Optical Engineering*, 31(4):718–731, 1992.

[37] S Amoruso, G Ausanio, R Bruzzese, M Vitiello, and X Wang. Femtosecond laser pulse irradiation of solid targets as a general route to nanoparticle formation in a vacuum. *Physical Review B*, 71(3):033406, 2005.

[38] Shutong He, Jijil JJ Nivas, KK Anoop, Antonio Vecchione, Minglie Hu, Riccardo Bruzzese, and Salvatore Amoruso. Surface structures induced by ultrashort laser pulses: Formation mechanisms of ripples and grooves. *Applied Surface Science*, 353:1214–1222, 2015.

[39] George D Tsibidis, Evangelos Skoulas, Antonis Papadopoulos, and Emmanuel Stratakis. Convection roll-driven generation of supra-wavelength periodic surface structures on dielectrics upon irradiation with femtosecond pulsed lasers. *Physical Review B*, 94(8):081305, 2016.

[40] Hao Zhang, Jean-Philippe Colombier, Chen Li, Nicolas Faure, Guanghua Cheng, and Razvan Stoian. Coherence in ultrafast laser-induced periodic surface structures. *Physical Review B*, 92(17):174109, 2015.

[41] JZP Skolski, GRBE Römer, J Vincenc Obona, V Ocelik, J Th M De Hosson, et al. Laser-induced periodic surface structures: Fingerprints of light localization. *Physical review B*, 85(7):075320, 2012.

[42] Hao Zhang, Jean-Philippe Colombier, and Stefan Witte. Laser-induced periodic surface structures: Arbitrary angles of incidence and polarization states. *Physical Review B*, 101(24):245430, 2020.

[43] Guoliang Deng, Guoying Feng, and Shouhuan Zhou. Experimental and fdtd study of silicon surface morphology induced by femtosecond laser irradiation at a high substrate temperature. *Optics Express*, 25(7):7818–7827, 2017.

[44] Qinghua Zhu and Mengyan Shen. Femtosecond laser irradiation-induced infrared absorption on silicon surfaces. *International Journal of Smart and Nano Materials*, 6(2):113–123, 2015.

[45] François Marquier, Karl Joulain, Jean-Philippe Mulet, Rémi Carminati, and Jean-Jacques Greffet. Engineering infrared emission properties of silicon in the near field and the far field. *Optics communications*, 237(4-6):379–388, 2004.

[46] M Auslender and S Hava. Zero infrared reflectance anomaly in doped silicon lamellar gratings. i. from antireflection to total absorption. *Infrared Phys. Technol*, 36(7):1077–1088, 1995.

[47] Daniel H Raguin and G Michael Morris. Analysis of antireflection-structured surfaces with continuous one-dimensional surface profiles. *Applied Optics*, 32(14):2582–2598, 1993.

[48] Daniel H Raguin and G Michael Morris. Antireflection structured surfaces for the infrared spectral region. *Applied optics*, 32(7):1154–1167, 1993.

[49] Faouzi Ghmari, Taoufik Ghbara, Marine Laroche, Rémi Carminati, and Jean-Jacques Greffet. Influence of microroughness on emissivity. *Journal of Applied Physics*, 96(5):2656–2664, 2004.

[50] Shlomo Hava, M Auslender, and D Rabinovich. Operator approach to electromagnetic coupled-wave calculations of lamellar gratings: infrared optical properties of intrinsic silicon gratings. *Applied optics*, 33(21):4807–4813, 1994.

[51] Reader J. Kramida A., Ralchenko Y. Nist database. *Natl. Inst. Stand. Technol.*, 237:379–388, 2016.

[52] Brendan Doggett and James G Lunney. Langmuir probe characterization of laser ablation plasmas. *Journal of Applied Physics*, 105(3):033306, 2009.

[53] TONY Donnelly, JAMES GERARD Lunney, S Amoruso, R Bruzzese, X Wang, and X Ni. Dynamics of the plumes produced by ultrafast laser ablation of metals. *Journal of Applied Physics*, 108(4):043309, 2010.

[54] Mengqi Ye and Costas P Grigoropoulos. Time-of-flight and emission spectroscopy study of femtosecond laser ablation of titanium. *Journal of Applied Physics*, 89(9):5183–5190, 2001.

[55] B Verhoff, SS Harilal, and A Hassanein. Angular emission of ions and mass deposition from femtosecond and nanosecond laser-produced plasmas. *Journal of Applied Physics*, 111(12):123304, 2012.

Chapter 4

Femtosecond laser texturing of fused silica and quartz

This chapter discusses the generation of various femtosecond laser-induced surface structures on fused silica and quartz (0001). The dependence of surface ripples on irradiation parameters such as the laser fluence and the number of pulses is studied. Modifications in the optical properties of the textured surfaces is investigated. Finally, large-area structuring of a fused silica surface, exhibiting superhydrophilic behaviour, is performed.

4.1 Introduction

Ultrashort pulsed lasers (fs-lasers) facilitate cost-effective micro-/nano-structuring for the fabrication of functional structures inside the bulk of transparent materials (e.g., nanogratings) [1, 2], as well as on the surface of materials [3]. These include the ability to alter the surface topography and optical properties (such as absorption, and reflection) permanently to fabricate super-hydrophilic/hydrophobic self-cleaning, anti-icing, anti-reflecting, and anti-bacterial surfaces. Despite the presence of various ongoing research activities in laser-induced periodic surface structures (LIPSS), large-area nano-

structuring of dielectric materials (in particular, optical grade glass) is still a challenging problem due to the nonlinear absorption of laser radiation, and the negligible number of available free charge carriers as compared to metals and semiconductors. Among different silica glasses, fused silica (amorphous) and quartz (crystalline) are the most studied optical glasses due to their relatively simple composition and superior optical quality. When exposed to fs pulses fused silica undergoes breakdown via different ionization mechanisms, which leads to surface modification and/or material removal, usually resulting in micro-/nano-structures formation [4–6].

As mentioned in the introduction chapter, LIPSSs are generally categorized into two types in literature based on the relation between the irradiating laser wavelength λ and the spatial period of the ripples Λ. These are referred to as Low Spatial Frequency LIPSS (LSFL) and High Spatial Frequency LIPSS (HSFL), respectively. In large band-gap materials (such as SiO_2, BaF_2), LSFL often exhibits a spatial periodicity which is either close to λ or to λ/n, where n is the refractive index of the dielectric material. The patterns are usually aligned parallel to the E-field vector [7]. Emmony et al. [8] first related the origin of LSFL to the interaction of the E-field of the laser and the surface electromagnetic waves (SEW) generated by the applied laser pulse. The efficacy factor theory was formulated based on SEW. Later, it was associated with the generation of surface plasmons polaritonss (SPP) [9], which is used in several studies for understanding the formation of LIPSS [10–12]. However, HSFL shows spatial periods much smaller than $\lambda/2$ appearing mainly for below band-gap excitation, and oriented either parallel or perpendicular to the polarization vector. HSFL is specifically observed in the case of irradiation with ultrashort (few ps to fs) pulses [7, 13]. Their origin, however, is yet not fully understood, and investigations are still ongoing. Possible explanations include self-organization [14], second-harmonic generation [15], and chemical surface alterations [16].

The SPP excitation condition is satisfied on metal surfaces because metals

have a negative permittivity, and the ambient air has a positive permittivity. In the case of dielectric materials the conditions for SPP excitation are not fulfilled because of their positive permittivity. However, for these materials, the excitation of free charge carriers occurs via multiphoton and avalanche ionization processes [17], turning the dielectric surface into a metallic state which leads to LIPSS generation [10, 12, 18]. Form an application point of view, LIPSS on dielectrics such as fused silica is of great significance, e.g., for influencing fluid dynamic properties in microfluidic channels, transforming the intrinsic wetting property, and cell growth [19–22]. Therefore, investigations on LIPSS formation on silica glasses are indispensable in view of their immense application potential.

This chapter reports various aspects of the periodic structures generated on fused silica and quartz targets by employing fs laser pulses. The growth and evolution of the ripples and their dependence on laser pulse number (N), fluence, and material crystallographic orientation are discussed. Laser-induced defects and structural modification of the material are studied by measuring Raman and photoluminescence (PL) spectra. Finally, modification of the optical and wetting properties of the laser textured samples also is investigated.

4.2 Experimental details

The schematic of the experimental setup is shown in Figure 2.8. We use a regeneratively amplified mode-locked Ti: Sapphire laser system (TSA-10, Spectra Physics), which generates linearly polarized ultrashort laser pulses (pulse duration $\tau \approx 100$ fs, central wavelength $\lambda \approx 800$ nm) at a repetition rate of 10 Hz. The energy of the incident laser pulse is measured by employing a pyroelectric detector. The energy can be varied by using a half-wave plate in combination with a polarizing cube beamsplitter (PBS). An electronically controlled mechanical shutter, which is time-synchronized with the laser system, is used

in the beam path to select the desired number of pulses for irradiating the sample. Double-sided polished fused silica (Scientific Silica Products, India) and one side epi-polished quartz (0001, Princeton Scientific Corp, USA) with dimensions of 20 mm $\times$ 20 mm $\times$ 1 mm, are used as the targets. The target is mounted on a stepper-motor controlled X-Y translation stage (Newport M-ILS50PP) positioned perpendicular to the beam propagation direction. Laser pulses (having Gaussian spatial profile) are focused on the sample using a plano-convex lens of 40 cm focal length, and the beam radius ($1/e^2$) at the focal point (ω_0) is found to be $\approx$38 µm. The experiments are performed in air ambient, and surface modifications of the laser textured target are characterized by using a high-resolution field emission scanning electron microscope (FESEM ULTRA Plus, Carl Zeiss). To avoid SEM imaging artifacts caused by surface charging due to structuring, the irradiated samples are coated with a 2 nm layer of platinum.

To investigate changes in the optical properties caused by fs laser texturing, a large-area surface of 6 mm $\times$ 6 mm is fabricated by the parallel line scanning method. Optimized conditions for large-area fabrication are achieved by controlling the parameters which are crucial for structuring, such as incident energy (E), number of pulses (N), and scan speed (for proper overlapping along the scan direction and Y-axis). The transmittance and reflection spectra of the textured surface are recorded using a UV/VIS/NIR Lambda 750 Spectrometer (Perkin-Elmer). Topographical changes and wettability of the surface are characterized by using an atomic force microscope (AFM) and contact angle meter (DM 501, Kyowa, Japan).

4.3 Variety of LIPSSs on fused silica and quartz

LIPSSs formation in dielectrics is a complex phenomenon and is still an ongoing topic of debate. Various types of LIPSSs having different orientations are obtained in the experiments conducted in this study, having average periodici-

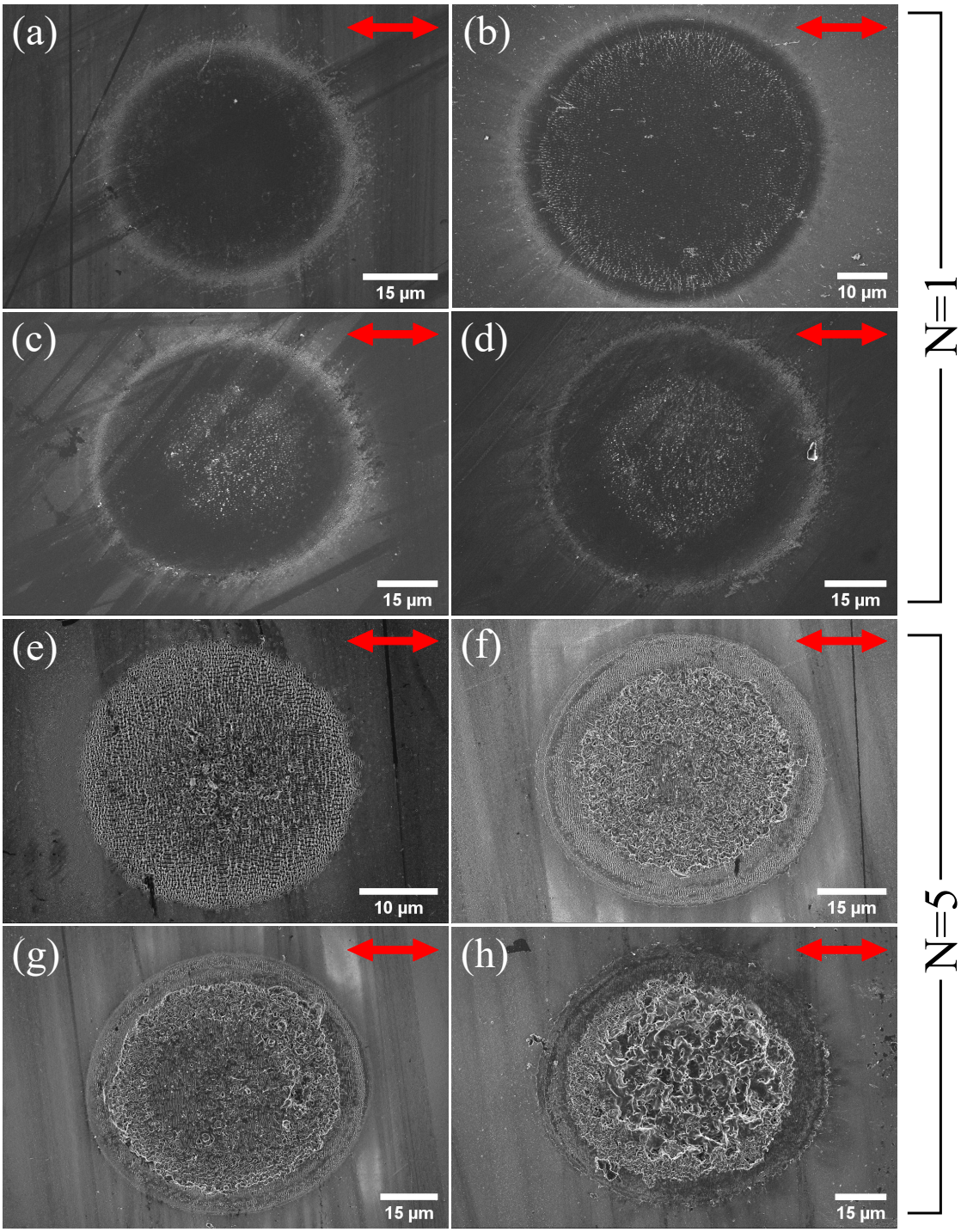

Figure 4.1: SEM micrographs of fused silica surface after irradiation with N=1(a-d) and N=5(e-h) laser pulses. Laser pulse energy: (a) 17.0 J/cm^2; (b) 21.3 J/cm^2; (c) 29.8 J/cm^2; (d) 34.0 J/cm^2; (e) 8.5 J/cm^2; (f) 17.0 J/cm^2; (g) 25.5 J/cm^2; (h) 38.3 J/cm^2 respectively. The direction of the laser beam polarization is shown by the red arrow for all the images.

ties compatible with the laser wavelength. Topographical changes happening at the early stages of laser-matter interaction result in the formation of SPPs. SPPs in turn facilitate the generation of LIPSS on the irradiated surface. Figure 4.1 shows SEM micrographs of fused silica surface irradiated with $N = 1$ (Figure 4.1 (a-d)) and $N = 5$(Figure 4.2 (e-h)) laser pulses of different peak fluences ranging from 17.0 J/cm^2 to 38.3 J/cm^2. Micrographs shown in Figure 4.1(a-d) reveal early stage surface roughness occurring due to single pulse ablation ($N = 1$) at different fluences. The single pulse ablated area consists of primary ripples structures that are in the development phase. These structures are localized around the edges of the ablated spot, and are not very prominent. Moreover, it is clear that the characteristic ripples do not appear after irradiation with one or two laser pulses, which indicates that a feedback mechanism is important in the formation of surface patterns [23]. However, after irradiating with consecutive laser pulses ($N = 5$), fine ripples having an orientation perpendicular to the laser polarization are formed on the fused silica surface (see Figure 4.1(e-h)). As we increase the fluence, the center part of the ablated area starts exhibiting periodic structures, which are mostly situated close to the rim. It is also noticed that even for single pulse ablation, the formation of nano-threads/fiber occurs, and their preferential orientation is radially outward. Zoomed views of the surface features are shown in Figure 4.2.

As we increase the number of pulses and/or the fluence, the surface structures become more visible. Figure 4.1(e-h) shows the evolution of nanostructures owing to the roughness created by the previous pulses and the corresponding feedback given by those defects. In the case of N $\geq$ 5, the ablation spots consist of two principal quasi-period features: (i) micro-wrinkles which form in the higher fluence part, covering the major portion of the ablation crater, and (ii) an annular disc near the crater edge, in the region of reduced local fluence, exhibiting relatively finer structures known as LSFL. We have analyzed the SEM micrographs employing two-dimensional Fast Fourier Transform (2D-FFT) to

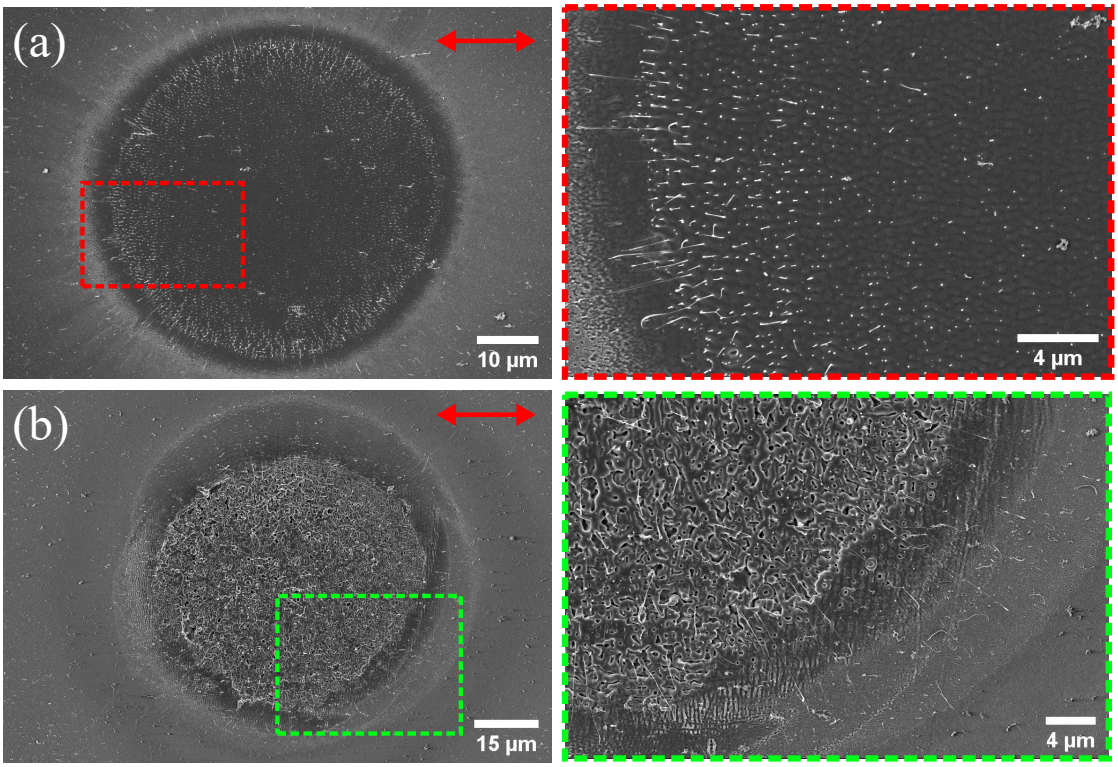

Figure 4.2: SEM micrographs showing the evolution of surface structures on fused silica upon irradiation with laser pulse of energy $E = 0.5$ mJ. The number of pulses are (a) $N = 1$ and (b) $N = 5$. The area enclosed by the green and red dashed boxes in the left panel are zoomed to give a magnified view in the right panel. The red arrows indicate the polarization direction of the incident laser pulses.

calculate the spatial periodicity of the structures (see Figure 4.3). The periodicity along the horizontal or vertical profile ($\Lambda = 1/f$) is calculated by measuring the frequency (f) of the ripples which corresponds to the average of the distances between the central peak and the adjacent peaks (right or left). From Figure 4.3(a-c), we have calculated the spatial periodicity of HSFL to be 395±5 nm (horizontal profile) corresponding to the frequency f = 2.53 μm^{-1}, aligned perpendicular to the laser polarization. The average spatial periodicity of LSFL is measured to be 540±8 nm (vertical profile) corresponding to the frequency f = 1.85 μm^{-1}, aligned parallel to the laser polarization. Furthermore, the relation between peak fluence and spatial periodicity of LSFL is clear from Figure 4.3(d-e). The spatial periodicity of LSFL is found to be 515 ± 8 nm (vertical profile) corresponding to the frequency f = 1.93 μm^{-1}, aligned parallel to the laser polar-

ization. Our experimental findings show that Λ_{LSFL} increases with the applied laser fluence. Furthermore, irradiation with a higher number of pulses (N=80) with peak fluence F_p=21.3 J/cm^2 reveals convection roll-driven hydrodynamic phenomena in the melted glass, causing ripples along the wall of the crater (see Figure 4.4). On comparing the formation of grooves with increasing N in semiconductors like silicon (characterized by a low Prandtl number), dielectrics (with a high Prandtl number) indicte the occurrence of different mechanisms. In semiconductors LIPSSs are first formed due to SPPs, and the excitation is then suppressed before further irradiation gives rise to convection rolls perpendicular to LIPSS, as fluid transport occurs along the wells of the ripples [24]. On the other hand, in the case of dielectrics, hydrodynamic instabilities facilitate convection roll-driven formation of these structures, which have been discussed in detail by Tsibidis et al. [25].

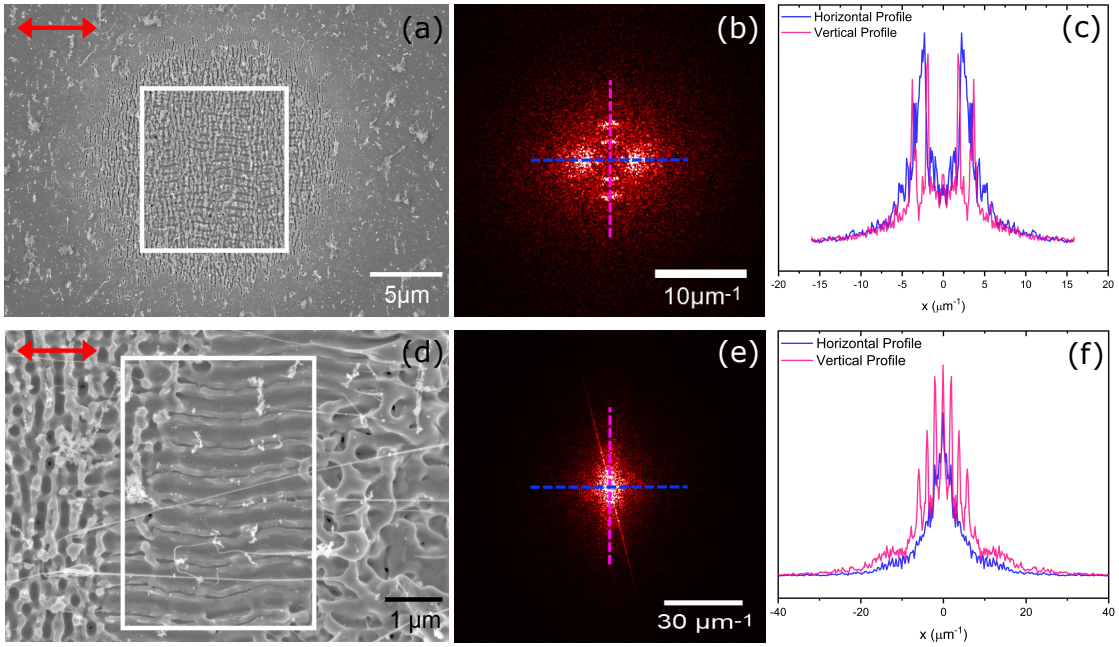

Figure 4.3: SEM micrographs of fused silica surface irradiated with N = 10, at peak fluences (a) F_p = 4.2 J/cm^2, and (b) F_p = 6.4 J/cm^2 respectively. (b) and (e) present the 2D-Fast Fourier transform (2D-FFT) of the areas marked within the white rectangles in (a) and (d) respectively. (c) and (f) show the profiles of the dashed horizontal and vertical lines of the corresponding 2D-FFTs. The red arrows indicate the direction of the laser polarization.

We performed a systematic study to investigate the role of crystallographic orientation in LIPSS, by structuring a one-side epi-polished quartz (0001) sample under the same irradiation conditions as fused silica. Figure 4.5 illustrates the surface modification of quartz due to irradiation with different peak fluences and number of pulses (N). We have found that distinct types of LSFL with preferential orientations and spatial periodicities (Λ) are formed simultaneously, when the target is ablated with different applied fluences (see Figure 4.6). The zoomed view of Figure 4.6(a) shows the development of LSFL structures of spatial periodicity ($\Lambda_{LSFL} = 516.3 \pm 20.7$ nm) which are oriented parallel to the laser polarization, over the HSFL structures ($\Lambda_{HSFL} = 382.4 \pm 47.2$ nm) which are aligned perpendicular to the laser polarization. Irradiation at the applied fluence value F_p= 10.4 J/cm^2 and N = 10 reveals a transition point where both HSFL and LSFL coexist in the ablated area. Furthermore, irradiation at higher fluence $\approx$ 41.5 J/cm^2 with N = 10 reveals the coexistence of two types of LSFL structures with different spatial periods ($\Lambda_{LSFL} = 524.6 \pm 26.1$ nm) and ($\Lambda_{LSFL} = 767.6 \pm 52.0$ nm). In this case, both LSFL structures, which form around the center of the molten crater are preferentially oriented perpendicular to the laser polarization. It appears that LSFL with ($\Lambda_{LSFL} = 767.6 \pm 52.0$ nm) is getting split and giving rise to LSFL with ($\Lambda_{LSFL} = 524.6 \pm 26.1$ nm). Moreover, the presence of HSFL is restricted to the edges of the ablation spot, where the fluence becomes significantly low. The coexistence of a variety of LIPSS is fascinating because these results are not reported earlier, and they need to be investigated in detail in future.

Our systematic studies of the evolution of LIPSS as well as the morphology of laser-irradiated fused silica and quartz substrates reveal that these structures depend predominantly on laser parameters such as polarization, fluence, irradiation dose (number of pulses) and wavelength(λ). Therefore, a precise estimation of the laser ablation threshold is essential. Since femtosecond laser surface patterning at fluences close to the ablation threshold of the material plays a very

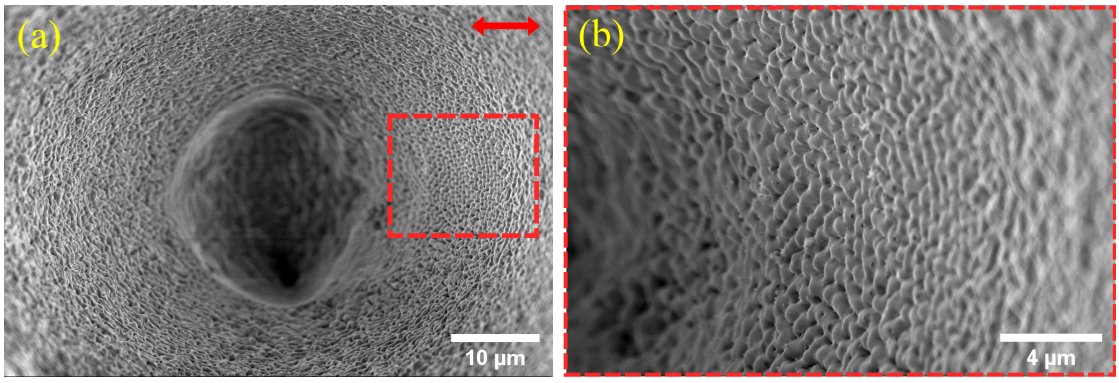

Figure 4.4: (a) Morphological changes occurring on fused silica following irradiation with N = 80 for the peak fluence $F_p = 21.3\,J/cm^2$. (b) zoomed view of the region marked in the red box in (a), revealing convection-driven formation of grooves along the wall of the crater. The red arrow indicates the laser beam polarization.

crucial role in surface structuring, understanding the incubation effects and the feedback mechanism due to the roughness created on the sample is of great importance.

4.3.1 Determination of ablation threshold

Ablation thresholds are core parameters for the durability of optical components and laser safety equipment. Moreover, the determination of ablation rates is of key importance for laser micro-machining applications. The threshold energy density (fluence) for ablation of a material is normally constant for a given set of experimental conditions (pulse duration, wavelength, repetition rate, and pulse number). Here, we will calculate single-pulse and multi-pulse ablation thresholds for fused silica and quartz. In this study, the sample is ablated by varying the number of pulses falling on the surface while keeping the pulse-to-pulse energy constant. The magnitude of fs laser-induced damage could be estimated by measuring the ablated area. Femtosecond laser surface patterning at fluences near the laser-induced damage threshold (LIDT) of the material plays a very crucial role in nano-structuring. The LIDT of fused silica is calculated by plotting the area of the laser processed region against the incident pulse energy [26] as shown in Figure 4.7. The following equation gives the relation

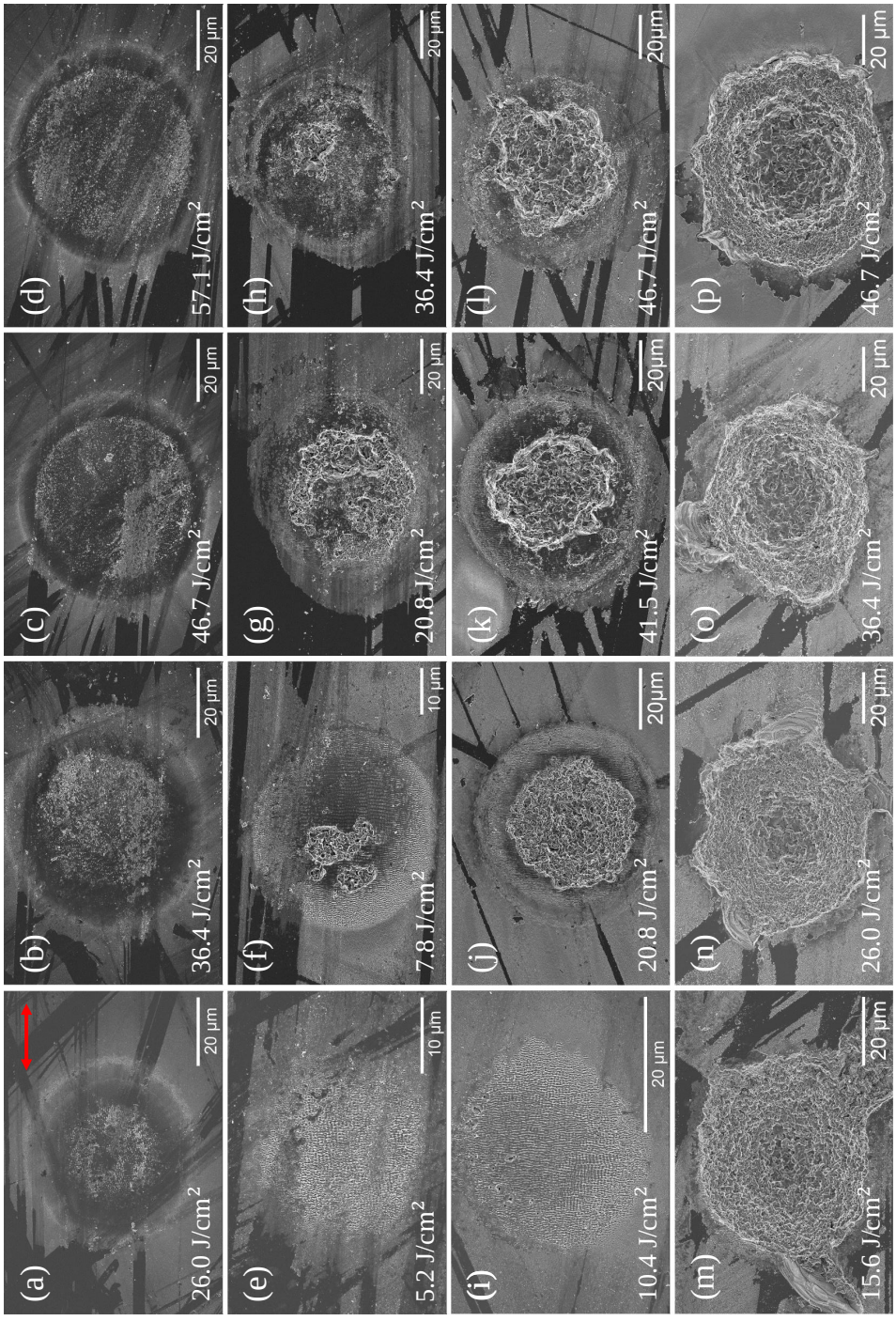

Figure 4.5: SEM micrographs depicting the surface modification of quartz for different laser fluences and irradiation doses (number of pulses). The red arrow in (a) indicates the direction of the laser polarization for all the cases.

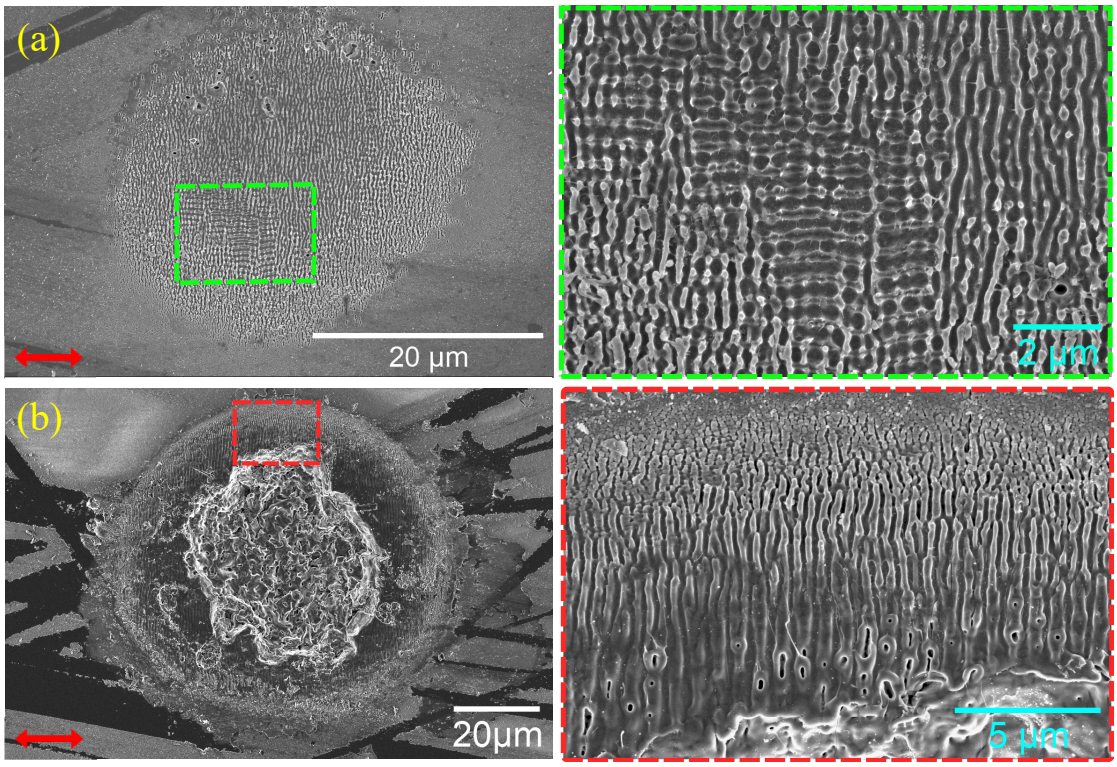

Figure 4.6: Distinct types of laser-induced surface structures formed on quartz under different conditions of peak fluence and pulse number: (a) LSFL structures ($\Lambda_{LSFL} = 516.3 \pm 20.7$ nm) parallel to the laser polarization overlapping with HSFL structures ($\Lambda_{HSFL} = 382.4 \pm 47.2$ nm) perpendicular to the laser polarization, at peak fluence = 10.4 J/cm^2, N = 10; (b) Two types of LSFL structures oriented perpendicular to the laser polarization with spatial period ($\Lambda_{LSFL} = 524.6 \pm 26.1$ nm) and ($\Lambda_{LSFL} = 767.6 \pm 52.0$ nm) respectively, forming around the centre of the crater at peak fluence 41.5 J/cm^2, N = 10. Red arrows indicate the direction of polarization of the laser.

between the ablated area and the incident pulse energy,

$$\sigma = \frac{\sigma_0}{2} \ln \frac{E_0}{E_{th}} \tag{4.1}$$

where σ is the area of fs laser-induced damage, and E_0 is the incident laser pulse energy. Here, σ, also known as the ablated spot-size, is obtained by measuring the laser-ablated/modified area from the SEM micrographs using the ImageJ software. The $1/e^2$ beam radius ω_0 and the threshold pulse energy E_{th} can be determined from the slope and intercept of the logarithmic dependence of σ on E_0. The threshold fluence F_{th} is the minimum pulse energy density required

to produce permanent surface modification, which can be calculated using the equation,

$$F_{th} = \frac{2E_{th}}{\pi\omega_0^2} \tag{4.2}$$

The values of multi-pulse ablation thresholds given in table 4.1 for fused sil-

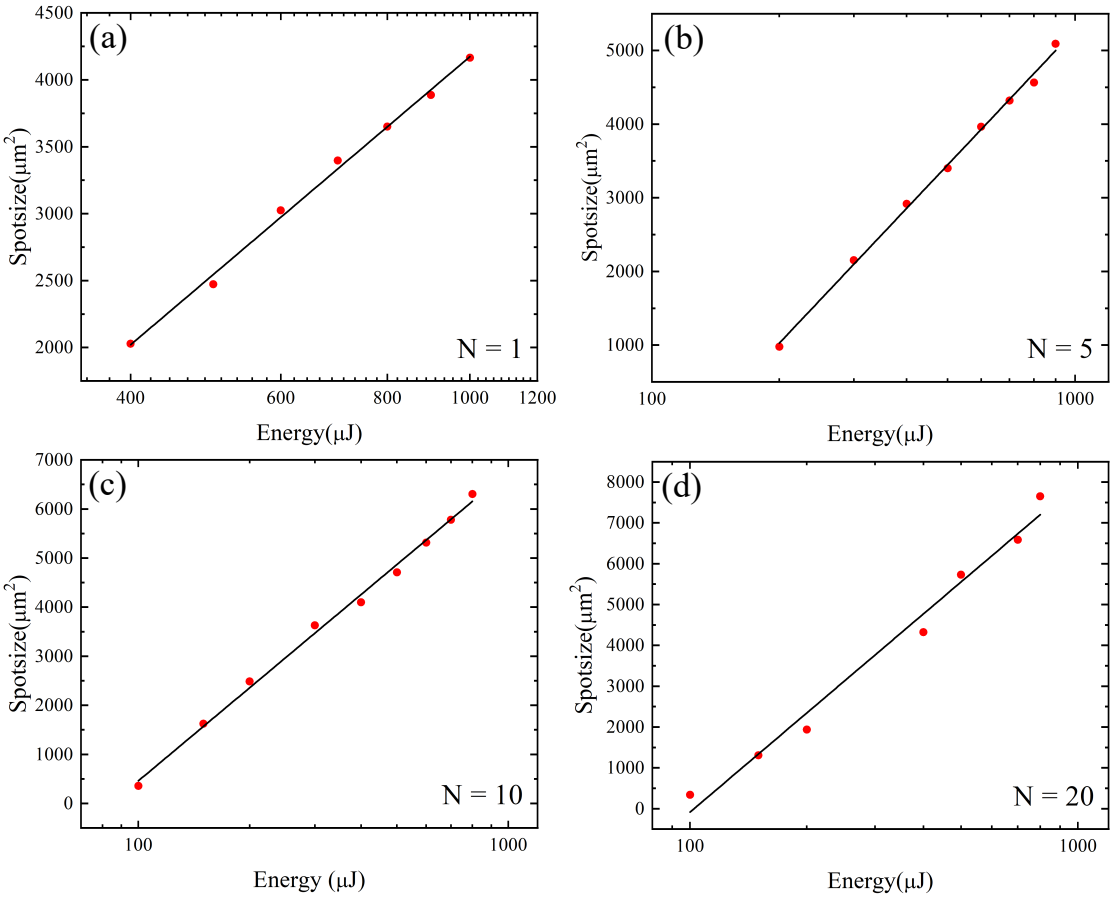

Figure 4.7: Graph showing a linear increase in the laser-induced damage area on fused silica as a function of the logarithm of the incident laser pulse energy. Irradiation is with N=1, 5, 10 and 20 pulses respectively.

ica are significantly lower than the single pulse ablation threshold. Obviously, the thresholds of modification and ablation depend on the number of applied laser pulses. This incubation effect is a non-ablating modification of the sample surface by the laser pulses in such a manner that the threshold for damage decreases with increase in the number of pulses. In the case of metals, incubation is related to an accumulation of energy into plastic stress-strain of the material.

Ablation condition (Number of pulses)	Peak threshold fluence $F_{th}(N)$ (J/cm^2)
N = 1	7.20
N = 5	5.13
N = 10	3.08
N = 20	2.92

Table 4.1: Femtosecond laser-induced ablation thresholds estimated for fused silica under atmospheric conditions.

The damage threshold follows the form of a power-law as given below:

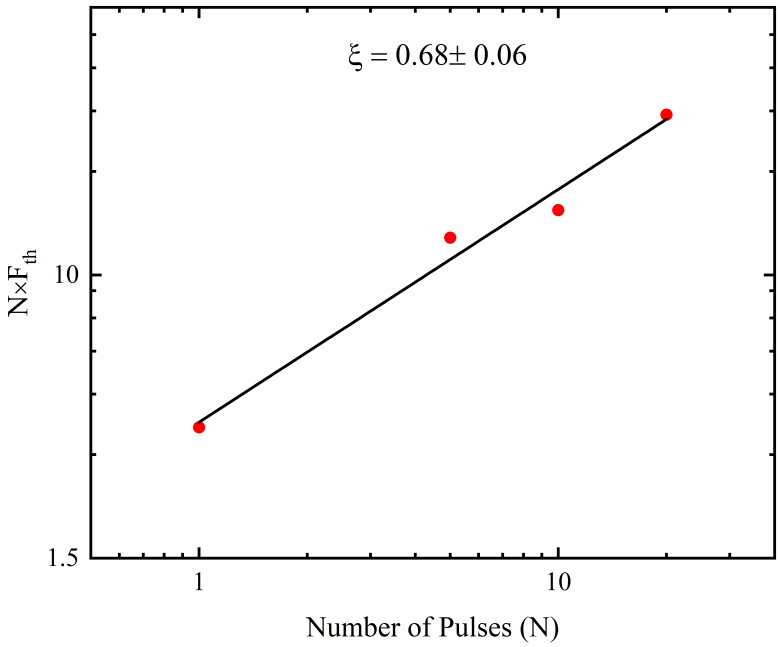

Figure 4.8: Threshold fluence variation with the number of pulses N, in the form $N \times F_{th}$.

$$F_{th}(N) = F_{th}(1) \times N^{\xi-1} \tag{4.3}$$

where $F_{th}(N)$ denotes the threshold fluence for N number of laser pulses, and ξ is a material-dependent coefficient. The value of E has been widely investigated for single-crystal metals [27], but not many reports are available for amorphous materials. J. Bonse et. al have successfully employed this formula in the case of indium phosphide (InP) [28], where it is not very clear whether the transi-

tional laser energy storage is mechanical or chemical (defects formation in several glasses-F centers) in nature [29]. In Figure 4.8, the dependence of $N \times F_{th}(N)$ on the number of pulses is plotted for our fused silica data, and the fit according to the above equation yields a coefficient $\xi = 0.67 \pm 0.06$. From the figure, we conclude that there is significant incubation in fused silica for pulses with a duration of $\approx$ 100 fs [23]. Similarly, we have calculated the threshold fluence of quartz for N = 1,10, and 20 to be 8.43 J/cm^2, 5.14 J/cm^2 and 4.05 J/cm^2 respectively, which is found to be slightly higher than that of fused silica. The value of incubation coefficient for quartz is $\xi = 0.77 \pm 0.12$. The studies in the following sections are related to the fabrication of large-area micro-/nano-structured fused silica and the effects of these micro-/nano-structures on the optical and morphological properties.

4.4 Laser-induced defects and surface modification

When fs laser irradiation of dielectric materials such as fused silica occurs, the energy deposited transforms matter at the ablated spot into liquid or to an excited solid state at high temperature and pressure. Both thermal diffusion and shock wave generation lead to rapid cooling or quenching of the modified region. While the exact process is uncertain, the end results are localized physical, chemical, and structural changes of the material exposed to the laser beam. These alterations can be involved with densification, refractive index changes, and/or defects formation [30–32]. In order to investigate laser-induced changes affecting the surface properties (optical and wetting) of fused silica, we have fabricated a large area surface of 6 $\times$ 6 mm^2 dimensions. Surface patterning at this scale is achieved by fabricating micro/nano trenches via line-by-line scanning, first along the horizontal direction, followed by a vertical step movement. From the understanding of multi-pulse ablation, we have optimized the fabrication of micro-/nano-structures by using a scanning speed of 0.05 mm/sec,

with the fs-laser peak fluence kept at ≈ 13.2 J/cm^2. The vertical step is fixed at $\Delta y = 40$ µm, selected for proper overlapping between the consecutive lines. The surface roughness of structured fused silica is measured using AFM (Figure 4.9) to understand the topography of the structured area. Raman and PL spectra are recorded for probing the structural modifications and laser-induced defects.

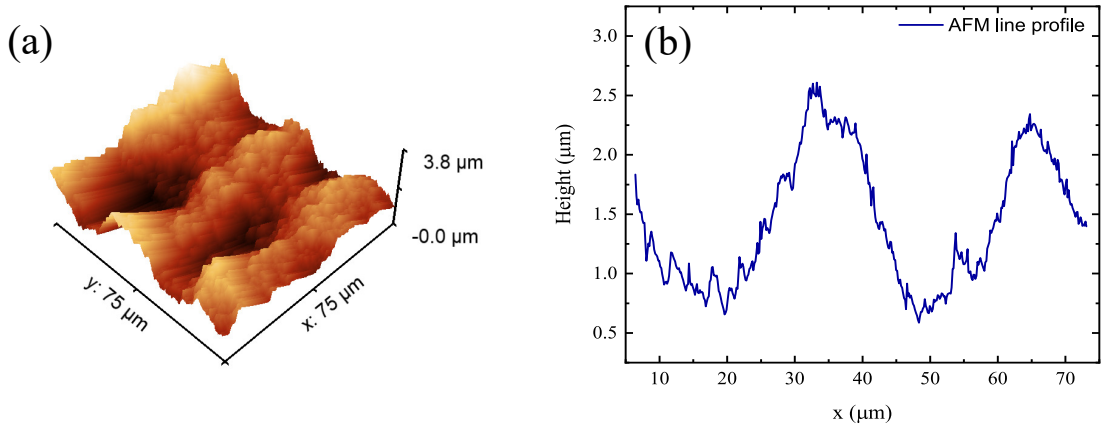

Figure 4.9: (a) AFM topographic image of fused silica surface irradiated at the peak fluence of 13.2 J/cm^2, (b) line profile extracted from the AFM image showing micro/nano trenches.

4.4.1 Raman and PL spectra

One of the main features of amorphous solids like fused silica is the lack of regularly repeating groups of atoms, which are the characteristic of crystalline materials. Amorphous fused silica belongs to the group of the so-called associated liquids [33], which form bonds in definite vectorial positions in space, leading to the formation of ring structures that connect molecules in a random network. These ring structures consist of tetrahedral atomic arrangements (one silicon atom surrounded by four oxygen atoms), indicating that the basic structural unit of such amorphous materials is a tetrahedron. There are six different ways to form a closed path starting from a structure denoted as O_1-Si_1-O_2, and

one looks for the shortest path to form a ring. In the past, densification of fused silica glass has been observed in neutron-irradiated samples [34]. Later, Chan et al. [35] employed Raman scattering to investigate changes in fused silica occurring due to femtosecond laser irradiation. Their investigations showed a relative increase in the intensity of the 495 cm^{-1} and 606 cm^{-1} bands with respect to the main peak 440 cm^{-1}, which was qualitatively explained to be associated with the densification of the material.

Raman spectroscopy has been established as an efficient method for the char-

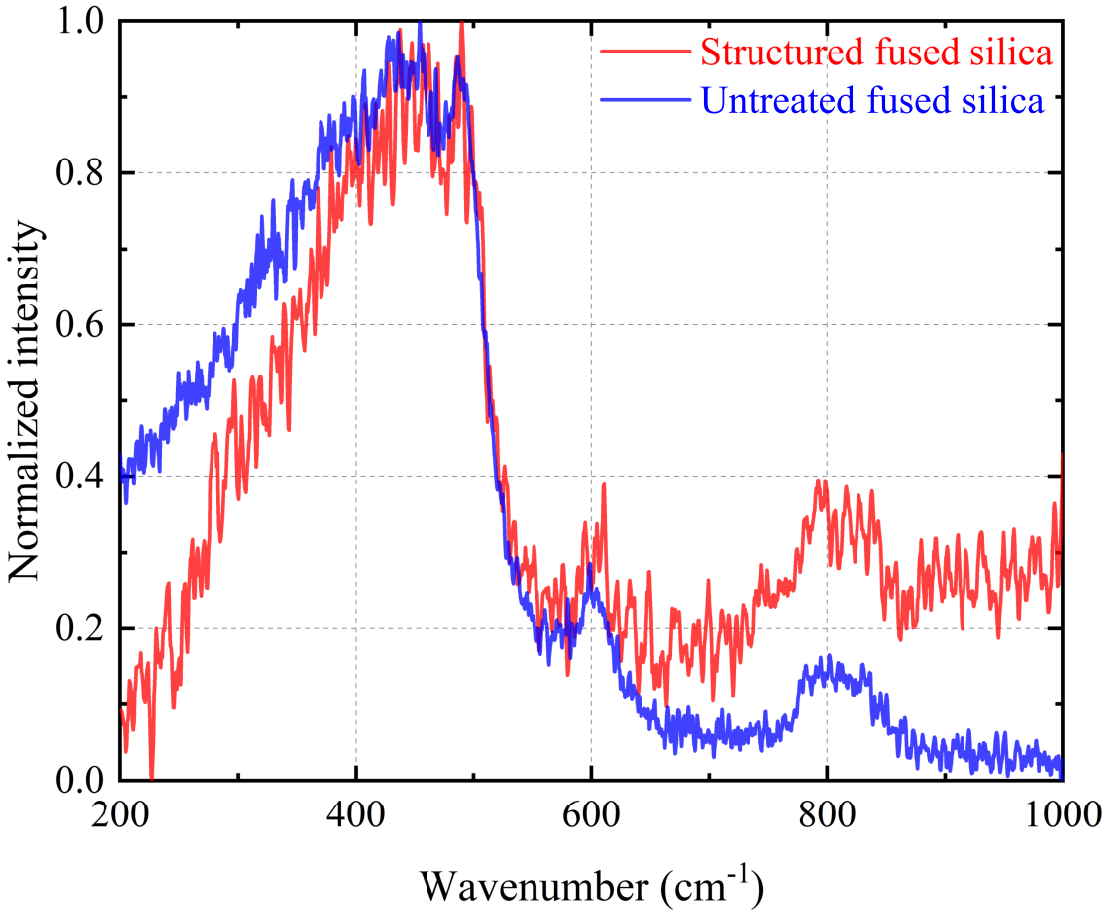

Figure 4.10: Normalized Raman spectra of (a) untreated fused silica, and (b) structured fused silica, processed at the peak fluence of 13.2 J/cm^2.

acterization of structural modifications in fused silica [36–39]. We employed Raman spectroscopy to explore the effects of laser irradiation on the molecular structure of the fused silica samples. Figure 4.10 shows Raman spectra

obtained for untreated as well as irradiated (at peak fluence F_p= 13.2 J/cm^2) fused silica samples. The main feature of the spectrum of fused silica is the broad-band centered at 440 cm^{-1} (ω_1), which is attributed to the motion of the bridging oxygen along the axis that bisects the Si-O-Si bond angle. Its width is considered to reflect the width of the Si-O-Si angle distribution [37, 39]. The two smaller and sharper bands at 490 cm^{-1} (D_1) and 604 cm^{-1} (D_2) are assigned to the in-phase breathing motions of oxygen atoms in puckered four- and planar three-membered ring structures, respectively. The broad overtone band centered around 800 cm^{-1} is attributed to the Si-O-Si symmetric stretching mode (ω_3). The offset found in the spectrum from about 650 nm onwards is because of fluorescence occurring in the treated sample [40].

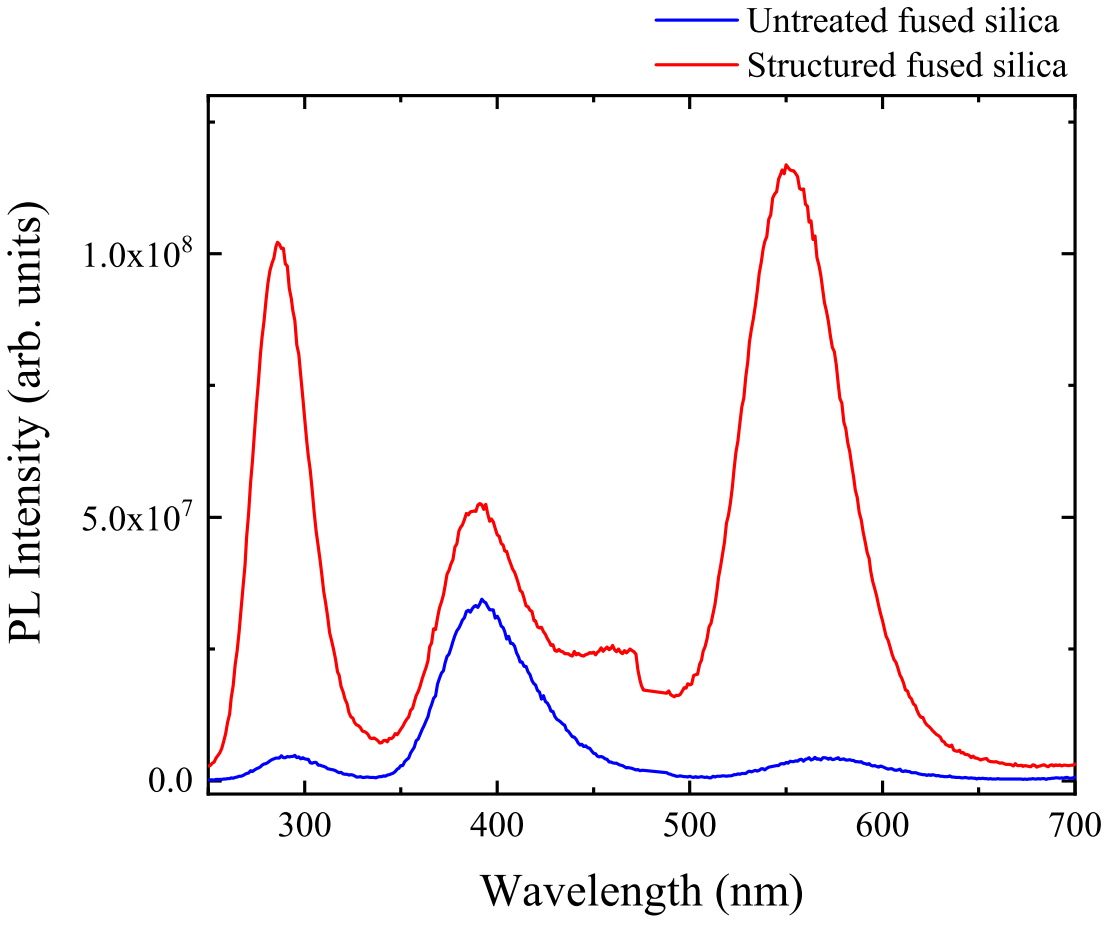

Figure 4.11: PL spectra measured for untreated and fs laser-structured fused silica samples.

There have been reports in literature correlating the optical properties of surfaces to defects, compositions, and surface morphologies. The defects originating due to texturing in particular can be either electronic or structural in nature. Electronics defects involve the re-distribution of local electron density to give rise to paramagnetic as well as diamagnetic centers, whereas structural defects are governed by the local atomic displacements from the normal random network structure of fused silica. In the strong interaction regime (at high fluence), multiple bond breaking (Si-O bonds) occurs continuously, and the bonds get reformed with numerous unbound atoms which dangle around. Since the diffusion coefficient of O is more than twice as that of Si, the O atoms diffuse away from the laser-irradiated areas by the generation of shockwaves [41]. Thus, Si-rich (Si^{3+} and Si^{2+}) structures generated from SiO_2 are formed at the center of the irradiated area causing localized oxygen deficient centers (ODCs). Apart from ODCs, various irradiation-induced defects, such as NBOHC (non-bridging oxygen hole center), STE (self-trapped exciton), E' center, and O_{int} (interstitial oxygen, peroxy radicals or O_2 molecules) also can be formed [30, 32, 38].

When SiO_2 is decomposed due to the high temperatures associated with plasma formation by laser irradiation, substoichiometric SiO_2, i.e., SiO_x $(0 < x < 2)$, would be the expected product. SiO_x would facilitate high absorption levels, which could be a reason for the continued growth of damage sites. We have therefore looked for signals in the PL spectrum indicating the presence of SiO_x or Si nanoparticles. The PL spectra obtained (for 240 nm line excitation) are given in Figure 4.11. The PL emission bands observed in structured fused silica are signatures of a variety of fundamental defects [38, 42, 43]. We observe 286 nm (3.21 eV) and 391 nm (3.17 eV) emission bands in laser-irradiated fused silica, which are attributed to intrinsic oxygen-deficient defects (ODCs) [44]. The new emission band centered at 460 nm (2.69 eV) seen for laser-irradiated fused silica corresponds to oxygen-deficient centers (ODCs) [42]. As seen in

Figure 4.11, there is a significant increase in the intensity of the 286 nm band for irradiated fused silica, indicating an increase in the concentration of the defects. The band centered at 550 nm (2.25 eV) is attributed to peroxy radicals (PORs), and/or small silicon clusters within SiO_x.

The non-bridging oxygen hole centers (NBOHCs), i.e., dangling oxygen bonds ($\equiv Si - O\bullet$), exhibit two different absorption bands at 1.9 eV (650 nm) and 4.8 eV (258 nm), respectively. However, we have not observed these NBOHCs bands in the measured PL spectra of both untreated and structured fused silica. The reason is that NBOHCs defects can recombine or inter-convert into different defects [45, 46]. For example, NBOHCs can become peroxy radicals ($\equiv Si - O - O\bullet$) by the addition of an interstitial O atom, or they can react with interstitial molecular hydrogen at room temperature to form ($\equiv Si - OH + H\bullet$). Another possible mechanism, proposed by L. Skuja et al., explains the absence of the 650 nm band via recombination of electrons in the highly localized non-bridging oxygen band-gap state, with holes in the valence band edge [47]. Another emission band which is usually observed around 1380 nm attributed to singlet oxygen transitions associated with interstitial neutral molecular oxygen (O_2) dissolved in the silica host lattice [48], is not seen due to instrumental limitations. Overall, The ODCs and PORs are the primary defect mechanisms observed in IR-laser irradiated fused silica. These are due to the Frenkel-type mechanism, expressed as [49]:

$$\equiv Si - O - Si \equiv \rightarrow \equiv Si - Si \equiv + O_{int} \quad (PORs\ and\ O_2) \tag{4.4}$$

The interstitial O_2 may escape from the sample surface, which induces sub-stoichiometric SiO_2, i.e. SiO_x $(0 < x < 2)$. Both Raman and PL spectra reveal densification and increase in various defects in laser-irradiated fused silica.

4.4.2 Transmittance, reflectivity and wettability

Figure 4.12 shows the influence of the hierarchical surface structures on the optical properties of the samples, measured with an integrating sphere in the wavelength range of 250 to 850 nm. The transmittance of the untreated substrate is almost constant at about 92% in the entire investigated spectral range (with the remaining 8% accounted by reflection losses). On the other hand, the overall transmittance is much lower for the structured sample. The transmittance T is ≈ 18 % at 250 nm and it gradually increases to to T ≈ 40 % at 850 nm. This behavior is due to an increased surface roughness that gives rise to diffuse reflectance at the irradiated surface. The latter increases with decreasing size of the surface structures, and it becomes significant when the measuring wavelength is of the order of the spatial period of the nanostructures [50, 51].

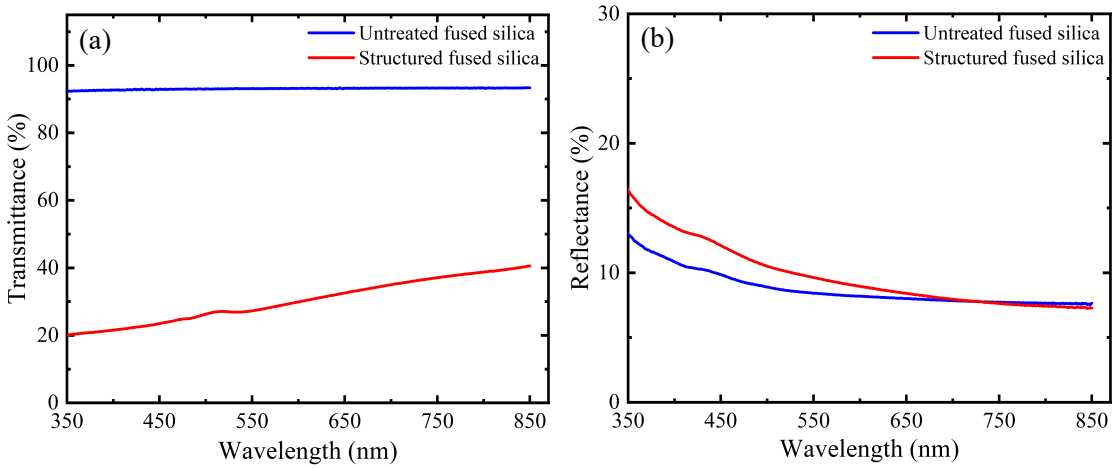

Figure 4.12: Optical characterization of untreated and structured fused silica surfaces: (a) transmittance and (b) reflectance measured in the wavelength range 350 to 850 nm using an integrating sphere.

As shown in Figure 4.12 (b), the laser irradiated surface shows a slightly increased reflection in comparison to that of plain fused silica. This can be attributed to the increased scattering and diffused reflectance caused by the micro-/nano-structures, and the degradation of the material by laser irradiation. Furthermore, the increase in defect concentration (ODCs) and the struc-

tural modification as indicated by Raman and PL spectra may change the transmittance and reflectivity of fs laser-irradiated fused silica.

We used the contact angle meter for measuring the wetting properties of fused silica before and after laser structuring. Photographs shown in Figure 4.13 depict the change in wetting properties due to fs-laser irradiation at the peak fluence of $F_p \approx 13.2$ J/cm^2. Figure 4.13(a) shows that the intrinsic water contact angle (CA) of fused silica is 47.2 $^\circ \pm 2.4^\circ$, making it hydrophilic in nature. Figure 4.13(b) is taken immediately after a single drop of distilled water (volume 1 µL) touches the textured surface. The droplet spreads almost instantaneously on the structured surface, exhibiting superhydrophilic nature, and the measured CA decreases significantly to 5.6 $^\circ \pm 0.7^\circ$ from 47.2 $^\circ \pm 2.4^\circ$.

The wetting properties of any substrate can be explained by the models given

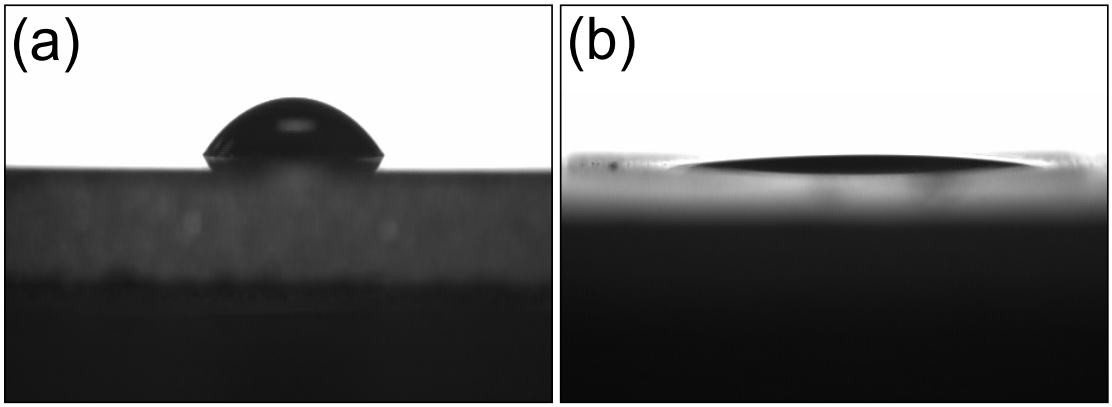

Figure 4.13: Photographs showing the wettability of fused silica. (a) untreated fused silica with the intrinsic contact angle (CA) = 47.2 $^\circ \pm 2.4^\circ$, (b) fs laser-structured fused silica exhibiting CA = 5.6 $^\circ \pm 0.7^\circ$.

by Cassie–Baxter [52] and Wenzel et al. [53–55]. These models are based on the effects of macroscopic surface roughness on the wettability of solid surfaces. The Cassie-Baxter model is usually considered for highly hydrophobic surfaces, because the multiscale surface morphology provides tiny air pockets, which enhance the hydrophobicity of the surface. On the other hand, hydrophilicity (homogeneous wetting) is best explained by the Wenzel model. According to Wenzel's theory, wetting of surfaces that have a CA less than 90° can be im-

proved by increasing the surface roughness. The equation relating the surface roughness to the contact angle is given by,

$$cos\theta_w = rcos\theta_f \tag{4.5}$$

where θ_w and θ_f are the apparent (macroscopic) and Young (intrinsic) contact angles measured on rough and flat surfaces of the same material, respectively, and r is the roughness factor (defined as the ratio between the actual and projected surface areas of the sample). Hydrophilic surfaces with a contact angle less than 65° can be changed to superhydrophilic surfaces by modulating r in the range of 1.2 to 2 [56]. The value of the roughness parameter in our experiment is about 1.1, which indicates that the superhydrophilicity seen for textured fused silica is related to the surface chemistry as well, in addition to the surface roughness. For example, the presence of silica nano-foam/hydroxy groups on the structured surface is an enhancing factor for the surface energy, leading to superhydrophilicity. In fact, these structures can be easily modified chemically with compounds that contain hydrophobic end groups to lower their surface energy, for transforming them into superhydrophobic surfaces. These results demonstrate the possibility to create tailored superhydrophilic and superhydrophobic surfaces with high precision, for making self-cleaning and antifouling smart windows, optical storage devices, microfluidic devices, and sensors [50, 57, 58].

4.5 Summary

This chapter reports salient aspects of fs laser-induced surface structuring of dielectric materials from measurements carried out in fused silica and quartz. The mechanisms involved in the generation of quasi-periodic surface structures are addressed. The effect of crystallographic orientation in ripples formation is explored in both materials under the same irradiation conditions. The variety of

fs-LIPSS quasi-periodic ripples and micron-sized grooves, formed with different preferential alignments (parallel and perpendicular) depending on the irradiation parameters (laser fluence and the number of pulses), are investigated in detail. The generation of ripples is explained as a result of the inhomogeneous absorption of the laser pulse energy due to an energy modulation over the laser-irradiated surface. A large area fused silica surface with optimized structures is fabricated to investigate the optical and morphological changes caused by fs-surface structuring. Raman and PL spectra indicate material densification and increase in the defects concentration (ODCs and PORs) upon structuring. The laser-irradiated surface exhibits reduced transmittance compared to that of untreated fused silica. The transmittance decrease is caused mostly by scattering from the micro-/nano-structures. Contact angle measurements indicate the formation of a superhydrophilic surface on fused silica due to fs-laser irradiation. Enhanced surface roughness (due to the presence of micro-/nano-structures) and increased surface energy result in the superhydrophilicity. The experimental results presented in this chapter show that femtosecond laser direct structuring is an efficient and convenient method to fabricate micro/nano-structured dielectric surfaces for a multitude of applications.

Bibliography

[1] Felix Zimmermann, Anton Plech, Sören Richter, Andreas Tünnermann, and Stefan Nolte. The onset of ultrashort pulse-induced nanogratings. *Laser & Photonics Reviews*, 10(2):327–334, 2016.

[2] Yasuhiko Shimotsuma, Peter G Kazansky, Jiarong Qiu, and Kazuoki Hirao. Self-organized nanogratings in glass irradiated by ultrashort light pulses. *Physical review letters*, 91(24):247405, 2003.

[3] Katherine C Phillips, Hemi H Gandhi, Eric Mazur, and SK Sundaram. Ultrafast laser processing of materials: a review. *Advances in Optics and Photonics*, 7(4):684–712, 2015.

[4] Zhou Fang, Jianda Shao, et al. Femtosecond laser-induced periodic surface structure on fused silica surface. *Optik*, 127(3):1171–1175, 2016.

[5] S Höhm, A Rosenfeld, Jörg Krüger, and Jörn Bonse. Femtosecond laser-induced periodic surface structures on silica. *Journal of Applied Physics*, 112(1):014901, 2012.

[6] Feng Liang, Réal Vallée, and See Leang Chin. Mechanism of nanograting formation on the surface of fused silica. *Optics express*, 20(4):4389–4396, 2012.

[7] Jörn Bonse, Jörg Krüger, S Höhm, and A Rosenfeld. Femtosecond laser-induced periodic surface structures. *Journal of Laser Applications*, 24(4):042006, 2012.

[8] DC Emmony, RP Howson, and LJ Willis. Laser mirror damage in germanium at 10.6 μm. *Applied Physics Letters*, 23(11):598–600, 1973.

[9] Jörn Bonse, Arkadi Rosenfeld, and Jörg Krüger. On the role of surface plasmon polaritons in the formation of laser-induced periodic surface structures upon irradiation of silicon by femtosecond-laser pulses. *Journal of Applied Physics*, 106(10):104910, 2009.

[10] Susanta Kumar Das, Hamza Messaoudi, Abishek Debroy, Enda McGlynn, and Ruediger Grunwald. Multiphoton excitation of surface plasmon-polaritons and scaling of nanoripple formation in large bandgap materials. *Optical Materials Express*, 3(10):1705–1715, 2013.

[11] Philipp Nürnberger, Hendrik M Reinhardt, Hee-Cheol Kim, Erik Pfeifer, Moritz Kroll, Sandra Müller, Fang Yang, and Norbert A Hampp. Orthogonally superimposed laser-induced periodic surface structures (lipss) upon nanosecond laser pulse irradiation of sio2/si layered systems. *Applied Surface Science*, 425:682–688, 2017.

[12] Min Huang, Fuli Zhao, Ya Cheng, Ningsheng Xu, and Zhizhan Xu. Origin of laser-induced near-subwavelength ripples: interference between surface plasmons and incident laser. *ACS nano*, 3(12):4062–4070, 2009.

[13] D Dufft, A Rosenfeld, SK Das, R Grunwald, and J Bonse. Femtosecond laser-induced periodic surface structures revisited: A comparative study on zno. *Journal of Applied Physics*, 105(3):034908, 2009.

[14] Jürgen Reif, Florenta Costache, Matthias Henyk, and Stanislav V Pandelov. Ripples revisited: non-classical morphology at the bottom of femtosecond laser ablation craters in transparent dielectrics. *Applied Surface Science*, 197:891–895, 2002.

[15] A Borowiec and HK Haugen. Subwavelength ripple formation on the surfaces of compound semiconductors irradiated with femtosecond laser pulses. *Applied Physics Letters*, 82(25):4462–4464, 2003.

[16] Xian-Feng Li, Cheng-Yun Zhang, Hui Li, Qiao-Feng Dai, Sheng Lan, and Shao-Long Tie. Formation of 100-nm periodic structures on a titanium surface by exploiting the oxidation and third harmonic generation induced by femtosecond laser pulses. *Optics express*, 22(23):28086–28099, 2014.

[17] BC Stuart, MD Feit, AM Rubenchik, BW Shore, and MD Perry. Laser-induced damage in dielectrics with nanosecond to subpicosecond pulses. *Physical review letters*, 74(12):2248, 1995.

[18] Rajamudili Kuladeep, Chakradhar Sahoo, and Desai Narayana Rao. Direct writing of continuous and discontinuous sub-wavelength periodic surface structures on single-crystalline silicon using femtosecond laser. *Applied Physics Letters*, 104(22):222103, 2014.

[19] R Jagdheesh, B Pathiraj, E Karatay, GRBE Romer, and AJ Huis in 't Veld. Laser-induced nanoscale superhydrophobic structures on metal surfaces. *Langmuir*, 27(13):8464–8469, 2011.

[20] Esther Rebollar, Irene Frischauf, Michael Olbrich, Thomas Peterbauer, Steffen Hering, Johannes Preiner, Peter Hinterdorfer, Christoph Romanin, and Johannes Heitz. Proliferation of aligned mammalian cells on laser-nanostructured polystyrene. *Biomaterials*, 29(12):1796–1806, 2008.

[21] Alexandre Cunha, Ana Paula Serro, Vitor Oliveira, Amélia Almeida, Rui Vilar, and Marie-Christine Durrieu. Wetting behaviour of femtosecond laser textured ti–6al–4v surfaces. *Applied Surface Science*, 265:688–696, 2013.

[22] K Wallat, D Dörr, R Le Harzic, F Stracke, D Sauer, M Neumeier, A Kovtun, H Zimmermann, and M Epple. Cellular reactions toward nanostruc-

tured silicon surfaces created by laser ablation. *Journal of Laser Applications*, 24(4):042016, 2012.

[23] Jörn Bonse, Steffen Baudach, Jörg Krüger, Wolfgang Kautek, and Matthias Lenzner. Femtosecond laser ablation of silicon–modification thresholds and morphology. *Applied Physics A*, 74(1):19–25, 2002.

[24] George D Tsibidis, Costas Fotakis, and Emmanuel Stratakis. From ripples to spikes: A hydrodynamical mechanism to interpret femtosecond laser-induced self-assembled structures. *Physical Review B*, 92(4):041405, 2015.

[25] George D Tsibidis, Evangelos Skoulas, Antonis Papadopoulos, and Emmanuel Stratakis. Convection roll-driven generation of supra-wavelength periodic surface structures on dielectrics upon irradiation with femtosecond pulsed lasers. *Physical Review B*, 94(8):081305, 2016.

[26] J. M. Liu. Simple technique for measurements of pulsed Gaussian-beam spot sizes. *Optics Letters*, 7(5):196, 1982.

[27] Yong Jee, Michael F Becker, and Rodger M Walser. Laser-induced damage on single-crystal metal surfaces. *JOSA B*, 5(3):648–659, 1988.

[28] Jörn Bonse, JM Wrobel, Jörg Krüger, and Wolfgang Kautek. Ultrashort-pulse laser ablation of indium phosphide in air. *Applied Physics A*, 72(1):89–94, 2001.

[29] OM Efimov, K Gabel, SV Garnov, LB Glebov, S Grantham, M Richardson, and MJ Soileau. Color-center generation in silicate glasses exposed to infrared femtosecond pulses. *JOSA B*, 15(1):193–199, 1998.

[30] Joe Wong, JL Ferriera, EF Lindsey, DL Haupt, ID Hutcheon, and JH Kinney. Morphology and microstructure in fused silica induced by high fluence ultraviolet 3ω (355 nm) laser pulses. *Journal of non-crystalline solids*, 352(3):255–272, 2006.

[31] A Kubota, M-J Caturla, JS Stölken, and Michael D Feit. Densification of fused silica due to shock waves and its implications for 351 nm laser induced damage. *Optics Express*, 8(11):611–616, 2001.

[32] Koichi Awazu. Ablation and compaction of amorphous sio2 irradiated with arf excimer laser. *Journal of Non-Crystalline Solids*, 337(3):241–253, 2004.

[33] Shirley V King. Ring configurations in a random network model of vitreous silica. *Nature*, 213(5081):1112–1113, 1967.

[34] Shiv K Sharma, Joseph F Mammone, and Malcolm F Nicol. Raman investigation of ring configurations in vitreous silica. *Nature*, 292(5819):140–141, 1981.

[35] James W Chan, Thomas Huser, S Risbud, and DM Krol. Structural changes in fused silica after exposure to focused femtosecond laser pulses. *Optics letters*, 26(21):1726–1728, 2001.

[36] W Reichman, James W Chan, and DM Krol. Confocal fluorescence and raman microscopy of femtosecond laser-modified fused silica. *Journal of Physics: Condensed Matter*, 15(31):S2447, 2003.

[37] Nadezda Varkentina, Marc Dussauze, Arnaud Royon, Marc Ramme, Yannick Petit, and Lionel Canioni. High repetition rate femtosecond laser irradiation of fused silica studied by raman spectroscopy. *Optical Materials Express*, 6(1):79–90, 2016.

[38] Shizhen Xu, Xiaodong Yuan, Xiaotao Zu, Haibin Lv, Xiaodong Jiang, Li Zhang, and Wanguo Zheng. Laser-induced defects in fused silica by uv laser irradiation. *Journal of non-crystalline solids*, 353(44-46):4212–4217, 2007.

[39] Alberto Salleo, Seth T Taylor, Michael C Martin, Wendy R Panero, Raymond Jeanloz, Timothy Sands, and François Y Génin. Laser-driven formation of a high-pressure phase in amorphous silica. *Nature materials*, 2(12):796–800, 2003.

[40] Siniša Vukelić, Panjawat Kongsuwan, Sunmin Ryu, and Y Lawrence Yao. Ultrafast laser induced structural modification of fused silica—part ii: Spatially resolved and decomposed raman spectral analysis. *Journal of manufacturing science and engineering*, 132(6), 2010.

[41] Koji Sugioka and Ya Cheng. *Ultrafast laser processing: from micro-to nanoscale*. CRC Press, 2013.

[42] Arnaud Zoubir, Clara Rivero, Rachel Grodsky, Kathleen Richardson, Martin Richardson, Thierry Cardinal, and Michel Couzi. Laser-induced defects in fused silica by femtosecond ir irradiation. *Physical Review B*, 73(22):224117, 2006.

[43] L Vaccaro, M Cannas, V Radzig, and R Boscaino. Luminescence of the surface nonbridging oxygen hole center in silica: Spectral and decay properties. *Physical Review B*, 78(7):075421, 2008.

[44] David L Griscom. Optical properties and structure of defects in silica glass. *Journal of the Ceramic Society of Japan*, 99(1154):923–942, 1991.

[45] Hiroyuki Nishikawa, Eiki Watanabe, Daisuke Ito, and Yoshimichi Ohki. Decay kinetics of the 4.4-ev photoluminescence associated with the two states of oxygen-deficient-type defect in amorphous sio 2. *Physical review letters*, 72(13):2101, 1994.

[46] Koichi Kajihara, Linards Skuja, Masahiro Hirano, and Hideo Hosono. Formation and decay of nonbridging oxygen hole centers in sio 2 glasses induced by f 2 laser irradiation: In situ observation using a pump and probe technique. *Applied Physics Letters*, 79(12):1757–1759, 2001.

[47] Linards Skuja. The origin of the intrinsic 1.9 ev luminescence band in glassy sio2. *Journal of Non-Crystalline Solids*, 179:51–69, 1994.

[48] Anatoly N Trukhin. Excitons in sio2: a review. *Journal of non-crystalline solids*, 149(1-2):32–45, 1992.

[49] Hideo Hosono, Hiroshi Kawazoe, and Noriaki Matsunami. Experimental evidence for frenkel defect formation in amorphous sio 2 by electronic excitation. *Physical Review Letters*, 80(2):317, 1998.

[50] Estela Baquedano, Lorena Torné, Pablo Caño, and Pablo A Postigo. Increased efficiency of solar cells protected by hydrophobic and hydrophilic anti-reflecting nanostructured glasses. *Nanomaterials*, 7(12):437, 2017.

[51] Yao-Chung Tsao, Thomas Søndergaard, Esben Skovsen, Leonid Gurevich, Kjeld Pedersen, and Thomas Garm Pedersen. Pore size dependence of diffuse light scattering from anodized aluminum solar cell backside reflectors. *Optics express*, 21(101):A84–A95, 2013.

[52] B D Cassie, A. B. D. Cassie, and S. Baxter. Of porous surfaces,. *Transactions of the Faraday Society*, 40(5):546–551, 1944.

[53] Robert N Wenzel. Surface roughness and contact angle. *The Journal of Physical Chemistry*, 53(9):1466–1467, 1949.

[54] Lin Yao and Junhui He. Recent progress in antireflection and self-cleaning technology–from surface engineering to functional surfaces. *Progress in Materials Science*, 61:94–143, 2014.

[55] Shi-zhen Xu, Hong-qiang Dou, Kai Sun, Ya-yun Ye, Zhaoxia Li, Haijun Wang, Wei Liao, Hao Liu, Xin-xiang Miao, Xiao-dong Yuan, et al. Scan speed and fluence effects in femtosecond laser induced micro/nanostructures on the surface of fused silica. *Journal of Non-Crystalline Solids*, 492:56–62, 2018.

[56] Jaroslaw Drelich and Emil Chibowski. Superhydrophilic and superwetting surfaces: definition and mechanisms of control. *Langmuir*, 26(24):18621–18623, 2010.

[57] Ilker S Bayer. On the durability and wear resistance of transparent superhydrophobic coatings. *Coatings*, 7(1):12, 2017.

[58] Clemens Kunz, Frank A Müller, and Stephan Gräf. Multifunctional hierarchical surface structures by femtosecond laser processing. *Materials*, 11(5):789, 2018.

Chapter 5

Fabrication of superhydrophilic silicon using nanosecond laser pulses

This chapter demonstrates the fabrication and characterization of large area micro-/nano-textured silicon surfaces using laser pulses of nanoseconds (ns) duration. The surface properties of the samples before and after texturing are investigated by employing EDX, XPS, and AFM. Wettability is measured from contact angle measurements. Models based on sample roughness and surface chemistry are discussed for explaining the wettability of the textured surface. Finally, durable superhydrophilic silicon is fabricated and the properties are explained using the Wenzel model.

5.1 Introduction

Laser micro/nano texturing of silicon for modifying and enhancing its electronic [1, 2], optical [3–5], and wetting properties [6–9] is a topic of active research interest. While the modification of electronic and optical properties of silicon is finding a wide variety of applications in opto-electronics, altering the wetting properties of solid surfaces by laser micromachining has attracted a

significant level of interest because of its ubiquitous advantages in both fundamental research and industrial applications [8, 10–13]. In recent years, short (nanosecond) and ultrashort (femto-/pico-second) laser microfabrication has received great attention as an efficient method for modifying the surface wettability of different solid materials. For industrial applications, the ability to create superhydrophilic solid surfaces using compact, robust and cost–effective nanosecond lasers is highly desirable.

It is well known that the wettability of any solid surface depends significantly on its chemical composition and morphology. The degree of wetting of a surface by a liquid can be determined by the contact angle (CA) measurement. The contact angle is determined at the triple point (where the solid, liquid and vapour interfaces intersect each other). According to Young's Equation [14], at the contact angle (θ_Y) the liquid drop is in thermodynamic equilibrium under the action of three interfacial tensions, namely, solid-vapour (γ_{SV}), solid-liquid (γ_{SL}), and liquid-vapour (γ_{LV}):

$$\gamma_{LV}\cos(\theta_Y) = \gamma_{SV} - \gamma_{SL} \tag{5.1}$$

Considering water as the liquid, the wetting state of solid surfaces can be classified as hydrophobic with contact angles higher than 90°, and hydrophilic with contact angles lower than 90°. Chemical composition determines the surface free energy, and a higher surface energy leads to higher hydrophilicity.

Nature exhibits a wide variety of either superhydrophobic or superhydrophilic wetting surfaces, which are at the extreme ends of the wetting behavior spectrum [15]. A superhydrophobic surface exhibits a contact angle higher than 150° with negligible contact angle hysteresis. These surfaces show unique properties such as self-cleaning (Lotus leaf effect), anti-icing (Butterfly wings) and super water-repulsion (Water strider's legs) [16, 17]. On the other hand, superhydrophilic surfaces are commonly recognized by their complete wetting by water, showing contact angles of approximately 0°.

Surfaces exhibiting 'super-wetting and super-spreading' of water are found in water-absorbing epiphytic growing Spanish moss (*Tillandsia Usneoides*) and several insect-consuming carnivorous plants (e.g., *Nepenthes Rafflesiana*, which traps insects using wet and slippery pitcher rims) respectively [15, 18]. Inspired by nature, artificial superhydrophilic materials are being manufactured for making self-cleaning and antifogging surfaces [19, 20], separation filters [21], heat exchangers [22], biosensors, biochips [23, 24] etc.

We have selected silicon for our investigations because of its broad range of applications in microelectronics and optoelectronics, where the problem of heat dissipation from small areas is a critical issue. A promising solution for heat transfer enhancement is the modification of the surface wettability property to increase the heat transfer coefficient (HTC) [25]. Superhydrophilic surfaces allow rapid spreading of liquids over them, enabling efficient heat transfer from the surface to the interface across the liquid film, resulting in rapid evaporation and a very high HTC [26–29]. Several physical and chemical patterning approaches have been employed for texturing surfaces to tailor their wettability, including electrochemical deposition [30], photolithography [31, 32], plasma treatments [33], and electron-beam lithography [34]. However, micro-structuring by femtosecond (fs) [5] and nanosecond (ns) lasers [35] in specific ambient conditions [19, 36] is especially attractive, because it achieves structuring of solid substrates at two different length scales through a maskless, simple one-step process. In the past, Vorobyev and Guo have demonstrated the transformation of silicon surfaces from the regular to superwicking nature through direct high-intensity femtosecond laser surface structuring [37]. The gravity-defying motion of water described in this work occurred due to the formation of supercapillaries on the textured surface. Currently, the fabrication of biomimetic surfaces with superhydrophilic and superhydrophobic properties has attracted significant research interest due to their widespread applications. Skoulas et al. has fabricated biomimetic

surfaces by employing radially and azimuthally polarized beams, giving rise to dual-scale, Lotus leaf-like superhydrophobic surfaces and Shark skin-like biomimetic morphologies [30].

To the best of our knowledge, the works published hitherto on nanosecond laser texturing have employed subsequent post processes (e.g. additional chemical processing for increasing the surface energy) for improving the hydrophilicity of hierarchical structures. In most cases the laser textured surface shows a high hydrophilic nature just after laser processing, but it gradually turns into hydrophobic/superhydrophobic surface when exposed to the atmosphere due to a change in the surface energy [8, 19, 21, 38]. In this context, the work reported in this chapter is conducted with the objective of studying the influence of laser-written micro-/nano-scale ripples on the improvement of the wettability of silicon substrates.

In this work, permanently superhydrophilic silicon surfaces have been obtained by mask-free, low cost, single step laser induced surface structuring under atmospheric conditions, without requiring any post-chemical processing. It is well known that ablation and surface oxidation occur simultaneously in the case of nanosecond laser irradiation of silicon in air. As a result, multiscale features consisting of micro-valleys (parallel line scan) and sub-wavelength scale nano-capillaries (along the edge of the irradiated spot) decorated with silica nanoparticles in the form of spherical nano-foam are formed. These features result in the superhydrophilicity of the textured surface, which is retained over a prolonged period. The simplicity of the technique and the convenient control of the resulting wetting properties make laser texturing of silicon an attractive option for several potential applications.

5.2 Experimental details

The schematic of the experimental setup has been shown earlier in chapter 2 (Figure 2.8). Single crystal n-type Si (100) wafer (Silicon Valley Microelectronics, USA) of resistivity 1-10 ohm-cm is mounted on a high-precision X–Y translation stage, normal to the incident laser beam. The irradiating source is a frequency-doubled Nd:YAG laser (Quanta-Ray, Spectra-Physics) of wavelength λ = 532 nm, delivering 7 ns pulses at the repetition rate of 10 Hz. The energy of the incident laser pulses is varied using an attenuator comprising of a half-wave plate and polarizing cube beam splitter. A mechanical shutter synchronized with the Q-switch signal of the Nd:YAG laser is used for varying the irradiation dose (number of pulses) falling on the target. The laser beam is focused onto the silicon sample using a 250-mm focal length plano-convex lens. The beam radius at the focal point (ω_0) is measured to be about 52 µm ($1/e^2$ criterion) [39]. Structuring is performed at different peak fluences $F_p = \frac{2E_L}{\pi\omega_0^2}$, ranging from 0.70 J/cm^2 to 18.84 J/cm^2. To study the influence of the applied fluence on the wetting property, three different large-area samples (6×6 mm^2) have been fabricated by the parallel line scanning method at peak fluences F_p = 0.94 J/cm^2, 1.41 J/cm^2 and 1.88 J/cm^2, respectively.

After laser irradiation, the samples are cleaned in ultrasonic baths of acetone and methanol, followed by blow-drying with pumped nitrogen to remove dust particles settled at the surface during the process. The morphology of the textured silicon surface is examined using a scanning electron microscope (SEM). The topology and depth profile (roughness) of the structures are characterized by means of an atomic force microscope (AFM) using the contact mode technique. To understand the chemical changes occuring due to laser irradiation, the chemical composition of the surface is investigated before and after irradiation by energy-dispersive X-ray (EDX) measurements. The valence states of the elements of the samples are measured by X-ray photoelectron spectroscopy

(XPS) to confirm the EDX measurements. Peak fitting is performed using Fityk software. Static contact angle measurements are performed to understand the effect of ns laser irradiation on the wetting properties of the sample by an automated contact angle meter (DM 501, Kyowa Japan), using the sessile drop method. A water droplet of volume 1 µL (distilled) is gently positioned on the surface using a microsyringe, and images are captured to measure the angle formed at the solid-liquid interface. The mean value of the contact angle is calculated from five individual measurements. Consecutive measurements give results reproducible to within $\pm 1^{\circ}$.

5.3 Features of nanosecond laser structuring

Laser-induced morphology changes on silicon generally show a strong dependence on the beam parameters (energy density, pulse duration, number of accumulated pulses, wavelength, etc). When a ns laser pulse is focused on a solid surface (e.g. silicon substrate) it generates plasma with high temperature and pressure, which bursts out of the ablation spot and expands, removing the ionized materials from the surface. The ejection of the ablated material leads to the formation of various rough micro-/nano-structures on the surface. In addition, a large number of ejected molten particles fall down and solidify (re-crystallization), resulting in abundant self-organized fine nano-protrusions coated on the microstructures [40]. In order to avoid heating effects and excessive melting, the effects of laser pulse fluence and the number of pulses falling on the surface have been studied prior to fabricating the structures.

The rapid heating of laser-irradiated silicon results in quick melting and evaporation (ablation), leading to the formation of surface craters. Most of the material carved out from the center of the crater will be redeposited in the area surrounding the crater. The degree of ablation depends on the applied laser fluence. We have found that the single pulse ablation threshold of silicon (F_{th}) in

air ambient is 0.48 J/cm^2 [41]. The ablation threshold (F_{th}) gets reduced with increasing number of pulses due to the cumulative deposition of laser energy onto the surface. This is described mathematically by the incubation model [32, 33] given by the Power-law

$$F_{th}(N) = F_{th}(1) \times N^{(\xi-1)} \tag{5.2}$$

where ξ is the incubation coefficient which describes the degree of incubation for a material, and $F_{th}(N)$ and $F_{th}(1)$ are the ablation threshold fluences for N number of pulses and for a single pulse, respectively. The dependence of $N \times F_{th}(N)$ on the number of pulses is plotted for N = 1, 3, 5, 10 and 20, and the fit to the data according to equation 5.2 yields a coefficient ξ=0.89$\pm$0.02.

Usually, when a semiconductor (e.g., silicon) is irradiated with intense laser pulses, laser energy is absorbed primarily by the electrons. If the absorbed photon energy is sufficient to overcome the energy band gap, electron/hole pairs will be generated in the conduction/valence bands. The excited electrons thermalize within the electron subsystem quickly, and thermal diffusion from the hot electrons facilitates energy transfer to the silicon lattice. When the absorbed energy exceeds the latent heat of melting, a melt pool is formed on the target surface. This transition from the solid to liquid phase occurs on a timescale of 10 to 100 picoseconds [34]. These dynamic processes in the melt pool can initiate the formation of self-organized periodic structures consisting of peak and valley like ripples, which become "frozen" after cooling [35].

We see that the bottoms of the craters formed due to single and multi-pulse laser irradiation show a flat topography, as shown in Figure 5.1(a). However, SEM images taken at higher magnifications show that in addition to the circular region formed due to excess melt [Figure 5.1(b)], another spatial feature of nanometer roughness appears along the rim of the craters at higher laser fluences [Figure 5.1(c)]. These nano-ripples, which are decorated concentrically are found to follow the circular shape of the irradiated spot. The spatial regu-

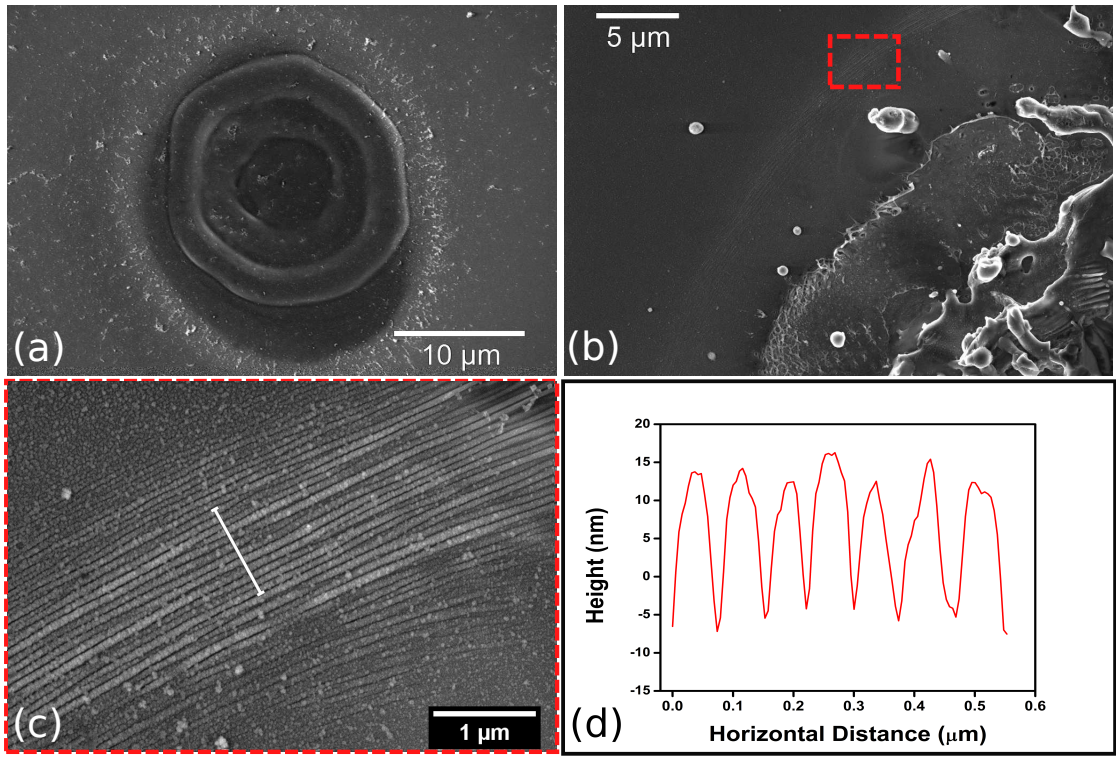

Figure 5.1: SEM images of the ablated area for different incident laser fluences (F_p) and number of pulses (N). (a) F_p = 0.70 J/cm^2, N = 20, (b) F_p = 18.84 J/cm^2, N = 10, (c) zoomed view of the concentric nano-ripples formed along the rim of the irradiated spot, and (d) spatial profile of nano-ripples with an average spatial periodicity of 74 $\pm$ 3 nm, calculated with the help of ImageJ software.

larity of these concentric nano-ripples having an average periodicity 74 $\pm$ 3nm [Figure 5.1(d)] has no relation to the laser wavelength (λ = 532 nm), but its occurrence depends on the laser fluence. This fact rules out the role of surface optical interference phenomena in their formation, because interference phenomena result in laser induced periodic surface structures (LIPSS) whose periodicity depends on the laser wavelength. However, these ripples have been discussed in the literature previously, and it is believed that these nano-structures are frozen capillary waves, which are characteristic of the relaxation of molten silicon [35].

Since the change in wetting behavior due to ablation might be linked with a change in surface composition and/or surface contamination, we have analyzed the surface state of the ablated samples by Energy Dispersive X-Ray (EDX) spectroscopy. EDX spectra given in Figure 5.2 indicate the formation of a

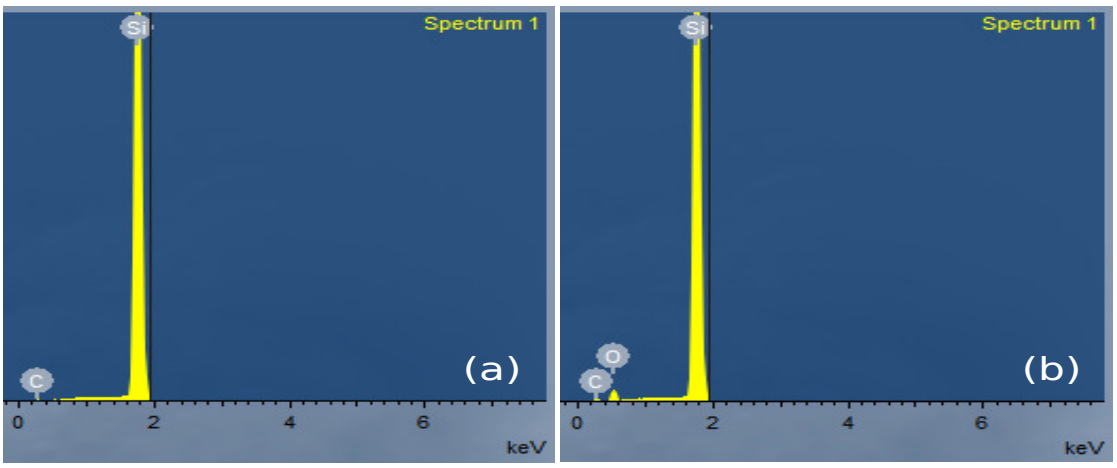

Figure 5.2: Energy Dispersive X-Ray (EDX) spectra measured for the silicon samples. (a) Untreated silicon, (b) textured silicon, revealing the formation of silicon oxide (F_p = 1.41 J/cm^2).

Applied Peak Fluence(J/cm^2)	Atomic % of Oxygen
0.00(Untreated)	0.00
0.94	8.51
1.41	10.16
1.88	12.39

Table 5.1: EDX data measured for samples textured at different laser fluences, giving the corresponding atomic percentages of oxygen.

silicon oxide layer due to surface oxidation in the course of laser processing in air ambient (an oxygen peak appears in the spectrum). We have also observed that the amount of oxidation increases with increase in the applied laser fluence, which signifies an enhancement in the absorption of atmospheric oxygen at higher laser fluences (Table 5.1). Besides, it is observed that both untreated as well as structured silicon surfaces contain carbon contaminants with surface concentration below 12-15%, possibly resulting from the surface incorporation of airborne hydrocarbons. In order to gain further insight into the valence states of the elements on the untreated and laser modified silicon surfaces, we carried out XPS measurements. The correction of the XPS spectra for charge accumulation is performed using C 1s peak (binding energy = 284.8 eV), which can be ascribed to adventitious carbon. The XPS spectra of Si 2p and O 1s are shown in

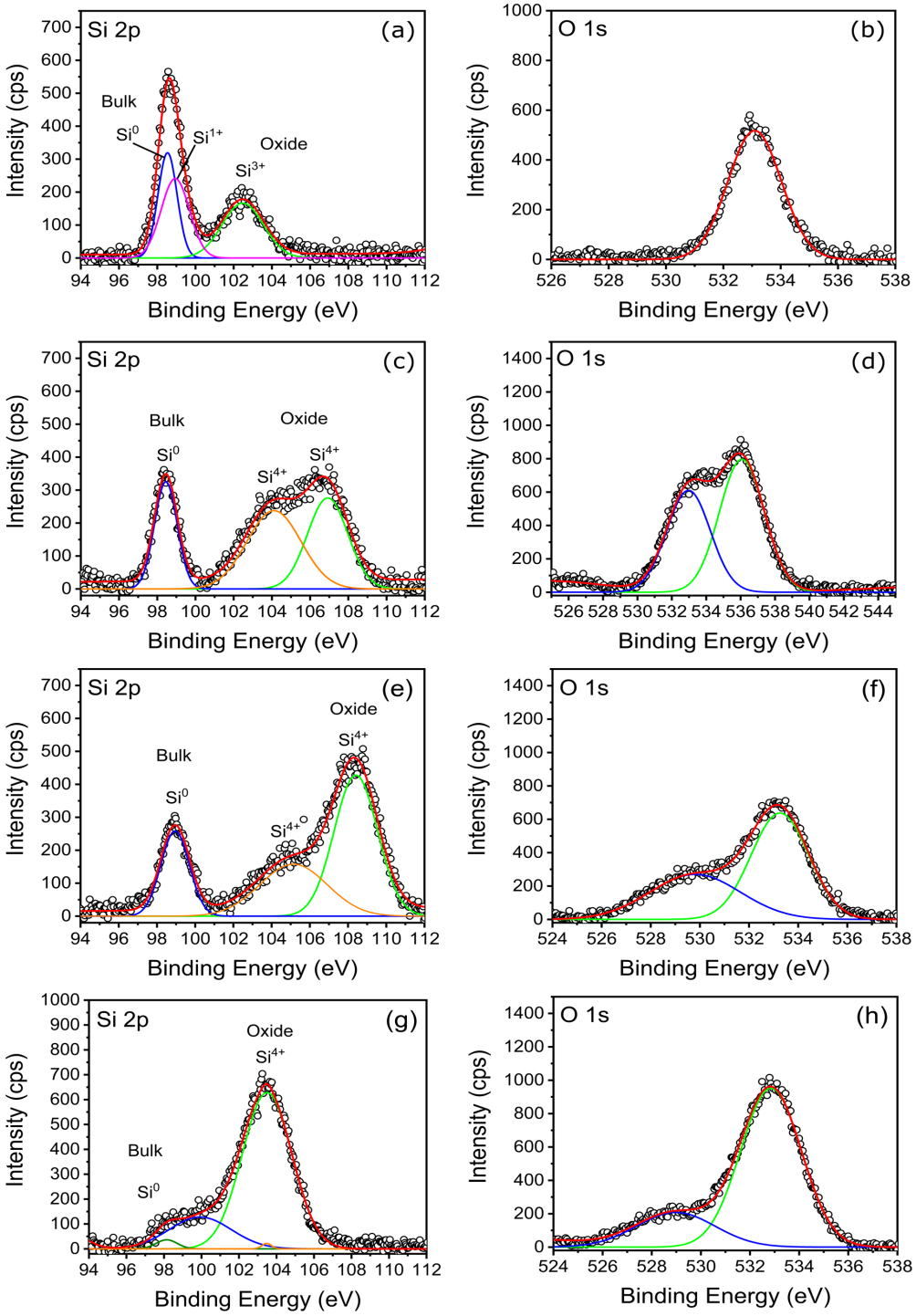

Figure 5.3: XPS data measured for the samples textured at different laser fluences. (a,b) untreated silicon, (c,d) F_p = 0.94 J/cm^2, (e,f) F_p=1.41 J/cm^2, and (g,h) F_p=1.88 J/cm^2. (a,c,e,g) show Si 2p peaks, and (b,d,f,h) show O 1s peaks. The spectra confirm the formation of silicon oxide.

Figures 5.3(a-h). For the untreated sample, Si 2p XPS peaks at 98.5 and 102.4 eV can be identified as those of Si^0p (unoxidized) and Si^{3+}2p (native oxide layer) [Figure 5.3(a)], respectively, while the peaks at 533.1 eV and 536 eV can be attributed to O 1s [Figure 5.3(b,d)]. Figures 5.3(c-h) show the XPS spectra of Si 2p and O 1s on the silicon surface measured after laser irradiation, at fluences F_p = 0.94 J/cm^2, F_p=1.41 J/cm^2, and F_p=1.88 J/cm^2, respectively.

The XPS spectra are fitted with Gaussian functions of the possible oxidized states (Si^{1+}(99.3 eV), Si^{2+}(100 eV), Si^{3+} (102.4), and Si^{4+}(104.2 eV and 106.0 eV) and the unoxidized state (Si^0-98.5 eV), in order to deconvolute the component peaks for each site type at its appropriate location, and the background has been removed by the Shirley subtraction method [42, 43]. Some intermediate oxidation states can also be present in very negligible amounts. Figure 5.3(c) indicates that most of the silicon atoms are oxidized to Si^{4+}(104.1 eV) and Si^{4+}(106.0 eV) which correspond to the Si-O-Si bond. Samples irradiated at higher fluences (shown in Figure 5.3(e,g)) exhibit higher oxidation indicated by an increase in the intensity of Si^{4+}(104.2 eV, 106.0 eV, and 108.0 eV). After laser irradiation the melted silicon gets solidified as the irradiated region cools down to room temperature. Along with this process most of the Si-O bonds of Si^{2+} and Si^{3+} become unstable and get converted to Si^{1+} by losing oxygen atoms, while some other Si–O bonds get changed to Si^{4+}(106 eV) upon receiving additional oxygen atoms [42].

5.4 Fabrication of permanent superhydrophilic silicon surface

Two models, given by Cassie–Baxter [44] and Wenzel et al. [45] respectively, have been proposed in the past to describe the effects of macroscopic surface roughness on the wettability of solid surfaces. For highly hydrophobic surfaces the Cassie-Baxter model is usually considered because the multiscale surface

morphology provides tiny air pockets, enhancing the hydrophobicity of the surface. On the other hand, hydrophilicity is best explained by the Wenzel model (homogeneous wetting). According to Wenzel's theory, wetting of surfaces that have a CA less than 90° can be improved by increasing the surface roughness. The relation between surface roughness and contact angle is given by,

$$cos\theta_w = rcos\theta_f \tag{5.3}$$

where θ_w and θ_f are the apparent (macroscopic) and Young (intrinsic) contact angles measured on rough and flat surfaces of the same material, respectively, and r is the roughness factor defined as the ratio between the actual and projected surface areas of the sample. The hydrophilic surface with contact angle less than 65° can be changed to a superhydrophilic surface by modulating r in the range of 1.2 to 2. Surfaces with higher contact angles can become surperhydrophilic by varying r from 2 to 6 [46].

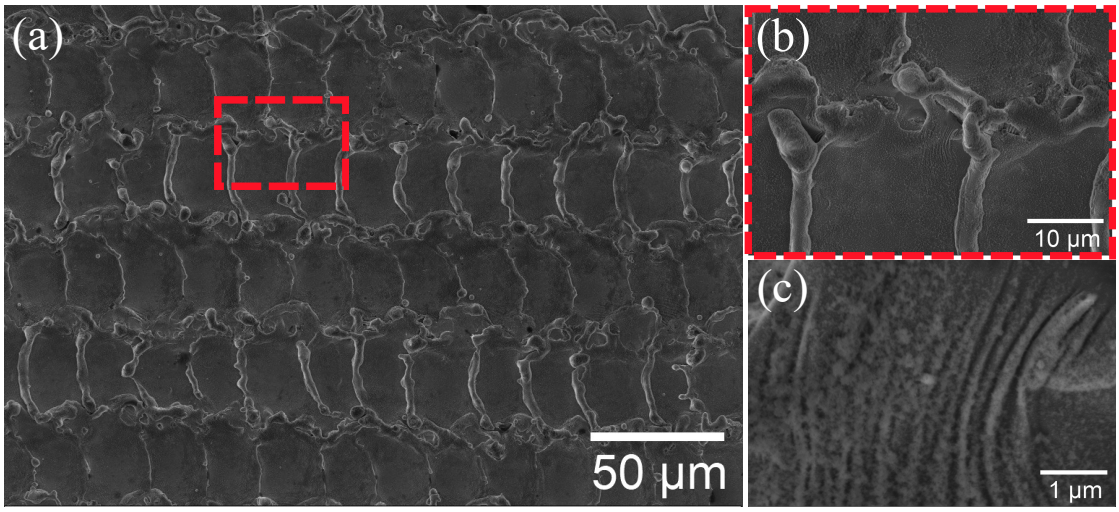

Figure 5.4: SEM images of silicon surface textured using laser pulses of peak fluence F_p = 1.41 J/cm^2, displaying morphological and wetting features. (a) parallel line scanning pattern, (b) zoomed view of the marked region, and (c) nano-capillaries along the edge of the irradiated spot.

When a drop of water is placed on a solid surface, if it gets flattened, the surface is hydrophilic (partial wetting), and if it spreads to cover the complete

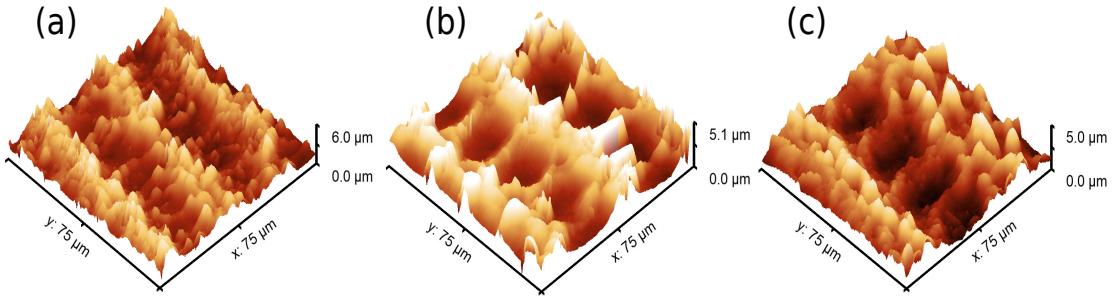

Figure 5.5: AFM images of silicon surfaces textured using 7 ns laser pulses at the laser fluence of (a) F_p = 0.94 J/cm^2 (mean roughness - 0.78 µm), (b) F_p = 1.41 J/cm^2 (mean roughness - 0.91 µm), and (c) F_p = 1.88 J/cm^2 (mean roughness - 0.70 µm).

solid surface (complete wetting), it is superhydrophilic. The term "superhydrophilic" was mentioned for the first time by Fujishima et al. [47], although the term "superwettable surface" was already introduced by Onda et al. [48]. The term superwettable typically refers to substrates in which the wetting characteristics are enhanced through the manipulation of substrate surface roughness. In the present work, the wetting properties of the silicon surface are modulated by writing parallel lines through a continuous bidirectional motion of the substrate along the horizontal direction, with the vertical shift optimized for 10 % overlap for creating uniform surface roughness. The scanning speed of v = 0.2 mm/sec is fixed for a maximum overlap of 40% along the horizontal scan direction. Large area surfaces (6×6 mm^2) are fabricated using three different peak laser fluences, F_p = 0.94 J/cm^2, 1.41 J/cm^2 and 1.88 J/cm^2, respectively.

SEM images of the large area surface textured at fluence F_p = 1.41 J/cm^2 show nano-capillaries around the edge of each laser-irradiated spot, along with nano-particles of silicon oxide decorated on the whole textured area [Figure 5.4]. The 3D morphology of the textured surface is also studied with the help of atomic force microscope (AFM). AFM images given in Figure 5.5 show that different applied fluences give rise to different mean roughnesses for the textured surface.

We have found that the mean surfaces roughness increases with the applied fluence initially, but when the fluence increases even further, it decreases.

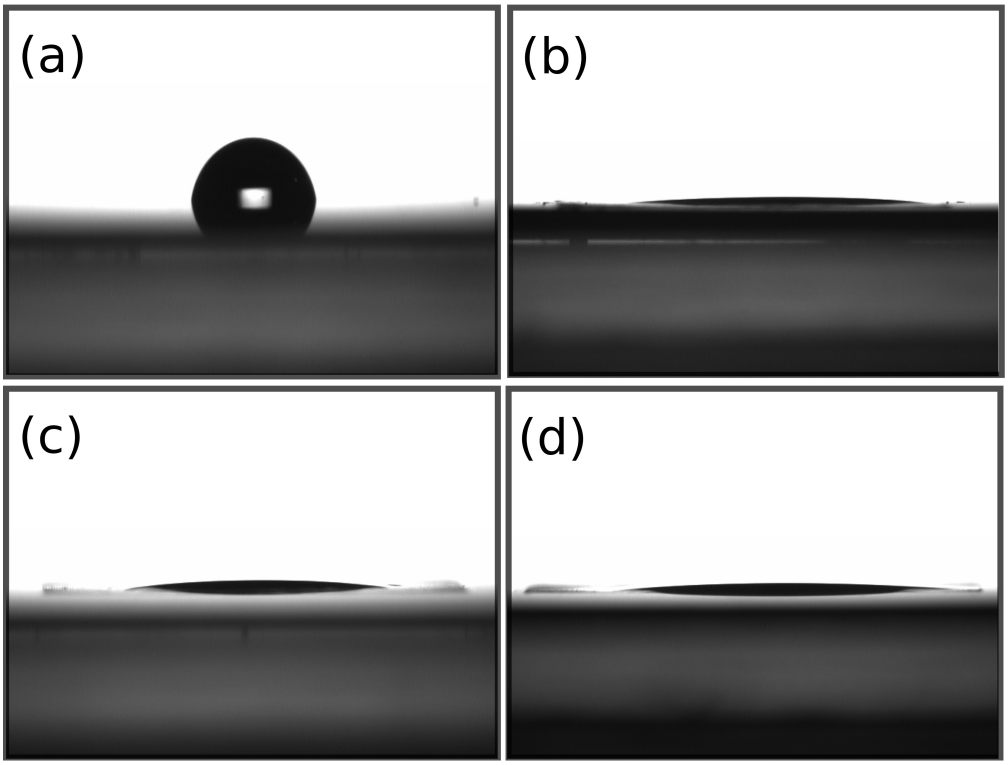

Figure 5.6: Photographs of distilled water $(1\mu L)$ droplets on textured silicon surfaces. (a) untreated silicon with CA = 80.9° ± 0.6°, (b)F_p = 0.94 J/cm^2 with CA = 5.4°± 0.6°, (c) F_p = 1.41 J/cm^2 with CA = 6.9° ± 0.5°, and (d) F_p = 1.88 J/cm^2 with CA = 4.9° ± 0.3°.

This could be the result of the accumulation of thermal energy leading to the formation of a pool of molten silicon, which forms nano-capillaries upon freezing. The modified wetting property of the structured silicon surfaces can be seen from Figure 5.6. These are optical images taken by using the contact angle meter. A distilled water droplet of volume 1µL is placed gently on the surface immediately after structuring with the help of an automated micro syringe, and the contact angle is measured by the sessile drop method. Microstructuring changes the contact angle from a wetting value of 80.9° ± 0.6° on flat silicon [Figure 5.6(a)] to a superhydrophilic value of about 5° ± 0.7° on the laser-microstructured surface [Figure 5.6(b,c,d)]. The variation of the mean surface roughness and contact angle as a function of applied peak fluence is shown in Figure 5.7. Each data point presented is the average value of three individ-

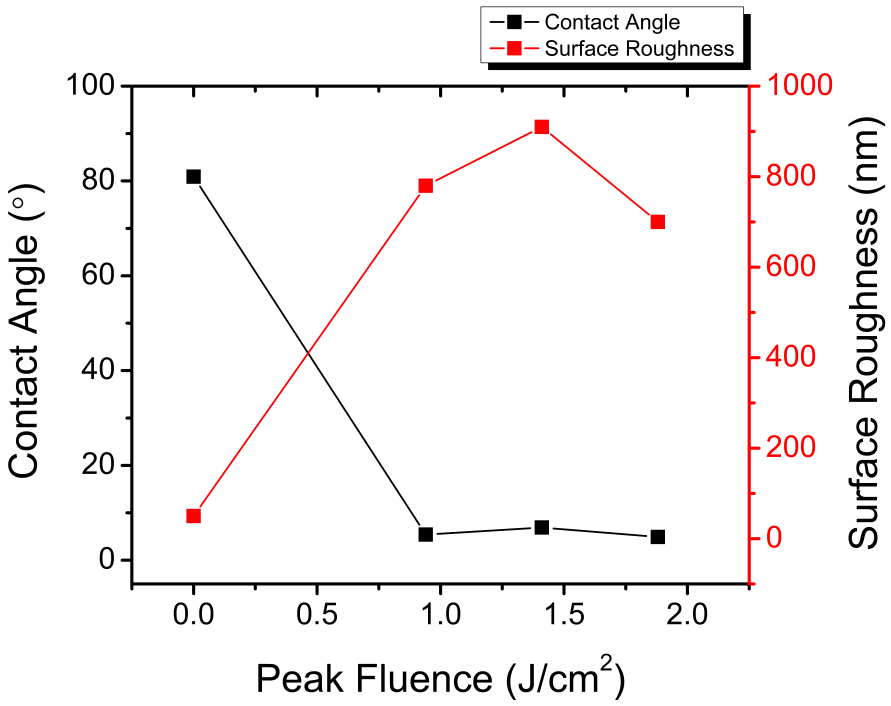

Figure 5.7: Variation of the wettability (contact angle) and mean surface roughness of micro-textured silicon surface as a function of the applied peak laser fluence.

ual measurements. The increase in the oxygen content of the surface at higher laser fluences, as shown in Table 5.1, in conjunction with the enhanced roughness, modulates the wettability of the textured surfaces. Beyond the fluence of 1 J/cm^2, mean surface roughness and contact angle do not vary much.

There are several reports describing the short-lived hydrophilic nature of laser micro-structured surfaces [49, 50]. When exposed to ambient conditions (e.g. atmospheric or specific ambient gas condition), the textured samples eventually transform to hydrophobic surfaces due to changes in the surface composition [51]. However, we found that this transformation does not happen for our samples. For instance, when we repeated the contact angle measurements after keeping the samples open to the atmosphere for 3 months, it was found that they continued to be in the superwetting state without losing the superhydrophilicity (Figure 5.8). This prolonged superhydrophilicity is attributed to two major factors. One is the presence of micro-channels and frozen nano-capillaries [Figure 5.4(b,c)] in the multi-scale (hierarchical) structure, and the

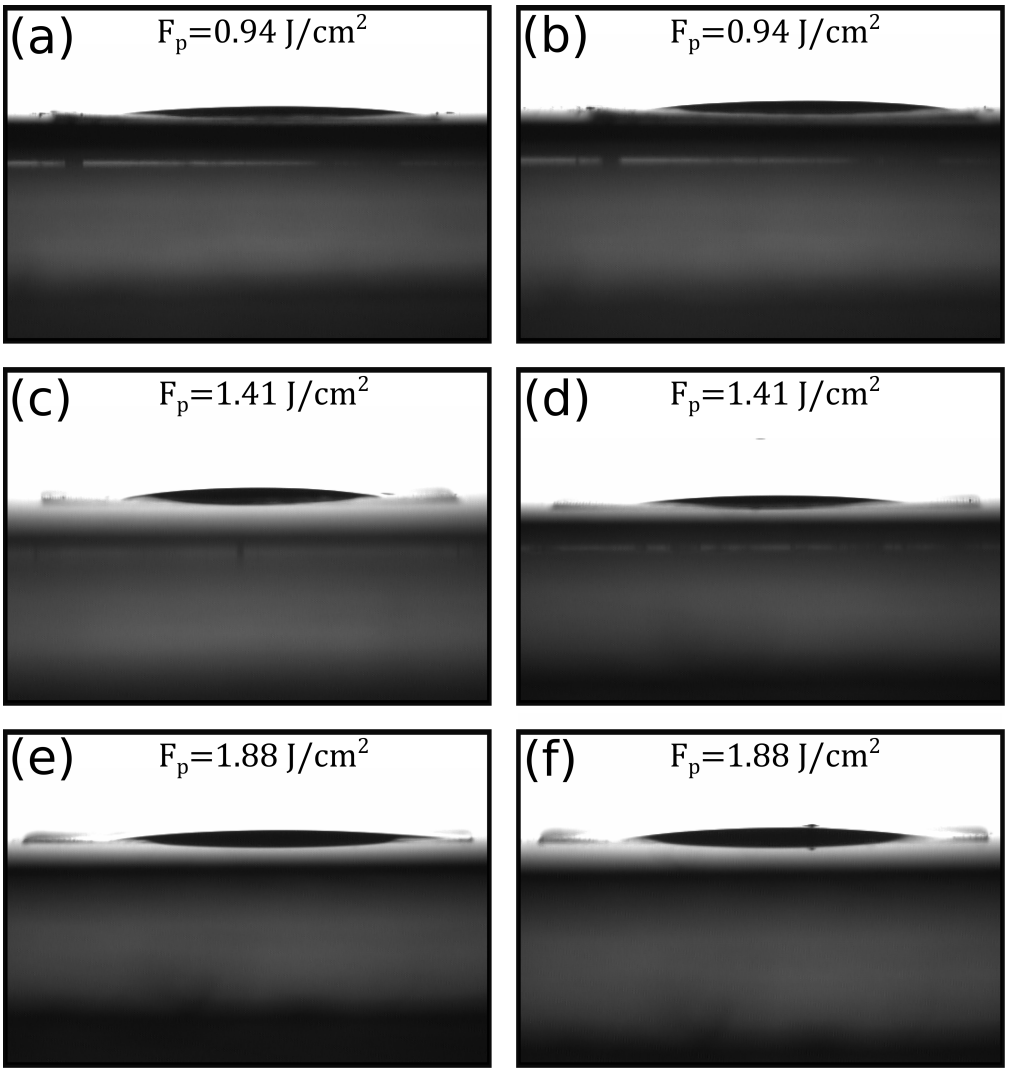

Figure 5.8: Photographs shown in the left panel are images of distilled water (1µL) droplets on silicon surfaces taken immediately after texturing (at different fluences). Photographs in the right panel are taken after keeping the sample in atmospheric conditions for three months. The long-lived superhydrophilicity of the samples is obvious from the images.

other is the presence of silica particle decoration on the micro-/nano-structures, which acts as a nano-foam. Due to the strong adhesion between water and the resulting superhydrophilic silica surface, water penetrates through the dust, debris, and other contaminants, ultimately serving as a blocking layer between the liquid contaminants (e.g., oil) and the surface. In other words, superhydrophilicity actually works better than superhydrophobicity when the contam-

ination is hydrophobic in nature. There are several potential applications for superhydrophilic silicon surfaces in devices such as heat-exchangers, biosensors, biochips, and self-cleaning solar cells [24].

5.5 Summary

Micro-/nano-textured silicon surfaces fabricated using nanosecond laser pulses have been investigated using SEM, AFM, EDX, XPS and contact angle measurements. The hierarchical structures obtained consist of microscale channels and self-organized surface nano-capillaries decorated with randomly distributed silicon nanoparticles. Concentric nano-ripples found around the crater rims show sub-wavelength spatial periodicity (50-100 nm) with silica nano-foam decoration on top. Silicon oxide is formed on the irradiated surface, with the atomic percentage of oxygen increasing with the laser fluence. These structures result in a durable superhydrophilic silicon surface (CA $\approx 5^{\circ}$), with the superhydrophilicity being stable even after being exposed to the atmosphere for about three months. The generalized Wenzel's equation describes the wetting behavior of these samples by taking into account homogeneous liquid penetration due to the formation of nano-capillaries and silica nano-foam. In short, this chapter demonstrates a direct-write, cost-effective and single-step method which does not need additional chemical processing for modifying the wettability of solid surfaces for multi-functional applications.

Bibliography

[1] V. Zorba, I. Alexandrou, I. Zergioti, A. Manousaki, C. Ducati, A. Neumeister, C. Fotakis, and G. A.J. Amaratunga. Laser microstructuring of Si surfaces for low-threshold field-electron emission. *Thin Solid Films*, 453-454:492–495, 2004.

[2] V. Zorba, P. Tzanetakis, C. Fotakis, E. Spanakis, E. Stratakis, D. G. Papazoglou, and I. Zergioti. Silicon electron emitters fabricated by ultraviolet laser pulses. *Applied Physics Letters*, 88(8):10–13, 2006.

[3] C. Wu, C. H. Crouch, L. Zhao, J. E. Carey, R. Younkin, J. A. Levinson, E. Mazur, R. M. Farrell, P. Gothoskar, and A. Karger. Near-unity below-band-gap absorption by microstructured silicon. *Applied Physics Letters*, 78(13):1850–1852, 2001.

[4] Yi Fan Huang, Surojit Chattopadhyay, Yi Jun Jen, Cheng Yu Peng, Tze An Liu, Yu Kuei Hsu, Ci Ling Pan, Hung Chun Lo, Chih Hsun Hsu, Yuan Huei Chang, Chih Shan Lee, Kuei Hsien Chen, and Li Chyong Chen. Improved broadband and quasi-omnidirectional anti-reflection properties with biomimetic silicon nanostructures. *Nature Nanotechnology*, 2(12):770–774, 2007.

[5] Anatoliy Y. Vorobyev and Chunlei Guo. Direct femtosecond laser surface nano/microstructuring and its applications. *Laser and Photonics Reviews*, 7(3):385–407, 2013.

[6] M. Barberoglou, V. Zorba, E. Stratakis, E. Spanakis, P. Tzanetakis, S. H. Anastasiadis, and C. Fotakis. Bio-inspired water repellent surfaces produced by ultrafast laser structuring of silicon. *Applied Surface Science*, 255(10):5425–5429, 2009.

[7] V. Zorba, L. Persano, D. Pisignano, A. Athanassiou, E. Stratakis, R. Cingolani, P. Tzanetakis, and C. Fotakis. Making silicon hydrophobic: Wettability control by two-lengthscale simultaneous patterning with femtosecond laser irradiation. *Nanotechnology*, 17(13):3234–3238, 2006.

[8] Yilun Li, Duy Xuan Luong, Jibo Zhang, Yash R. Tarkunde, Carter Kittrell, Franklin Sargunaraj, Yongsung Ji, Christopher J. Arnusch, and James M. Tour. Laser-Induced Graphene in Controlled Atmospheres: From Superhydrophilic to Superhydrophobic Surfaces. *Advanced Materials*, 29(27):1–8, 2017.

[9] Tianchi Chen, Hongtao Liu, Shuhua Teng, Wei Yan, Haifeng Yang, and Jiande Li. Water transport control on a patterned superhydrophobic surface via laser direct writing. *Journal of Vacuum Science & Technology A: Vacuum, Surfaces, and Films*, 34(6):061103, 2016.

[10] Mangirdas Malinauskas, Albertas Žukauskas, Satoshi Hasegawa, Yoshio Hayasaki, Vygantas Mizeikis, Ričardas Buividas, and Saulius Juodkazis. Ultrafast laser processing of materials: From science to industry, 2016.

[11] Henri Jansen, Meint De Boer, Rob Legtenberg, and Miko Elwenspoek. The black silicon method: A universal method for determining the parameter setting of a fluorine-based reactive ion etcher in deep silicon trench etching with profile control. *Journal of Micromechanics and Microengineering*, 5(2):115–120, 1995.

[12] Koji Sugioka and Ya Cheng. Ultrafast lasers-reliable tools for advanced materials processing. *Light: Science and Applications*, 3(390):1–12, 2014.

[13] A. Khakbaznejad, B. Chehroudi, and D. M. Brunette. Effects of titanium-coated micromachined grooved substrata on orienting layers of osteoblast-like cells and collagen fibers in culture. *Journal of Biomedical Materials Research - Part A*, 70(2):206–218, 2004.

[14] T. Young. Iii. an essay on the cohesion of fluids. *Philosophical Transactions of the Royal Society of London*, pages 65 – 87.

[15] Bharat Bhushan. Biomimetics: Lessons from Nature - an overview. *Philosophical Transactions of the Royal Society A: Mathematical, Physical and Engineering Sciences*, 367(1893):1445–1486, 2009.

[16] Zhiguang Guo and Weimin Liu. Biomimic from the superhydrophobic plant leaves in nature: Binary structure and unitary structure. *Plant Science*, 172(6):1103–1112, 2007.

[17] Huan Mei, Ding Luo, Peng Guo, Cheng Song, Chengcheng Liu, Yongmei Zheng, and Lei Jiang. Multi-level micro-/nanostructures of butterfly wings adapt at low temperature to water repellency. *Soft Matter*, 7(22):10569–10573, 2011.

[18] Kerstin Koch and Wilhelm Barthlott. Superhydrophobic and superhydrophilic plant surfaces: An inspiration for biomimetic materials. *Philosophical Transactions of the Royal Society A: Mathematical, Physical and Engineering Sciences*, 367(1893):1487–1509, 2009.

[19] Vassilia Zorba, Xiaobo Chen, and Samuel S. Mao. Superhydrophilic TiO2 surface without photocatalytic activation. *Applied Physics Letters*, 96(9):3–6, 2010.

[20] Jaroslaw Drelich and Abraham Marmur. Physics and applications of superhydrophobic and superhydrophilic surfaces and coatings. *Surface Innovations*, 2(4):211–227, 2014.

[21] Yongjin Wang and Xiao Gong. Special oleophobic and hydrophilic surfaces: approaches, mechanisms, and applications. *Journal of Materials Chemistry A*, 5(8):3759–3773, 2017.

[22] A. S. Surtaev, V. S. Serdyukov, and A. N. Pavlenko. Nanotechnologies for thermophysics: Heat transfer and crisis phenomena at boiling. *Nanotechnologies in Russia*, 11(11-12):696–715, 2016.

[23] Inseong You, Nayeon Yun, and Haeshin Lee. Surface-tension-confined microfluidics and their applications. *ChemPhysChem*, 14(3):471–481, 2013.

[24] P Shukla, D G Waugh, J Lawrence, and R Vilar. *10 - Laser surface structuring of ceramics, metals and polymers for biomedical applications: a review*. Elsevier Ltd, 2016.

[25] Jorge Padilla and Van P Carey. Water droplet vaporization on superhydrophilic nanostructured surfaces at high and low superheat. In *ASME International Mechanical Engineering Congress and Exposition*, volume 46569, page V08BT10A070. American Society of Mechanical Engineers, 2014.

[26] Zhi-Fu Zhou, Yan-Ke Lin, Hong-Lin Tang, Yu Fang, Bin Chen, and Ye-Chun Wang. Heat transfer enhancement due to surface modification in the close-loop r410a flash evaporation spray cooling. *International Journal of Heat and Mass Transfer*, 139:1047–1055, 2019.

[27] Md Mahamudur Rahman, Emre Olceroglu, and Matthew McCarthy. Role of wickability on the critical heat flux of structured superhydrophilic surfaces. *Langmuir*, 30(37):11225–11234, 2014.

[28] Beom Seok Kim, Hwanseong Lee, Sangwoo Shin, Geehong Choi, and Hyung Hee Cho. Interfacial wicking dynamics and its impact on critical heat flux of boiling heat transfer. *Applied Physics Letters*, 105(19):191601, 2014.

[29] An Zou and Shalabh C Maroo. Critical height of micro/nano structures for pool boiling heat transfer enhancement. *Applied Physics Letters*, 103(22):221602, 2013.

[30] Evangelos Skoulas, Alexandra Manousaki, Costas Fotakis, and Emmanuel Stratakis. Biomimetic surface structuring using cylindrical vector femtosecond laser beams. *Scientific Reports*, 7(February):1–11, 2017.

[31] A. Sandoval-Amador, Y. M. Bayona-Alvarez, H. Carreno Garcia, P. Escobar-Rivero, and D. Y. Pena-Ballesteros. HOS cell adhesion on Ti6Al4V ELI texturized by CO 2 laser. *Journal of Physics: Conference Series*, 935(1), 2017.

[32] Yong Jee, Michael F. Becker, and Rodger M. Walser. Laser-induced damage on single-crystal metal surfaces. *Journal of the Optical Society of America B*, 5(3):648, 1988.

[33] C Momma, S Nolte, B. Chichkov, A. Tuennermann, and F. von Alvensleben. Precise laser ablation with ultra-short pulses. In *Conference on Lasers and Electro-Optics Europe - Technical Digest*, page 318, 1996.

[34] E. G. Gamaly, A. V. Rode, B. Luther-Davies, and V. T. Tikhonchuk. Ablation of solids by femtosecond lasers: Ablation mechanism and ablation thresholds for metals and dielectrics. *Physics of Plasmas*, 9(3):949–957, 2002.

[35] M. S. Trtica, B. M. Gakovic, B. B. Radak, D. Batani, T. Desai, and M. Bussoli. Periodic surface structures on crystalline silicon created by 532 nm picosecond Nd:YAG laser pulses. *Applied Surface Science*, 254(5):1377–1381, 2007.

[36] C. H. Crouch, J. E. Carey, J. M. Warrender, M. J. Aziz, E. Mazur, and F. Y. Génin. Comparison of structure and properties of femtosecond and nanosecond laser-structured silicon. *Applied Physics Letters*, 84(11):1850–1852, 2004.

[37] A. Y. Vorobyev and Chunlei Guo. Laser turns silicon superwicking. *Optics Express*, 18(7):6455, 2010.

[38] Anne-Marie Kietzig, Mehr Negar Mirvakili, Saeid Kamal, Peter Englezos, and Savvas G Hatzikiriakos. Laser-patterned super-hydrophobic pure metallic substrates: Cassie to wenzel wetting transitions. *Journal of Adhesion Science and Technology*, 25(20):2789–2809, 2011.

[39] J. M. Liu. Simple technique for measurements of pulsed Gaussian-beam spot sizes. *Optics Letters*, 7(5):196, 1982.

[40] Jiale Yong, Qing Yang, Chunlei Guo, Feng Chen, and Xun Hou. A review of femtosecond laser-structured superhydrophobic or underwater superoleophobic porous surfaces/materials for efficient oil/water separation. *RSC advances*, 9(22):12470–12495, 2019.

[41] J. Krüger, M. Lenzner, S. Martin, M. Lenner, C. Spielmann, A. Fiedler, and W. Kautek. Single- and multi-pulse femtosecond laser ablation of optical filter materials. *Applied Surface Science*, 208-209(1):233–237, 2003.

[42] Xue-Qing Liu, Lei Yu, Zhuo-Chen Ma, and Qi-Dai Chen. Silicon three-dimensional structures fabricated by femtosecond laser modification with dry etching. *Applied Optics*, 56(8):2157–2161, 2017.

[43] Da Chen and Shihua Huang. Effect of oxygen-doping concentration on electrical properties of silicon oxycarbide films for memory application. *Journal of Micro/Nanolithography, MEMS, and MOEMS*, 15(3):035005, 2016.

[44] B D Cassie, A. B. D. Cassie, and S. Baxter. Of porous surfaces,. *Transactions of the Faraday Society*, 40(5):546–551, 1944.

[45] Robert N. Wenzel. Resistance of solid surfaces to wetting by water. *Industrial and Engineering Chemistry*, 28(8):988–994, 1936.

[46] Jaroslaw Drelich and Emil Chibowski. Superhydrophilic and superwetting surfaces: definition and mechanisms of control. *Langmuir*, 26(24):18621–18623, 2010.

[47] M Machida, K Norimoto, T Watanabe, K. Hashimoto, and A. Fujishima. Effect of SiO2 addition in super-hydrophilic property of TiO2 photocatalyst. *Journal of Materials Science*, 34(11):2569–2574, 1999.

[48] T. Onda, S. Shibuichi, N. Satoh, and K. Tsujii. Super-water-repellent fractal surfaces. *Langmuir*, 12(9):5–7, 1996.

[49] Duong V Ta, Andrew Dunn, Thomas J Wasley, Robert W Kay, Jonathan Stringer, Patrick J Smith, Colm Connaughton, and Jonathan D Shephard. Nanosecond laser textured superhydrophobic metallic surfaces and their chemical sensing applications. *Applied Surface Science*, 357:248–254, 2015.

[50] Anne-Marie Kietzig, Savvas G Hatzikiriakos, and Peter Englezos. Patterned superhydrophobic metallic surfaces. *Langmuir*, 25(8):4821–4827, 2009.

[51] Van Duong Ta, Andrew Dunn, Thomas J. Wasley, Ji Li, Robert W. Kay, Jonathan Stringer, Patrick J. Smith, Emre Esenturk, Colm Connaughton, and Jonathan D. Shephard. Laser textured surface gradients. *Applied Surface Science*, 371:583–589, 2016.

Chapter 6

Fabrication of silicon micro-needles using femtosecond optical vortex beams

This chapter discusses surface structuring of silicon (100) using fs optical vortex (OV) beams, which are generated by employing a spiral phase plate (SP-plate) having topological charge $\ell = 4$. OV beams with linear and circular states of polarization (SoP) in the transverse plane are employed to generate interesting surface features. Loosely focused OV beams (with linear as well as circular SoP) generate patterns consisting of ripples and grooves whereas tightly focused OV beams produce micro-pillars. The application of a silicon surface patterned with arrays of micro-pillars as a SERS substrate to detect a low concentration (10^{-5} M) of the dye rhodamine 6G is demonstrated.

6.1 Introduction

The degrees of freedom of light, such as its polarization, frequency, and spatial modes, play a crucial role in laser induced-surface structuring. The previous chapters illustrated the unique capabilities of laser surface texturing in fabricating hierarchical micro-/nano-structures at nano-/micro-scales on silicon and

fused silica by employing fs and ns pulses having Gaussian spatial intensity profiles. The experimental findings demonstrate that the properties of the irradiating beam, such as polarization, spatial intensity distribution, number of pulses and laser fluence, have direct effect on surface structuring and related processes. In recent years, structured light having unconventional beam shapes have been employed in research fields as diverse as biophysics [1–3], micromechanics [4] or microfluidics [5], super high-density optical data storage [6], imaging, and metrology [7–10]. These include Bessel, Laguerre-Gaussian, Airy, and in particular optical vortex (OV) beams. An OV beam can be described as a spatially structured beam having a donut-shaped (annular) intensity profile, caused by the helical nature of its wave-front, advancing along the direction of propagation [11, 12]. The phase of the beam varies in a corkscrew-like manner around its propagation axis creating a phase singularity that is characterized by a $2\ell\pi$ azimuthal phase (here ℓ is termed as topological charge). The topological charge gives rise to an orbital angular momentum (OAM) $\mathcal{L} = \ell\hbar$ per photon where ℓ corresponds to the number of twists in the helical wave-front in one wavelength of propagation. The topological charge can be negative or positive depending on the handedness (chirality) of the helical structure. The higher the number of twists, the faster the light spins around its axis of propagation. OV beams can also carry spin angular momentum (SAM) $\mathcal{S} = s\hbar$ per photon which is associated with the spin of the transverse electric field giving rise to circular polarization, with helicity values of $s = \pm 1$ corresponding to left and right circular polarizations, respectively. Because of their unique properties, applications employing OV beams have attracted a great deal of research interest ranging from surface structuring [13–17] to free-space communications [18, 19].

When compared to the typical Gaussian beam profile, the distinctive spatial profile and the OAM associated with the OV beam presents the possibility for generating various complex surface structures [16, 20–22]. OV beams carrying OAM $\ell = 1$ exhibit two general types of polarization configuration (Radial,

and Azimuthal). The experimental findings reported by R. Dorn et al. [23] show that under tight focusing conditions, radial/azimuthal polarized OV beams can generate/hinder a strong longitudinal electric field, which in turn influences the shape of the focal spot. They have reported that radial SoP results in sharper focus with a spot size of 0.16 λ^2, providing maximum intensity at the focal plane, compared to the larger spot size of 0.26 λ^2 achieved with linear SoP. In contrast, an OV beam with azimuthal SoP has no longitudinal field component, which facilitates precise nanostructuring for donut-shaped annular structure fabrication.

OV beams have indeed attracted substantial of research interest in the fields of materials processing and surface functionalization owing to their numerous advantages. In the last decade, there has been a great advancement in laser ablation using OV beams, which has proved their capabilities for fs laser surface texturing. For example, C. Hnatovsky et al. [13, 24] have employed OV beams to generate micrometer-size ring-shaped structures on silicon and fused silica. Other experimental findings using ns laser pulses in materials such as stainless steel, brass and copper demonstrate that both azimuthal and radial polarizations are better for drilling fine deep holes, when compared to conventional beams having linear or circular polarizations [25]. Researchers from the University of Naples have explored the influence of SoP and OAM on laser ablation with fs OV laser beams [26–29]. They have also investigated direct fs laser surface structuring under loose focusing conditions with generalized vector beams, which are realized by electrically tuning the optical retardation of a q-plate with $q = +1/2$. However, under tight focusing conditions, fs-ablation using the annular laser beam depends on the SoP, which becomes more definite close to the ablation threshold of the material [24].

Toyoda and coworkers have discussed the twisting effect happening on metal surfaces due to ablation with an OV beam. Here, chiral nanoneedles are formed because of helicity transfer from the optical vortex to the melted

material. They have also shown that the chirality of the nanoneedles can be controlled by changing the helicity of the optical vortex [16, 17]. Another work done by Takahashi et al. using OV beams of ps duration has reported the formation of a mono-crystalline silicon needle recrystallized by laser ablation [30]. They have also achieved an enhancement in the height of the needle by applying multiple vortex pulses on the target, resulting in a needle height of approximately 40 µm after 12 consecutive pulses. Recently, Omatsu and group have demonstrated the transformation of twisted nanoneedles on aluminium into non-twisted microneedles, upon ablation with multiple overlaid OV pulses [31]. They have also found that the OAM of an optical vortex field can twist high viscosity (4 Pa.s) donor materials to form micron-scale 'spin jets'. This could enable the development of next generation printed photonic/electric/spintronic circuits using ultrahigh viscosity donor dots containing functional nanoparticles, via the optical vortex laser induced forward mass transfer (OV-LIFT) patterning technique. In another work reported by Yoo et al. [32], an effective collection of molten silicon in the beam center is illustrated. Here a nanodome of significantly increased height is created via the thermocapillarity induced dewetting process, when the donut-shaped laser beam interacts with an amorphous silicon film deposited over a fused silica substrate. A phase transformation from amorphous to crystalline silicon occurs due to the fast melting and re-solidification process. Syubaev et al. [33] have demonstrated direct ns-laser printing of chiral silver nanoneedles by employing zero-OAM ($\ell = 0$) spiral beams with variable intensity profiles, and also perfect optical vortex (POV) beams having fixed donut-shaped intensity pattern and variable topological charge. Moreover, in a recent theoretical and experimental work, Tsibidis et al. have investigated the surface profile and ripple periodicity of irradiated Ni with radially polarized fs laser pulses, demonstrating that the incident beam polarization has a significant influence on both the morphological profile and size of the produced structures [34].

This chapter reports experimental findings of surface structures produced on crystalline silicon(100) samples upon laser ablation under atmospheric conditions, by employing a fs OV beams carrying definite OAM. The ring-shaped intensity profile and controllable polarization of the OV beam make it possible to generate various complex surface textures, which are not possible if a Gaussian beam profile is used. In order to achieve an accurate and reliable determination of the OV beam properties, a detailed understanding of the threshold fluences for ablation and the effects of different SoP in the formation of the various surface features is required. We have used an OV beam having different SoP, generated by using a spiral phase plate with $\ell = 4$, for carrying out the structuring work reported in this chapter. Under loose focusing conditions fs OV beams are found to generate sub-wavelength scale ripples and grooves, which are influenced by the SoP of the incident beam. In contrast, under tight focusing conditions, the OV beam generates micro needle-like structures on the surface.

6.2 Experimental details

The schematic of the experimental setup is shown in Figure 2.8. The irradiation source is a regeneratively amplified mode-locked Ti: Sapphire laser system (`TSA-10`), delivering linearly polarized ultrashort laser pulses (pulse duration $\tau \approx 100$ fs, central wavelength $\lambda \approx 800$ nm) at a repetition rate of 10 Hz. The energy of the laser pulses is controlled by using an assembly of a half-wave plate and a polarizing cube beam splitter. The Gaussian beam output from the laser is converted into an anti-clockwise optical vortex beam with topological charge $\ell = 4$, by employing a fused silica spiral phase plate (`SP-plate, Holo/Or Ltd, VL-218-1-Y-A`) which provides an azimuthal phase of $2\ell\pi$. Additionally, we insert a quarter-wave plate before the SP-plate, which enables the constructive addition of the spin angular momentum associated with the

circular polarization of the OV beam. The OV beam is focused onto the silicon sample using a plano-convex lens of F_L = 10 cm focal length, and an objective lens (RMS10x-PF) of numerical aperture (N.A. = 0.30), for loose and tight focusing of the beam, respectively. The number of pulses N falling on the target is controlled by an electro-mechanical shutter which is synchronized with the 'Q-switch Out' signal provided by the Nd:YAG laser pumping the TSA-10.

The morphology of the textured silicon surface is examined by using a scanning electron microscope (SEM). To understand the chemical changes occurring due to laser irradiation, the chemical composition of the surface is investigated before and after irradiation by energy-dispersive X-ray (EDX) measurements. The sample textured with arrays of microneedles is sputtered with gold (Au) to get a thin 50 nm Au film, and then annealed at a temperature of 400° C for 2 hours. For performing SERS measurements, Rhodamine 6G (R6G) dye solutions of different molar concentrations are prepared by sequential dilution in ethanol. 2 µL volume of the dye solution is then drop-casted on the substrates consisting microneedles, which are then air dried at room temperature. SERS spectra of R6G molecules on the substrates have been recorded using a Raman spectrometer (Jobin-Yvon T64000) at 633 nm excitation wavelength. Static contact angle measurements are performed to understand the effect of fs laser irradiation on the wetting properties of the sample by an automated contact angle meter (DM 501, Kyowa Japan), using the sessile drop method. A distilled water droplet of 1 µL volume is gently positioned on the surface using a microsyringe, and images are captured to measure the angle formed at the solid-liquid interface.

6.3 Generation of the OV beam

Optical vortex beams can be obtained by imposing a spiral phase distribution onto the input beam. There are various methods to generate OV beams carrying

OAM such as astigmatic lens converter, computer generated fork hologram [35], spatial light modulator (SLM) [36], Q-plates [37, 38] and spiral phase plate [39]. In our experiment, we have used spiral phase plate of topological charge $\ell = 4$. A spiral phase plate (SP-plate) is a light-transmitting plane-parallel plate, one side of which is a staircase kind of relief. This increasing thickness of the SP-plate introduces a phase retardation which is proportional to the azimuthal angle around a point in the middle of the plate. When an input beam is passed through an SP-plate it acquires a helical wavefront due to the variable phase retardation. The transmission function of an ideal SP-plate is described by the equation

$$T(r,\phi) = \exp\{i\ell\phi\} circ\left(\frac{r}{R}\right) \tag{6.1}$$

where (r, ϕ) are the polar coordinates in the SPP plane at $z = 0$, z is the optical axis, R is the radius of the SP-plate, and $\ell = \pm 1, \pm 2, ...$ is the topological charge.

6.4 Surface structuring with OV beams

Beam polarization is an intrinsic and crucial parameter which presents novel and fascinating surface features in fs laser material processing. With the help of the OV beam, we can produce numerous complex polarization dependent structures with single and multi-pulse ablation. When we vary the SoP of the input beam (such as horizontal, vertical, and circular) falling on the SP-plate, we see that the output OV beam also exhibits different SoP. In this section, we discuss the effect of SoP and irradiation dose (number of pulses, N) falling on the sample under loose focusing condition, i.e., with a plano-convex lens of focal length $f_L = 10$ cm placed in the beam path. Figures 6.1 and 6.2 show SEM micrographs of the area structured with horizontally and vertically polarized OV beams with incident pulse energy E=100 μJ, and different number of pulses N = 5, 20, 50, 100, and 200.

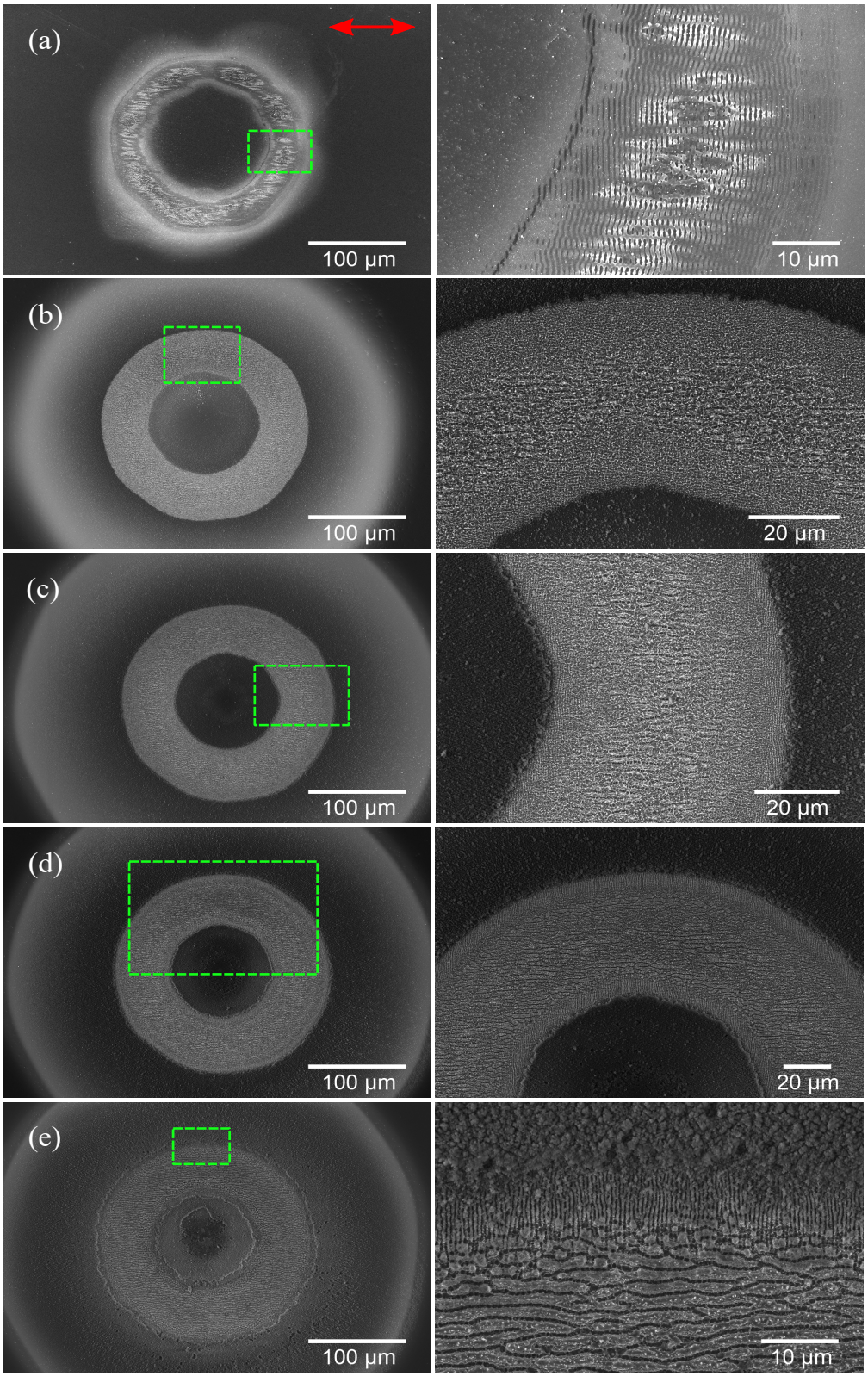

Figure 6.1: SEM micrographs of the ablated area irradiated with incident pulse energy E = 100 µJ: (a) N = 5, (b) N = 20, (c) N = 20, (c) N = 50, (d) N = 80, (e) N = 100, (f) N = 200. The red arrow in (a) shows the SoP of the incident OV beam.

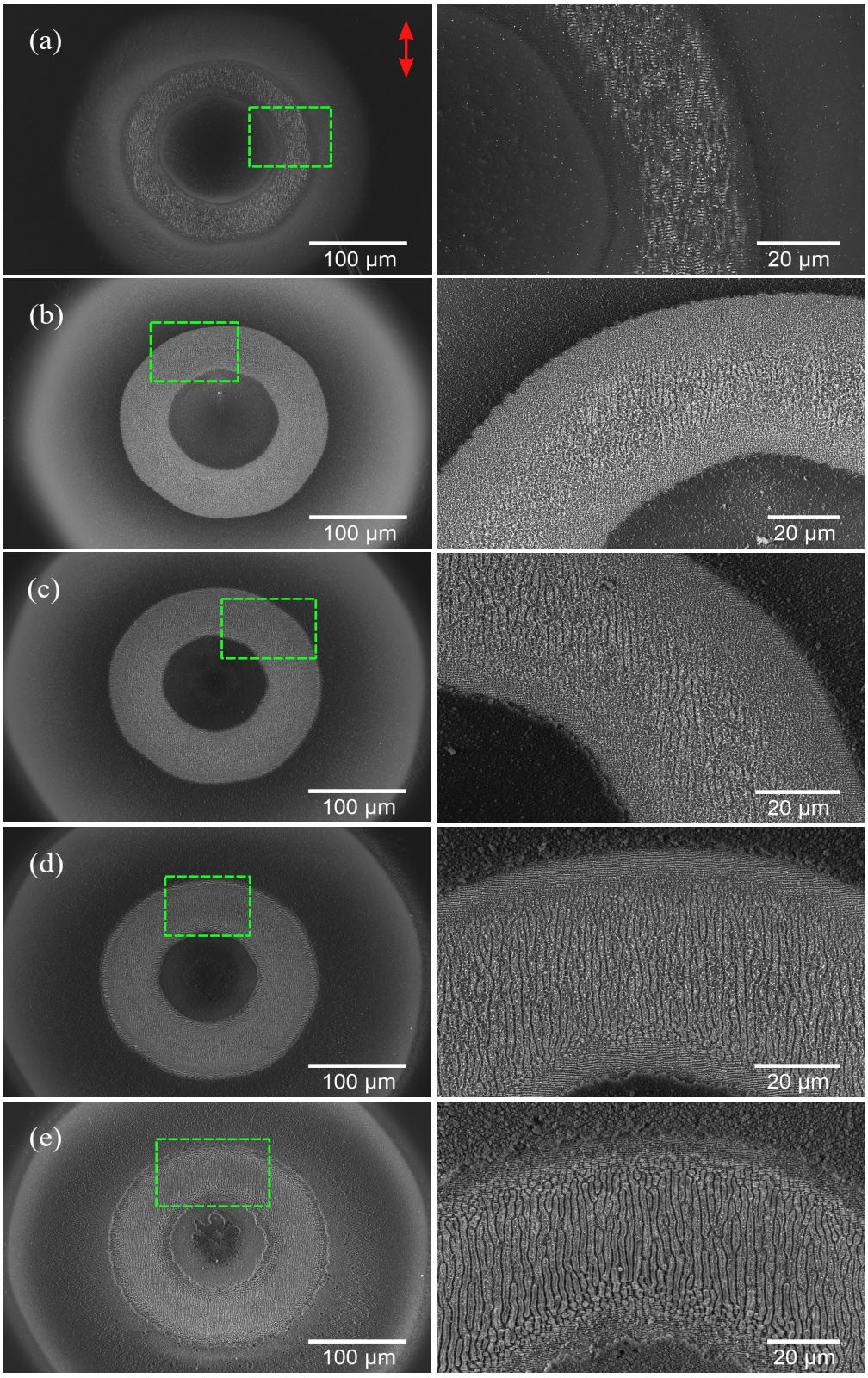

Figure 6.2: SEM micrographs of the ablated area irradiated with incident pulse energy E = 100 µJ: (a) N = 5, (b) N = 20, (c) N = 20, (c) N = 50, (d) N = 80, (e) N = 100, (f) N = 200. The red arrow in (a) shows the SoP of the incident OV beam.

The left column of Figure 6.1 illustrates changes in surface features with increasing number of pulses, and the right column presents zoomed views of the areas marked by green dashed boxes in the corresponding left column. Similarly, Figure 6.3 shows SEM micrographs of areas structured with OV beams having circular SoP, with incident pulses of energy E=100 µJ, and different number of pulses N = 5, 20, 50, 100, and 200.

The irradiated surface presents well oriented annular regions containing different surface morphologies. Due to the near-zero intensity at the center of the OV beam, the center area remains unaffected upon irradiation. However, the inner non-irradiated region consists of a large number of nanoparticles, which increases with the increase of the number of pulses. Moreover, another layer of nanoparticles also is visible beyond the external radius of the OV beam. This suggests that a random deposition of nanoparticles is favored in the region where local fluence is lower than the ablation threshold (visible in the internal and external areas of the OV beam). Evidently, the ablated annular region exhibits ripples as well (also termed as LSFL), which are preferentially oriented normal to the local beam polarization (see zoomed views of Figures 6.1(a) and 6.2(a) which correspond to N = 5). In the case of multi-pulse ablation with N $>$ 5, the transformation from LSFL to grooves occurs, which becomes significant at N $\geq$ 100. These micron-sized grooves are preferentially aligned parallel to the local beam polarization. With increasing irradiation dose, the grooves tend to cover the major part of the annular region as shown in Figures 6.1 and 6.2(d-e). This grooved region is found to be surrounded by two adjacent, narrow ring-shaped areas (in both internal and external peripheries) with the characteristic sub-wavelength ripples having an orientation normal to the local beam polarization. Furthermore, ablation with OV beam having circular SoP exhibits surface features which are different from those observed for ablation with OV beam having linear SoP.

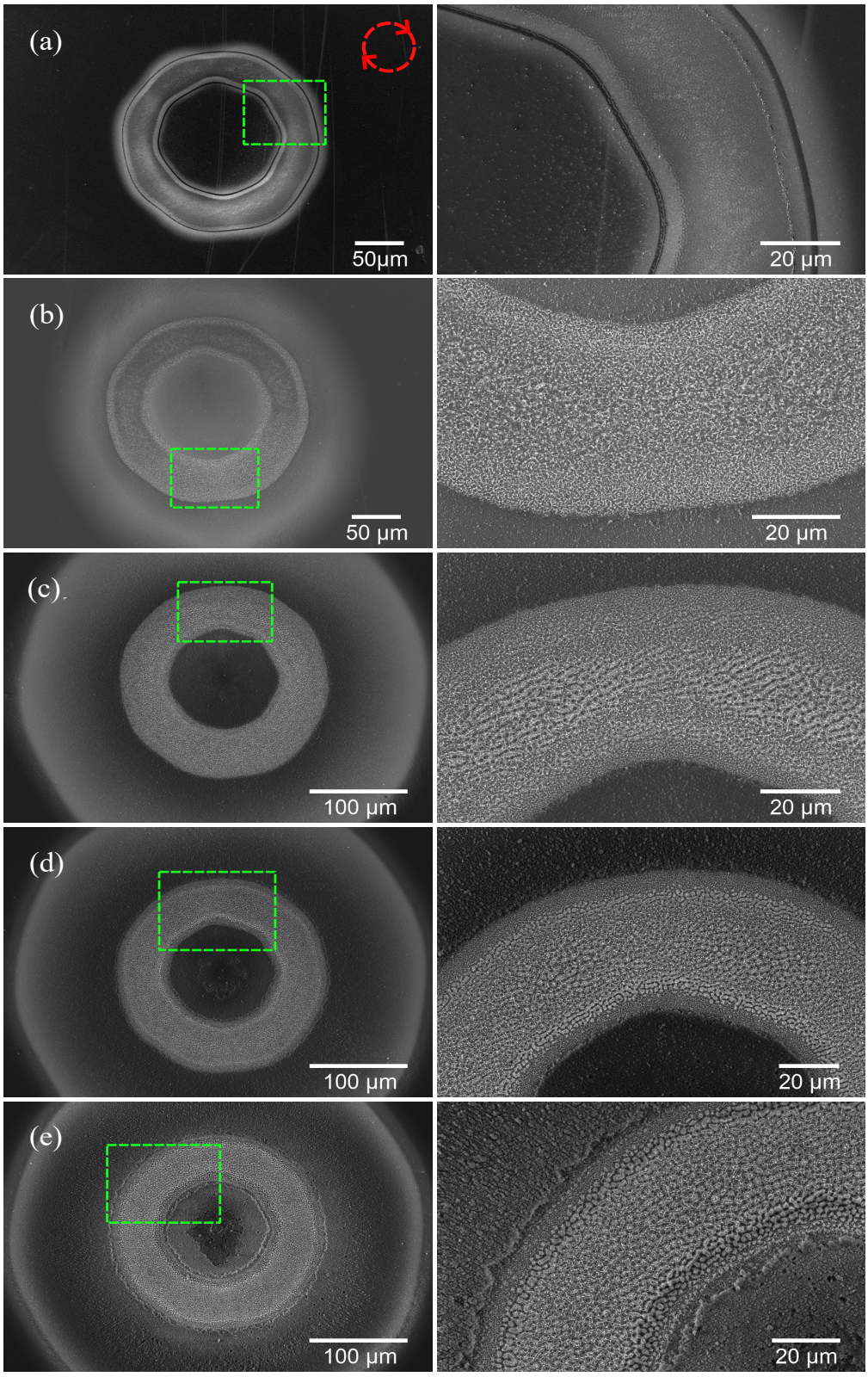

Figure 6.3: SEM micrographs of the ablated area irradiated with incident pulse energy E = 100 µJ: (a) N = 5, (b) N = 20, (c) N = 20, (c) N = 50, (d) N = 80, (e) N = 100, (f) N = 200. The red arrow in (a) shows the SoP of the incident OV beam.

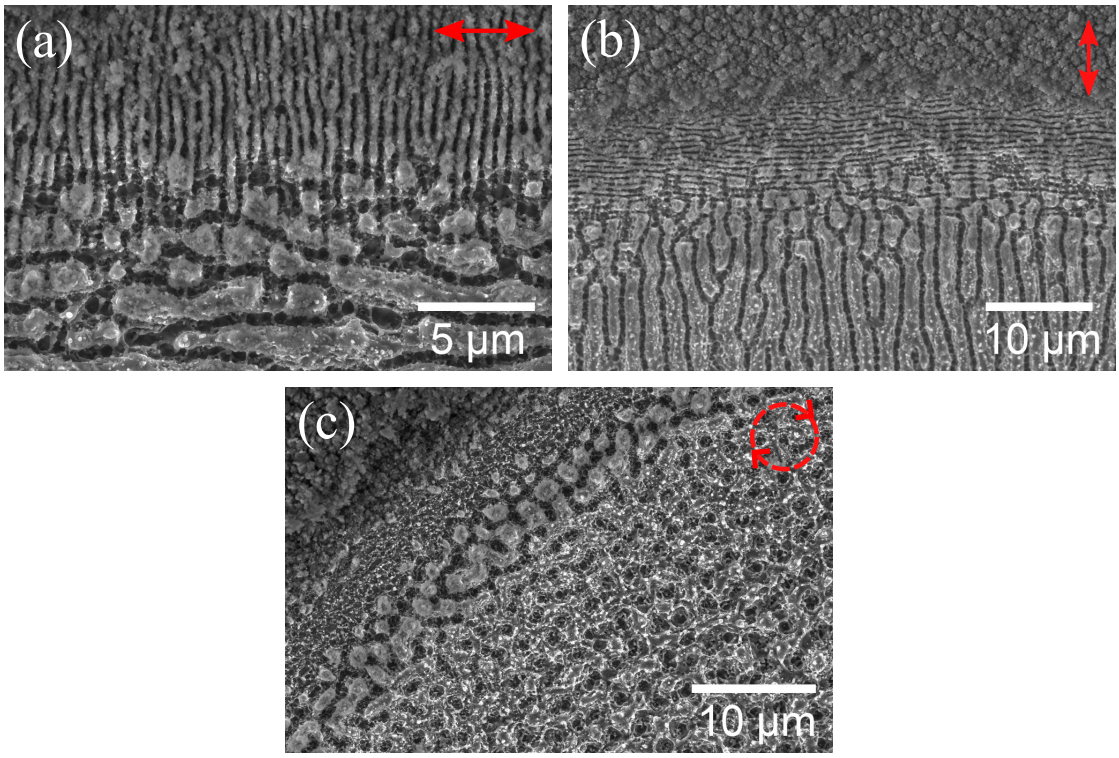

Figure 6.4: SEM micrographs presents the zoomed view of the ablated area irradiated with incident pulse energy E = 100 µJ and number of pulses N = 200 having (a) horizontal, (b) vertical, and (c) circular SoP of the incident OV beam.

OV beam with circular SoP leads to the generation of disordered, random surface structures with many intersections and bifurcations resulting in single nano-pores and ripples (as shown in Figure 6.3). These results are in agreement with previously reported results describing the polarization dependent generation of LIPSS on metals and semiconductors [40, 41]. In the case of N = 5, the annular region contains localized hotspots around which short-length ripples are generated. With increasing N these features get wiped out by the disordered rough textures. However, with N = 50, short range grooves ($\approx$ 15 µm) covered with nano-pores (as shown in Figure 6.3(c)) are formed. These short range grooves start disappearing due to prominent bifurcations and intersections upon ablation with a higher number of pulses (see Figure 6.3(d,e)). When $N \geq 100$ the annular region becomes completely covered with nano-pores surrounded by two adjacent, narrow ring-shaped areas (in both internal and

external peripheries) consisting of disordered rough surfaces as in the case of N = 20. Figure 6.4 presents the SEM micrographs illustrating the peculiar features generated upon irradiation by OV beams having different SoP (shown by red arrows in the micrographs) with incident pulse energy E = 100 µJ, number of pulses N = 200. Another noticeable difference between the structures created using linear and circular SoP is the amount of nano-particle generation and deposition in both internal and external peripheral regions. Nanoparticle deposition is slightly higher in the case of circular SoP, and the orientation of the patterns is relatively random when compare to linear SoP [40].

6.4.1 Optimization of micro-needle formation

This section demonstrates fs-structuring employing OV beam under tight focusing conditions, i.e., by using an objective lens (RMS10x-PF) of numerical aperture (N.A.) 0.30. The purpose of tight focusing is the fabrication of uniquely structured silicon substrates (in particular Si micro-needles) which have potential scientific and industrial applications. We employ fs OV beams with linear as well as circular SoP to understand the role of local beam polarization in the formation of the micro-needles. We also investigate the effect of single and multiple fs OV beam ablation under tight focusing condition to understand the surface morphology. Figure 6.5 shows SEM micrographs of the ablated area irradiated with horizontally polarized fs OV beam with pulse energy E = 15 µJ, and different number of pulses (N) ranging from 5 to 200. LSFL with period ≈ 750 nm aligned normal to the local beam polarization is observed in the case of N = 5. When N increases to 10, grooves start covering up the LSFL, and the presence of LSFL becomes limited to the low fluence area (for both internal and external narrow peripheries). With further increase of N to 20, the inner area adjacent to the narrow ring shows melting, and the surrounding annular region gets covered by grooves of spatial period $\approx$ 2.2 µm. When N = 50 supra-grooves appear in the inner region adjacent the narrow ring containing LSFL.

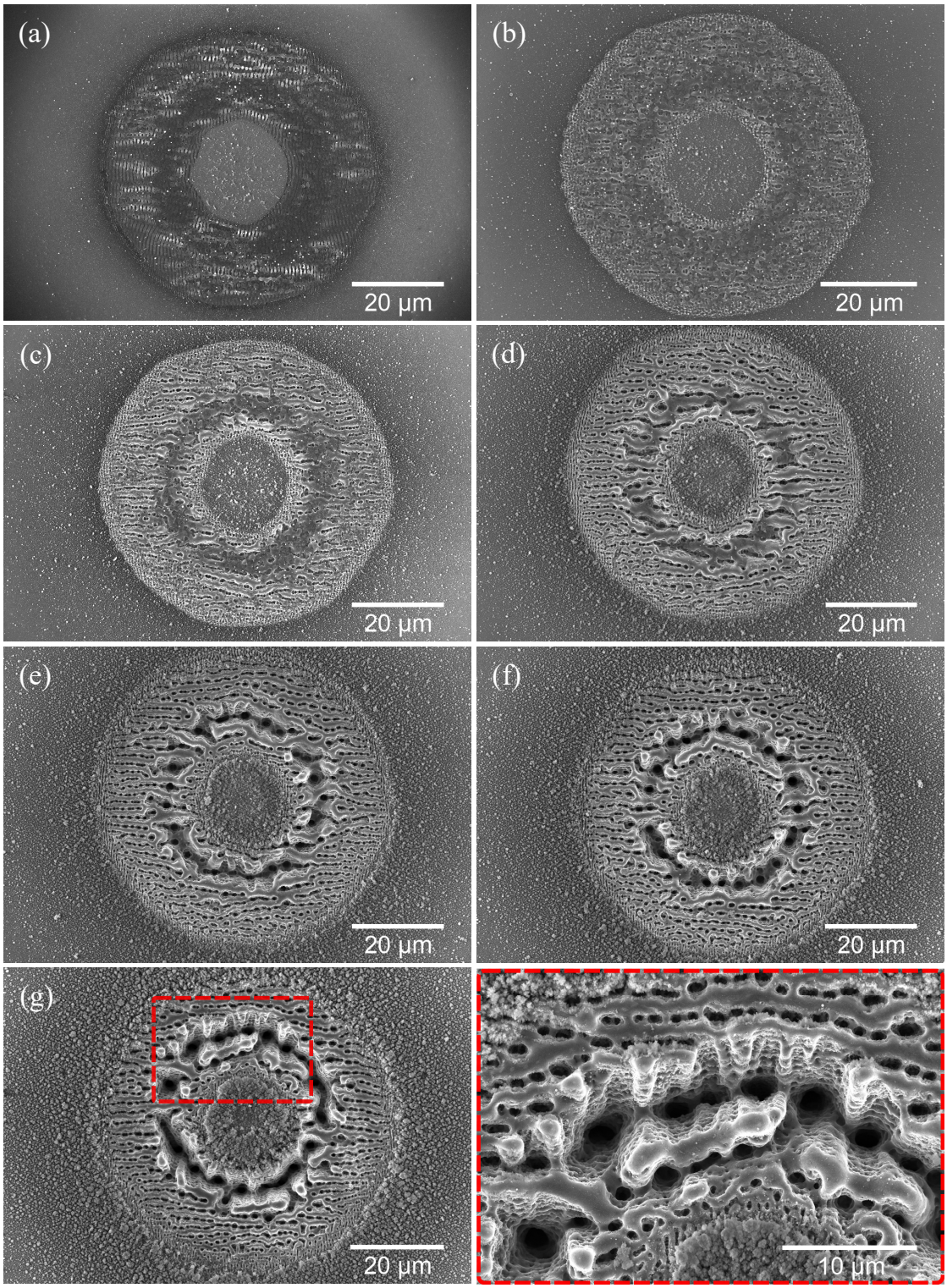

Figure 6.5: SEM micrographs of the ablated area irradiated with incident pulse energy E = 100 µJ: (a) N = 5, (b) N = 10, (c) N = 20, (d) N = 50, (e) N = 80, (f) N = 100, (g) N = 200. A zoomed view of the crater area marked with the red dash box detailing the center area of the irradiated spot also is shown.

The spatial period of these supra-grooves is almost double that of the periodicity of the grooves ($\approx$ 4.0 µm). With further increase in the number of pulses (N $\geq$ 80), the area containing supra-grooves gets drilled as shown in Figure 6.5 (e-g). These results indicate that micro-needle formation is not favoured in the low fluence regime even if we increase the number of pulses. To achieve micro-needles we have to increase the incident pulse energy, and also optimize the number of pulses. Figure 6.6 shows the surface morphology obtained with a single OV pulse having horizontal SoP, for different pulse energies. Unlike in the case of multi-pulse ablation with loose focusing, single OV beam irradiation at higher energy creates a protuberance at the center of the processed surface where the OV beam intensity is almost null. From Figure 6.6 it is evi-

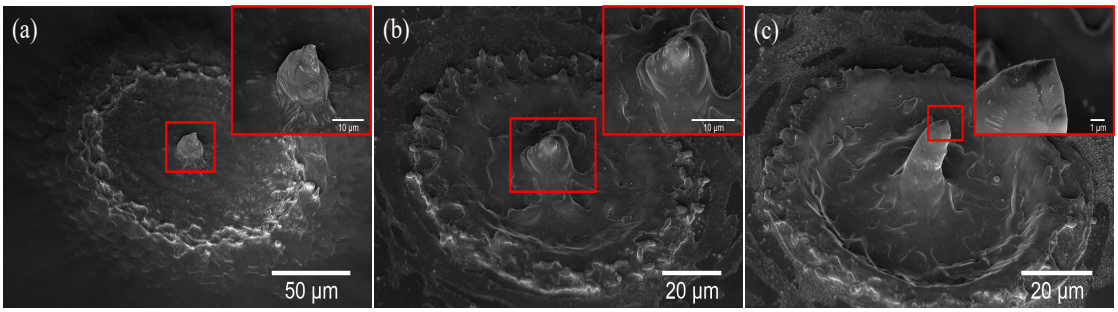

Figure 6.6: SEM micrographs showing the ablated area for single pulse ablation. Pulse energy: (a) E = 2.0 mJ, (b) E = 0.6 mJ, (c) E = 0.4 mJ.

dent that micro-needle formation with single pulse irradiation is tricky because pulses of higher energy will result in more molten Si. This pool of molten Si will self-organize in ns timescales because the reinforcement of this molten Si into a needle shape by the fs OV beam is not possible as the pulse is long gone.

Figure 6.7 illustrates the instability of the micro-needles fabricated using a single fs OV beam with horizontal SoP. It is seen that ablation with comparatively low energy E = 0.6 mJ (Figure 6.7(a)) results in the fall of the needle within the annular region, whereas in the case of E = 2.0 mJ (Figure 6.7(b)), the top part of the needle breaks away and moves out of the annular region. This could be due to the excess molten Si which falls outside the annular region once

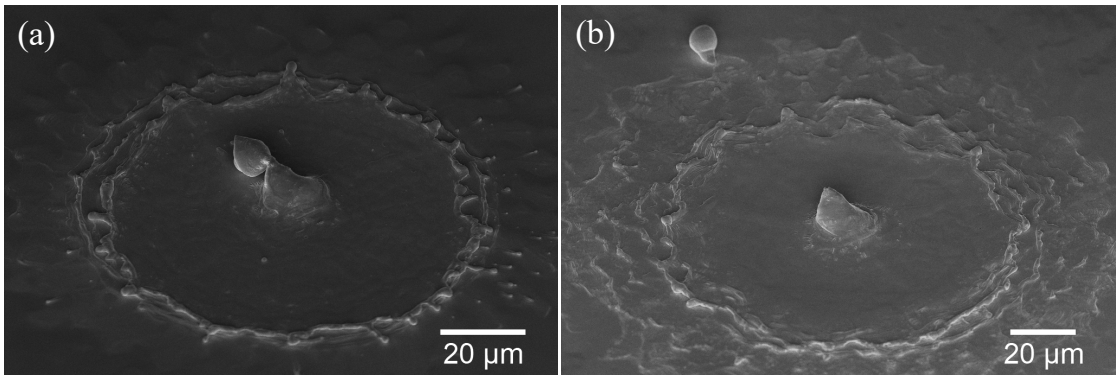

Figure 6.7: SEM micrographs of the ablated area with a single horizontally polarized OV beam: (a) E = 0.6 mJ, (b) E = 2.0 mJ.

the beam is gone. One possible solution to this problem is irradiation with successive pulses to shape the central protuberance into micro-needles. In order to further understand and optimize micro-needle fabrication, we follow the model described by Omatsu et al. [21].

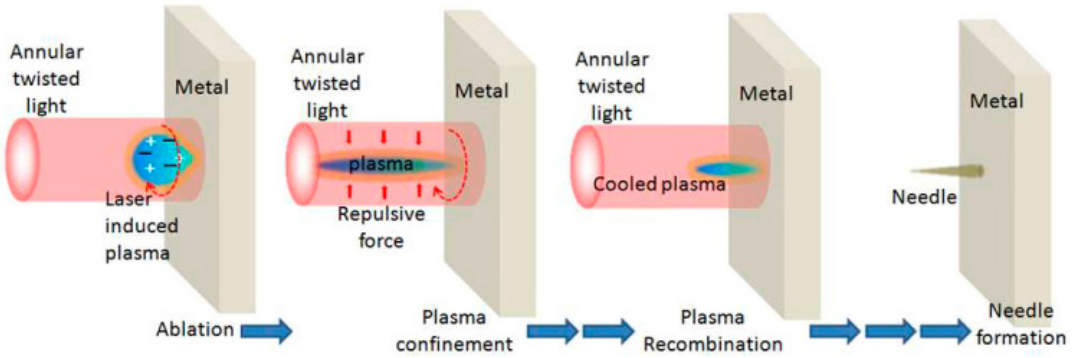

Figure 6.8: Model illustrating micro-needle fabrication on metal surfaces by using fs OV beam [21].

Figure 6.8 presents the model to illustrate the mechanism of micro-needle fabrication using OV beam ablation. The focused OV beam provides OAM to the laser-induced plasma, thereby yielding rotation of plamsa along the azimuthal direction, i.e. along the ring-shaped intensity profile of the OV beam. The SAM associated with the OV beam reinforces the orbital motion of the plasma so that it revolves around the propagation axis. Due to these motions the plasma is directed efficiently toward the on-axis null intensity region origi-

nating from the phase singularity, and gets confined in the hole by photon pressure. The plasma confined in the center by the repulsive photon pressure then recombines and accumulates at the center of the processed surface, resulting in a structured micro-needle. This model is valid in the case of OV beams with higher topological charge, and in all types of materials. Figure 6.9 shows SEM micrographs of the region structured with horizontally polarized overlaid, OV pulses of energy E = 0.6 mJ, detailing the micro-needle formation, crater morphology and chirality of the produced needle.

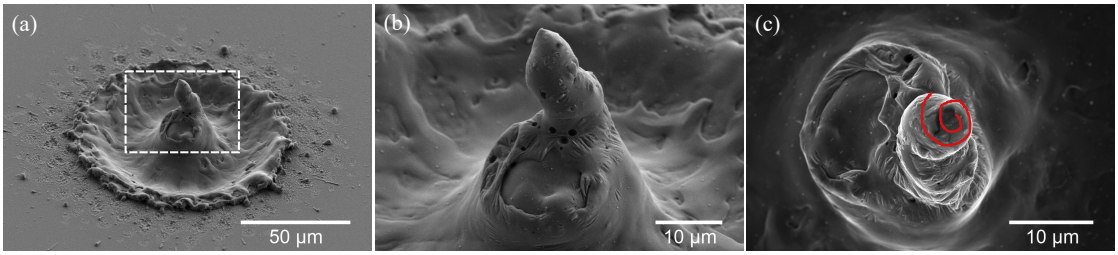

Figure 6.9: SEM micrographs of the ablated area with horizontally polarized OV beam of energy E = 0.6 mJ and N = 10: (a) Tilt view at 45° angle taken from the secondary detector in SEM, (b) Zoomed view of the area marked by the white dash box showing the morphology of the micro-needle, and (c) Top view of the micro-needle.

By varying the incident beam energy and the number of pulses being superimposed on a given spot, we find that OV pulses with energy E = 1.0 mJ and N = 10 offer an optimized irradiation condition. We have performed experiments with both linear and circular SoP to study the influence of the local SoP on the needle structure. Figure 6.10 shows SEM micrographs of the array of micro-needles fabricated with OV beam (left circular polarization) with incident beam energy E = 1.0 mJ, and zoomed views of the selected area in the micrographs illustrating the crater and micro-needle structures in detail. We observe that the local (linear or circular) SoP which generates SAM (0, ± 1) in the OV beam does not have a significant effect on micro-needle formation. This is because the role of the SAM is to augment the orbital motion of the melted Si, making its movement towards the central low intensity area either faster or slower. It must be noted that the SAM ($s = \pm 1$) can play a crucial role when combined with the

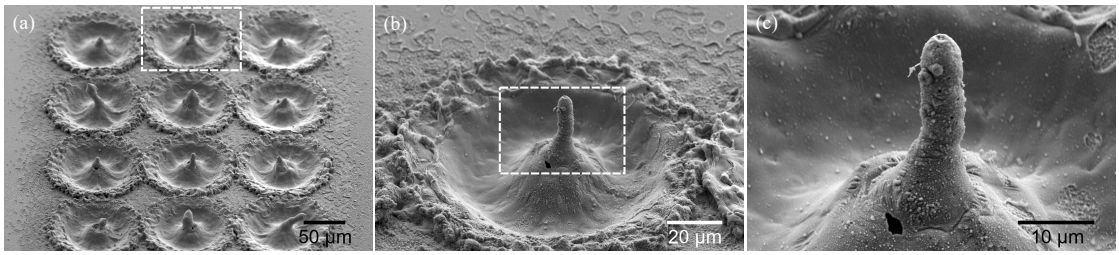

Figure 6.10: SEM micrographs illustrating (a) array of micro-needles fabricated with OV beam (left circular polarization) with incident beam energy E = 1.0 mJ, (b),(c) zoomed views of the area indicated by the white dashed box in the corresponding left SEM micrograph illustrating the crater and micro-needle structure, taken with the secondary detector. Tilt angle is 50°).

OAM of the beam ($\ell = \pm 1$), giving the total angular momentum (TAM) to be $-2 \leq J \leq 2$. We fabricated micro-needle arrays of 1×1 mm^2 and 4×4 mm^2 areas to study the SERS and wetting properties of the structured surfaces. In the next section we discuss modifications observed in the structural properties of the areas containing micro-needle arrays.

6.5 SERS and wetting applications of Si micro-needles

In the previous sections we discussed the structural properties obtained for OV beam ablated areas (planar, micro-needle) under loose and tight focusing conditions. In this section we discuss the SERS and wetting applications of the fabricated Si micro-needles. In recent years, fs laser processed surfaces have been used for SERS applications because of the high SERS enhancement factors obtained by coating with a thin film of gold (Au) or silver (Ag) after texturing [42, 43]. Even though Ag is known as the most efficient plasmonic material, its chemical instability is a drawback which limits its use in SERS substrates. In contrast, Au has a higher chemical and molecular stability compared to Ag, making it a better option for SERS. Therefore, we fabricated 100 micro-needles in 1×1 mm^2 area of silicon by fs laser irradiation and coated the

sample with a 50 nm thin film of Au for molecular detection using SERS. The sample is then annealed at a temperature of 400°C for 2 hours, which is then allowed to cool slowly overnight. Figures 6.11(a,b) show SEM micrographs of the micro-needles after sputtering 50 nm Au thin film, and after annealing the Au coated substrate, respectively. Due to annealing we observe the formation

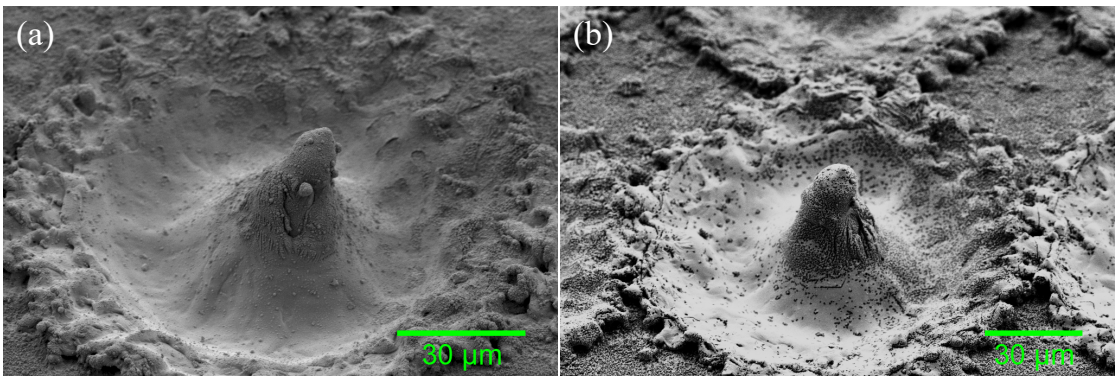

Figure 6.11: SEM micrographs showing a micro-needle fabricated using OV beam (left circular polarization) with incident beam energy E = 1.0 mJ, and N = 10. (a) after coating with 50 nm gold film via sputtering, (b) after annealing at 400°C for 2 hours.

of Au islands on the tip of the micro-needles (Figure 6.11(b)). To understand the surface composition before and after annealing, we have taken EDX spectra of different regions revealing the changes. Figures 6.12(a-c) show the regions of interest selected for EDX measurement from the Au-coated and annealed micro-needles. The inset images are the EDX spectra of the areas enclosed within the pink boxes of the respective micrographs. We use these annealed Au/Si micro-needles as SERS substrate and the dye rhodamine 6G (R6G) as a model analyte. The R6G solution of 1×10^{-3} M concentration is prepared in ethanol and the remaining concentrations are prepared by successive dilution. 2 µL volume each of the prepared R6G solutions is dropped onto the substrate with the help of a micro-syringe. The solvent evaporates off in a short period of time. Figure 6.13(a) shows Raman spectra (at 633 nm excitation) measured on a smooth bare Si wafer drop-coated with R6G-ethanol solution of concentration 1×10^{-3} M. Figure 6.13(b) presents Raman spectra obtained for concentrations ranging from 10^{-3} to 10^{-5} M, measured at the tip of the micro-needles. The spectra ex-

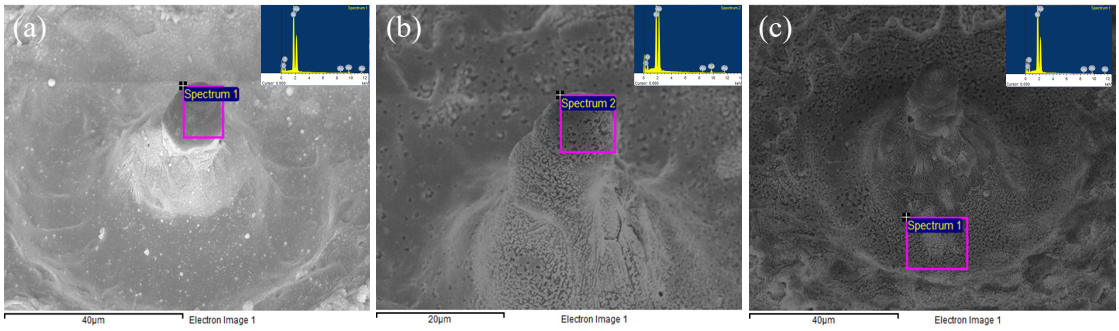

Figure 6.12: SEM micrographs of micro-needles fabricated using OV beam (left circular polarization) with incident beam energy E = 1.0 mJ and N = 10. (a) 50 nm gold-coated micro-needle, (b),(c) annealed micro-needle. Insets show EDX spectra of the areas enclosed within the pink boxes of the respective micrographs.

hibit sharp peaks at 612, 775, 1190, 1315, 1360, 1507, and 1645 cm^{-1}, respectively. The Raman peaks at 612, 775, and 1190 cm^{-1} can be attributed to the C-C-C ring in-plane vibration mode, the C-H out-of plane bending mode, and the C-H in-plane bending mode of the R6G molecule, respectively. The peak at 1313 cm^{-1} arises from the N-H in-plane bending mode while those at 1360, 1507 and 1645 cm^{-1} correspond to in-plane C-C stretching [44].

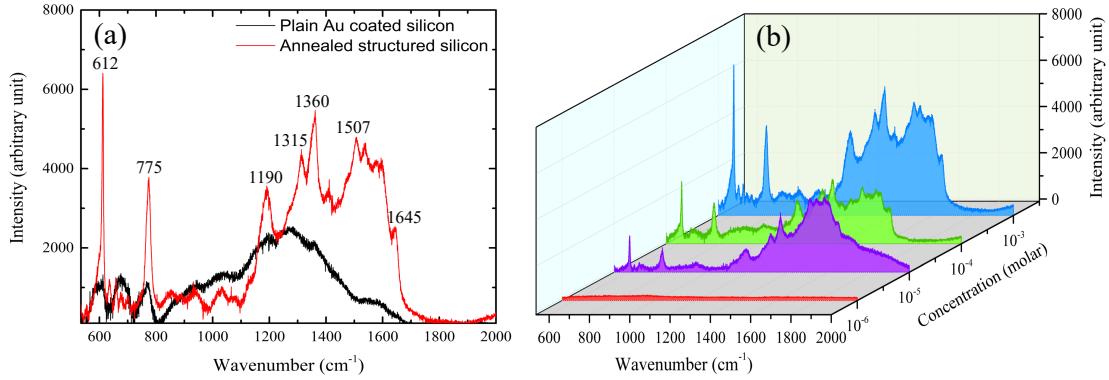

Figure 6.13: (a) Raman spectra of R6G dye ($10^{-3}M$ concentration) measured on plain silicon (without needle structure) and at the tip of the annealed micro-needle, (b) Raman spectra measured on the tips of the annealed micro-needles coated with R6G of different molar concentrations.

As the concentration of R6G decreases the intensities of the Raman peaks also decrease, and finally the spectrum vanishes at the concentration 10^{-5} M, showing that the detection limit is 10^{-5} M in the present case. The analytical

enhancement factor (AEF) of the annealed Au/Si micro-needles containing surface is calculated by the following relation [45]

$$AEF = \frac{I_{SERS}/C_{SERS}}{I_{RS}/C_{RS}} \tag{6.2}$$

where I_{SERS} is the SERS intensity measured from the SERS substrate and I_{RS} is the Raman intensity measured on the reference sample (in our case plain Au coated silicon surface) for R6G dye. C_{RS} is the concentration of R6G dye (usually higher concentration) and C_{SERS} the concentration of R6G (usually much smaller than C_{RS}) used in SERS measurement. The AEF for $C_{SERS} = 10^{-5}$ M is calculated to be $\approx 10^2$.

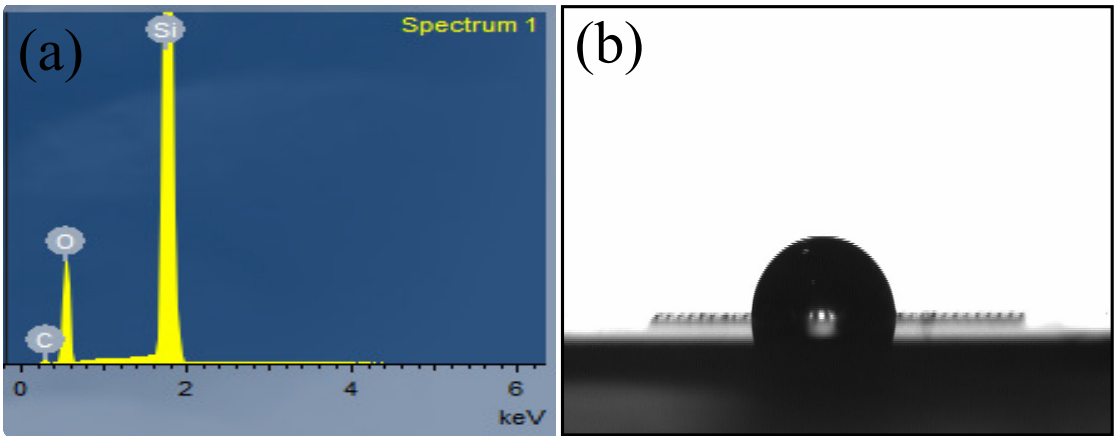

Figure 6.14: (a) Energy Dispersive X-Ray (EDX) spectrum showing the presence of silicon oxide due to structuring, (b) contact angle measurement taken after 9 months of fabrication revealing changes in the wettability (CA = 80.9 $\pm$ 4.1).

Apart from exploring the potential of Si micro-needles as SERS substrates, we have also investigated the changes induced in the surface composition of Si by fs OV beam processing. Since changes in the wetting behavior of any surface due to ablation is linked with a change in its surface composition and/or surface contamination, we analyzed the surface state of the large area containing micro-needles by using Energy Dispersive X-Ray (EDX) spectroscopy. EDX spectra measured for the structured samples (Figure 6.14(a)) show the formation of a silicon oxide layer due to oxidation in the course of laser processing in

air ambient (an oxygen peak appears in the spectrum). The laser processed area is generally found to be superhydrophilic; however contact angle (CA) measurements taken after 9 months of fabrication reveal changes in the wettability of the structured surface (Figure 6.12(b)). These findings might indicate potential applications for the wettability of the Si micro-needles.

6.6 Summary

Experimental investigations of direct surface texturing of silicon using fs OV beams generated by means of a spiral phase plate of topological charge $\ell = 4$ are reported in this chapter. Results obtained for loose focusing conditions present a way for visualizing the spatial characteristics of intense fs OV beams. An influence of the local beam polarization is observed on the generated surface structures, which suggests that this approach enables us not only to generate various unique surface structures, but also to understand and characterize the specific features of the OV beam. In particular, we have found that ripples and grooves emerge according to the incident energy and the local SoP of the OV beams. Appropriate optimization of the OV beam energy and irradiation dose allows the generation of micro-needles under tight focusing conditions. Experimental results suggest that in the case of OV beam carrying higher OAM, local SoP does not affect the formation of Si micro-needles. However, the chirality of the needle is defined by the handedness of the OV beam, providing a direct visualization of the helical beam. SERS measurements illustrate the applicability of Si micro-needles as an efficient SERS substrate. The uniqueness and versatility of fs OV beams enable the creation of complex surface structures, establishing the OV beam as a powerful tool for designing specific and well-controlled structures on solid targets.

Bibliography

[1] H He, MEJ Friese, NR Heckenberg, and H Rubinsztein-Dunlop. Direct observation of transfer of angular momentum to absorptive particles from a laser beam with a phase singularity. *Physical review letters*, 75(5):826, 1995.

[2] Kishan Dholakia, Michael Macdonald, and Gabriel Spalding. Optical tweezers: the next generation. *Physics world*, 15(10):31, 2002.

[3] David G Grier. A revolution in optical manipulation. *nature*, 424(6950):810–816, 2003.

[4] Péter Galajda and Pál Ormos. Complex micromachines produced and driven by light. *Applied Physics Letters*, 78(2):249–251, 2001.

[5] Kosta Ladavac and David G Grier. Microoptomechanical pumps assembled and driven by holographic optical vortex arrays. *Optics express*, 12(6):1144–1149, 2004.

[6] Robbert Jan Voogd, Mandeep Singh, Silvania F Pereira, AS van de Nes, and Joseph JM Braat. The use of orbital angular momentum of light beams for super-high density optical data storage. In *Frontiers in Optics*, page FTuG14. Optical Society of America, 2004.

[7] Stefan W Hell. Toward fluorescence nanoscopy. *Nature biotechnology*, 21(11):1347–1355, 2003.

[8] Lluis Torner, Juan P Torres, and Silvia Carrasco. Digital spiral imaging. *Optics express*, 13(3):873–881, 2005.

[9] Grover A Swartzlander Jr. The optical vortex lens. *Optics and photonics news*, 17(11):39–43, 2006.

[10] Stefan Bernet, Alexander Jesacher, Severin Fürhapter, Christian Maurer, and Monika Ritsch-Marte. Quantitative imaging of complex samples by spiral phase contrast microscopy. *Optics Express*, 14(9):3792–3805, 2006.

[11] L Allen, MJ Padgett, and M Babiker. Iv the orbital angular momentum of light. *Progress in optics*, 39:291–372, 1999.

[12] Les Allen, Marco W Beijersbergen, RJC Spreeuw, and JP Woerdman. Orbital angular momentum of light and the transformation of laguerre-gaussian laser modes. *Physical review A*, 45(11):8185, 1992.

[13] Cyril Hnatovsky, Vladlen G Shvedov, Wieslaw Krolikowski, and Andrei V Rode. Materials processing with a tightly focused femtosecond laser vortex pulse. *Optics letters*, 35(20):3417–3419, 2010.

[14] Kai Lou, Sheng-Xia Qian, Xi-Lin Wang, Yongnan Li, Bing Gu, Chenghou Tu, and Hui-Tian Wang. Two-dimensional microstructures induced by femtosecond vector light fields on silicon. *Optics express*, 20(1):120–127, 2012.

[15] Jijil JJ Nivas, HE Shutong, KK Anoop, A Rubano, R Fittipaldi, A Vecchione, D Paparo, L Marrucci, R Bruzzese, and S Amoruso. Laser ablation of silicon induced by a femtosecond optical vortex beam. *Optics letters*, 40(20):4611–4614, 2015.

[16] Kohei Toyoda, Katsuhiko Miyamoto, Nobuyuki Aoki, Ryuji Morita, and Takashige Omatsu. Using optical vortex to control the chirality of twisted metal nanostructures. *Nano letters*, 12(7):3645–3649, 2012.

[17] Kohei Toyoda, Fuyuto Takahashi, Shun Takizawa, Yu Tokizane, Katsuhiko Miyamoto, Ryuji Morita, and Takashige Omatsu. Transfer of light helicity to nanostructures. *Physical review letters*, 110(14):143603, 2013.

[18] Jian Wang, Jeng-Yuan Yang, Irfan M Fazal, Nisar Ahmed, Yan Yan, Hao Huang, Yongxiong Ren, Yang Yue, Samuel Dolinar, Moshe Tur, et al. Terabit free-space data transmission employing orbital angular momentum multiplexing. *Nature photonics*, 6(7):488–496, 2012.

[19] Graham Gibson, Johannes Courtial, Miles J Padgett, Mikhail Vasnetsov, Valeriy Pas'ko, Stephen M Barnett, and Sonja Franke-Arnold. Free-space information transfer using light beams carrying orbital angular momentum. *Optics express*, 12(22):5448–5456, 2004.

[20] Jijil JJ Nivas, Filippo Cardano, Zhenming Song, Andrea Rubano, Rosalba Fittipaldi, Antonio Vecchione, Domenico Paparo, Lorenzo Marrucci, Riccardo Bruzzese, and Salvatore Amoruso. Surface structuring with polarization-singular femtosecond laser beams generated by a q-plate. *Scientific reports*, 7(1):1–10, 2017.

[21] Takashige Omatsu, Keisuke Chujo, Katsuhiko Miyamoto, Masahito Okida, Kazuki Nakamura, Nobuyuki Aoki, and Ryuji Morita. Metal microneedle fabrication using twisted light with spin. *Optics express*, 18(17):17967–17973, 2010.

[22] Sergey Syubaev, Alexey Zhizhchenko, A Kuchmizhak, A Porfirev, E Pustovalov, O Vitrik, Yu Kulchin, S Khonina, and S Kudryashov. Direct laser printing of chiral plasmonic nanojets by vortex beams. *Optics Express*, 25(9):10214–10223, 2017.

[23] Ralf Dorn, Susanne Quabis, and Gerd Leuchs. Sharper focus for a radially polarized light beam. *Physical review letters*, 91(23):233901, 2003.

[24] Cyril Hnatovsky, Vladlen G Shvedov, Natalia Shostka, Andrei V Rode, and Wieslaw Krolikowski. Polarization-dependent ablation of silicon using tightly focused femtosecond laser vortex pulses. *Optics Letters*, 37(2):226–228, 2012.

[25] Matthias Meier, Valerio Romano, and Thomas Feurer. Material processing with pulsed radially and azimuthally polarized laser radiation. *Applied Physics A*, 86(3):329–334, 2007.

[26] KK Anoop, A Rubano, R Fittipaldi, X Wang, D Paparo, A Vecchione, L Marrucci, R Bruzzese, and S Amoruso. Femtosecond laser surface structuring of silicon using optical vortex beams generated by a q-plate. *Applied Physics Letters*, 104(24):241604, 2014.

[27] Jijil JJ Nivas, Shutong He, Zhenming Song, Andrea Rubano, Antonio Vecchione, Domenico Paparo, Lorenzo Marrucci, Riccardo Bruzzese, and Salvatore Amoruso. Femtosecond laser surface structuring of silicon with gaussian and optical vortex beams. *Applied Surface Science*, 418:565–571, 2017.

[28] Jijil JJ Nivas, Shutong He, Andrea Rubano, Antonio Vecchione, Domenico Paparo, Lorenzo Marrucci, Riccardo Bruzzese, and Salvatore Amoruso. Direct femtosecond laser surface structuring with optical vortex beams generated by a q-plate. *Scientific reports*, 5(1):1–12, 2015.

[29] E Allahyari, J Jj Nivas, F Cardano, R Bruzzese, R Fittipaldi, L Marrucci, D Paparo, A Rubano, A Vecchione, and S Amoruso. Simple method for the characterization of intense laguerre-gauss vector vortex beams. *Applied Physics Letters*, 112(21):211103, 2018.

[30] Fuyuto Takahashi, Katsuhiko Miyamoto, Hirofumi Hidai, Keisaku Yamane, Ryuji Morita, and Takashige Omatsu. Picosecond optical vortex

pulse illumination forms a monocrystalline silicon needle. *Scientific reports*, 6(1):1–10, 2016.

[31] Ablimit Ablez, Kohei Toyoda, Katsuhiko Miyamoto, and Takashige Omatsu. Nanotwist of aluminum with irradiation of a single optical vortex pulse. *OSA Continuum*, 4(2):403–408, 2021.

[32] Jae-Hyuck Yoo, Jung Bin In, Cheng Zheng, Ioanna Sakellari, Rajesh N Raman, Manyalibo J Matthews, Selim Elhadj, and Costas P Grigoropoulos. Directed dewetting of amorphous silicon film by a donut-shaped laser pulse. *Nanotechnology*, 26(16):165303, 2015.

[33] Sergey Syubaev, Aleksey Zhizhchenko, Oleg Vitrik, Aleksey Porfirev, Sergey Fomchenkov, Svetlana Khonina, Sergey Kudryashov, and Aleksandr Kuchmizhak. Chirality of laser-printed plasmonic nanoneedles tunable by tailoring spiral-shape pulses. *Applied Surface Science*, 470:526–534, 2019.

[34] George D Tsibidis, Evangelos Skoulas, and Emmanuel Stratakis. Ripple formation on nickel irradiated with radially polarized femtosecond beams. *Optics letters*, 40(22):5172–5175, 2015.

[35] V Yu Bazhenov, MS Soskin, and MV Vasnetsov. Screw dislocations in light wavefronts. *Journal of Modern Optics*, 39(5):985–990, 1992.

[36] Andrew Forbes, Angela Dudley, and Melanie McLaren. Creation and detection of optical modes with spatial light modulators. *Advances in Optics and Photonics*, 8(2):200–227, 2016.

[37] Filippo Cardano, Ebrahim Karimi, Sergei Slussarenko, Lorenzo Marrucci, Corrado de Lisio, and Enrico Santamato. Polarization pattern of vector vortex beams generated by q-plates with different topological charges. *Applied optics*, 51(10):C1–C6, 2012.

[38] Lorenzo Marrucci. The q-plate and its future. *Journal of Nanophotonics*, 7(1):078598, 2013.

[39] Keiichi Sueda, G Miyaji, Noriaki Miyanaga, and M Nakatsuka. Laguerre-gaussian beam generated with a multilevel spiral phase plate for high intensity laser pulses. *Optics express*, 12(15):3548–3553, 2004.

[40] Stephan Gräf and Frank A Müller. Polarisation-dependent generation of fs-laser induced periodic surface structures. *Applied Surface Science*, 331:150–155, 2015.

[41] Olga Varlamova, Florenta Costache, Markus Ratzke, and Jürgen Reif. Control parameters in pattern formation upon femtosecond laser ablation. *Applied Surface Science*, 253(19):7932–7936, 2007.

[42] Xudong Tan, Lan Jiang, Jie Hu, Pengjun Liu, Andong Wang, and Yong Lu. Highly sensitive and homogeneous sers substrate fabricated by a femtosecond laser combined with dewetting. *Chinese Optics Letters*, 13(11):111401, 2015.

[43] ZhiQing Zhu, ZhenDong Yan, Peng Zhan, and ZhenLin Wang. Large-area surface-enhanced raman scattering-active substrates fabricated by femtosecond laser ablation. *Science China Physics, Mechanics and Astronomy*, 56(9):1806–1809, 2013.

[44] Yunbo Guo, Maung Kyaw Khaing Oo, Karthik Reddy, and Xudong Fan. Ultrasensitive optofluidic surface-enhanced raman scattering detection with flow-through multihole capillaries. *Acs Nano*, 6(1):381–388, 2012.

[45] Eric C Le Ru, Evan Blackie, Matthias Meyer, and Pablo G Etchegoin. Surface enhanced raman scattering enhancement factors: a comprehensive study. *The Journal of Physical Chemistry C*, 111(37):13794–13803, 2007.

Chapter 7

Summary and future perspectives

7.1 Summary

The main problems addressed in this thesis are based on laser ablation of silicon, fused silica and quartz in the soft ablation regime (i.e. near threshold ablation) which results in laser-induced surface structures. Femtosecond and nanosecond laser pulses having Gaussian and OV beam profiles, are used to investigate the surface modifications. Laser-induced surface structuring with fs and ns laser pulses facilitates surface functionalization of solid materials by modifying their surface properties (such as optical, mechanical, chemical, biological, wetting, etc). This structuring technique enables the generation of diverse surface structures with high precision and great spatial resolution for various applications. We have investigated silicon, fused silica and quartz for structuring because of their diverse applications ranging from biophysics to opto-electronics.

The initial work reported in this thesis illustrates various aspects of fs laser-induced periodic surface structuring of crystalline silicon, which provides in-depth information about the generation of various quasi-periodic structures and the mechanisms involved in their formation. We have investigated the role of laser parameters (laser pulse energy (E), wavelength (λ) and polarization), and irradiation parameters (number of pulses (N), ambient pressure) on

the fabrication of fs-LIPSS patterns. In particular, we have investigated the influence of different ambient pressures ranging from 10^{-5} Torr to 760 Torr on ripples formation. Our experimental findings indicate that there is a substantial backward deposition of the nanoparticles fraction of the ablated material at higher pressures, which significantly influences the generation and morphology of the surface structures. To fabricate large area surfaces consisting of LIPSS, we have optimized the irradiation conditions (E = 80 μJ and N = 100 at 800 nm, and E = 4 μJ and N = 100 at 400 nm, respectively). The spatial period of the induced structures is found to be slightly lower than that of the laser wavelength in both cases, verifying the validity of the static (interference) model of LIPSS formation. A substantial reduction in optical reflectivity is observed from the structured surface because of multiple reflections from the nanostructures. Laser-induced breakdown spectroscopy (LIBS) measurements exhibit a discernible enhancement in the optical emission intensity of the plasma by 50% - 90%, whereas Faraday cup (FC) measurements show an enhancement in ion current by about 34%. These results give clear evidence of improved laser coupling when the Si target is nanostructured. Another interesting indication of enhanced light coupling is the appearance of spectral lines associated with the doubly ionized Si species from Si-LIPSS plasma. These experiments establish the laser-induced periodic surface structuring technique as a versatile tool for making anti-reflective surfaces.

Next, we investigated fs laser-induced surface structuring of two dielectric materials: fused silica and quartz. We have addressed the mechanisms involved in the generation of quasi-periodic surface structures. The effect of crystallographic orientation in ripples formation is explored by using the targets under identical irradiation conditions. The variety of fs-LIPSS quasi-periodic ripples and micron-sized grooves with different preferential alignments (parallel and perpendicular) depending on the irradiation parameters (laser fluence and the number of pulses) are investigated in detail. Ripples generation is explained as

a result of inhomogeneous absorption of the laser pulse energy due to an energy modulation over the laser-irradiated surface. A large area is structured after optimizing the surface structures with the optimized scan speed, to investigate optical and morphological modifications caused by fs-surface structuring. Raman and PL spectra indicate material densification process and increase in the number of defects (ODCs and PORs) upon structuring. The laser-irradiated surface exhibits reduced transmittance in comparison to that of untreated fused silica. The transmittance decrease can be explained by scattering from micro-/nano-structures and material property degradation by laser irradiation. Furthermore, contact angle measurements indicate the formation of superhydrophilic fused silica surface via fs-laser irradiation. The surface roughness (due to the presence of micro-/nano-structures) and the surface energy result in superhydrophilicity.

We then demonstrated fabrication of micro-/nano-textured silicon surfaces using nanosecond laser pulses. The hierarchical structures obtained consist of microscale channels and self-organized surface nano-capillaries decorated with randomly distributed silicon nanoparticles. Concentric nano-ripples found around the crater rim show sub-wavelength spatial periodicity (50-100 nm) with silica nano-foam decoration on top. Our experimental findings suggest the formation of silicon oxide on the irradiated surface, with the atomic percentage of oxygen increasing with laser fluence. These structures result in a durable superhydrophilic silicon surface (C.A. $\approx 5^{\circ}$), with the superhydrophilicity being stable even after being exposed to the atmosphere for about three months. The generalized Wenzel's equation describes the wetting behavior of these samples by taking into account homogeneous liquid penetration due to the formation of nano-capillaries and silica nano-foam. In short, we have illustrated a cost-effective and single-step method which does not need additional chemical processing for modifying the wettability of solid surfaces for multi-functional applications.

In addition to the studies performed using a conventional laser beam with

Gaussian intensity profile, we have studied the ablation of crystalline silicon with the optical vortex (OV) beam (having dough-nut shaped intensity profile) as well. In particular, we have experimentally investigated surface texturing using fs-OV beams generated by means of a spiral phase plate of topological charge $\ell = 4$. We have observed the influence of local beam polarization on the generated surface structures, which suggests that this approach enables us not only to generate various unique surface structures but also to understand and characterize specific features of the OV beam. In particular, we have found that ripples and grooves emerge according to the incident energy and the local polarization state of the OV beams. Optimization of the OV beam energy and irradiation dose (number of pulses) allow the generation of complex surface structures such as micro-needles under tight focusing conditions. Experimental findings suggest that in the case of OV beam carrying higher orbital angular momentum, local polarization state of the OV beam does not affect the formation of Si micro-needles. However, the chirality of the needle is defined by the handedness of the OV beam which provides direct visualization of the helical beam shape. Our SERS measurements illustrate the applicability of Si micro-needles as an efficient SERS substrate. The uniqueness and versatility of the fs-OV beams enables both the design of unconventional surface structures, and also the characterization of complex ultrashort laser beams.

7.2 Future perspectives

The surface structures generated after optimizing various parameters such as pulse energy (E), number of pulses (N), state of polarization (SoP), ambient pressure, spatial beam profile (Gaussian or OV) etc. can be exploited for tuning the surface properties of various materials (such as anti-reflection or structural coloration, superhyrophilicity/superhydrophobicity, and plasmonic nature). Additionally, OV beams carrying OAM facilitate more complex surface

texturing. Recent studies in laser ablation by OV pulses of ps or ns duration have revealed the formation of chiral nano-needles in metals which may lead to advanced photonic devices (for instance, metamaterials for ultrasensitive detection and reactions for chiral chemical composites). Moreover, micro-/nano-needles formation by employing fs-OV beam with higher topological charge has not been explored thoroughly. Femtosecond OV beams having higher OAM and complex profile can be generated by tuning the state of polarization, topological charge and spatial profile, and these can be employed to fabricate exotic surface patterns on variety of materials. Arrays of complex surface structures will be fabricated in future for numerous diverse applications ranging from biological and chemical-sensing to metamaterials and plasmonic devices.